Optical, microphysical and physico-chemical properties of aerosols using in situ and remote sensing measurements in Athens Metropolitan and the Eastern Mediterranean Area

by

Stergios Vratolis

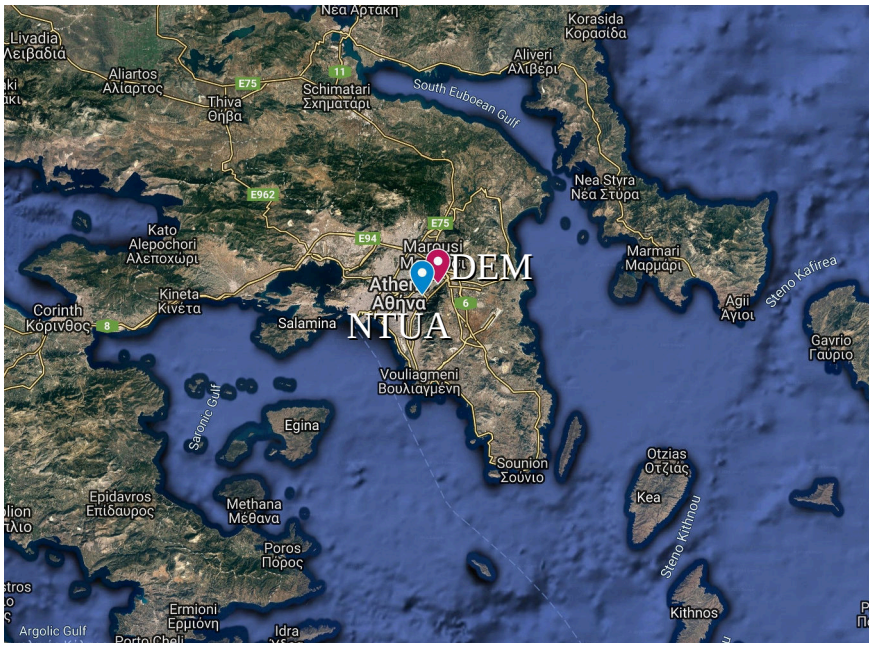

Ph.D. Thesis Supervisor: Prof. Alexandros Papayannis
NATIONAL TECHNICAL UNIVERSITY OF ATHENS
School of Applied Mathematical and Physical Sciences

November 28, 2019

Abstract

The main objective of this Ph.D. Thesis was to study the concentration, physical properties, and chemical composition of aerosols and their contribution to cloud formation in the Eastern Mediterranean, with emphasis on the Athens Metropolitan Area, using in situ and remote sensing measurement techniques. Other objectives include the contribution to new methods to deduct properties of the atmospheric aerosol and the comparison of aerosol measurements conducted by in situ and remote sensing instruments.

This Thesis is structured in five chapters. In Chapter 1, we present the physical, chemical and optical properties of aerosols, their impact on climate and health, and the factors affecting aerosol concentration in the study area. We also present the NTUA Raman Lidar (EOLE) and the operation principle of Wind Doppler Lidar.

In Chapter 2, we introduce the current situation of aerosol particle number concentration in City-Centre Urban Background, Urban Background and Regional Background stations in Greece. Based on the diurnal variations and previous studies, main sources for the City-Centre Urban Background station that were identified are traffic (freshly emitted and aged) and the regional background concentration. Sources for the Urban Background stations include fresh traffic and nucleation, aged traffic and cooking, and the regional background concentration. The Regional Background station dominant sources are local aged sources (cooking and other sources related to tourism) and the regional background concentration. Size distribution modal analysis was applied to the particle number concentration data and the results were subsequently divided in clusters. If we make the assumption that the accumulation cluster identified at the Regional Background station corresponds to the transported from other areas particle fraction, and use the median number concentration from each cluster, we conclude that 18% of the particle number distribution is transported at the City-Centre Urban Background site, 37% at the Urban Background sites, and 59% at the Regional Background site. Based on the air mass origin clustering of the regional background concentration, we concluded that the regional particle number concentrations when air masses originate from the Mediterranean Sea is much lower than when they originate from the North-East and North-West direction. Etesian flow conditions were found to increase the regional background particle concen-

tration in the Mediterranean basin by a factor of 2.5 to 4.

Chapter 3 deals with the deduction of a new method to retrieve the real part of the equivalent refractive index of atmospheric aerosols by combining the size distributions obtained by a Scanning Mobility Particle Sizer (SMPS) and an Optical Particle Counter (OPC). The objective is to show that size distribution data acquired at in situ measurement stations can provide an insight to the physical and chemical properties of aerosol particles, leading to better understanding of aerosol impact on human health and earth radiative balance. The resulting ERI could be used in radiative transfer models to assess aerosol forcing direct effect, as well as an index of aerosol chemical composition. To validate the method, a series of calibration experiments were performed using compounds with known refractive index (RI). This led to a corrected version of the ERI values, (ERI_{COR}). The ERI_{COR} values were subsequently compared to model estimates of RI values, based on measured $PM_{2.5}$ chemical composition, and to aerosol RI retrieved values by inverted lidar measurements on selected days.

The subject of Chapter 4 is to find the atmospheric conditions that allow the direct comparison of in situ and remote sensing measurements. This is a very important point as it will allow collocating in situ and remote sensing aerosol measurement stations to combine their measurements, so as to investigate the vertical mixing of aerosols and acquire a profile of aerosol properties extending from ground level to several km above ground level (agl). Thus, we will obtain an insight on how regional aerosol is added to local aerosol, especially during pollution events due to long range transport (Sahara dust, Biomass Burning, etc.). On selected days that displayed significant turbulence up to approximately 1,000 m above ground level (agl), we acquired the aerosol extinction or scattering coefficient by in situ instruments using three methods. In the first method the aerosol extinction coefficient was acquired by adding a Nephelometer scattering coefficient in ambient conditions and an Aethalometer absorption coefficient. The correlation between the in situ and remote sensing instruments was good (coefficient of determination R^2 equal to 0.74). In the second method we acquired the aerosol refractive index by fitting dry Nephelometer and Aethalometer measurements with Mie code calculations of the scattering and absorption coefficients for the size distribution up to 1,000 nm obtained by in situ instruments. The correlation in this case was reasonably good (R^2

equal to 0.62). Our next step was to compare the extinction coefficient acquired by remote sensing instruments to the scattering coefficient calculated by Mie code using the size distribution up to 1,000 nm and ERI_{COR}, which is the real part of the equivalent refractive index acquired by the comparison of the size distributions obtained by a Scanning Mobility Particle Sizer (SMPS) and an Optical Particle Counter (OPC). The agreement between the in situ and remote sensing instruments in this case was not good (R^2 equal to 0.45). The last comparison for the selected days was between the aerosol extinction Ångström exponent acquired by in situ and remote sensing instruments. The correlation was not good (R^2 equal to 0.4), probably due to differences in the number size distributions present in the air volumes measured by in situ and remote sensing instruments. Nevertheless, if turbulent conditions prevail in the atmosphere, extending from ground level up to the height at which the lidar measurements take place, good agreement between the extinction coefficients of in situ and remote sensing instruments can be achieved, as indicated by the first two methods mentioned earlier. Furthermore, we also present a day that a Saharan dust event occurred in Athens. At first, the Saharan dust layer was evident in lidar measurements at a height of 2,000 m agl. Due to the high turbulence in the atmosphere, in the afternoon the Saharan dust layer gradually descended to ground level and it was detected by in situ instruments. The origin of air masses from North Africa reaching Athens was also depicted by FLEXPART air mass transport model 3-hourly plots. Thus, we obtained an insight on how regional aerosol is added to local aerosol, especially during pollution events due to long range transport.

Finally, the conclusions and perspectives for future studies are provided in Chapter 5.

Greek Abstract

Ο κύριος στόχος της διατριβής αυτής ήταν η μελέτη της συγκέντρωσης, των φυσικών ιδιοτήτων και της χημικής σύστασης των αιωρούμενων σωματιδίων και η συνεισφορά τους στον σχηματισμό των σύννεφων στην Ανατολική Μεσόγειο με έμφαση στην Μητροπολιτική περιοχή της Αθήνας. Έπίσης ο προσδιορισμός των ιδιοτήτων των αιωρούμενων σωματιδίων με νέες μεθόδους και η σύγκριση των μετρήσεων ανάμεσα σε επιτόπια όργανα και όργανα τηλεπισκόπησης.

Η παρούσα περίληψη της διδακτορικής διατριβής περιέχει τρία κεφάλαια. Στο πρώτο κεφάλαιο παρουσιάζουμε την παρούσα κατάσταση της κατανομής μεγέθους και αριθμού των αιωρούμενων σωματιδίων σε σταθμούς αστικού υποβάθρου Κέντρου Πόλης (ΑΥΚΠ), αστικού υποβάθρου (ΑΥ) και σταθμούς αντιπροσωπευτικούς της ευρύτερης περιοχής της Ανατολικής Μεσογείου (ΕΥ). Με βάση την ημερήσια διακύμανση των κατανομών και προηγούμενες μελέτες, οι κύριες πηγές αιωρούμενων σωματιδίων για τον σταθμό ΑΥΚΠ είναι η κυκλοφορία οχημάτων (πρόσφατες και γηρασμένες εκπομπές) και οι συγκεντρώσεις υποβάθρου της ευρύτερης περιοχής. Οι πηγές για τους σταθμούς ΑΥ περιλαμβάνουν πρόσφατες εκπομπές οχημάτων, πυρηνοποίηση νέων σωματιδίων, γηρασμένες εκπομπές οχημάτων, εκπομπές λόγω μαγειρέματος και συγκεντρώσεις υποβάθρου της ευρύτερης περιοχής. Οι πηγές για τον σταθμό ΕΥ περιλαμβάνουν τοπικές πηγές (γηρασμένο αεροζόλ από μαγείρεμα και άλλες δραστηριότητες που συνδέονται με τον τουρισμό και τις γειτονικές πόλεις στην Κρήτη) και την συγκέντρωση υποβάθρου της ευρύτερης περιοχής. Αναλύσαμε τις κατανομές μεγέθους και αριθμού αιωρούμενων σωματιδίων σε άθροισμα λογαριθμικών κατανομών τις οποίες κατόπιν χωρίσαμε με βάση ανάλυση ομάδων. Με βάση την υπόθεση ότι η ομάδα στην περιοχή συσσώρευσης αιωρούμενων σωματιδίων που αναγνωρίστηκε στον σταθμό ΕΥ περιέχει αυτά που μεταφέρονται από μακρινές περιοχές και την χρήση της διάμεσης τιμής της συγκέντρωσης για κάθε ομάδα, συμπεραίνουμε ότι 18% της συγκέντρωσης αιωρούμενων σωματιδίων στον σταθμό ΑΥΚΠ μεταφέρεται από μακρινές περιοχές, το 37% για τους σταθμούς ΑΥ και το 59% για τον σταθμό ΕΥ. Βασισμένοι στον χωρισμό σε ομάδες με βάση την προέλευση των αερίων μαζών για την ομάδα που αναγνωρίστηκε ως μεταφερόμενη από μακρινές περιοχές, συμπεραίνουμε ότι η συγκέντρωση αιωρούμενων σωματιδίων όταν οι αέριες μάζες προέρχονται από την Μεσόγειο Θάλασσα είναι πολύ χαμηλότερες από οταν προέρχονται από Βόρειο-Ανατολική ή Βόρειο-Δυτική κατεύθυνση. Όταν επικρατούν οι Ετησίες η συγκέντρωση υποβάθρου στην περιοχή της Μεσογείου αυξάνεται από

2,5 έως 4 φορές.

Στο δεύτερο κεφάλαιο αναπτύσσεται μία νέα μέθοδος για την απόκτηση του πραγματικού μέρους του ισοδύναμου δείκτη διάθλασης του ατμοσφαιρικού αερολύματος με τον συνδυασμό των κατανομών μεγέθους και αριθμού ενός διαφορικού καταμετρητή αιωρούμενων σωματιδίων με βάση την ηλεκτρική κινητικότητα (ΔΚΗΚ) και έναν οπτικό καταμετρητή σωματιδίων (ΟΚΣ). Ο σκοπός είναι να δείξουμε ότι τα δεδομένα κατανομής αριθμού σωματιδίων που λαμβάνονται σε σταθμούς μετρήσεων μπορούν να μας δώσουν μια αίσθηση για τις φυσικές και χημικές ιδιότητες των αιωρούμενων σωματιδίων και να οδηγήσουν έτσι σε καλύτερη κατανόηση των επιδράσεών τους στο κλίμα και την ανθρώπινη υγεία. Ο προκύπτων ενεργός δείκτης διάθλασης (ERI) μπορεί να χρησιμοποιηθεί σε μοντέλα μεταφοράς ακτινοβολίας και ως δείκτης της χημικής σύστασης των αιωρούμενων σωματιδίων. Για την πιστοποίηση της μεθόδου, έγιναν μια σειρά από πειράματα βαθμονόμησης με χρήση ενώσεων και υλικών με γνωστό δείκτη διάθλασης (ΔΔ). Έτσι λάβαμε τον διορθωμένο δείκτη διάθλασης (ERI_{COR}). Οι τιμές ERI_{COR} κατόπιν συγκρίθηκαν με υπολογισμούς της τιμής του δείκτη διάθλασης των αιωρούμενων σωματιδίων RI βασισμένες στη χημική σύσταση φίλτρων $PM_{2.5}$ και σε μετρήσεις lidar .

Το τρίτο κεφάλαιο ασχολείται με την εύρεση των απαραίτητων συνθηκών ώστε να επιτραπεί η απευθείας σύγκριση των μετρήσεων με επιτόπια όργανα και με όργανα τηλεπισκόπησης. Το θέμα αυτό είναι πολύ σημαντικό, καθώς θα επιτρέψει σε σταθμούς με επιτόπια όργανα και με όργανα τηλεπισκόπησης εγκατεστημένους σε μικρή απόσταση μεταξύ τους να συνδυάσουν τις μετρήσεις τους, έτσι ώστε να είναι δυνατή η διερεύνηση της καθ'ύψος ανάμιξης των αιωρούμενων σωματιδίων και η λήψη της κατακόρυφης κατανομής των ιδιοτήτων τους από το έδαφος έως αρκετά χιλιόμετρα πάνω από το έδαφος (agl). Για επιλεγμένες μέρες όπου είχαμε σημαντική τύρβη στην ατμόσφαιρα μέχρι ένα ύψος περίπου 1.000 μέτρων πάνω από το έδαφος, υπολογίσαμε τον συντελεστή εξασθένισης με βάση δεδομένα από τα όργανα επιτόπιων μετρήσεων χρησιμοποιώντας τρεις μεθόδους. Στην πρώτη μέθοδο ο συντελεστής εξασθένισης των αιωρούμενων σωματιδίων προέκυψε από την πρόσθεση του συντελεστή σκέδασης του οργάνου «Νεφελόμετρο» και του συντελεστή απορρόφησης του οργάνου «Αιθαλόμετρο». Κατόπιν τον συγκρίναμε με τον συντελεστή εξασθένισης του οργάνου τηλεπισκόπησης. Η συσχέτιση στην περίπτωση αυτή ήταν καλή (συντελεστής προσδιορισμού R^2 ίσος με 0,74). Στην δεύτερη μέθοδο υπολογίσαμε τον δείκτη διάθλασης προσαρμόζοντας τις μετρήσεις συντελεστών σκέδασης και απορρόφησης Νεφελομέτρου και

Αιθαλομέτρου χρησιμοποιώντας υπολογισμούς κώδικα Mie με βάση την κατανομή αριθμού και μεγέθους σωματιδίων που λάβαμε από τα όργανα επιτόπιων μετρήσεων. Κατόπιν με τον δείκτη διάθλασης που υπολογίστηκε και την κατανομή μεγέθους και αριθμού των αιωρούμενων σωματιδίων, υπολογίσαμε τον συντελεστή εξασθένισης και τον συγκρίναμε με τις μετρήσεις τηλεπισκόπησης. Η συσχέτιση και στην περίπτωση αυτή ήταν ικανοποιητική (R^2 ίσος με 0,62). Επίσης παρουσιάζουμε μία ημέρα όπου στην περιοχή της Αθήνας είχαμε ένα επεισόδιο ρύπανσης από σκόνη της Σαχάρας. Αρχικά το στρώμα της ατμόσφαιρας που περιείχε την σκόνη της Σαχάρας ανιχνεύθηκε από το όργανο τηλεπισκόπησης σε ύψος μεγαλύτερο των 1.500 μέτρων πάνω από την επιφάνεια της θάλασσας. Λόγω της ισχυρής τύρβης στην ατμόσφαιρα, το απόγευμα το στρώμα αυτό αναμίχθηκε με το τοπικό αερόλυμα και ανιχνεύθηκε από τα όργανα επιτόπιων μετρήσεων. Η προέλευση των αερίων μαζών από την Νότια Αφρική παρουσιάζεται επίσης με χρήση του μοντέλου ατμοσφαιρικής μεταφοράς FLEXPART.

Κατανομή μεγέθους και αριθμού των αιωρούμενων σωματιδίων σε αστικούς σταθμούς, σταθμούς αστικού υποβάθρου, και σταθμούς αντιπροσωπευτικούς της ευρύτερης περιοχής της Ανατολικής Μεσογείου.

Αποτελέσματα

Το καλοκαίρι του 2012 πραγματοποιήσαμε μετρήσεις κατανομής μεγέθους και αριθμού αιωρούμενων σωματιδίων σε σταθμούς αστικού υποβάθρου κέντρου πόλης, σταθμούς αστικού υποβάθρου, και σταθμούς αντιπροσωπευτικούς της ευρύτερης περιοχής της Ανατολικής Μεσογείου.

Παρουσίαση κατανομών μεγέθους και αριθμού

Στο Σχήμα i παρουσιάζουμε τον γεωμετρικό μέσο g_m και το 16^o - 84^o εκατοστημόριο της κατανομής μεγέθους και αριθμού για τους σταθμούς Αστικού Υποβάθρου Κέντρου Πόλης (ΑΥΚΠ), Αστικού Υποβάθρου (ΑΥ), Ευρύτερου Υποβάθρου (ΕΥ) για τις χρονικές περιόδους του πίνακα i.

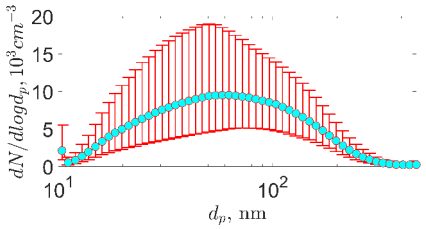

(α′) Αστικό Υπόβαθρο Κέντρου Πόλης

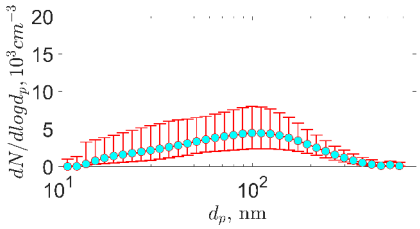

(β′) Αστικό Υπόβαθρο

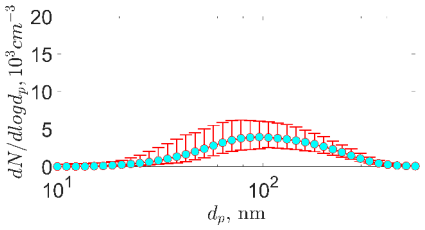

(γ′) Ευρύτερο Υπόβαθρο

Σχήμα i: Γεωμετρική μέση τιμή g_m , 16^o - 84^o εκατοστημόριο της κατανομής μεγέθους και αριθμού.

Πίνακας i: Χρονικές περίοδοι μετρήσεων κατανομής μεγέθους και αριθμού αιωρούμενων σωματιδίων που παρουσιάζονται στην παρούσα εργασία.

Σταθμός	**Πόλη**	**Περίοδος Δειγματοληψίας**	**Είδος Σταθμού**	**Χρονική Κάλυψη**
Patras-C	Πάτρα	$8^{η}$ Ιουνίου - $26^{η}$ Ιουλίου	Αστικό Υπόβαθρο Κέντρου Πόλης	95%
ICE-HT	Πάτρα	$8^{η}$ Ιουνίου - $21^{η}$ Ιουλίου	Αστικό Υπόβαθρο	89%
DEM	Αθήνα	$1^{η}$ Ιουνίου - $2^{η}$ Αυγούστου	Αστικό Υπόβαθρο	82%
EPT	Θεσσαλονίκη	$9^{η}$ Ιουνίου - $22^{η}$ Ιουλίου	Αστικό Υπόβαθρο	99%
FIN	Φινοκαλιά	$1^{η}$ Ιουνίου - $31^{η}$ Ιουλίου	Ευρύτερο Υπόβαθρο	94%

Ο σταθμός Αστικού Υποβάθρου Κέντρου Πόλης εμφανίζει κορυφή στα 60 nm , υποδεικνύοντας ένα μίγμα από πρόσφατες εκπομπές οχημάτων και πιο γηρασμένες εκπομπές οχημάτων, ενώ παρουσιάζει τις υψηλότερες τιμές συγκέντρωσης αιωρούμενων σωματιδίων. Στην βιβλιογραφία δηλώνεται ότι σε έναν σταθμό αστικού υποβάθρου στην Βαρκελώνη (περίοδος δειγματοληψίας $30^{η}$ Ιουλίου 2012 - $4^{η}$ Αυγούστου 2013) τοποθετημένο σε απόσταση 350 μέτρων από έναν πολυσύχναστο αυτοκινητόδρομο (9.000 οχήματα ανά εργάσιμη ημέρα), η συγκέντρωση αιωρούμενων σωματιδίων κυμαινόταν ανάμεσα στα $7.500 \pm 5.000\ cm^{-3}$ (μέση συγκέντρωση $\pm$ σταθερά απόκλισης). Στο ίδιο εύρος διαστήματος μεγέθους στον σταθμό Αστικού Υποβάθρου Κέντρου Πόλης (ΑΥΚΠ) οι αντίστοιχες τιμές ήταν 8.200 ± 5.800 cm^{-3}. Η κατανομή μεγέθους και αριθμού στους σταθμούς Αστικού Υποβάθρου παρουσιάζει μια επιμήκη μορφή, υποδεικνύοντας πολλαπλές πήγες οι οποίες έχουν αναμιχθεί. Εκτός από το γηρασμένο τμήμα της κατανομής που αντιστοιχεί στο κλάσμα συσσώρευσης, διακρίνεται επίσης μια κορυφή που αντιστοιχεί στο κλάσμα Aitken. Οι σταθμοί Αστικού Υποβάθρου επηρεάζονται σημαντικά από τις εκπομπές οχημάτων και την κατοπινή αύξηση μεγέθους των αιωρούμενων σωματιδίων λόγω απορρόφησης αερίων και συμπύκνωσης υδρατμών. Στην βιβλιογραφία δηλώνεται ότι στον σταθμό Montelibretti (περίοδος

δειγματοληψίας $26^{η}$ Σεπτεμβρίου 2007 - $7^{η}$ Μαΐου 2009), έναν σταθμό τοποθετημένο σε απόσταση 30 km βορειοδυτικά της Ρώμης, η συγκέντρωση αιωρούμενων σωματιδίων στο εύρος 17,5 - 100 nm ήταν $5.000 \pm 3.000\ cm^{-3}$ (μέση συγκέντρωση ± σταθερά απόκλισης). Ο σταθμός Ευρύτερου Υποβάθρου παρουσιάζει κορυφή στα 100 nm και την χαμηλότερη συγκέντρωση από όλους του σταθμούς. Στην βιβλιογραφία δηλώνεται ότι ένα γηρασμένο κλάσμα συσσώρευσης με κορυφή στα 100 nm παρατηρείται συχνά στην Φινοκαλιά. Το κλάσμα της κατανομής με κορυφή στα 100 nm μπορεί να αποδοθεί σε ένα μίγμα γηρασμένου αερολύματος (μεταφερόμενο από πηγές της ευρύτερης περιοχής) και αερολύματος ενδιάμεσης γήρανσης από κοντινές πόλεις στο νησί της Κρήτης.

Η κατανομή μεγέθους και αριθμού σωματιδίων σε κάθε σταθμό χωρίστηκε σε τμήματα με βάση το μέγεθος των σωματιδίων. Με χρήση της ημερήσιας διακύμανσης των τμημάτων αυτών και προηγούμενες μελέτες, συμπεράναμε ότι οι κύριες πηγές για τον ΑΥΚΠ σταθμό είναι εκπομπές οχημάτων και το υπόβαθρο της ευρύτερης περιοχής, για τους ΑΥ σταθμούς πρόσφατες εκπομπές οχημάτων, γηρασμένες εκπομπές οχημάτων και το υπόβαθρο και για τον ΕΥ σταθμό οι τοπικές ασχολίες (τουρισμός, μαγειρεμα) και η συγκέντρωση υποβάθρου. Η μεσαία τιμή της συγκέντρωσης αριθμού που οφείλεται στην συγκέντρωση του ευρύτερου υποβάθρου είναι 13% για τον σταθμό ΑΥΚΠ, 29% για τους σταθμούς ΑΥ και 45% για τον σταθμό ΕΥ.

Παραγωγή νέων σωματιδίων με πυρηνοποίηση

Στην Φινοκαλιά σε 61 μέρες μετρήσεων είχαμε 5 περιπτώσεις παραγωγής σωματιδίων με πυρηνοποίηση, 5 περιπτώσεις πυρηνοποίησης στον σταθμό DEM σε 54 ημέρες και 4 περιπτώσεις στον σταθμό EPT σε 43 ημέρες, ενώ στους σταθμούς Patras-C, ICE-HT δεν βρέθηκε καμία. Στον πίνακα ii παρουσιάζεται το πόσο ισχυρή ήταν η συνεισφορά της πυρηνοποίησης σε κάθε σταθμό. Βρέθηκε ότι τα σωματίδια στην περιοχή μεγέθους 10-20 nm , για όλο το χρονικό διάστημα της καμπάνιας μετρήσεων, προέρχονται από πυρηνοποίηση σε ποσοστό 4% για τον σταθμό DEM, 12% για τον σταθμό EPT και 1% για τον σταθμό FIN.

Επομένως η συνεισφορά της πυρηνοποίησης στον σχηματισμό νεφών ήταν ασήμαντη στην Ανατολική Μεσόγειο την εξεταζόμενη περίοδο.

Πίνακας ii: Απόλυτη και σχετική συνεισφορά στους σταθμούς DEM, EPT, FIN στο εύρος μεγέθους N_{10-20}, (cm^{-3}). N_{NPF} είναι η μέση ημερήσια συγκέντρωση αιωρούμενων σωματιδίων που έχουν παραχθεί με πυρηνοποίηση, N_{Bg} είναι η μέση ημερήσια συγκέντρωση αιωρούμενων σωματιδίων υποβάθρου και, $N_{NPF-PERC}$ είναι η σχετική συνεισφορά της πυρηνοποίησης κατά την διάρκεια των ημερών στις οποίες έχουν ανιχνευθεί. $N_{NPF-CONTR}$ είναι η συνεισφορά της πυρηνοποίησης σε όλη την περίοδο των μετρήσεων.

Σταθμός	N_{NPF}	N_{Bg}	$N_{NPF-PERC}$	$N_{NPF-CONTR}$
DEM	350	700	30%	4%
EPT	500	400	56%	12%
FIN	30	100	20%	1%

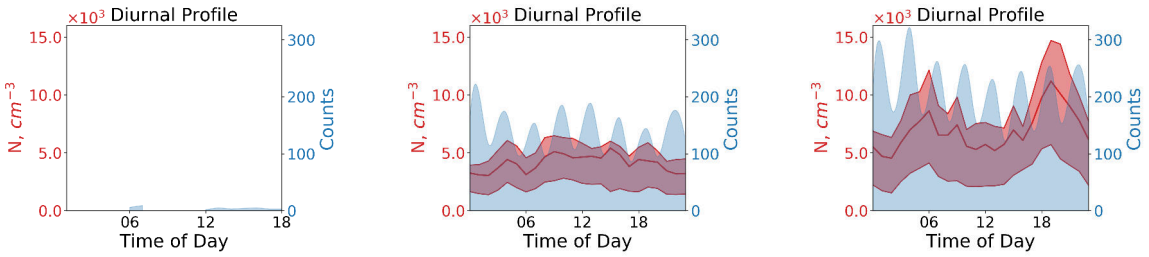

(α′) ΑΥΚΠ-ΟΜΑΔΑ1 (β′) ΑΥΚΠ-ΟΜΑΔΑ2 (γ′) ΑΥΚΠ-ΟΜΑΔΑ3

Σχήμα ii: Ημερήσια διακύμανση της συχνότητας εμφάνισης (μπλε χρώμα) και της μεσαίας τιμής συγκέντρωσης (κόκκινη γραμμή) για τις Ομάδες λογαριθμικών κατανομών που έχουν προσδιοριστεί. Η κόκκινη περιοχή γύρω από την μεσαία τιμή αντιστοιχεί στο 16^o και το 84^o εκατοστημόριο της ολικής συγκέντρωσης αιωρούμενων σωματιδίων.

Αποτελέσματα ανάλυσης ομάδων λογαριθμικών κατανομών

Αναλύσαμε τις κατανομές μεγέθους και αριθμού αιωρούμενων σωματιδίων σε άθροισμα λογαριθμικών κατανομών τις οποίες κατόπιν κατατάξαμε ως προς την γεωμετρική μέση διάμετρο, την γεωμετρική σταθερά απόκλισης και τον συνολικό αριθμό με βάση ανάλυση ομάδων.

Στον σταθμό ΑΥΚΠ (Σχήμα ii) η πηγή - ομάδα που κυριαρχεί στην κατανομή αριθμού σωματιδίων

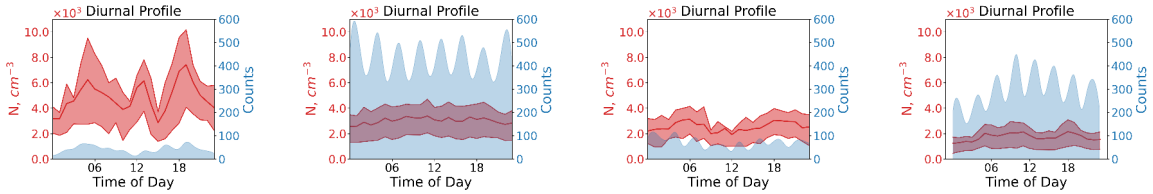

(α′) ΑΥ-ΟΜΑΔΑ1 (β′) ΑΥ-ΟΜΑΔΑ2 (γ′) ΑΥ-ΟΜΑΔΑ3 (δ′) ΑΥ-ΟΜΑΔΑ4

Σχήμα iii: Ημερήσια διακύμανση της συχνότητας εμφάνισης (μπλε χρώμα) και της μεσαίας τιμής συγκέντρωσης (κόκκινη γραμμή) για τις Ομάδες λογαριθμικών κατανομών που έχουν προσδιοριστεί. Η περιοχή γύρω από την μεσαία τιμή αντιστοιχεί στο 16^o και το 84^o εκατοστημόριο της ολικής συγκέντρωσης αιωρούμενων σωματιδίων.

και στην συχνότητα εμφάνισης σχετίζεται με πρόσφατες και γηρασμένες εκπομπές οχημάτων (ΟΜΑΔΑ3). Η ομάδα αυτή παρουσιάζει αυξημένη συγκέντρωση αιωρούμενων σωματιδίων και συχνότητα εμφάνισης τις πρωινές και απογευματινές ώρες όπου έχουμε αυξημένη κίνηση οχημάτων. Η ΟΜΑΔΑ2 προέρχεται από την συσσώρευση αιωρούμενων σωματιδίων που μεταφέρονται από μακρινές περιοχές και την αύξηση μεγέθους των σωματιδίων που παράγονται τοπικά λόγω συμπύκνωσης αερίων και υδρατμών σε αυτά.

Στους σταθμούς ΑΥ (Σχήμα iii) η ΟΜΑΔΑ1 μπορεί να αποδοθεί στις εκπομπές οχημάτων, καθώς έχει μεγάλη αύξηση συγκέντρωσης αριθμού σωματιδίων και συχνότητας εμφάνισης τις πρωινές και απογευματινές ώρες όπου έχουμε αυξημένη κίνηση. Παρουσιάζει επίσης αύξηση της συγκέντρωσης το μεσημέρι, άρα συνδέεται επίσης με σωματίδια που παράγονται με πυρηνοποίηση. Η ΟΜΑΔΑ2 είναι σταθερή σε όλη τη διάρκεια της ημέρας και προέρχεται από την μεταφερόμενη συγκέντρωση σωματιδίων από την ευρύτερη περιοχή και την αύξηση μεγέθους των σωματιδίων που παράγονται τοπικά. Η ΟΜΑΔΑ3 επίσης συνδέεται με την κίνηση των οχημάτων, καθώς εμφανίζει μέγιστα το πρωί και το απόγευμα, αλλά προέρχεται από εκπομπές που έχουν υποστεί γήρανση. Η ΟΜΑΔΑ4 παρουσιάζει μέγιστο το μεσημέρι, ιδίως στην συχνότητα εμφάνισης, και αντιστοιχεί σε μεταφερόμενες εκπομπές από γειτονικές περιοχές.

Στον σταθμό ΕΥ (Σχήμα iv) η ΟΜΑΔΑ2 συνδέεται με εκπομπές ενδιάμεσης γήρανσης που προέρχονται από εκπομπές των πόλεων της Κρήτης. Η ΟΜΑΔΑ3 συνδέεται με το υπόβαθρο της ευρύτερης περιοχής. Η ΟΜΑΔΑ1 προέρχεται από πολύ σπάνιες περιπτώσεις τοπικής ρύπανσης.

.

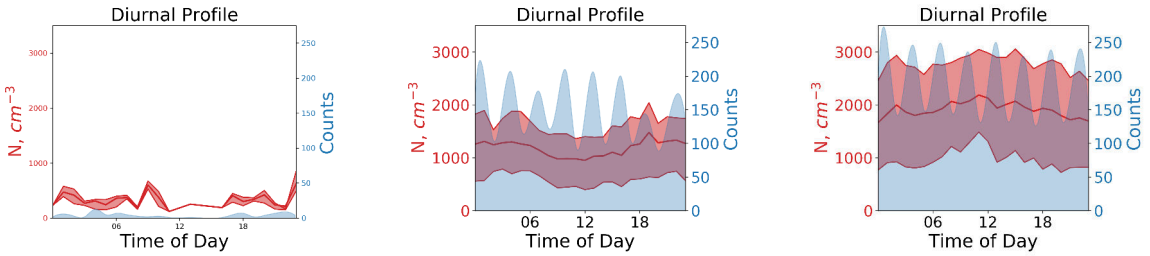

(α΄) ΕΥ-ΟΜΑΔΑ1 (β΄) ΕΥ-ΟΜΑΔΑ2 (γ΄) ΕΥ-ΟΜΑΔΑ3

Σχήμα iv: Ημερήσια διακύμανση της συχνότητας εμφάνισης (μπλε χρώμα) και της μεσαίας τιμής συγκεντρωσης (κόκκινη γραμμή) για τις Ομάδες λογαριθμικών κατανομών που έχουν προσδιοριστεί. Η κόκκινη περιοχή γύρω από την μεσαία τιμή αντιστοιχεί στο 16^o και το 84^o εκατοστημόριο της ολικής συγκέντρωσης αιωρούμενων σωματιδίων.

Αφού υπολογίσουμε την διάμεση τιμή της συγκέντρωσης για κάθε ομάδα σε κάθε τύπο σταθμού και με βάση την υπόθεση ότι η ομάδα στην περιοχή συσσώρευσης αιωρούμενων σωματιδίων που αναγνωρίστηκε στον σταθμό ΕΠ είναι αυτά που μεταφέρονται από μακρινές περιοχές και την χρήση της διάμεσης τιμής της συγκέντρωσης για κάθε ομάδα, συμπεραίνουμε ότι 18% της συγκέντρωσης αιωρούμενων σωματιδίων στον σταθμό ΑΥΚΠ μεταφέρεται από μακρινές περιοχές, το 37% για τους σταθμούς ΑΥ και το 59% για τον σταθμό ΕΥ.

Μεταβολή στην συγκέντρωση υποβάθρου βασιζόμενη στην προέλευση των αερίων μαζών

Η ΟΜΑΔΑ3 του σταθμού ΕΥ που αντιστοιχεί στο κλάσμα συσσώρευσης της κατανομής μεγέθους και αριθμού των αιωρούμενων σωματιδίων θεωρούμε ότι αντιστοιχεί στην συγκέντρωση υποβάθρου της ευρύτερης περιοχής της Ανατολικής Μεσογείου. Αναλύσαμε σε ομάδες την προέλευση των αερίων μαζών για την ΟΜΑΔΑ3 του σταθμού ΕΥ και τα αποτελέσματα παρουσιάζονται στο Σχήμα v. Μετά τον υπολογισμό της μέσης τιμής συγκέντρωσης αιωρούμενων σωματιδίων για κάθε ομάδα που αναγνωρίστηκε με βάση την προέλευση των αερίων μαζών, συμπεραίνουμε ότι η συγκέντρωση αιωρούμενων σωματιδίων όταν οι αέριες μάζες προέρχονται από την Μεσόγειο Θάλασσα είναι πολύ χαμηλότερες από οταν προέρχονται από Βόρειο-Ανατολική ή Βόρειο-Δυτική κατεύθυνση. Όταν επικρατούν οι Ετησίες η συγκέντρωση υποβάθρου στην περιοχή της Μεσογείου αυξάνεται από 2.5 έως 4 φορές.

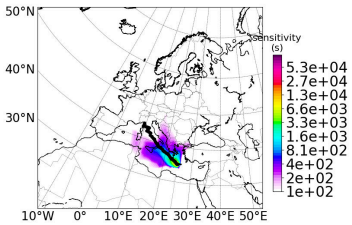

(α′) ΕΥ-ΠΑΕ-ΟΜΑΔΑ1

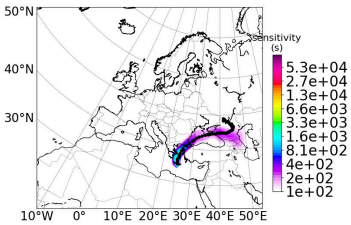

(β′) ΕΥ-ΠΑΕ-ΟΜΑΔΑ2

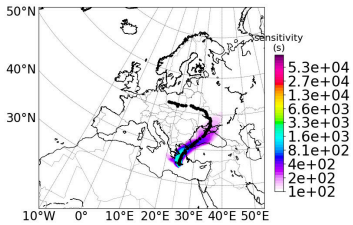

(γ′) ΕΥ-ΠΑΕ-ΟΜΑΔΑ3

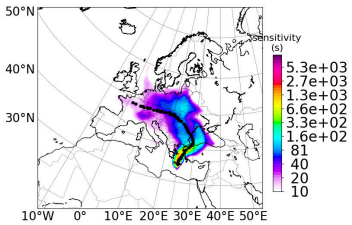

(δ′) ΕΥ-ΠΑΕ-ΟΜΑΔΑ4

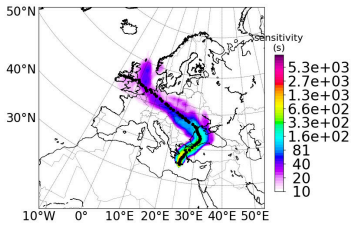

(ε′) ΕΥ-ΠΑΕ-ΟΜΑΔΑ5

Σχήμα v: Χάρτες που υποδυκνείουν τις ομάδες που προέκυψαν με βάση την ανάλυση ομάδων προέλευσης αερίων μαζών. Η ΕΥ-ΠΑΕ-ΟΜΑΔΑ1 αντιστοιχεί στην πρώτη ομάδα προέλευσης αερίων μαζών που αναγνωρίστηκε από την ανάλυση της ΟΜΑΔΑΣ3 του σταθμού ΕΥ.

Αποτελέσματα σύγκρισης του ισοδύναμου δείκτη διάθλασης του ατμοσφαιρικού αερολύματος με δείκτες διάθλασης που προκύπτουν από την χημική σύσταση και τις οπτικές ιδιότητες τους

Στο Σχήμα vi παρουσιάζεται ο ισοδύναμος δείκτης διάθλασης ERI_{COR} για όλη την διάρκεια της καμπάνιας μετρήσεων HygrA-CD (276 3ωρα). Ο ισοδύναμος δείκτης διάθλασης είναι ο πραγματικός αριθμός που συνδυάζει με τη μικρότερη δυνατή απόκλιση τις κατανομές που προκύπτουν από τα όργανα: Διαφορικός καταμετρητής αιωρούμενων σωματιδίων με βάση την ηλεκτρική κινητικότητα (ΔΚΗΚ) και οπτικός καταμετρητής σωματιδίων (ΟΚΣ). Στο ιστόγραμμα 6 φαίνεται ότι η πλειοψηφία των τιμών του ERI_{COR} βρίσκεται εντός του εύρους 1,62-1,68.

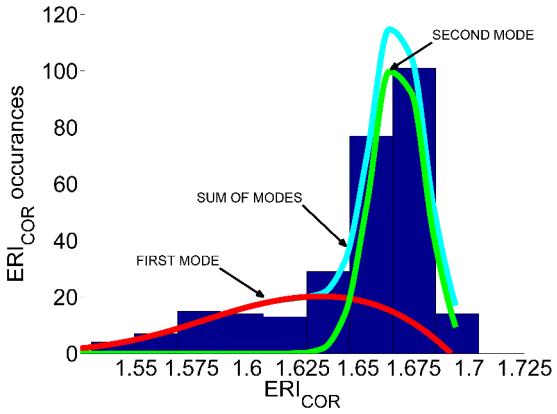

Σχήμα vi: Ιστόγραμμα της διακύμανσης της μέσης τιμής ανά 3ωρο του ERI_{COR} για όλη την περίοδο της καμπάνιας HygrA-CD. Τα μπλε παραλληλόγραμμα δηλώνουν την συχνότητα εμφάνισης της τιμής του ERI_{COR} ενώ η μπλε γραμμή παρουσιάζει την καλύτερη προσέγγιση ως άθροισμα γκαουσιανών κατανομών.

Δείκτης διάθλασης από την χημική σύσταση RI_{IC} και σύγκριση με τον ERI_{COR}

Με βάση μετρήσεις ιοντικής χρωματογραφίας σε φίλτρα πήραμε τα ανιόντα και κατιόντα των αιωρούμενων σωματιδίων για τα χρονικά διαστήματα του Πίνακα iii. Κατόπιν έγινε ανάλυση των φίλτρων με την τεχνική XRF και πήραμε την περιεκτικότητα των αιωρούμενων σωματιδίων σε μέταλλα. Μετά από ανάλυση από όργανο μέτρησης οργανικού και στοιχειακού άνθρακα EC-OC λάβαμε τις αντίστοιχες συγκεντρώσεις. Με συνδυασμό των παραπάνω μετρήσεων λάβαμε τον δείκτη διάθλασης από την χημική σύσταση των αιωρούμενων σωματιδίων και τον συγκρίναμε με τον ισοδύναμο δείκτη διάθλασης ERI_{COR}.

Στο Σχήμα vii τα RI_{IC} και ERI_{COR} έχουν καλή συσχέτιση ($R^2 = 0{,}88$). Όταν το κλάσμα μάζας της σκόνης είναι υψηλό, ο ERI_{COR} είναι υψηλός.

Σύγκριση δείκτη διάθλασης RI_{LI} και ERI_{COR}

Το lidar με μετρήσεις σε 6 μήκη κύματος που λειτουργεί στο Εθνικό Μετσόβιο Πολυτεχνείο (EOLE) παρείχε την κατανομή καθ' ύψος του συντελεστή οπισθοσκέδασης αιωρούμενων σωματιδίων. Μετά από επεξεργασία των μετρήσεων λάβαμε τον δείκτη διάθλασης των αιωρούμενων σωματιδίων καθ' ύψος

Πίνακας iii: Σύγκριση RI_{IC} και ERI_{COR}

Ημερομηνία, ώρα (UTC)	ERI_{COR}	RI_{IC}
$21^{η}$ Μαΐου 2014, 19:00-22:00	1,66±0,1	1,58±0,15
$28^{η}$ Μαΐου 2014, 08:30-13:30	1,65±0,1	1,59±0,15
$28^{η}$ Μαΐου 2014, 19:00-22:00	1,67±0,1	1,59±0,15
$30^{η}$ Μαΐου 2014, 08:30-13:30	1,65±0,1	1,58±0,15
$30^{η}$ Μαΐου 2014, 19:00-22:00	1,63±0,1	1,57±0,15
$6^{η}$ Ιουνίου 2014, 19:00-22:00	1,65±0,1	1,58±0,15
$6^{η}$ Ιουνίου 2014, 19:00-22:00	1,65±0,1	1,58±0,15

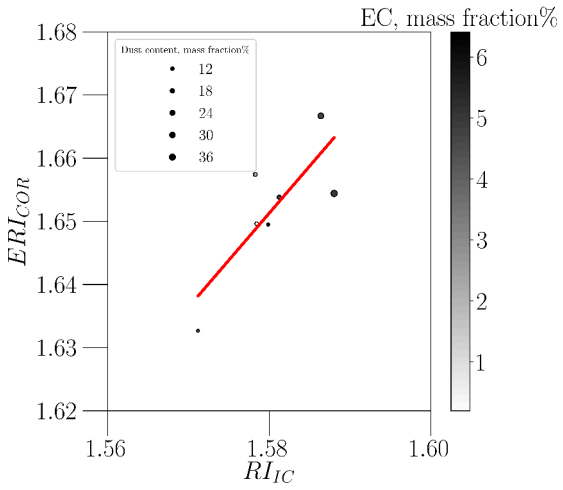

Σχήμα vii: Σύγκριση RI_{IC} και ERI_{COR}. Η κόκκινη γραμμή παρουσιάζει την γραμμική προσαρμογή ανάμεσα στα δύο μεγέθη. Το χρώμα του ενδεικτικού κύκλου αντιστοιχεί στο κλάσμα μάζας μαύρου άνθρακα (πιο σκούρο χρώμα αντιστοιχεί σε μεγαλύτερη συγκέντρωση) ενώ η επιφάνεια του κύκλου αντιστοιχεί στο κλάσμα μάζας της σκόνης (μεγαλύτερη επιφάνεια αντιστοιχεί σε μεγαλύτερη συγκέντρωση).

Πίνακας iv: Σύγκριση RI_{LI} και ERI_{COR}

Ημερομηνία, ώρα (UTC)	ERI_{COR}	RI_{LI}
$23^{η}$ Μαΐου 2014, 19:00-20:00	1,61±0,1	1,56±0,1
$26^{η}$ Μαίου 2014, 19:00-20:00	1,63±0,1	1,6±0,1
$7^{η}$ Ιουνίου 2014, 22:00-23:00	1,67± 0,1	1,61±0,1
$10^{η}$ Ιουνίου 2014, 18:45-19:45	1,68±0,1	1,62±0,1
$17^{η}$ Ιουνίου 2014, 19:00-20:00	1,66±0,1	1,59±0,1
$18^{η}$ Ιουνίου 2014, 19:00-20:00	1,58±0,1	1,59±0,1
$22^{η}$ Ιουνίου 2014, 19:00-20:00	1,6±0,1	1,56±0,1

RI_{LI}. Στον πίνακα ι παρουσιάζονται οι ημερομηνίες και ώρες στις οποίες είχαμε κοινές μετρήσεις των προαναφερόμενων μεγεθών.

Στο Σχήμα viii παρουσιάζεται η σύγκριση των RI_{LI} και ERI_{COR} και παρατηρούμε ότι υπάρχει σχετικά καλή συσχέτιση μεταξύ τους. Η σχετική υγρασία στο ύψος που μετρά το lidar κυμαινόταν ανάμεσα στο 40 και το 65%, αυξάνοντας τις διαφορές ανάμεσα στα δύο μεγέθη. Παρόλα αυτά, ο κύριος μηχανισμός που φαίνεται να επηρεάζει τη συσχέτιση των RI_{LI} και ERI_{COR} είναι η μίξη των αερίων μαζών καθ' ύψος.

Σύγκριση επιτόπιων μετρήσεων και μετρήσεων τηλεπισκόπησης στην Μητροπολιτική Περιοχή των Αθηνών

Σύγκριση του συντελεστή απορρόφησης αιωρούμενων σωματιδίων που λήφθηκε από το EOLE lidar με τον αντίστοιχο συντελεστή που λήφθηκε από τα όργανα Νεφελόμετρο, Αιθαλόμετρο

Για να μπορέσουμε να συγκρίνουμε τις μετρήσεις επιτόπιων οργάνων και οργάνων τηλεπισκόπησης, υπολογίσαμε τον μέσο συντελεστή εξασθένισης στα 355 και 532 nm για ύψος από 1.200 έως 1.300 μέτρα πάνω από το επίπεδο της Θάλασσας (asl) για επιλεγμένες ημέρες στις οποίες είχαμε ισχυρή τύρβη στην

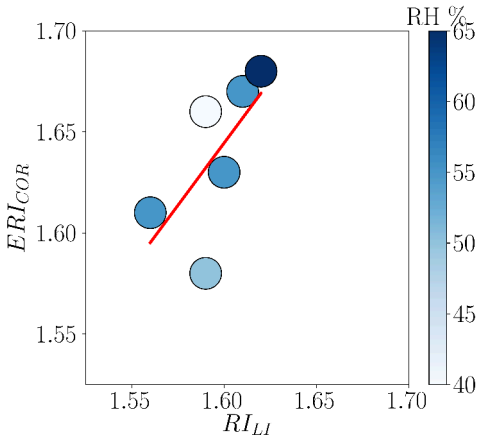

Σχήμα viii: Σύγκριση ισοδύναμου δείκτη διάθλασης ERI_{COR} με τον δείκτη διάθλασης RI_{LI}. Η κόκκινη γραμμή παρουσιάζει την γραμμική προσαρμογή ανάμεσα στα δύο μεγέθη. Το χρώμα αντιστοιχεί στη σχετική υγρασία στο ύψος όπου μετρά το lidar (40-65 %).

ατμόσφαιρα. Ο συντελεστής εξασθένισης για τις επιτόπιες μετρήσεις υπολογίστηκε από το άθροισμα του συντελεστή σκέδασης που παρείχε το όργανο Νεφελόμετρο και του συντελεστή απορρόφησης που παρείχε το όργανο Αιθαλόμετρο. Για να μετατρέψουμε τον συντελεστή σκέδασης από ξηρές συνθήκες μέτρησης σε ατμοσφαιρικές συνθήκες, χρησιμοποιήσαμε ένα συντελεστή αύξησης σκέδασης ίσο με 0,57. Υποθέσαμε ότι ο συντελεστής απορρόφησης δεν μεταβάλλεται με την σχετική υγρασία.

Παρατηρούμε στο Σχήμα ix ότι υπάρχει καλή συμφωνία ανάμεσα στους συντελεστές εξασθένισης επιτόπιων οργάνων και οργάνων τηλεπισκόπησης για ημέρες με ισχυρή τύρβη στην ατμόσφαιρα. Οι μετρήσεις με το υψηλότερο ϵ βρίσκονται στο κέντρο της διασποράς, ενώ ο συντελεστής αύξησης μεγέθους λόγω υγροσκοπικότητας δεν φαίνεται να επηρεάζει σημαντικά την συσχέτιση. Συμπεραίνουμε επομένως ότι ο σημαντικότερος μηχανισμός που επηρεάζει τη συσχέτιση είναι η ανάμιξη καθ' ύψος.

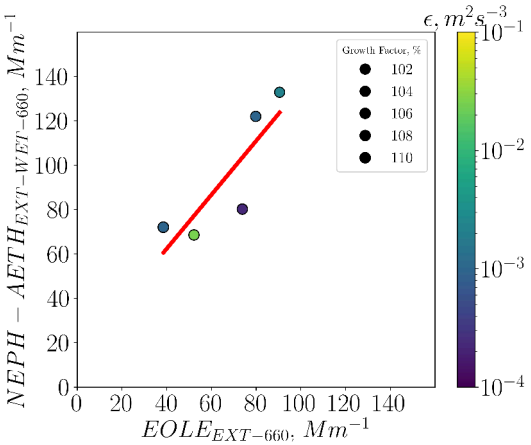

Σχήμα ix: Σύγκριση του συντελεστή εξασθένισης σε ατμοσφαιρικές συνθήκες μετρημένου από τα όργανα Νεφελόμετρο και Αιθαλόμετρο και τον αντίστοιχο συντελεστή εξασθένισης μετρημένο από το EOLE. Το μέγεθος του κύκλου αντιστοιχεί στον συντελεστή αύξησης μεγέθους λόγω υγροσκοπικότητας και το χρώμα του κύκλου στον ρυθμό απώλειας ενέργειας λόγω τύρβης ϵ. Και τα δύο μεγέθη κανονικοποιούνται ανάμεσα στο 100 και το 200. Σκούρο χρώμα αντιστοιχεί σε υψηλές τιμές ρυθμού απώλειας ενέργειας λόγω τύρβης, ενώ η μεγαλύτερη επιφάνεια αντιστοιχεί σε υψηλότερο συντελεστή αύξησης μεγέθους λόγω υγροσκοπικότητας. Η κόκκινη γραμμή παρουσιάζει την σχέση $NEPH - AETH_{EXT-WET-660} = 1{,}21 * EOLE_{EXT-660} + 13{,}8\ Mm^{-1}$, η οποία είναι η καλύτερη γραμμική προσαρμογή με R^2 ίσο με 0,74.

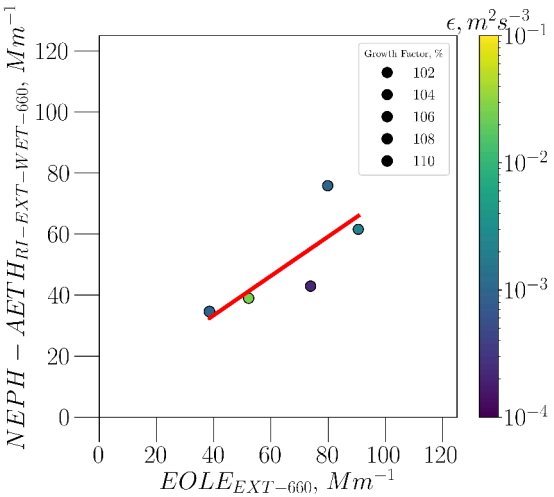

Σχήμα x: Σύγκριση του συντελεστή εξασθένισης σε ατμοσφαιρικές συνθήκες υπολογισμένο με κώδικα Mie και τον αντίστοιχο συντελεστή εξασθένισης μετρημένο από το EOLE. Το μέγεθος του κύκλου αντιστοιχεί στον συντελεστή αύξησης μεγέθους λόγω υγροσκοπικότητας και το χρώμα του κύκλου στον ρυθμό απώλειας ενέργειας λόγω τύρβης ϵ. Και τα δύο μεγέθη κανονικοποιούνται ανάμεσα στο 100 και το 200. Σκούρο χρώμα αντιστοιχεί σε υψηλές τιμές ρυθμού απώλειας ενέργειας λόγω τύρβης, ενώ η μεγαλύτερη επιφάνεια αντιστοιχεί σε υψηλότερο συντελεστή αύξησης μεγέθους λόγω υγροσκοπικότητας. Η κόκκινη γραμμή παρουσιάζει την σχέση $NEPH - AETH_{RI-EXT-WET-660} = 0{,}64 * EOLE_{EXT-660}$+7,6 Mm^{-1}, η οποία είναι η καλύτερη γραμμική προσαρμογή με R^2 ίσο με 0,62.

Σύγκριση του συντελεστή απορρόφησης αιωρούμενων σωματιδίων που λήφθηκε από το EOLE lidar με τον αντίστοιχο συντελεστή που λήφθηκε με κώδικα Mie.

Υπολογίσαμε τον δείκτη διάθλασης προσαρμόζοντας τις μετρήσεις συντελεστών σκέδασης και απορρόφησης Νεφελομέτρου και Αιθαλομέτρου χρησιμοποιώντας κώδικα Mie με βάση την κατανομή αριθμού και μεγέθους σωματιδίων που λάβαμε από τα όργανα επιτόπιων μετρήσεων. Το επόμενο βήμα ήταν να ανάγουμε τον δείκτη διάθλασης και την κατανομή μεγέθους και αριθμού αιωρούμενων σωματιδίων σε ατμοσφαιρικές συνθήκες ως προς την σχετική υγρασία. Κατόπιν με τον δείκτη διάθλασης που υπολογίστηκε και την κατανομή μεγέθους και αριθμού των αιωρούμενων σωματιδίων, υπολογίσαμε τον συντελεστή εξασθένισης και τον συγκρίναμε με τις μετρήσεις τηλεπισκόπησης (Σχήμα x).

Στο Σχήμα x παρατηρούμε ότι υπάρχει καλή συμφωνία ανάμεσα στους συντελεστές εξασθένισης επιτόπιων οργάνων και οργάνων τηλεπισκόπησης για ημέρες με ισχυρή τύρβη στην ατμόσφαιρα. Πρέπει να έχουμε υπόψιν μας ότι η κατανομή αριθμού και μεγέθους των αιωρούμενων σωματιδίων που χρησιμοποιήθηκε για τον υπολογισμό του συντελεστή εξασθένισης φτάνει μέχρι τα 1.000 nm και αυτό μπορεί να οδηγεί σε λάθη σχετιζόμενα με σωματίδια μεγαλύτερου μεγέθους που βρίσκονται στην ατμόσφαιρα. Οι μετρήσεις με το υψηλότερο ϵ βρίσκονται στο κέντρο της διασποράς, ενώ ο συντελεστής αύξησης μεγέθους λόγω υγροσκοπικότητας δεν φαίνεται να επηρεάζει σημαντικά την συσχέτιση. Συμπεραίνουμε επομένως ότι ο σημαντικότερος μηχανισμός που επηρεάζει τη συσχέτιση είναι η ανάμιξη καθ΄ ύψος.

Ανάμιξη τοπικού και μεταφερόμενου αερολύματος την $27^{η}$ Μαΐου 2014

Την $27^{η}$ Μαΐου 2014 στην περιοχή της Αθήνας είχαμε ένα επεισόδιο ρύπανσης από σκόνη της Σαχάρας. Στο Σχήμα xi(α΄) παρουσιάζεται το διορθωμένο σήμα ως προς την απόσταση σε A.U του EOLE. Αρχικά το στρώμα της ατμόσφαιρας που περιείχε την σκόνη της Σαχάρας ανιχνεύθηκε από το όργανο τηλεπισκόπησης σε ύψος μεγαλύτερο των 1.500 μέτρων πάνω από την επιφάνεια της θάλασσας (06:00-09:00 UTC). Σε χαμηλότερο υψόμετρο την ίδια ώρα διακρίνεται ένα στρώμα που περιέχει τους τοπικούς ρύπους. Στις 12:00 UTC, λόγω της ισχυρής τύρβης στην ατμόσφαιρα, όπως φαίνεται στο Σχήμα xii(α΄), τα δύο στρώματα αναμιγνύονται. Το απόγευμα, ένα καλά αναμιγμένο στρώμα εμφανίζεται από το έδαφος έως τα 2.000 μέτρα πάνω από τη θάλασσα. Το γεγονός αυτό υποδεικνύεται και στο Σχήμα xi(β΄), όπου ο συντελεστής Ångström για την χρονική περίοδο 11:30-12:30 UTC και για ύψος 1.800 έως 2.500 μέτρα πάνω από το ύψος του εδάφους είναι μικρότερος του 1, ενώ για την περίοδο 19:30-20:30 UTC το στρώμα της σκόνης από την Σαχάρα έχει κατέβει σε ύψη χαμηλότερα των 1.000 μέτρων πάνω από έδαφος, καθώς ο συντελεστής Ångström είναι μεγαλύτερος του 1 για όλα τα ύψη που απεικονίζονται. Στο Σχήμα xii(α΄) παρουσιάζεται η τιμή του ϵ. Από τις 09:00 UTC μέχρι σχεδόν το τέλος της μέρας, υπάρχει ισχυρή τύρβη στην ατμόσφαιρα μέχρι το ύψος των 1.000 μέτρων πάνω από το έδαφος. Στο Σχήμα xii(β΄), μετά τις 12:00 UTC, οι τιμές των συντελεστών σκέδασης αερολύματος οι οποίοι μετρούνται στο έδαφος από το όργανο Νεφελόμετρο (μήκος κύματος 470 και 660 nm) πλησιάζουν μεταξύ τους (ο συντελεστής Ångström μειώνεται, μία ένδειξη ότι έχουμε σκόνη Σαχάρας στο αερόλυμα), μέχρις ότου στις 18:00 UTC, η σκόνη της Σαχάρας κυριαρχεί στο αερόλυμα καθώς η σκέδαση στα 660 nm είναι ισχυρότερη

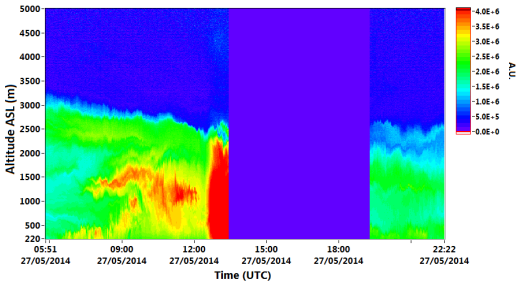

(α′) Χρονική εξέλιξη του διορθωμένου σήματος ως προς την απόσταση στα 1.064 nm του EOLE, (A.U.)

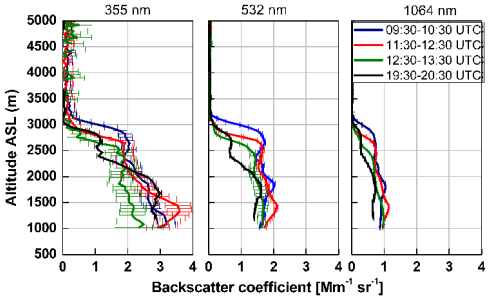

(β′) Κατακόρυφη κατανομή του συντελεστή οπισθοσκέδασης των αερολυμάτων του EOLE στα 355, 532 και 1.064 nm.

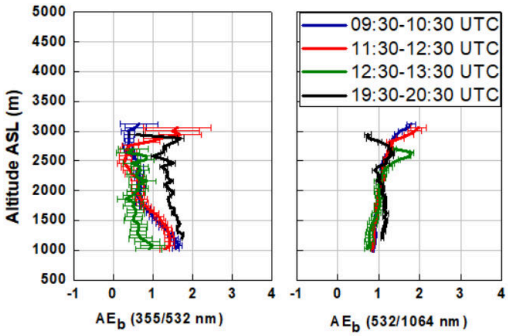

(γ′) Κατακόρυφη κατανομή του συντελεστή Ångström των αερολυμάτων.

Σχήμα xi: α′: Διακρίνεται σε ύψος άνω των 1.500 μέτρων πάνω από το έδαφος η σκόνη της Σαχάρας, η οποία σταδιακά αναμιγνύεται με την τοπική ρύπανση λόγω υψηλής τύρβης στην ατμόσφαιρα. β′: Κατακόρυφη κατανομή του συντελεστή οπισθοσκέδασης των αερολυμάτων του EOLE στα 355, 532 και 1.064 nm. γ′: Παρατηρούμε ότι τις πρωινές ώρες (9:30-12:30), ο συντελεστής Ångström των αερολυμάτων σε υψος άνω των 1.500 μέτρων πάνω από το έδαφος έχει τιμές χαμηλότερες του 1, υποδηλώνοντας στρώμα σκόνης από την Σαχάρα.

από την σκέδαση στα 470 nm. Στο Σχήμα xii(γ′) παρουσιάζονται οι αέριες μάζες που φτάνουν στο σταθμό του Δημόκριτου. Παρατηρούμε ότι έχουν σημαντικό χρόνο παραμονής στην Βόρεια Αφρική σε ύψος χαμηλότερο των 100 μέτρων πάνω από το έδαφος.

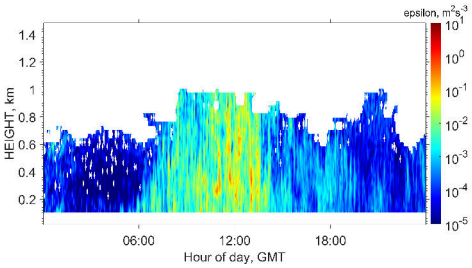

(α′) Κατανομή καθ′ ύψος του ϵ

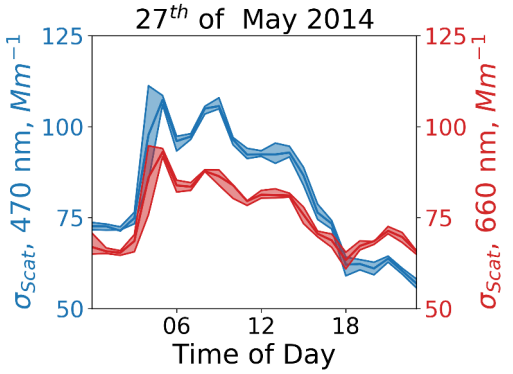

(β′) Συντελεστής σκέδασης Νεφελομέτρου, 470-660 nm.

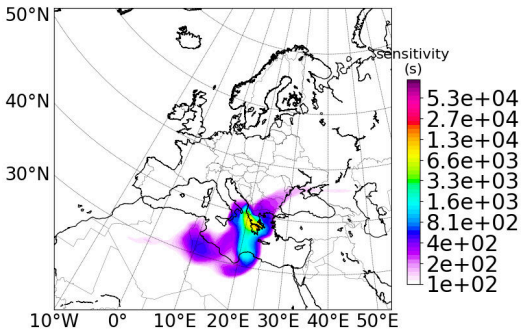

(γ′) Προέλευση αερίων μαζών από ύψος έως 100 μέτρα πάνω από την επιφάνεια του εδάφους.

Σχήμα xii: α′: Παρατηρούμε ενισχυμένη τύρβη στην ατμοσφαιρα τις μεσημβρινές ώρες που οδηγεί σε ανάμιξη τοπικών και μεταφερόμενων αιωρούμενων σωματιδίων. β′: Ο συντελεστής σκέδασης Νεφελομέτρου στα 470 nm παρουσιάζει χαμηλότερες τιμές από τον αντίστοιχο στα 660 nm τις απογευματινές ώρες, υποδηλώνοντας την έντονη παρουσία σκόνης Σαχάρας. γ′: Προέλευση αερίων μαζών από την Βόρεια Αφρική (ύψος έως 100 μέτρα πάνω από την επιφάνεια του εδάφους).

Acknowledgements

I would like to thank my supervisors Prof. Dr. AlexanDros Papayannis and Dr. K. Eleftheriadis for giving me the opportunity to develop this thesis in the Laser Remote Sensing Unit of the National Technical University of Athens and the Environmental Radioactivity Laboratory of the NCSR Demokritos. During the thesis, I had plenty of support and freedom to find my research interests. Moreover, I should admit that this thesis would have been poorer without their detailed comments. I am specially grateful to Prof. Dr. Nikos Michalopoulos. I was feeling always welcome in his group. Furthermore, I would like to thank the Ph.D. committee members and especially Dr Griša Močnik and Prof. Dr. George Kutsumbas, as they were keeping track of my progress so as everything goes smoothly until the day of my defense. I have to say a big thank you to Prof. Dr. Athanasios Nenes and Prof. Dr. Spyros Pandis. They helped me very much with their suggestions on the publications to peer reviewed journals during this thesis. Special thanks to Prof. Dr. Detlef Müller and Dr Ewan O' Connor. They helped a lot also with the publications.

I personally thank my colleagues Dr. Maria Gini, Dr. Prodromos Fetfatzis, Dr. Katerina Bougiatioti, Dr. Spyros Bezantakos, Dr. Athina Argyrouli, Dr. Athina Kalogridi, Dr. Ioannis Binietoglou, Dr. Lev Labzovsky, Maria Mylonaki and Dr. Iason Stavroulas.

This research has been co-funded by the EnTeC FP7 Capacities program (REGPOT-2012-2013-1, FP7 (ID:316173)), People Program (ITN Marie Curie Actions) – REA GA no 289923 (ITARS) and Greek national funds through the Operational Program "Education and Lifelong Learning" of the National Strategic Reference Framework (NSRF) – Research Funding Program: THALES. I also acknowledge support of this work by the project "PANhellenic infrastructure for Atmospheric Composition and climatE change" (MIS 5021516) which is implemented under the Action "Reinforcement of the Research and Innovation Infrastructure", funded by the Operational Programme "Competitiveness, Entrepreneurship and Innovation" (NSRF 2014-2020) and co-financed by Greece and the European Union (European Regional Development Fund). I would like to thank John F. Burkhart for the provision of pflexible module for displaying FLEXPART results. I also gratefully acknowledge Professor George Kallos, as the dust mass concentration output of SKIRON model was used to quantify the Sahara dust influence on aerosol measurements in the AMA. Development of

lidar retrieval algorithms was supported by Russian Science Foundation; (project No 16-17-10241).

Finally, my beloved wife Rania, read the thesis and suggested corrections in the use of the English and Greek language.

Contents

List of Tables

List of Figures

Chapter 1

Introduction

1.1 Optical, microphysical and physico-chemical properties of aerosols and their role in climate change

Aerosols are relatively stable suspensions of solid or liquid particles in a gas. Particles may be either directly emitted into the atmosphere or formed in the atmosphere via photochemical reactions. The former particles are called primary while the latter ones are called secondary particles. The formation mechanism for primary aerosols is twofold (a) bulk-to-particle conversion (e.g., mineral dust) and (b) liquid-to-particle conversion (e.g., sea salt). Secondary aerosols form only within the atmosphere from precursor substances like gases, hence through the physical mechanism of gas-to-particle conversion. Aerosol principal modes, sources, particle formation and removal mechanisms are indicated in Figure 1.1. The size distribution of aerosol particle surface area is presented in Figure 1.2.

Through physical and chemical aging processes, when the thermodynamic state of the atmosphere permits it, aerosols function as CCN and enhance cloud development processes. Aerosols lifetime is generally short - from few days to few weeks. They are transported to remote regions following the wind trajectories, and finally, they are removed from the atmosphere via dry deposition due to the gravitation force or wet deposition in the form of precipitation.

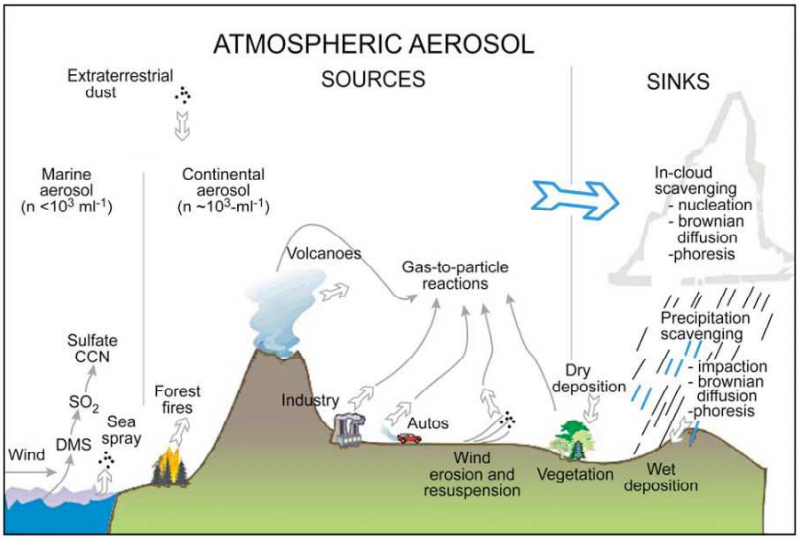

Figure 1.1: Idealized schematic of atmospheric aerosol sources and sinks.

We usually discriminate atmospheric aerosols with respect to their size range and their origin, making a distinction between "fine" and "coarse" particles referring to particles smaller and larger than 1 μm respectively. In fact, particles falling in "fine" mode are further classified to the "nucleation", "Aitken" and "accumulation" modes. "Aitken" and "accumulation" modes consist of both primary and secondary aerosols, while the nucleation mode refers exclusively to secondary particles and its formation involves the nucleation of a new phase (liquid or solid) from a supersaturated gas phase.

Aerosol sources have been grouped into two big classes; the anthropogenic sources due to emissions from vehicles, domestic heating, industry, power plants and the natural sources. The most common aerosols of natural origin are mineral dust, sea salt, biological aerosols like bacteria and pollen. Aerosols of anthropogenic origin include sulfates, nitrates, Black Carbon (BC) and particular organic matter; sulfates may also originate from natural sources through dimethyl sulfide (DMS), which is emitted by phytoplankton species after their death. Due to the high concentration

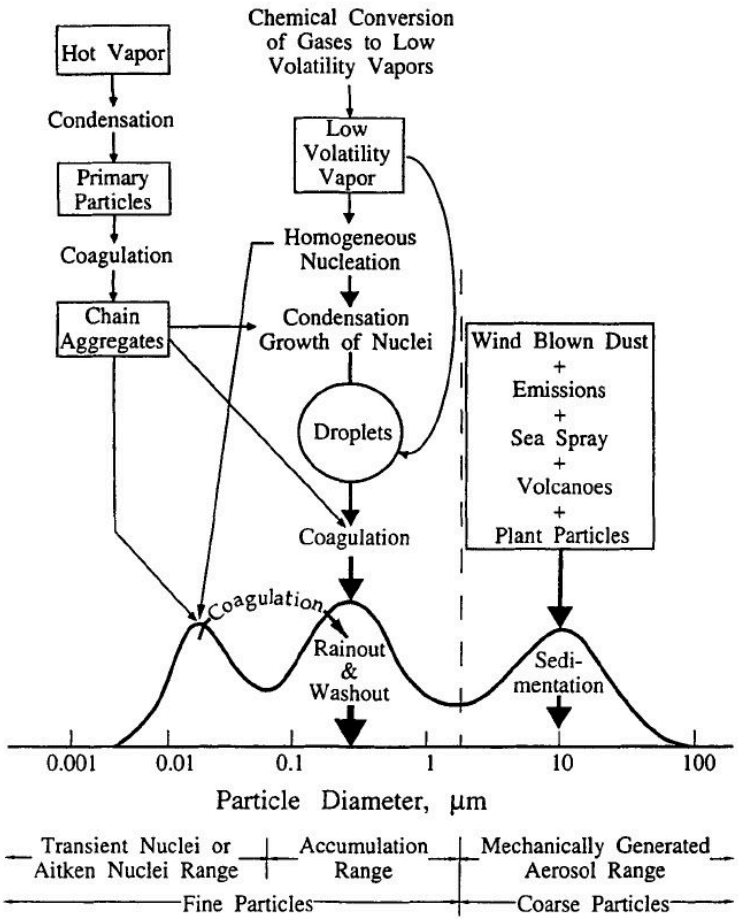

Figure 1.2: Idealized schematic of the distribution of particle surface area of an atmospheric aerosol. Principal modes, sources, particle formation and removal mechanisms are indicated. [81]

of oxygen, DMS by its reaction with O_2 produces sulfur dioxide SO_2 and a secondary product is sulfate SO_4^{-2}. Apart from the ocean, DMS is also released to the atmosphere through vegetation. Lastly, volcanoes (via eruption and continuous degassing) may be substantial natural sources of SO_2 which functions as an effective sulfate precursor. SO_2 is mainly emitted to the atmosphere through anthropogenic activities, mainly ship emissions and fossil fuel combustion. Biomass Burning (BB) is an important source for BC and Particulate Organic Matter (POM): main products of incomplete combustion of biomass. Large quantities of BC and POM are also emitted into the atmosphere as a result of fossil fuel combustion. The anthropogenic activities are also responsible for nitrates NO_x although a small fraction of such emissions comes from natural sources (lightning and the soil which produces NO).

Aerosols can be externally mixed (heterogenic) with respect to the species that they consist of, or they can be an internal mix, where the different constituents are homogeneously mixed in a solid or a liquid phase. This discrimination between externally and internally mixed aerosols is convenient, but the true mixing state stands between these two extremes.

We often use the population mixing state to define the distribution of chemical compounds across the particle population and the morphological mixing state to express the distribution of chemical compounds within and on the surface of the particle.

Mineral dust is insoluble when it is in pure form, close to the emitting source areas. However, when mineral dust is internally mixed with soluble components e.g. sea salt, the resulting aerosol becomes prone to water uptake. In nature, the internally-mixed particles can be decomposed into an insoluble and hydrophobic component, like OC, and a soluble and hygroscopic component, like sulfate.

Regarding optical properties of aerosols, the refractive index of a medium is a pure number which describes how fast light propagates through it. The light intensity scattered by an aerosol particle in all angles can be calculated by the Mie theory, provided the particle is spherical, and that its refractive index and geometric diameter are known [10].

Aerosols influence climate both directly by the scattering and absorption of solar radiation, and indirectly through their role as cloud condensation nuclei. Light can be scattered or absorbed by

aerosol particles suspended in the atmosphere. Light scattering dominates over absorption in the visible. Nevertheless, absorption of light cannot be ignored, as it influences considerably the total radiation balance. The reduction in the intensity of a light beam during its propagation through an aerosol medium is determined simultaneously by absorption and scattering processes. The sum of total light scattering (i.e. in all directions) and absorption is called extinction. Energy, which is absorbed by particles, is not contained in them indefinitely, but radiates at larger wavelengths (emission).

The magnitude of the direct-forcing of aerosols (measured in Wm^{-2}) at a particular time and location depends on the amount of radiation scattered back to space, which itself depends on the size, concentration, and optical properties of the particles and the solar zenith angle. The so-called indirect effect emerges when increases in aerosol number concentrations from anthropogenic sources lead to increased concentrations of cloud condensation nuclei, which, in turn, lead to clouds with larger number concentrations of droplets with smaller radii, which, in turn, lead to higher cloud albedos [81].

Particles can both scatter and absorb radiation. As particles become increasingly absorbing versus scattering, a point is reached, depending on their size and the albedo of the underlying surface, where the overall effect of the particle layer changes from one of cooling to heating. Moreover, if the particles consist of a mixture of purely scattering material, e.g. ammonium sulfate, and partially absorbing material, e.g. soot, the cooling-heating effect depends on the manner in which the two substances are mixed throughout the particle population. The two extremes are when every particle contains some absorbing material and when the absorbing material is distinct from the scattering particles. These effects are further perplexed when a cloud is present. Particles exist above and below clouds and, to some extent, even in the cloud itself. The amount of light scattered back to space depends on the properties of both the aerosols and the cloud.

The direct effect can be observed visually as the sunlight is reflected upward from haze when viewed from above (e.g., from a mountain or an airplane). The result of the process of scattering of sunlight is an increase in the amount of light reflected by the planet and hence a decrease in the amount of solar radiation reaching the surface. The amount of light reflected upward by aerosol

is approximately proportional to the total column mass burden of particles (usually reported in grams per square meter). The direct effect of aerosols on climate is a result of the same physics that describes the reduction of visibility that occurs in airmasses laden with particles. The main difference is that, while visibility reduction is attributed to aerosol scattering in all directions, the direct climatic effect of aerosols results only from radiation that is scattered in the upward direction, back to space.

Indirect climate effects of aerosols are more complex and more difficult to determine than direct effects because they depend on a chain of phenomena that relate aerosol levels to concentrations of cloud condensation nuclei, cloud condensation nuclei concentrations to cloud droplet number concentrations (and size), and these, in turn, to cloud albedo and cloud lifetime. Changes in the particle number concentration of aerosols cause variations in the population and sizes of cloud droplets, which are expected to trigger changes in cloud albedo and areal extent. Other meteorological influences might occur as a result of perturbations in the particle number concentration of aerosols, such as changes in precipitation.

In contrast to Green House Gases (GHGs), which act only on outgoing, infrared radiation, aerosol particles can influence both sides of the energy balance. Particles of diameters less than 1 μm are highly effective at scattering incoming solar radiation, sending a portion of that scattered radiation back to space. Therefore, these particles reduce the amount of incoming solar energy in comparison to their absence and consequently cool the Earth. Sulfate particles produced by the oxidation of anthropogenically emitted SO_2 in the industrialized parts of the world, constitute much of this light-scattering aerosol. Biomass burning of forests and savannas is a dominant source of airborne particles in the tropics, consisting mainly of organic matter and soot. Wind acting on soils produces mineral dust, which is always present in the atmosphere to some degree. Human activities, though, such as disruption of soils by changing use of land in arid and sub-arid regions, can increase the loading of dust over that present "naturally". Mineral dust particles can scatter and absorb incoming and outgoing radiation due to their size and composition. The light-scattering effect dominates in the visible part of the spectrum, and mineral dust exerts an overall cooling effect, while in the infrared region, mineral dust is an absorber and acts like a greenhouse gas.

Greenhouse gases such as CO_2, CH_4, N_2O, and the CFCs are virtually uniform globally. Aerosol concentrations, contrarily, are highly variable in space and time. Sulfate aerosols, with lifetimes of about a week, are most abundant close to their sources in the industrialized areas of the Northern Hemisphere. During the dry season in tropical areas, biomass aerosols are emitted predominantly. Large arid regions produce downwind high concentrations of mineral dust. What is more, greenhouse gas forcing operates day and night; aerosol forcing operates only during daytime. Aerosol radiative effects depend in a complicated way on the solar angle, relative humidity, particle size and composition, and the albedo of the underlying surface. When superimposed on each other, the spatial distribution of GHG warming and aerosol cooling do not occur at the same locations [81].

Aerosol residence times in the troposphere are approximately 1-2 weeks. If all SO_2 sources were shut off today, anthropogenic sulfate aerosols would disappear from the planet in 2 weeks. By contrast, GHG residence times are measured in decades to centuries, but because of the great inertia of the climate system, the effect of GHG forcing takes decades to be fully transformed into equilibrium climate warming [81]. If both CO_2 and aerosol emissions were to cease today, the Earth would continue to warm as the climate system continues to respond to the amount of CO_2 already in the atmosphere.

The inability to reconcile the observed temperature trend since the preindustrial period with that predicted by general circulation models (GCMs) based on GHG increases alone led to severe uncertainties about our understanding of the climate effects of GHG forcing, until recently. Inclusion of aerosol effects in climate models has made a decisive difference in the ability to simulate observed temperature trends. Significant similarities between patterns of observed temperature changes with GCM predicted changes are observed when aerosols are included, while less similarities are observed if GHGs alone are considered.

Overall, the aerosol radiative forcing over the years from 1750 to 2011 is estimated as –0.9 [–1.9 to 0.1] Wm^{-2} (medium confidence). Radiative forcing from aerosols has two competing components: a dominant cooling effect from most aerosols and their cloud adjustments and a partially offsetting warming contribution from black carbon absorption of solar radiation. There is high certainty that the global mean total aerosol radiative forcing has canceled out a substantial portion of radiative

forcing from well-mixed GHGs. Aerosols continue to contribute the largest uncertainty to the total radiative forcing estimate [68].

1.2 Factors affecting aerosol concentration in the study area

Atmospheric aerosol particles affect air quality, human health, atmospheric visibility, and the climate [23]. To understand these effects, measurements of their size distribution and chemical composition are highly needed.

Ground based in situ and remote sensing measurement platforms are essential tools for continuous monitoring and evaluation of global, regional, and local air quality. In situ instruments provide comprehensive measurements of aerosol and trace gas chemistry as well as physical properties. They also possess excellent temporal resolution. Remote sensing instruments provide the vertical profile of aerosol particle size distribution, their optical and physical properties [79].

Furthermore, measurements of vertical distributions of aerosol concentration, as well as the understanding of vertical mixing processes, provide an important input for understanding the dispersion of aerosols from local pollution sources and effective control of air quality. In studies of air quality, information about the depth and dynamics of the atmospheric boundary layer (BL) is essential to interpreting in situ measurements of atmospheric species. To understand the processes that affect concentrations of species emitted within the surface layer, one needs knowledge of transport and mixing conditions including mean horizontal wind speed and direction profiles, strength of turbulence, and depth of the atmospheric BL. The BL is defined here as the layer of atmosphere in turbulent connection with the surface of the earth and the height of the BL, referred to in this article as the mixing height (MH), defines the volume of atmosphere in which gas-phase or aerosol chemical species, emitted within the BL, are mixed and dispersed. Based on surface-level in situ measurements of aerosol properties and size distributions, knowledge about the height to which particles may be mixed can also improve assumptions about aerosol properties aloft for the purpose of aerosol-cloud interaction studies. The combination of MH, updrafts, wind speed and direction, and other meteorological information is crucial to understanding of in situ atmospheric chemistry measurements made during air quality studies. Well-mixed BLs often occur over/near land in the

unstable daytime convective boundary layer (CBL), typically as a result of surface heating. Stable boundary layer (SBL) conditions may be observed over land, typically at night where, in the absence of surface heating, the BL is in general not well mixed. SBL conditions are also observed over cold oceans. Very stable boundary layers (vSBL), typically observed over land, exhibit weak shear turbulence and strong temperature gradients near the surface [92].

A key challenge in relating the remote sensing (Lidar) and in situ aerosol measurements is that the former are made under ambient Relative Humidity (RH) conditions, while the latter are made under dry RH conditions (typically $\leq$ 20 $\%RH$) [108, 107]. At high RH, hygroscopic aerosols uptake water, which affects their optically relevant properties (e.g., size, morphology, and refractive index). In order to address the influence of hygroscopic growth, we use two methods: First we apply scattering enhancement due to hygroscopic growth f(RH) factor to in situ data, and second we convert the dry aerosol properties measured in situ to ambient conditions using a hygroscopic growth adjustment. In both cases, we compare these data to those obtained via multi-wavelength lidar measurements.

The Athens Metropolitan Area (AMA) is an ideal location to study these issues. It is densely populated and hosts many commercial and industrial activities in a relatively small area. High aerosol concentrations can be present during long periods of time [100]. Strong vertical aerosol gradients in the lower troposphere can form in regions surrounded by mountains, under stable atmospheric conditions with weak air circulation and high anthropogenic activity [103].

During summer and early autumn (warm period), the circulation over the Eastern Mediterranean is dominated by a persistent northerly flow known as the Etesians [93]. When the Etesians prevail, the advection of air masses is evident over the Eastern Mediterranean, rendering the long range transport as the most important factor for high concentrations of gases and aerosol particles. Airborne measurements performed during an Etesian outbreak [89] clearly show that neutral to stable atmospheric conditions prevail over the Northern and Central Aegean Sea, with reduced friction velocities and absolute turbulent fluxes (momentum or heat) cumulating the concentrations below the planetary boundary layer and mainly inside the shallow marine atmospheric boundary layer. Unstable conditions are observed only over the South Eastern Aegean Sea, in the vicinity of Crete,

resulting in enhanced friction velocities and large positive values of sensible heat flux. In previous studies, the fine aerosol fraction over the Aegean Sea has been related to regional sources of pollution which is enhanced by long-range transport during the Etesian flow. A mixture of anthropogenic [43], biogenic [35], and biomass burning emissions [12] originating mainly from the Balkan area, as well as the central and Eastern Europe, results in enhanced aerosol concentrations in the Southern Aegean Sea.

At the same time, high number concentrations of nucleation-mode particles are observed in the Northern Aegean Sea [91], associated with polluted air masses transported from Istanbul. [39] proposed that based on simulations, what contributed to new particle formation (NPF) events was the clean air masses of low preexisting aerosol particles with sufficient H_2SO_4 from high altitudes. During the NPF period, the air masses pass over the greater Istanbul area, avoiding mixing with the local emissions. Thereafter, they penetrate at lower levels (due to the Etesian flow structure) over North Western Turkey. During the non-NPF period, the air masses suffered a strong mixing during their longer journey over the Turkish mainland. Without excluding the role of photochemistry in NPF, it was shown by both measurements and simulations that the plume over the Aegean Sea moved fast with rather negligible mixing, especially above the marine atmospheric boundary layer. The fast advection above marine atmospheric boundary layer and the low number of preexisting concentrations inside the plume prevented the subsequent growth of the nucleated particles towards the central Aegean Sea. Although long datasets of particle number concentration data in the Eastern Mediterranean are not available, [4] report a mean particle concentration of 1.6×10^3 particles per cm^3 at Finokalia (FIN) regional station during 2008 and 2009.

1.3 Remote sensing of the atmosphere

The science of making inferences about objects from measurements, made at a distance, without coming into physical contact with the objects under study, is called remote sensing. Remote sensing includes all methods that use a force field (i.e., acoustic, gravity, magnetic, electromagnetic etc.) in order to obtain remotely information about an object. Remote sensing has acquired quite an attention, in the last decades, because of the many possibilities to obtain information about the

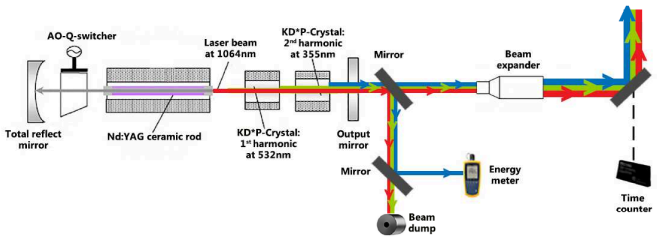

Figure 1.3: EOLE lidar Transmit Unit [3]

structure and the constitution of the atmosphere with a high vertical resolution. In the current work, lidar is the fundamental active remote sensing instrument which was used to study the structure of the lower troposphere (including the PBL) and to obtain the optical and microphysical properties of aerosols.

1.3.1 The NTUA Raman lidar EOLE

The NTUA Raman lidar system is called EOLE and its transmitting unit is demonstrated in Figure 1.3. A pulsed solid state Nd:YAG (Neodymium-doped Yttrium Aluminium Garnet) laser (Spectra-Physics LAB-170-10 model) is the laser source. The primary laser beam is emitted at 1064 nm with a repetition frequency of 10 Hz. At the beginning, the energy of each laser pulse is 850 mJ. The second and third harmonic frequencies of the Nd:YAG system (at 532 nm and 355 nm, respectively) are produced with the use of two non-linear KD*P (Potassium Dideuterium Phosphate) crystals. The laser beam has a Gaussian profile, a 10 mm diameter and its beam divergence is smaller than 0.5 mrad. The energy of the laser beam is controlled by an energy meter at the beginning of each measurement, while the laser is getting heated (see Figure 1.3).

A 100% reflective dichroic mirror allows only the laser beam at 355 nm to reach the energy

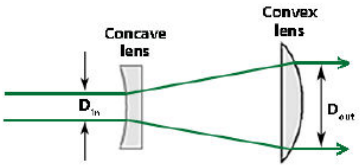

Figure 1.4: Beam expander: Galilean type [3]

meter, while the other two laser beams at 532 and 1064 nm are transmitted through the mirror and are guided to a beam dump. When the laser is sufficiently heated, it is turned to the Q-Switch mode. The main turning mirror is rotated 90° around its axis, allowing the three laser beams (at three wavelengths) to expand with a factor of 3. Then, they are transmitted to the atmosphere by a highly reflective mirror (reflection coefficient of 99.9% at all three wavelengths). The beam expander type is Galilean. A Galilean beam expander consists of a concave lens followed by a convex lens as demonstrated in Figure 1.4. The magnification power is determined by the ratio of the outgoing beam diameter D_{out} over the incoming beam diameter D_{in}. The beam expander consists of four lenses; three made of Barium crown $[N - BaK_2]$ and one of Calcium Fluoride $[CaF_2]$ manufactured by Dorotek GmbH. It provides a magnification of a factor 3 and thus, the outgoing expanded beam has a diameter of 30 mm. Likewise, the beam divergence is 3 times smaller (0.17 mrad Full Width at Half Maximum (FWHM) at 95% of energy) than the one of the incoming laser beam. The final turning mirror (manufactured by Laseroptik GmbH), the one that guides the laser beam to the atmosphere, is highly reflective at all operational wavelengths when the incident angle of the laser beam to the mirror is 45°.

The receiver unit of EOLE is demonstrated in Figure 1.5. A Cassegrain type telescope collects the backscattered light. At the telescope's bottom there is a concave parabolic mirror of diameter d=300 mm and focal length f=600 mm. Thus, the telescope has a half-angle divergence θ of roughly 244 mrad. An illustration of the telescope focal point is given in Figure 1.6. The parabolic mirror has a substrate of magnesium fluoride $[MgF_2]$, an inorganic compound which increases the reflectivity at the spectral region of 355-1064 nm. On top of the MgF_2 a substrate of silicon dioxide $[SiO_2]$ protects the former. Finally, the reflectivity of the telescope mirror is above 85% for light beams at the detected wavelengths (in particular lower reflectivity of 85% at 1064 nm and higher reflectivity

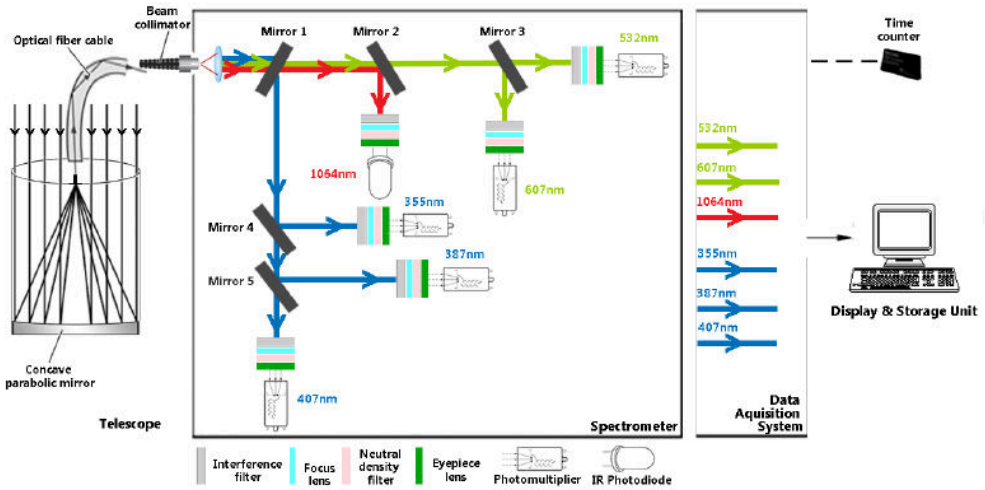

Figure 1.5: EOLE lidar Receiver Unit [3]

of 98% at 355 nm).

The light collected is guided to the detection unit through an optical fiber, which is mounted to a base that can be mechanically adjusted at the focal point of the telescope mirror. The optical fiber is manufactured by A.R.T Photonics GmbH and it is of a SiO_2 type. The fiber's core has a diameter of 1.5 whereas the cladding (with refractive index $n_2 > n_1$) is of a 1.6 mm diameter. The light propagation in an optical fiber is presented in Figure 1.7. A beam of light will be guided through the fiber only if the beam enters the core with an angle lower than a certain angle which is called acceptance cone angle of the fiber φ_a. In any other case, the beam of light will be lost in the cladding. The Numerical Aperture (NA) of the fiber, which is a simplified measure of the fiber's light gathering capacity, is indicated by the maximum angle of acceptance. The Numerical Aperture (NA) is expressed mathematically as the sine of the acceptance cone angle. The NA of EOLE optical fiber has been estimated equal to 0.22 ± 0.02 and the resulting final field of view of the EOLE system is 1.5 mrad (Full Width at Half Maximum (FWHM)) [3].

The light received, which propagates through the optical fiber, passes through a beam collimator before entering to the optical detection unit. The collimated light beam is splitted into several beams by a series of dichroic filters (beamsplitters), as can be seen in Figure 1.5. All of EOLE's beamsplitters have been manufactured by Omega Optical.

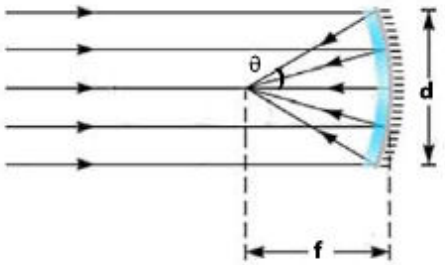

Figure 1.6: Focal length of a concave parabolic mirror [3]

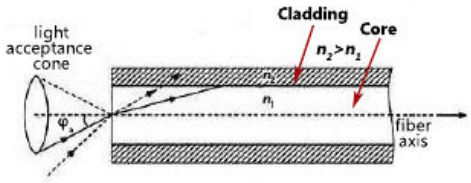

Figure 1.7: Light propagation in an optical fiber cable [3]

In order to reduce the intensity of the backscattered signal as well as the atmospheric background noise, the spectrally separated light beams are transmitted through a series of optical filters. These optical filters are consisted of a narrow-band Interference Filter (IFF), followed by a focusing lens and a/some Neutral Density (ND) filter(s). The purpose of the use of ND filters, which are manufactured by Melles Griot-CVI, is to reduce the signal intensity of the elastically-backscattered light beams at 355, 532 and 1064 nm. Lastly, an eyepiece lens is used right before the light beam enters the photo-detectors. Hence, the Signal to Noise Ratio (SNR) is definitely increased, provided that the narrow spectral width of the interference filters permit only the detected wavelengths to be transmitted through the filter.

The selection of the IFF is based on its transmissivity (T), its Optical Density (OD) and its spectral width. The blocking ability of the interference filter is demonstrated by its OD with respect to the amount of radiation which is transmitted through it. The OD is related to the filter percent transmission (T) as

$$OD = -log_{10}\left(\frac{T}{100}\right) \tag{1.1}$$

A filter's bandwidth is the wavelength range used to indicate the part of the spectrum that a beam of light is transmitted through it. It is also referred as Full Width at Half Maximum (FWHM). The focusing lenses have a diameter 25.4 mm and a focal length of 40 mm. The ND filters are only used at the backscattered lidar signals at 355, 532 and 1064 nm, to reduce their amplitude, as there is a strong elastic backscattering component from the lower layers of the atmosphere. This could cause saturation to the data acquisition unit and therefore, ND filters are necessary as light intensity attenuators. The collected light in EOLE detection unit is attenuated up to 70% by ND filters used. The presence of ND filters at all detected wavelengths is displayed in Figure 1.5. The ND filters used at 387, 407 and 607 nm attenuate the collected light only up to 20%, as the inelastically backscattered light from atmospheric gases is, in general, weak. The eyepiece lens consists of two plano-convex lenses (doublet type, a sequence of two plano-convex lenses with their convex sides to osculate aside, paired together such as spherical and chromatic aberrations are reduced when a light ray is transmitted through a doublet lens) manufactured by Thorlabs S.A. The effective focal length is 29.79 mm for all wavelengths, except for 1064 nm, which has a total focal length of 14.89 mm. The reason for this difference is the use of an avalanche photodiode which has a detection cross-section of 1.5 mm, much smaller than the one that photomultipliers have (used at all other wavelengths), which is 5 mm. Due to the inhomogeneity of radiation's spatial distribution when reaching the receiving area of the photo-detectors, the use of an eyepiece lens is crucial. When eyepiece lenses are used, the advantages are:

1. the range-dependence of the lidar backscattering effect on the final image at the photocathode is significantly decreased (i.e., backscattered signal from lower altitudes does not appear at different spots on the detector effective area than backscattered signal from higher altitudes).

2. the spatial inhomogeneity problem at the photocathode of the photomultiplier is eliminated.

Hamamatsu S.A. manufactured the PMTs used (type R7400: P and Y series). The photocathode of the photomultipliers is an alloy multialkali (Na-K-Sb-Cs) with quantum efficiency (quantum efficiency, expressed as a percent, is the number of photoelectrons emitted from the photocathode

divided by the number of incident photons) of 12% at 532 nm, 20% at 387 and 407 nm, 22% at 607 nm and 23% at 355 nm. The Avalanche Photo-Diode (APD) used for the detection of the 1064 nm radiation is also manufactured by Hamamatsu S.A. (model APD-1.5).

When the detected backscattered light (at all wavelengths mentioned above, from UV to the near IR) is exiting from the PMTs and the APD, it enters the data acquisition system in analog detection mode or photon counting detection mode. When the pulse exits the PMT at the analog detection mode, it is being recorded as output current, while at the photon counting detection mode, all the produced photoelectrons by the PMT are recorded as counts. The latter detection mode is more accurate under low Signal to Noise Ratios and provides high stability of the lidar signal. The photon counting mode can be applied only to lidar signals backscattered from higher altitudes (e.g. $>$ 4-5 km), as at low altitudes the PMTs cannot detect photoelectrons that arrive at a very high rate due to the dead time effect.

In EOLE system, the lidar signals at 355, 532 and 1064 nm are detected both in the analog and photon counting mode, whereas the signals at 387, 407 and 607 nm are detected only in the photon counting mode. LICEL GmbH has manufactured the EOLE data acquisition system. When the signal is detected in analog mode, the digitization of the signal is required. The Analog-to-Digital conversion is done with an accuracy of 12 bits for 8192 time bins with the possibility of integrating up to 4000 pulses. If the laser pulse repetition frequency is 10 Hz, in order to achieve a signal with a time resolution of 100 seconds, 1000 pulses are integrated in each recording. The resulting raw spatial resolution is 7.5 m, keeping in mind that the EOLE transient recorders have a 20 MHz sampling rate. The amplitude range of the detected analog signals is in the order of 40-150 mV. The photon counting detector consists of a three-order pre-amplifier and a signal discriminator of 64 tuning levels. The maximum theoretical photon counting rate is 250 MHz but the actual rate is 50 MHz due to the photomultiplier dead time constrain. For the accurate recording of the backscattered laser photons, the operation of the detection unit should remain within its "linear" region. The upper limit of the recording rate is set when the dead time constrain is applied, which has been measured equal to 6.5 ns (i.e., recording rate of 153 MHz). High energy photons, originating from cosmic rays should be excluded as well, using the relevant discrimination levels.

1.3.2 Doppler Wind Lidar

When the source or the receiver of radiation move relative to one another, a change of perceived frequency is occuring. It was first described by the Austrian physicist Christian Doppler (1803–1853) for acoustic waves, but it occurs for electromagnetic waves as well. Provided that we measure the change of frequency, the relative speed of the source with respect to the receiver can be determined, if the group velocity of the radiation in the respective medium is known. The speed of light in air and vacuum has been known with high accuracy, therefore the optical Doppler effect lends itself ideally for the remote measurement of the speed of very distant objects. Provided that the object does not move directly toward or directly away from the observer, the use of the optical Doppler effect yields the component of the speed of the object along the line of sight. For a velocity measurement the object must emit electromagnetic radiation. This happens for stars and galaxies. An application of the optical Doppler effect was the determination of the shift of light from distant stars to longer wavelengths, leading to our present notion of an expanding universe. As the relative shift of optical frequencies, $\frac{\Delta f}{f}$, is proportional to $\frac{v}{c}$ (the ratio of the velocity v of the object to the speed of light c) and since very distant stars move away fast, these measurements were comparatively easy to make.

1.3.2.1 The Optical Doppler Effect

Unlike sound, light is not "advected" by some medium. Therefore, in the optical Doppler effect, there is no distinction between the case of the moving transmitter and the moving receiver, or both transmitter and receiver moving in a medium. Provided that the emitted light has a wavelength of λ_0 and a frequency of $f_0 = \frac{c}{\lambda_0}$ and the relative speed along the line of sight is v, then the frequency observed is

$$f = f_0(1 + \frac{v}{c}) \tag{1.2}$$

Air and aerosols do not emit light, therefore, for a measurement of their speed they have to be illuminated by light from the lidar transmitter.

If the frequency of that light is f_0, then its apparent frequency on the aerosol particle is provided by Eq. (1.2). The light is reemitted, or back-scattered, at this frequency. As the particle is moving while scattering, the reemitted light is detected by the lidar receiver as being shifted to frequency

$$f = f_0 + \Delta f = f_0(1 + 2\frac{v}{c}) \tag{1.3}$$

The particle (or wind) velocity is defined in such a way that a movement toward the lidar which leads to a positive frequency shift is characterized by a positive line-of-sight velocity, and vice versa. We occasionally use the term "radial velocity" v_r or radial component of a velocity vector that is not parallel to the line of sight instead of the line-of-sight velocity v_{LOS} or velocity component along the line of sight. The quantities v_{LOS} and v_r are fully synonymous, with the same sign convention. The collective movement of air masses which we call wind is superimposed by the individual, thermal, random movement of the molecules, which normally move much faster than the wind speed. In fact, the faster they move, the higher the temperature. The relative shift of their velocity distribution with the wind speed is therefore small. Aerosol particles, due to their higher mass, move more slowly at the same temperature and have a narrower velocity distribution. They are shifted by the same amount, but relative to its width this shift is much larger and therefore measurable.

1.3.2.2 Doppler Wind Lidar Wavelength Considerations

The laser wavelength can be chosen at random in Doppler wind lidar . Nevertheless, as the aerosol contribution to the return signal is much better suited for frequency analysis than the molecular signal, the wavelength to be used will depend on the expected magnitude of the return signal and the expected ratio of aerosol-to-molecular backscatter. The molecular signal is proportional to λ^{-4}, while the aerosol signal, depending on wavelength range and particle properties, is proportional to something between λ^{-2} and λ^{+1}. Hence, even if the aerosol return signal decreases with an increase in wavelength, the molecular "background" signal decreases much faster so the aerosol-to-molecular backscatter ratio gets more favorable.

1.3.2.3 Doppler Wind Lidar Heterodyne Detection Technique

In heterodyne detection the return signal is mixed with the radiation from a local optical oscillator ("LO"). The mixed signal incorporates the sum and the difference frequencies of the two components. The sum is far above the frequency cutoff of the detector, while the difference is a low-frequency

signal that can be determined accurately. Thus, for heterodyne-detection lidar what is needed is a pulsed transmitter laser with high frequency stability of the output frequency f_0 and a second, continuous-wave laser with frequency f_{LO}. The mixing of the two leads to frequencies $f_{LO} \pm (f_0 + \Delta f)$, where $f_0 + \Delta f$ is the Doppler- shifted frequency backscattered from the atmosphere. The superposition, apart from a DC component, results in a detector current equal to

$$i_{AC} = \rho \left(\sqrt{2P_{LO}P(x,\lambda)} \cos\left[2\pi(f_{LO} - (f_0 + \Delta f))\right] + \sqrt{2P_{LO}P(x,\lambda)} \cos\left[2\pi(f_{LO} + (f_0 + \Delta f))\right] \right) \tag{1.4}$$

Only the first component, or beat signal

$$i_{DET} = \rho\sqrt{2P_{LO}P(x,\lambda)} \cos\left[2\pi(f_{LO} - (f_0 + \Delta f))\right] \tag{1.5}$$

is measured by the detector, with

ρ	the detector sensitivity
P_{LO}, f_{LO}	the power and frequency of the reference laser
$P(x,\lambda), f_0 + \Delta f$	the power and frequency of the backscattered radiation

$P(x,\lambda)$, $f_0 + \Delta f$ are the only ones that vary with range x. The frequency difference between the frequency of the transmitted laser pulse, f_0, and the local oscillator, f_{LO}, is determined with great accuracy and preserved as stable as possible during the measurement. The frequency difference is also a key parameter in the subsequent signal evaluation. A coherent Doppler lidar (Figure 1.8) is consisted of a high-power, frequency-controlled, pulsed laser transmitter (TE), a transmitter-receiver telescope, two heterodyne detectors (D1, D2) in which the local-oscillator radiation is mixed with the outgoing pulse (D1) and with the Doppler-shifted backscatter signal (D2), and a signal processing system (not shown in Figure 1.8).

The two lasers are connected through a locking loop (LL). The laser pulse length is normally a few microseconds. The temporal distribution of the pulse power is either gaussian (for solid-state lasers) or like a gain-switched spike (for CO2 lasers). If a CO2 laser is used at a wavelength around 10.6 μm, a frequency shift Δf of 189 kHz corresponds to a radial velocity component of 1 ms^{-1} [105]. The optical signal contains speckle that results from constructive and destructive interference

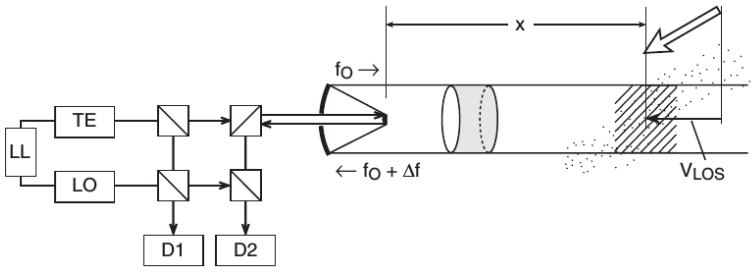

Figure 1.8: Principle of a heterodyne-detection Doppler lidar [105].

of waves scattered by randomly distributed particles. Different shots into the same part of the atmosphere hence lead to different return signals due to the random distribution of the scatterers. Heterodyne-detection lidars therefore differ from most other lidars by their need for

1. a pulsed, narrow-frequency, ultrastable high-power laser.
2. a second narrow-frequency laser, which is usually referred to as local oscillator (LO).
3. a fast detector in which the return and LO signals are mixed.
4. a second fast detector in which the transmitted and LO signals are mixed (the so-called pulse monitor).
5. the time for averaging over several shots to average out speckle.
6. the presence of aerosol particles.

The main advantages of the heterodyne-detection technique are the high tolerance of background light and the independence of temperature and all properties of the optical components of the system.

1.3.2.4 Doppler Wind Lidar Scan Techniques

Since pulsed Doppler lidars measure profiles of the line-of-sight wind velocity, vertically pointed systems provide the profile of the vertical wind velocity. The lidars must be tilted out of the vertical in order to measure the horizontal wind. Thus, the horizontal wind produces a line-of-sight component to the lidar signal, and with appropriate scanning schemes, the three-dimensional wind vector can be derived. A necessary assumption is the horizontal homogeneity of the wind field in the sensed volume. Nonetheless, vertical homogeneity is not required.

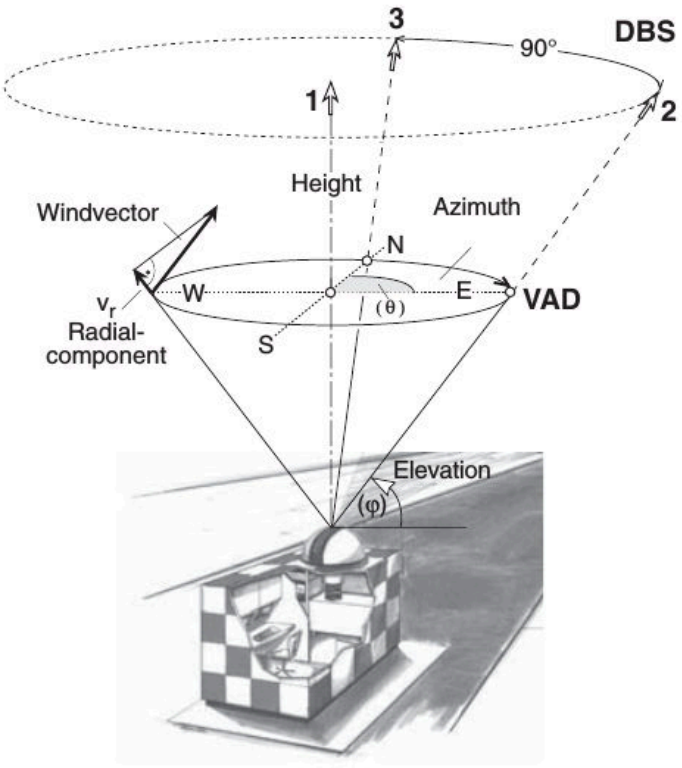

Figure 1.9: Schematic of the scan technique of a Doppler lidar. Lower part: VAD scan, upper part: DBS scan [105].

VAD Technique When a conical scan is carried out with the apex of the cone at the lidar scanner as depicted in Figure 1.9 and, for a given height or distance, the velocity signal is displayed as a function of azimuth angle, a plot as the one shown in Figure 1.10 is obtained [105].

The technique got its name from this display of velocity versus azimuth (velocity-azimuth display, VAD). In the ideal case that there is a homogeneous atmosphere, the measured LOS component shows a sine-like behavior (Figure 1.10) given by

$$\upsilon_r = -u \sin\theta \cos\varphi - \upsilon \cos\theta \cos\varphi - \omega \sin\varphi \tag{1.6}$$

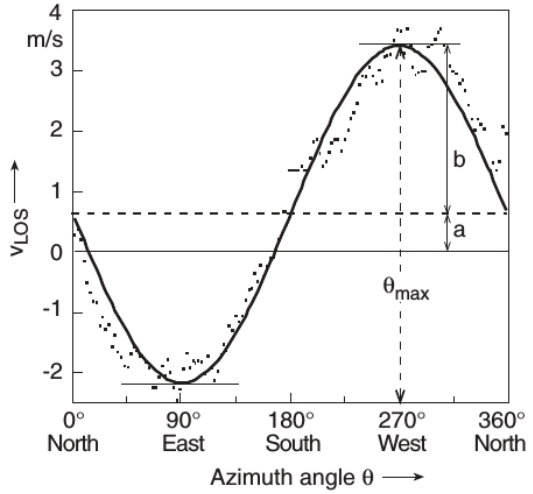

Figure 1.10: Example of sine fitting of the radial wind velocity simulated with the use of the VAD technique [105]

u the west–east component

υ the south–north component

ω the vertical component

ϑ the azimuth angle, clockwise from North

φ the elevation angle

Fitting this to a function of type

$$v_r = a + b\cos(\theta - \theta_{max}) \tag{1.7}$$

with offset a, amplitude b, and phase shift θ_{max} , we acquire the three-dimensional wind vector

$$u = (u, v, \omega) = (-b\frac{\sin\theta_{max}}{\cos\varphi}, -b\frac{\cos\theta_{max}}{\cos\varphi}, -\frac{a}{\sin\varphi}) \tag{1.8}$$

With this, the horizontal wind speed v_{hor} is

$$v_{hor} = (u^2 + v^2)^{\frac{1}{2}} = \frac{b}{\cos\varphi} \tag{1.9}$$

the horizontal wind direction dd, as westwind, e.g., blows from the west,

$$dd = \theta_{max} \tag{1.10}$$

vertical wind velocity w, defined as positive for wind up, is

$$\omega = \frac{a}{sin\varphi} \tag{1.11}$$

and total wind speed is

$$|u| = (u^2 + v^2 + \omega^2)^{\frac{1}{2}} \tag{1.12}$$

.

In order to obtain a VAD scan, a separate sine-wave fit is done for each height interval. From each height interval, one set of data a, b, θ_{max} and, consequently, u, v, ω is obtained.

The smoothness of the sine-wave fit and thus the precision of its parameters depends on instrumental parameters, turbulence and therefore roughness of the terrain, and on weather data such as atmospheric stratification stability. These factors must be taken into account in addition to lidar data such as pulse-repetition frequency and time-bin width, if a planned measurement is to yield the desired data in a predetermined time.

DBS Technique If we make the assumption of cellular flow with little turbulence which would lead to a smooth sinusoidal behavior in the VAD scan, it could be expected that four measurements at azimuth-angle intervals of 90°, or three at 120°, or even two at right angles should be sufficient, along with one measurement in the vertical. In the case of three directions (vertical, tilted east, and tilted north), the three components u, v, ω are obtained as follows:

$$u = -\frac{(v_{r2} - v_{r1}\sin\varphi)}{\cos\varphi} \tag{1.13}$$

$$v = -\frac{(v_{r3} - v_{r1}\sin\varphi)}{\cos\varphi} \tag{1.14}$$

$$\omega = -v_{r1} \tag{1.15}$$

Here v_{r1}, v_{r2}, and v_{r3} are the vertical, east, and north radial velocities, respectively. The Doppler beam swinging, or DBS, technique is faster and simpler in the hardware and in the data evaluation algorithm. However, it lacks the goodness-of-fit information as a measure for the reliability of the results. This drawback is partially compensated by information about the temporal behavior of the

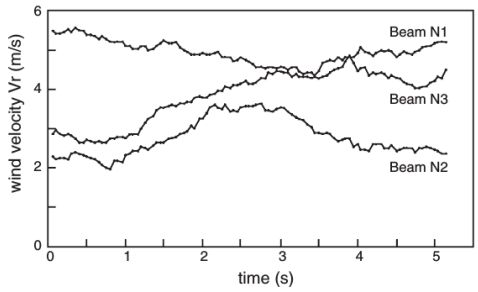

Figure 1.11: Simulation of the behavior of turbulent wind components in the boundary layer [105]

data. Figure 1.11 presents results of a simulation of high-frequency data obtained from three slant lidar beams oriented such that the projections onto the horizontal plane form three angles of 120°.

Using data such as those of Figure 1.11, the degree of smoothing (or temporal integration) necessary to obtain the wind speed and direction data required for a given application can directly be inferred. Moreover, turbulence is easily determined for any time scale as dictated by the particular process investigated, particularly as turbulence depends critically on ground roughness length and atmospheric stratification stability.

Since parameters such as maximum range, range resolution, temporal resolution (or scan rate), and wind-speed and wind-direction sensitivity all depend on each other, these dependencies must be known and observed when planning a measurement for a given purpose.

1.3.2.5 Doppler Wind Lidar Used In The Current Study

In this study we utilize data from a Stream Line Pro system scanning Doppler lidar manufactured by Halo Photonics. All Halo Photonics Stream Line versions are 1.5 μm pulsed Doppler lidars with a heterodyne detector that can switch between co- and cross-polar channels [72]. The Stream Line Pro version is designed for harsh environmental conditions with no exterior moving parts, which limits the scanning to within a cone of 20° from the vertical.

The minimum range is 90 m, and the telescope focus of the Stream Line Pro lidar is user-configurable between 300 m and infinity. Integration time per ray is user-adjustable and can be optimized between high sensitivity (long integration time) and high temporal resolution (short integration time) depending on the environmental conditions and research questions.

In measurement mode the Halo Doppler lidar provides three parameters along the beam direction: radial Doppler velocity (υ_r), signal to noise ration (SNR) and attenuated backscatter (β), which is calculated from SNR taking into account the telescope focus.

The Doppler scanning lidar system (StreamLine Wind Pro model, HALO Photonics) at 1.5 μm was operated in the vertical azimuth display (VAD) mode and the 3-beam Doppler beam swinging (DBS) mode. It mainly provided the vertical profiles of the radial wind and 2-3D wind fields, as well as the atmospheric turbulent properties (e.g. turbulent dissipation rate, ϵ) [67]. The wind velocity is provided with accuracy better than 0.1 and 0.5 ms^{-1} for VAD and DBS mode, respectively. The range resolution of the measurements is 30 m, and the temporal resolution is 14 seconds and 15 min for DBS and VAD modes, respectively; the maximum range achieved is 2-3 km (or even 10 km height, under the presence of clouds) depending on the atmospheric aerosol load [71].

Chapter 2

Particle number size distribution statistics at City-Centre Urban Background, Urban Background, and Remote stations in Greece during summer

Particle number size distribution measurements were conducted during the summer of 2012 at City-Centre Urban Background (Patras-C), Urban Background (ICE-HT in Patras, DEM in Athens, EPT in Thessaloniki), and Regional Background stations (FIN in Crete). At the City-Centre Urban Background station, the average number distribution had a geometric mean diameter peak approximately at 60 nm and the highest number concentration, whereas at the Regional Background station and the Urban Background stations it displayed a major peak approximately at 100 nm, with the Regional Background station exhibiting the lowest number concentration. The particle number size distribution at each site was divided into size fractions and, based on their diurnal variation and pre-

vious studies, we concluded that the main sources for the City-Centre Urban Background station are traffic and the regional background concentration, for the Urban Background stations fresh traffic, aged traffic, cooking and the regional background concentration, and for the Regional Background station local activities (tourism, cooking) and regional background concentration. The median number concentration that is attributed to regional background concentration for the City-Centre Urban Background, the Urban Background and the Regional Background stations are respectively 13, 29 and 45% of the total number concentration. Nucleation events were identified at DEM station, where the newly formed particles accounted for 4% of the total particle concentration for the measurement period in the size range 10-20 nm, EPT, where they accounted for 12%, and FIN, where they accounted for 1%, respectively. New Particle Formation events contribution during summer to Condensation Cloud Nuclei were therefore insignificant in the Eastern Mediterranean. Modal analysis was performed on the number distributions and the results were classified in clusters. At the City-Centre Urban Background station, the cluster-source that dominated number concentration and frequency is related to fresh and aged traffic emissions, at the Urban Background stations aged traffic emissions, while at the Regional Background station number and frequency were dominated by the regional background concentration. Based on cluster analysis, 18% of the median number distribution was due to long range transport at the City-Centre Urban Background site, 37% at the Urban Background sites, and 59% at the Regional Background site. The Flexible Particle Dispersion Model (FLEXPART) was used in order to acquire geographic origin clusters and we concluded that the Etesian flow increases the median regional background number concentration in the Mediterranean basin by a factor of 2.5 to 4.

2.1 Materials and Methods

Simultaneous particle size distribution measurements were performed at five sampling stations in Greece. The measurements were conducted in Patras, Athens, Thessaloniki and Finokalia (Figure 2.1), during June and July 2012.

Patras is located at the foothills of a mountain with a height of approximately 2 km, at the Gulf of Patras. It is an urban area with a population of approximately 300,000 inhabitants. Measurements

Figure 2.1: City-Centre Urban Background (red color circle), Urban Background (yellow color circle), and Regional Background (white color circle) stations.

were conducted simultaneously at two stations in Patras.

The City-Centre Urban Background station (Patras-C) was located at the central square of Patras (38.238° N, 21.74° E, at 50 m a.s.l.) on the roof of a seven-floor building. This station was near the harbor and it was influenced by traffic. The particle number size distributions in Patras-C were measured by a Scanning Mobility Particle Sizer (SMPS, model 3936, TSI) operated so as to cover the particle size range between 10 to 470 nm (electrical mobility diameter). The sheath flow rate was 4 $Lmin^{-1}$ and the sample flow rate was 1 $Lmin^{-1}$. The duration of each measurement was 3 minutes. The inlet line length was 2 m, the tube diameter was 1/4 in and the inlet flow rate was 1 $Lmin^{-1}$. At Patras-C, due to diffusion losses, penetration was 84% for 10 nm particles and 90% for 15 nm particles. The calculations were carried out according to [32]. The mean concentration in the size range 10 to 15 nm represents 4% of the mean concentration of the total particle number size distribution in Patras-C station. As reported by [106], in a series of EUSAAR-ACTRIS workshops, instruments used at EUSAAR-ACTRIS network were within an uncertainty range of 10% for all sizes between 20 to 200 nm against a reference system. For particles larger than 200 nm, the uncertainty

range increases to 30%. For particles in the size range 10 to 20 nm, the uncertainty is expected to be significantly larger than 10%. Keeping these information in mind, we consider that a correction for diffusion losses is not necessary for Patras-C station.

The second station (ICE-HT Patras) was located at the ICE-HT Institute (38.3° N, 21.81° E, at 100 m a.s.l.), 8 km north-east from Patras city center, 2 km from the sea and 1 km south from the Patras-Athens highway, in a suburban area surrounded by olive tree fields, while some small settlements are within a distance of 1 km. At ICE-HT station, a Scanning Mobility Particle Sizer (SMPS, classifier model 3080, DMA model 3081, CPC model 3787, TSI) was deployed for the measurement of the number size distribution in the range 10 to 496 nm. The SMPS operated at a sheath flow rate of 5 $Lmin^{-1}$ and a sample flow rate of 1 $Lmin^{-1}$. Each measurement had a duration of 3 minutes. The inlet line length was 8 m, the tube diameter was 3/4 in and the inlet flow rate was 3 $Lmin^{-1}$. Due to diffusion losses, penetration was 80% for 10 nm particles and 88% for 15 nm particles [32]. The mean concentration in the size 10 to 15 nm represents 3% of the mean concentration of the total particle size distribution. Diffusion losses are considered insignificant when compared to the total particle number size distribution and the measurement uncertainty in the size range 10 to 15 nm, therefore, we do not apply a correction.

The measurements reported here for Athens have been conducted at the Demokritos station (DEM, 37.995° N, 23.816° E, at 270 m a.s.l.), which is a member of the GAW (Global Atmosphere Watch) and ACTRIS (Aerosols, Clouds, and Trace gases Research Infrastructure) Networks, and is situated on the foot of Mount Hymettus in Agia Paraskevi. The DEM monitoring station belongs to the National Centre of Scientific Research "Demokritos", which is situated about 7 km north from the center of Athens, in a pine forest [99]. It is representative of the atmospheric aerosol in the suburbs of the Athens Metropolitan area (AMA), which is densely populated (3,750,000 inhabitants) and hosts many commercial and industrial activities in a relatively small area (approximately 4.5×10^2 km^2). [61] report that for DEM station dependence on traffic and weather parameters was minor, but there was a strong seasonal variation. It is frequently influenced by katabatic winds [20], during which, air masses from mount Hymettus (peak height 1024 m) are brought over the station. Also, the lowering of nocturnal boundary layer height (NBLH) occasionally results in an increase in particle number

concentration, even in the absence of aerosol particle sources. In Athens, particle size distribution measurements were conducted with an SMPS, consisting of an Electrostatic Classifier model 3080, a DMA column model 3081, and a Condensation Particle Counter (CPC 3022A, TSI Inc). The size range measured extended from 13 to 661 nm. Each measurement had a duration of 5 minutes (including 15 s down scan time). Flows within the DMA were checked and adjusted if necessary every week, with the sheath and inlet flows set at 3 and 0.3 $Lmin^{-1}$ respectively. The inlet line consisted of two parts: The first part had a length of 6 m with a tube diameter of 2.5 cm and a flow rate of 9.5 $Lmin^{-1}$. The second part had a length of 25 cm with a tube diameter of 1/4 in and a flow rate of 0.3 $Lmin^{-1}$. Due to diffusion losses, penetration was 88% for 13 nm particles and 90% for 15 nm particles [32]. The mean concentration in the size 10 to 15 nm represents 5% of the mean concentration of the total particle number size distribution. Diffusion losses are considered insignificant when compared to the total particle number size distribution and the measurement uncertainty in the size range 13 to 15 nm, therefore, we do not apply a correction.

Thessaloniki is a densely populated (16,000 inhabitants per km^2) coastal city in Northern Greece with a total population of approximately 1,000,000 inhabitants. The city is located NE of the Thermaikos Gulf, and is surrounded by residential communities and an industrial zone on the NW. The daily mean air temperature and relative humidity (RH) vary from 5.5 to 28.1 °C and from 47 to 80%, respectively [98]. The station is located on Agrafon Street at Eptapyrgion (EPT) (40.63° N, 22.95° E, at 174 m a.s.l.) next to small residences, a park on the West, and the city ring road 1 km away on the East. In EPT station, an SMPS (TSI, Model 3034) was employed to measure the size distributions in the range of 10 to 487 nm. The SMPS 3034 operates at a fixed 1 $Lmin^{-1}$ sample flow rate (4 $Lmin^{-1}$ sheath flow rate). Each measurement had a duration of 3 minutes. The inlet line length was 1.5 m, the internal tube diameter was 0.5 cm, and the inlet flow rate was 1 $Lmin^{-1}$. Due to diffusion losses, penetration was 85% for 10 nm particles and 91% for 15 nm particles [32]. The mean concentration in the size 10 to 15 nm represents 3% of the mean concentration of the total particle size distribution. Diffusion losses are considered insignificant when compared to the total particle number size distribution and the measurement uncertainty in the size range 10 to 15 nm, therefore, we do not apply a correction.

Finokalia (FIN) station is a European super-site for aerosol research, part of the ACTRIS Network (35.3° N, 25.67° E, at 250 m a.s.l.). The station is situated on the NE part of the island of Crete, facing the Mediterranean Sea in the wide north sector, located on the top of a hill over the coastline. FIN station is representative of the background marine conditions of Eastern Mediterranean [48], with little anthropogenic influence. The nearest city is Heraklion with approximately 170,000 inhabitants, located about 50 km west of Finokalia. [37] report that nighttime new particle formation (NPF) events with very limited growth are relatively common in Finokalia, and such events tend to be associated with air mass transport over the island of Crete (local origin). A detailed description of the FIN station and the climatology of the area can be found in [60]. At FIN station, the particle number size distributions were measured in the diameter range 9 to 848 nm using an SMPS built at TROPOS - Leibniz Institute for Tropospheric Research [37]. It is a closed-loop system, at 5 $Lmin^{-1}$ to 1 $Lmin^{-1}$ ratio between the sheath and aerosol flows, and it is operated according to the recommendations by [106]. Each measurement had a duration of 5 minutes. The inlet line consisted of two parts: The first part had a length of 3 m with a tube diameter of 1 in and a flow rate of 16.7 $Lmin^{-1}$. The second part had a length of 0.5 m with a tube diameter of 1/8 in and a flow rate of 1 $Lmin^{-1}$. The measured number size distributions were corrected for diffusion losses according to the methodology described in [106]. Additional information on the sampling stations are provided in Table 2.1.

All inlet aerosol flows were dried to relative humidity (RH) below 40%. All results presented in this work are expected to be within the uncertainty limits provided by [106], which were mentioned earlier in this section.

2.1.1 Size Distribution Modal Analysis

The obtained particle number size distributions (NSD) were analyzed and the modal structure along with the number concentration in each mode were calculated by applying a curve-fitting algorithm. The algorithm used in this study employed the least squares method to fit the sum of up to 4 log-normal distributions to the measurements [34]. The algorithm starts by fitting a uni-modal log-normal distribution, and successively tests the possibility of increasing it to a bi-

Table 2.1: Particle size distribution measurements reported in this work

Station ID	**City**	**Sampling Period**	**Site Location**	**Data Coverage**
Patras-C	Patras	8^{th} of June - 26^{th} of July	City-Centre Urban Background	95%
ICE-HT	Patras	8^{th} of June - 21^{st} of July	Urban Background	89%
DEM	Athens	1^{st} of June - 2^{nd} of August	Urban Background	82%
EPT	Thessaloniki	9^{th} of June - 22^{nd} of July	Urban Background	99%
FIN	Finokalia	1^{st} of June - 31^{st} of July	Regional Background	94%

, a tri- and finally a tetra-modal distribution based on the root mean square error (RMSE), the estimated number concentration of each mode, the geometric mean diameter, and the geometric standard deviation of the neighboring modes. The RMSE of the difference between the SMPS measured number size distributions ($NSD^{MEASURED}$) and the sum of the fitted modes number size distributions (NSD^{FITTED}) is calculated by the following equation:

$$\text{RMSE} = \frac{100}{\sqrt{\text{n}}} \left(\sum_{i=1}^{n} \left[N_{d_{pi}}^{MEASURED} - N_{d_{pi}}^{FITTED} \right]^2 \right)^{0.5} \tag{2.1}$$

where n is the number of size bins of the SMPS size distribution. $N_{d_{pi}}^{MEASURED}$ is the number concentration measured by the SMPS at size bin i corresponding to particle diameter d_{pi}, and $N_{d_{pi}}^{FITTED}$ is the number concentration of the sum of fitted modes at diameter d_{pi}. We performed the modal analysis in order to classify our data in log-normal modes that are determined by the internal structure of each Particle Number Size Distribution. Thus, the identification of possible particle sources is pursued for log-normal modes that are determined impartially.

2.1.2 New Particle Formation (NPF) Events Analysis

In order to locate New Particle Formation events, we used a simplified variant of the procedure described by [18]. Particle number size distributions were visually inspected for the City-Centre

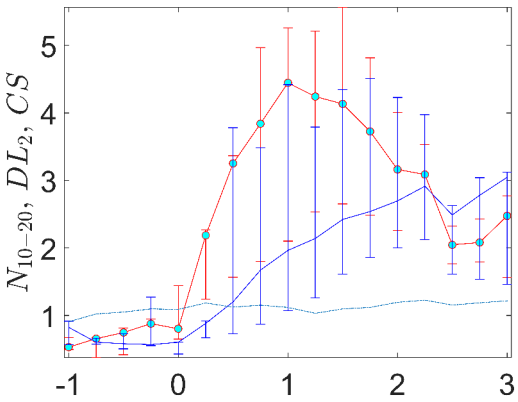

(a) Time relative to start of event, hrs

Figure 2.2: Median temporal evolution of the parameters N_{10-20} (red line), DL_2 (blue line) and CS (cyan dotted line) in the set of the 4 selected nucleation events depicted in Figure A.7 (Appendix). The error bars correspond to the 25^{th} and 75^{th} percentiles.

Urban Background, Urban Background and Regional Background stations. The requirements for a day to qualify as a NPF event day were: 1) a substantial increase in the number concentration of particles in the size bins from 10-20 nm during the time window 09:00-18:00 Local Time, 2) N_{10-20} being significantly elevated above the nocturnal background, 3) the burst having a minimum duration of 1 h, and 4) a decrease in N_{10-20} towards the end of the day. The observation of a gradual increase in nucleation mode diameter was not a necessary criterion to qualify a day as a NPF day, but was nevertheless visible in most cases.

The results obtained by this method were subsequently evaluated using the method proposed by [30]. Four exemplary nucleation events were used as a model set (cf. Figure A7, Appendix).

The parameters used in order to distinguish NPF events were N_{10-20}, the median length diameter (DL_2; a parameter reflecting the decrease in the median particle diameter during a nucleation event) from 10 to 30 nm electrical mobility diameter, and condensation sink (CS) [82].

DL_2 is calculated by the following equation:

$$DL_2 = 0.5 \int_{log(10)}^{log(30)} \frac{dN dlogd_p}{dlogd_p} d_p dlogd_p \tag{2.2}$$

where dN is the concentration of particles in the size range $dlogd_p$.

The condensation sink CS is a parameter defining if volatile species (e.g. sulphuric acid vapors),

will form new particles or condense onto existing particles. It is given by:

$$CS = 2\pi D \sum_i \beta_{mi} d_{pi} N_{d_{pi}} \tag{2.3}$$

Here D is the particle diffusion coefficient, d_{pi} the particle diameter of size bin i, $N_{d_{pi}}$ is the respective number concentration and β_{mi} the transitional correction factor [22].

$$\beta_m = \frac{Kn + 1}{0.377Kn + 1 + \frac{4}{3}\alpha^{-1}Kn^2 + \frac{4}{3}\alpha^{-1}Kn} \tag{2.4}$$

α is the sticking coefficient, which is assumed to be unity, and Kn the Knudsen number given by:

$$Kn = \frac{\lambda_v}{r} \tag{2.5}$$

where λ_v is the mean free path of the condensing vapor molecules and r its radius [46]. It should be noted that the CS is calculated based on the SMPS measurements, covering particles having diameters from 10 to ca. 500 nm, and not the entire particle size range. This assumption adds an error to the estimation of CS that can be in the order of 100% when compared to $PM_{2.5}$ (particulate matter with aerodynamic diameter smaller than 2.5 μm) measurements [82].

In Figure 2.2 the temporal evolution of the median value of the above mentioned parameters (N_{10-20}, DL_2, CS) for the four exemplary nucleation events is presented.

Using the algorithm proposed by [30], we succeeded in distinguishing potential NPF events, but the algorithm identified as NPF event cases without a substantial increase of particle concentration in the size bin 10-20 nm. Additionally, there were cases of events distinguished as potential NPF by the algorithm, that started in another location, leading to a banana plot that did not have a high particle concentration in the smaller particle sizes measured by the SMPS, as also observed by [82]. These cases were excluded after visual inspection.

In order to evaluate the strength of the nucleation events, we used the method proposed by [52]. Ultrafine particle concentrations at the Regional Background and Urban Background stations were divided in a mean background concentration and a new particle formation mean concentration.

2.1.3 Clustering methods of Size Distribution Modal Analysis Results

Cluster analysis places objects in clusters suggested by the data, not defined a priori, such that objects in a given cluster tend to be similar to each other, and objects in different clusters tend to be dissimilar. The size distribution modal analysis results were clustered using two different algorithms: K-means [7] and HDBSCAN [59], available by [73]. The most widely used technique for clustering is the K-means algorithm, which is dependent on the choice number of clusters, K. K-means partitions the dataset to K clusters by minimizing intra-partition distances. In order to evaluate the performance of the algorithm, we used a minimum K of 2 clusters and a maximum K of 10 clusters, as it is difficult to work with more than 10 deducted clusters. It should also be noted that the campaign period was 2 months and we do not expect to have such a large number of clusters at each station. The K-means algorithm was initiated 10 times for each case, each with a different centroid seed.

HDBSCAN algorithm first transforms space according to the density/sparsity of data points, constructs a cluster hierarchy of connected components, condenses the cluster hierarchy based on minimum cluster size, and extracts the stable clusters. In order to evaluate the algorithm, we used a minimum cluster size of 3 data points and we increased that by one to 100 points.

In an attempt to determine how accurately the clusters reflect the data, we used the Silhouette width [78], the Caliński-Harabasz [15] and the Dunn Index methods [7, 97, 104]. The Silhouette width shows which objects lie well within their cluster, and which ones are merely somewhere in between clusters. Its value ranges from -1 to 1. A value of 1 indicates well separated clusters, while a value of 0 indicates overlapping clusters. Caliński-Harabasz method reconciles, in a sense, two different approaches to the investigation of the spatial relationships between the points, the agglomerative and the divisive methods. The index it provides is defined as ratio between the within-cluster dispersion and the between-cluster dispersion. A higher index relates to better defined clusters. The Dunn Index illustrates the minimum ratio of the minimum distance between two objects of different clusters divided by the maximum distance between two objects belonging to one cluster. The higher the Dunn Index the better the cluster homogeneity. Modal analysis results (Geometric standard deviation of mode σ_g, Geometric mean diameter of mode d_g, Total number of particles in mode

N) were normalized between their minimum and maximum values before applying the clustering algorithms. Each algorithm was applied for the minimum sample size (HDBSCAN) and the number of clusters (K-means) mentioned earlier. For each result, the Dunn Index, the Caliński-Harabasz index and the Silhouette width were calculated. The Silhouette width was favoring results with very few clusters (usually 2 clusters), therefore, we used the Caliński-Harabasz index in order to acquire the ideal number of clusters for the K-means and HDBSCAN algorithms. Then, we compared the two solutions (one from K-means method and one from HDBSCAN) based on the Dunn Index results (i.e. the ideal solution for HDBSCAN Dunn Index was compared to the Dunn Index of the K-means result with the same number of clusters and vice versa). In all cases HDBSCAN algorithm outperformed K-means algorithm (based on the Dunn Index criterion). We used two algorithms so as to apply two independent statistical methods on the dataset in order to obtain results with minimum overlap between clusters and at the same time a minimum number of clusters for each dataset.

2.1.4 Air mass origin clustering and Potential Source Contribution Factor Analysis

The Flexible Particle Dispersion Model (FLEXPART) was used in order to acquire residence times over geographic grid cells (sensitivity) [85, 84]. These indicate how sensitive the measurements at a station are to emissions occurring at each geographic grid cell. FLEXPART runs account for grid scale wind as well as for turbulent and mesoscale wind fluctuations. Drift correction, to prevent accumulation of the released computational particles, and density correction, to account for the decrease of air density with height, were both applied. Seven-day backward runs with the release of 4×10^4 air parcels every 3 hours beginning from FIN station were produced. Residence times in each grid cell, for a height from 0 to 100 m above ground level (agl), were acquired. The center of mass (centroid) of the residence times in all cells for each 3-hour time step in backward runs, was also calculated. Observing the distance between centroids provides a measure of the speed at which the air masses travel between consecutive 3-hour intervals. Based on centroids for each 3-hour release, we clustered the origin of air masses with a procedure similar to the one described in the

previous section. The PSCF method applied is described in [74]. PSCF frequency maps indicate the probability that a geographic region is the source of the aerosol particle concentration measured.

2.2 Results and Discussion

2.2.1 Overview of concentration levels and size distributions

Comparisons between measured and modeled concentrations are usually done using the arithmetic means of the relevant quantities. A typical arithmetic mean comparison is of less use for these distributions, as the values of linear means are strongly affected by the outlier values. A way to compare the results would then be the ability of a model to reproduce the measured concentration histograms. In this article we use mostly the percentile values of the number size distributions in order to represent the histogram. We present a comparable mean value (g_m) and some indication of the histogram shape and the concentration variance (other percentiles).

Figure 2.3 illustrates the geometric mean g_m and the middle (16^{th} and 84^{th}) percentiles of the size distributions at the three station types for the time periods indicated in Table 2.1. We only present g_m, 16^{th} and 84^{th} percentiles in the figure for practical reasons, but the 5^{th}, 16^{th}, 50^{th}, 84^{th} and 95^{th} percentiles are all presented in Tables 2.2 and 2.3.

The City-Centre Urban Background station displays in Figure 2.3 a peak at 60 nm, indicating a mixture of freshly emitted road traffic exhaust and more aged traffic, while it exhibits the highest peak values (twice as high as Urban Background stations). [13] report that at an urban background station in Barcelona (sampling period 30^{th} of July 2012 - 4^{th} of August 2013), located close (350 m) to a major highway (Diagonal Avenue: 9×10^4 vehicles per working day), the particle number concentration in the size range 17.5 to 100 nm was $7.5 \times 10^3 \pm 5 \times 10^3$ cm^{-3} (mean concentration $\pm$ standard deviation). In the same size range at the City-Centre Urban Background station, the corresponding values were $8.2 \times 10^3 \pm 5.8 \times 10^3$ cm^{-3}.

The size distributions at the Urban Background stations demonstrate an elongated shape, indicating multiple mixed sources. Apart from the well-aged accumulation mode, an Aitken mode was observed, as well. The Urban Background stations are strongly affected by road traffic exhaust and

subsequent particle growth. [13] report that at Montelibretti (sampling period 26^{th} of September 2007 - 7^{th} of May 2009), a sampling site located 30 km NE from the Rome city centre, the particle number concentration in the size range 17.5 to 100 nm was $5 \times 10^3 \pm 3 \times 10^3$ cm^{-3} (mean concentration $\pm$ standard deviation). In the same size range at the Urban Background stations, the corresponding values were $3.3 \times 10^3 \pm 5.4 \times 10^3$ cm^{-3}. In more detail, at ICE-HT station, the corresponding values were $3.2 \times 10^3 \pm 8.2 \times 10^3$ cm^{-3}, at DEM station they were $4.4 \times 10^3 \pm 3.4 \times 10^3$ cm^{-3} and at EPT station they were $2.5 \times 10^3 \pm 1.9 \times 10^3$ cm^{-3}.

The Regional Background station displays a peak at 100 nm and has the lowest particle concentration values. [8] report that a well-aged accumulation mode with a peak above 100 nm is frequently observed at Finokalia. We observe here an average peak at 100 nm, which we may attribute to a mixture of well-aged aerosol (probably transported from distant areas) and aerosol of intermediate aging stemming from nearby cities in the island of Crete. [101] reports that at Finokalia, during the period from 10^{th} of July 2000 to 30^{th} of July 2000, the particle number concentration in the size range 8 to 327 nm was $1.7 \times 10^3 \pm 1.6 \times 10^3$ cm^{-3} (mean concentration $\pm$ standard deviation). The corresponding values in our study (10^{th} of July 2012 - 30^{th} of July 2012) are $3.3 \times 10^3 \pm 1.1 \times 10^3$ cm^{-3}.

The geometric mean (g_m), 16^{th} and 84^{th} percentiles of the size distributions at the three Urban Background stations are provided in Figure A.1 (Appendix).

As shown in Table 2.3, the observed mean number concentration for the size fraction from 30 to 50 nm electrical mobility diameter (N_{30-50}) at the City-Centre Urban Background station was 2.8×10^3 cm^{-3}, while at Cabauw station (representative of Central European aerosol), it was 2.1×10^3 cm^{-3}, during the period 2008-2009 [4]. For the size fraction from 50 to 500 nm (N_{50}), the observed mean number concentration at the City-Centre Urban Background station was 5.8×10^3 cm^{-3}, while at JRC-Ispra station it was 5.6×10^3 cm^{-3}. We conclude that the City-Centre Urban Background site has similarities to stations representative of the background concentrations in polluted areas of Central Europe and Northern Italy.

The mean number concentration at the Regional Background site for the size fraction from 30 to 50 nm was 0.6×10^3 cm^{-3}, while at Harwell station (a rural station representative of large scale

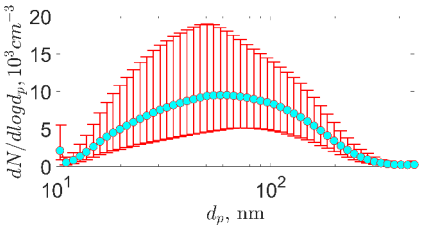

(a) City-Centre Urban Background station

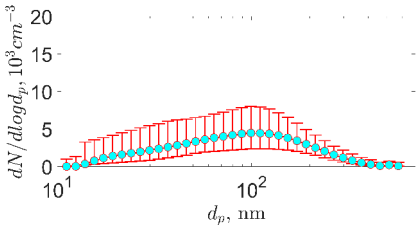

(b) Urban Background

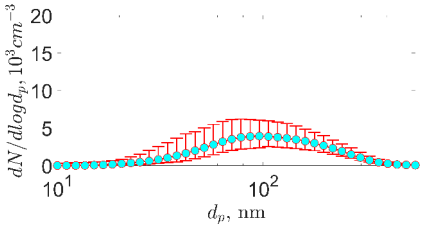

(c) Regional Background

Figure 2.3: Overview of Particle Size Distribution statistics for each size bin in thousands of particles per cm^3: geometric mean (G_m, cyan dots), the 16^{th} and 84^{th} percentiles of the measured concentrations. The area below the lower end of the error bars corresponds to the 16^{th} percentile, while the area below the higher end of the error bars corresponds to the 84^{th} percentile. The City-Centre Urban Background station (CCUB) corresponds to Patras-C, the Urban Background stations (UB) correspond to ICE-HT, DEM, EPT, while the Regional Background station corresponds to FIN.

Table 2.2: Descriptive statistics during the campaign reported in this work. $\bar{N}$ is the mean concentration, μ_{05} to μ_{95} are the 5^{th} to the 95^{th} percentile, Max the maximum number concentration during the campaign, and Stdev the standard deviation of the number concentration. CCUB refers to the City-Centre Urban Background station (Patras-C), RB refers to the Regional Background station (FIN), and UB to the Urban Background stations (ICE-HT, DEM, EPT).

Size bin, nm	$\bar{N} \times 10^3$	μ_{05}	μ_{16}	μ_{50}	μ_{84}	μ_{95}	**Max**	**StDev**
CCUB, N_{10-20}	**1.1**	**0.2**	**0.4**	**0.9**	**1.8**	**2.7**	**19**	**1**
CCUB, N_{20-50}	**4.1**	**0.9**	**1.5**	**3.2**	**6.6**	**10.1**	**71.4**	**3.5**
CCUB, N_{50-100}	**3.5**	**1**	**1.6**	**2.9**	**5.1**	**8**	**39.8**	**2.4**
CCUB, $N_{100-200}$	**2**	**0.6**	**1**	**1.8**	**2.9**	**3.9**	**36.6**	**1.4**
CCUB, $N_{200-500}$	**0.4**	**0.1**	**0.2**	**0.4**	**0.6**	**0.8**	**7.6**	**0.3**
CCUB, N_{tot}	**11.1**	**3.6**	**5.4**	**9.5**	**16.5**	**24.2**	**112.3**	**7.1**
UB, N_{10-20}	**0.5**	**0.03**	**0.09**	**0.3**	**0.8**	**1.7**	**48.8**	**1**
UB, N_{20-50}	**1.4**	**0.3**	**0.4**	**1**	**2.2**	**3.8**	**111.2**	**2.2**
UB, N_{50-100}	**1.7**	**0.5**	**0.7**	**1.4**	**2.3**	**3.4**	**238.9**	**3.7**
UB, $N_{100-200}$	**1.5**	**0.5**	**0.7**	**1.3**	**2**	**2.6**	**199.8**	**2.6**
UB, $N_{200-500}$	**0.5**	**0.2**	**0.3**	**0.5**	**0.8**	**1**	**19.7**	**0.4**
UB, N_{tot}	**5.5**	**1.8**	**2.6**	**4.5**	**7.4**	**11.2**	**456.3**	**8**
RB, N_{10-20}	**0.2**	**0.004**	**0.01**	**0.05**	**0.2**	**0.7**	**9.4**	**0.5**
RB, N_{20-50}	**0.7**	**0.1**	**0.2**	**0.5**	**1.3**	**2.1**	**5.2**	**0.6**
RB, N_{50-100}	**1.4**	**0.5**	**0.7**	**1.3**	**2.1**	**2.7**	**5.5**	**0.7**
RB, $N_{100-200}$	**1.2**	**0.5**	**0.7**	**1.1**	**1.6**	**1.8**	**3.8**	**0.4**
RB, $N_{200-500}$	**0.4**	**0.2**	**0.3**	**0.4**	**0.6**	**0.7**	**1.2**	**0.2**
RB, N_{tot}	**3.5**	**1.4**	**2.2**	**3.4**	**4.8**	**6**	**14.1**	**1.4**
ICE-HT, N_{10-20}	**0.4**	**0.02**	**0.05**	**0.2**	**0.6**	**1.4**	**48.8**	**1.2**
ICE-HT, N_{20-50}	**1.2**	**2.4**	**3.7**	**0.8**	**1.9**	**3.1**	**111.2**	**2.8**
ICE-HT, N_{50-100}	**1.9**	**0.6**	**0.9**	**1.4**	**2.2**	**3.1**	**238.9**	**5.9**
ICE-HT, $N_{100-200}$	**1.7**	**0.6**	**0.9**	**1.4**	**2.1**	**2.6**	**199.8**	**4.2**
ICE-HT, $N_{200-500}$	**0.4**	**0.1**	**0.2**	**0.4**	**0.6**	**0.9**	**19.7**	**0.5**
ICE-HT, N_{tot}	**5.5**	**2.1**	**2.7**	**4.3**	**6.8**	**9.6**	**456.3**	**12.3**
DEM, N_{10-20}	**0.9**	**0.1**	**0.2**	**0.5**	**1.4**	**2.6**	**23**	**1.3**
DEM, N_{20-50}	**1.9**	**0.4**	**0.6**	**1.3**	**3.1**	**5.3**	**27.3**	**2**
DEM, N_{50-100}	**2.1**	**0.9**	**1.2**	**1.8**	**3.1**	**4.8**	**10.5**	**1.2**
DEM, $N_{100-200}$	**1.9**	**0.7**	**1.1**	**1.8**	**2.5**	**3.3**	**19.6**	**0.8**
DEM, $N_{200-500}$	**0.7**	**0.3**	**0.4**	**0.7**	**1**	**1.4**	**5.5**	**0.4**
DEM, N_{tot}	**7.6**	**3.7**	**4.5**	**6.3**	**10.3**	**15.9**	**58.8**	**0.4**
EPT, N_{10-20}	**0.4**	**0.05**	**0.1**	**0.2**	**0.6**	**1.2**	**7.5**	**0.5**
EPT, N_{20-50}	**1.3**	**0.2**	**0.4**	**0.9**	**2**	**3.4**	**22.2**	**1.2**
EPT, N_{50-100}	**1.2**	**0.4**	**0.5**	**1**	**1.8**	**2.6**	**29.3**	**0.8**
EPT, $N_{100-200}$	**0.9**	**0.4**	**0.6**	**0.9**	**1.3**	**1.7**	**10.6**	**0.4**
EPT, $N_{200-500}$	**0.5**	**0.2**	**0.3**	**0.5**	**0.7**	**0.8**	**2.1**	**0.2**
EPT, N_{tot}	**4**	**1.5**	**2.1**	**3.5**	**5.7**	**8.5**	**44.5**	**2.4**

Table 2.3: Comparison of City-Centre Urban Background, Urban Background and Regional Background stations in Greece with other measurement campaigns [4]. N_{30-50} refers to particles with mobility diameter from 30 to 50 nm, N_{50} refers to particles with mobility diameter from 50 to 500 nm, and N_{100} refers to particles with mobility diameter from 100 to 500 nm. $\bar{N}$ is the mean concentration, g_m is the geometric mean concentration, μ_{05} to μ_{95} are the 5^{th} to the 95^{th} percentile. CCUB refers to the City-Centre Urban Background station (Patras-C), RB refers to the Regional Background station (FIN), and UB to the Urban Background stations (ICE-HT, DEM, EPT).

Station	Fraction	$\bar{N} \times 10^3$	g_m	μ_{05}	μ_{16}	μ_{50}	μ_{84}	μ_{95}
Harwell		**0.8**	**0.5**	**0.1**	**0.2**	**0.6**	**1.3**	**2.1**
K-Puszta		**1**	**0.7**	**0.2**	**0.4**	**0.7**	**1.4**	**2.7**
Cabauw		**2.1**	**1.6**	**0.4**	**0.8**	**1.9**	**3.4**	**4.6**
Jungfraujoch		**0.1**	**0.08**	**0.02**	**0.04**	**0.08**	**0.2**	**0.3**
JRC-Ispra		**1.6**	**1.3**	**0.5**	**0.7**	**1.3**	**2.4**	**3.7**
CCUB	N_{30-50}	**2.8**	**2.2**	**0.6**	**1**	**2.2**	**4.4**	**7**
RB		**0.6**	**0.4**	**0.1**	**0.2**	**0.4**	**1**	**1.7**
UB		**1**	**0.7**	**0.2**	**0.3**	**0.7**	**1.5**	**2.5**
ICE-HT		**0.8**	**0.6**	**0.2**	**0.3**	**0.5**	**1.2**	**2**
DEM		**1.3**	**1**	**0.3**	**0.5**	**0.9**	**2**	**3.7**
EPT		**0.9**	**0.6**	**0.2**	**0.3**	**0.6**	**1.4**	**2.3**
Harwell		**1.8**	**1.3**	**0.3**	**0.5**	**1.3**	**3.3**	**5**
K-Puszta		**3.7**	**3**	**1.1**	**1.7**	**3.1**	**5.6**	**8**
Cabauw		**2.9**	**2.9**	**0.6**	**1.3**	**3.4**	**6.5**	**9.1**
Jungfraujoch		**0.3**	**0.2**	**0.03**	**0.07**	**0.2**	**0.6**	**1**
JRC-Ispra		**5.6**	**4.2**	**1**	**2**	**4.4**	**9.3**	**14**
CCUB	N_{50}	**5.8**	**5**	**1.9**	**2.9**	**5.1**	**8.4**	**12**
RB		**2.8**	**2.6**	**1.2**	**1.8**	**2.8**	**3.7**	**4.4**
UB		**3.6**	**3**	**1.3**	**1.8**	**3.1**	**4.8**	**6.7**
ICE-HT		**3.9**	**3.1**	**1.4**	**2**	**3.2**	**4.5**	**5.7**
DEM		**4.8**	**4.4**	**2.3**	**3**	**4.2**	**6.4**	**8.8**
EPT		**2.5**	**2.3**	**1.1**	**1.5**	**2.3**	**3.4**	**4.6**
Harwell		**0.8**	**0.5**	**0.1**	**0.2**	**0.6**	**1.5**	**2.4**
K-Puszta		**2**	**1.6**	**0.5**	**0.9**	**1.7**	**3**	**4.4**
Cabauw		**1.2**	**0.8**	**0.2**	**0.3**	**1**	**2.2**	**3.3**
Jungfraujoch		**0.2**	**0.08**	**0.008**	**0.03**	**0.09**	**0.3**	**0.6**
JRC-Ispra		**2.9**	**1.9**	**0.4**	**0.8**	**2.1**	**5**	**8.3**
CCUB	N_{100}	**2.4**	**2**	**0.7**	**1.2**	**2.1**	**3.4**	**4.4**
RB		**1.6**	**1.5**	**0.7**	**1**	**1.6**	**2.1**	**2.4**
UB		**2**	**1.7**	**0.7**	**1**	**1.7**	**2.7**	**3.6**
ICE-HT		**2.1**	**1.7**	**0.7**	**1.1**	**1.7**	**2.6**	**3.2**
DEM		**2.6**	**2.4**	**1.1**	**1.6**	**2.5**	**3.5**	**4.8**
EPT		**1.4**	**1.3**	**0.7**	**0.9**	**1.4**	**1.9**	**2.4**

air masses affecting Southern England) it was $0.8 \times 10^3\ cm^{-3}$, during the period 2008-2009. For the fraction N_{50}, the mean number concentration at the Regional Background site was $2.8 \times 10^3\ cm^{-3}$, while at Harwell it was $1.8 \times 10^3\ cm^{-3}$. For the fraction N_{100}, the mean number concentration at the Regional Background site was $1.6 \times 10^3\ cm^{-3}$, while at Harwell it was $0.8 \times 10^3\ cm^{-3}$. We conclude that the Regional Background site is more polluted than the rural site of Harwell, as its particle number concentrations in the size ranges N_{50} and N_{100} are higher. The main difference in these two sites is found on the N_{100} size fraction (as N_{100} is included in N_{50}), relating it mainly to the long range transport of polluted air masses in the Eastern Mediterranean.

The overall mean concentration and percentiles for all size fractions of the Urban Background sites are very similar to the K-Puszta station (representative of the Central-Eastern European regional conditions). We conclude that the Urban Background sites have similarities to the aerosol concentrations measured at the Central-Eastern Europe during the Etesians.

Figure 2.4 displays the diurnal variation of the aerosol particle concentration size distributions for all site types.

At the City-Centre Urban Background station, we observe distinctive peaks during the morning and evening traffic rush hour for size bins N_{10-20}, N_{20-50}, N_{50-100}, and N_{tot}. $N_{100-200}$ and $N_{200-500}$ are more or less stable throughout the day.

At the Urban Background stations, N_{50-100} is the fraction that mainly displays morning and evening peaks, attributed to traffic. We observe that N_{10-20}, N_{20-50} fractions display a similar evening peak and a small morning peak, but their maximum concentration is reached during noon. [45] reported that 5 organic aerosol sources were identified at ICE-HT station and 4 at DEM. These were very oxygenated OA (V-OOA, 19%), moderately oxygenated OA (M-OOA, 38%), biogenic oxygenated OA (b-OOA, 21%), Hydrocarbon-like OA (HOA-1, 7%), and HOA-2 (15%) at ICE-HT and V-OOA (35%), M-OOA (30%), HOA-1 (18%), and HOA-2 (17%) at DEM (Figure A.6, Appendix). By comparing the diurnal cycle of these sources and the diurnal cycle of the size fractions, HOA-1 and HOA-2 mainly correspond to the N_{50-100} size fraction, while V-OOA to the fractions $N_{100-200}$ and $N_{200-500}$. M-OOA and N_{10-20}, N_{20-50} correlate in the diurnal variation, and hence could be originating from the same source.

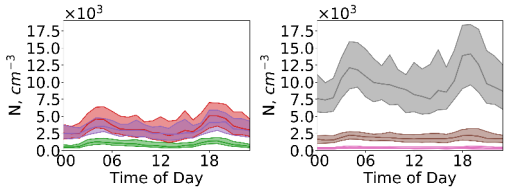

(a) N_{10-20}, N_{20-50}, N_{50-100} CCUB (b) $N_{100-200}$, $N_{200-500}$, N_{tot} CCUB

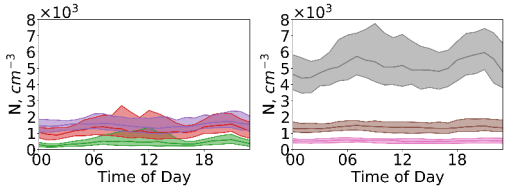

(c) N_{10-20}, N_{20-50}, N_{50-100} UB (d) $N_{100-200}$, $N_{200-500}$, N_{tot} UB

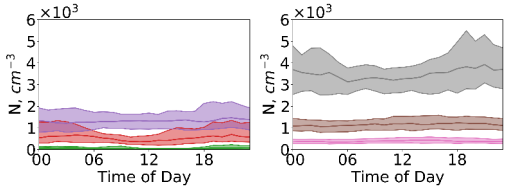

(e) N_{10-20}, N_{20-50}, N_{50-100} RB (f) $N_{100-200}$, $N_{200-500}$, N_{tot} RB

Figure 2.4: Diurnal variation (UTC) of the particle number concentration (vertical axis) for the size fractions N_{10-20} (green color), N_{20-50} (red), N_{50-100} (blue), $N_{100-200}$ (brown), $N_{200-500}$ (pink), and (N_{tot}) at City-Centre Urban Background (Patras-C, in subfigures a,b), Urban Background (ICE-HT, DEM, EPT, in subfigures c,d), and Regional Background stations (FIN, in subfigures e,f).

The peaks corresponding to HOA-1, HOA-2 and M-OOA cannot be identified for the size fractions at the Regional Background station. Nevertheless, a small peak in the evening in the size fractions N_{20-50}, N_{50-100} is apparent at the Regional Background station and may be attributed to aerosol of intermediate aging, transported from source areas within Crete. [75] report that at the Regional Background station, 80% of the PM1 (particulate matter with aerodynamic diameter smaller than 1 μm) organic aerosol was water soluble and its OC/EC ratio was equal to 5.4, indicating that the organic aerosol content was mainly secondary and highly oxidized. This is in-line with the diurnal variation of N_{tot}, which is almost stable throughout the day. As shown in Table 2.2, the median values of the fraction N_{50-100} at the Regional Background station and the Urban Background stations have similar values but their diurnal patterns are dissimilar. While at the Urban Background this fraction appears to be related to traffic, there is no such relation at the Regional Background station. The median concentrations for the size ranges N_{10-20}, N_{20-50}, N_{50-100}, $N_{100-200}$, $N_{200-500}$, N_{tot} (Table 2.2) at the Regional Background station, are the 5%, 16%, 45%, 63%, 99% and 36% of the respective median concentrations of the City-Centre Urban Background station. The remainder percentages at the City-Centre Urban Background station may be attributed to traffic, shipping (as it is situated close to Patras harbor), other locally produced particles and condensational growth. When compared to the Urban Background stations, the Regional Background median concentrations correspond to the 17%, 55%, 97%, 91%, 79% and 77% of the respective median of the Urban Background stations. By combining these estimations and diurnal variation of the size fractions in Figure 2.4, we conclude that those that are similar in number mean concentration and diurnal variation at all station types are $N_{100-200}$ and $N_{200-500}$. Assuming that these fractions measured at the Regional Background station constitute the regional background concentration, we conclude that the transported part of the median particle number concentrations for the City-Centre Urban Background station is 13%, for the Urban Background stations 29%, and for the Regional Background station 45%. Other fractions should mainly be attributed to NPF, freshly emitted traffic exhaust, aged traffic, cooking and other local sources. We have to keep in mind though that this estimation is based on an empirical division of size fractions.

It is worthwhile mentioning that N_{tot} resembles very much N_{50-100} at the Regional Background

station, since N_{50-100} is the dominating size fraction in terms of particle concentration. At the Urban Background stations N_{50-100} and N_{20-50} are the dominant size fractions.

The City-Centre Urban Background station displays significantly higher particle number concentrations than the Urban Background and Regional Background stations (cf. Figure A.2 in Appendix). In Figure A.3 (Appendix), the time-series for the size fractions are displayed. It is observed that the particle concentrations are similar at the Urban Background and Regional Background stations for the size bins N_{50-100}, $N_{100-200}$, and $N_{200-500}$. For the size bin $N_{200-500}$, all station types exhibit similar number concentrations (cf. Figure A.3 in Appendix). In Figure A.4 (Appendix), we present the diurnal variation for each size bin for the three Urban Background stations, while in Figure A.5 the time-series for the same stations.

2.2.2 Statistics and phenomenology of size distribution at different station types

Each mode identified by the size distribution modal analysis algorithm was classified according to its geometric mean diameter (d_g) in a structure consisting of two submodes corresponding to the Nucleation mode ($N_{<15}$, N_{15-30}), two submodes corresponding to the Aitken mode (A_{30-60}, A_{60-90}) and two submodes corresponding to the Accumulation mode (C_{90-120}, $C_{>120}$). This finer classification was carried out in order to distinguish the aerosol sources more precisely. The nomenclature of this work is provided in Table 2.4.

The most frequent mode combinations for the City-Centre Urban Background, the Urban Background and the Regional Background stations are displayed in Tables 2.5 to 2.7. The dataset acquired by modal analysis and subsequent classification in six submodes, was separated in 2-hour intervals, in order to obtain the diurnal variation of modes for the whole period of the campaign. The diurnal variation of the classified modes are presented as Appendix (Figures A.14 to A.22).

2.2.2.1 City-Centre Urban Background station (Patras-C)

Table 5 demonstrates the most frequent mode combination for the City-Centre Urban Background station during the campaign. We observe that Aitken mode dominates the City-Centre Urban

Table 2.4: Nomenclature

Symbol	**Explanation**
σ_g	Geometric standard deviation of mode
d_g	Geometric mean diameter of mode, referring to dry electrical mobility diameter
N	Total number of particles in mode
n	Number of size bins of the SMPS particle size distribution
Mode $N_{<15}$	Mode with d_g smaller than 15 nm, gas to particle conversion
Mode N_{15-30}	Mode with d_g larger than 15 nm and smaller than 30 nm, related to vehicle emissions and growth of nucleated particles
Mode A_{30-60}	Mode with d_g larger than 30 nm and smaller than 60 nm, related to vehicle emissions, growth of nucleated particles
Mode A_{60-90}	Mode with d_g larger than 60 nm and smaller than 90 nm, related to traffic and growth of nucleated particles
Mode C_{90-120}	Mode with d_g larger than 90 nm and smaller than 120 nm, related to condensational growth
Mode $C_{>120}$	Mode with d_g larger than 120 nm, related to condensational growth

Table 2.5: City-Centre Urban Background station most frequent mode combinations. $A_{30-60}C_{>120}$ refers to size distributions that consist of an A_{30-60} mode and a $C_{>120}$ mode, described in detail in Table 2.4.

Mode	$\mathbf{A_{30-60}C_{>120}}$	$\mathbf{A_{30-60}}$	$\mathbf{A_{30-60}C_{90-120}}$	$\mathbf{N_{15-30}A_{60-90}}$	$\mathbf{N_{15-30}C_{90-120}}$
Combination	**Median**	**Median**	**Median**	**Median**	**Median**
N_{15-30} σ_g	-	-	-	1.5	1.6
N_{15-30} d_g	-	-	-	24	27
N_{15-30} N	-	-	-	2.5×10^3	3.5×10^3
A_{30-60} σ_g	2	2	1.9	-	-
A_{30-60} d_g	43	50	37	-	-
A_{30-60} N	7.2×10^3	10.3×10^3	5.9×10^3	-	-
A_{60-90} σ_g	-	-	-	1.9	-
A_{60-90} d_g	-	-	-	77	-
A_{60-90} N	-	-	-	6.6×10^3	-
C_{90-120} σ_g	-	-	1.6	-	1.7
C_{90-120} d_g	-	-	109	-	101
C_{90-120} N	-	-	3.6×10^3	-	5×10^3
$C_{>120}$ σ_g	1.45	-	-	-	-
$C_{>120}$ d_g	137	-	-	-	-
$C_{>120}$ N	2×10^3	-	-	-	-
Frequency %	27	15	15	13	9

Table 2.6: Urban Background stations most frequent mode combinations. $A_{30-60}C_{>120}$ refers to size distributions that consist of an A_{30-60} mode and a $C_{>120}$ mode, described in detail in Table 2.4.

Mode	$\mathbf{A_{30-60}C_{>120}}$	$\mathbf{N_{15-30}C_{90-120}}$	$\mathbf{A_{60-90}C_{>120}}$	$\mathbf{N_{15-30}C_{>120}}$	$\mathbf{C_{90-120}}$
Combination	**Median**	**Median**	**Median**	**Median**	**Median**
N_{15-30} σ_g	-	1.6	-	1.9	-
N_{15-30} d_g	-	22	-	25	-
N_{15-30} N	-	1.4×10^3	-	1.4×10^3	-
A_{30-60} σ_g	2	-	-	-	-
A_{30-60} d_g	43	-	-	-	-
A_{30-60} N	2×10^3	-	-	-	-
A_{60-90} σ_g	-	-	2.2	-	-
A_{60-90} d_g	-	-	69	-	-
A_{60-90} N	-	-	2.3×10^3	-	-
C_{90-120} σ_g	-	1.9	-	-	1.9
C_{90-120} d_g	-	105	-	-	100
C_{90-120} N	-	3.2×10^3	-	-	3.7×10^3
$C_{>120}$ σ_g	1.6	-	1.5	1.8	-
$C_{>120}$ d_g	157	-	180	135	-
$C_{>120}$ N	1.9×10^3	-	1.1×10^3	2.6×10^3	-
Frequency %	21	9	8	6	6

Background station, as it is present at 4 out of 5 of the most frequent mode combinations. Overall, an Aitken mode (A_{30-60} or A_{60-90}) was present at the City-Centre Urban Background station more than 75% of the time, during the campaign. This finding indicates that the site PSD is dominated by traffic emissions, fresh and aged.

2.2.2.2 Urban Background stations (ICE-HT, DEM and EPT)

Table 2.6 demonstrates the most frequent mode combinations. One may observe that the most frequent modes are Aitken and Accumulation. This indicates that the main sources affecting these sites are vehicle emissions fresh (A_{30-60})) and aged (A_{60-90})) and condensational growth of existing particles.

Table 2.7: Regional Background station most frequent mode combinations. $A_{30-60}C_{>120}$ refers to size distributions that consist of an A_{30-60} mode and a $C_{>120}$ mode, described in detail in Table 2.4.

Mode	$\mathbf{A_{30-60}C_{>120}}$	$\mathbf{C_{90-120}}$	$\mathbf{A_{60-90}C_{>120}}$	$\mathbf{C_{>120}}$	$\mathbf{N_{15-30}A_{60-90}C_{>120}}$
Combination	**Median**	**Median**	**Median**	**Median**	**Median**
N_{15-30} d_g	-	-	-	-	23
N_{15-30} N	-	-	-	-	0.24×10^3
A_{30-60} σ_g	1.5	-	-	-	-
A_{30-60} d_g	46	-	-	-	-
A_{30-60} N	1×10^3	-	-	-	-
A_{60-90} σ_g	-	-	1.7	-	1.5
A_{60-90} d_g	-	-	73	-	73
A_{60-90} N	-	-	1.7×10^3	-	1.3×10^3
C_{90-120} σ_g	-	1.8	-	-	-
C_{90-120} d_g	-	106	-	-	-
C_{90-120} N	-	3.5×10^3	-	-	-
$C_{>120}$ σ_g	1.5	-	1.5	1.8	1.5
$C_{>120}$ d_g	152	-	169	129	180
$C_{>120}$ N	1.8×10^3	-	1.2×10^3	3×10^3	0.84×10^3
Frequency %	20	12	11	9	8

2.2.2.3 Regional Background station (FIN)

Table 2.7 shows the most frequent mode combinations, which are Aitken mode – Accumulation mode. Therefore, the main sources are aged traffic and condensational growth.

2.2.3 Cluster Analysis Results

In the previous section we classified and thus simplified the complex data sets measured at City-Centre Urban Background, Urban Background and Regional stations using empirically determined fractions in the particle size distribution and submodes on the results of the modal analysis. In order to evaluate our conclusions on local sources and transported aerosol, we needed to utilize an impartial method so as to group the aerosol size distributions. We used the results of the Size Distribution Modal Analysis as input data and subsequently we used the clustering algorithms presented in the Materials and Methods section.

2.2.3.1 City-Centre Urban Background station (Patras-C) identified clusters

The HDBSCAN algorithm results for a minimum cluster size of 38 data points (3 clusters) has the highest Caliński-Harabasz score comparing to the rest of the HDBSCAN results (results for minimum cluster sizes ranging from 3 to 100). They also have a Dunn Index equal to 7.2×10^{-3} while the K-means algorithm results for 3 clusters have a Dunn Index equal to 2.5×10^{-3}. The highest Dunn Index for the K-means results is equal to 3.5×10^{-3} and corresponded to 4 clusters. Nevertheless, it is still less than the Dunn Index acquired by the HDBSCAN algorithm results for a minimum cluster size of 38 data points. Figure 2.5 shows the frequency of occurrence at each hour of the day for each cluster. The frequency of CCUB-SD-Cluster2 (Cluster2 for the Size Distribution clustering at the City-Centre Urban Background site) is almost stable throughout the day, while the particle concentration increases during noon, due to the accumulation of particles that are produced locally. This profile is similar to the M-OOA source identified at ICE-HT, and corresponds to aerosol of medium oxygenation, and therefore aging. Its 50^{th} percentile d_g corresponds to accumulation mode. CCUB-SD-Cluster2 is a sum of the Regional Background particle concentration and condensational growth of locally produced particles. CCUB-SD-Cluster3 has increased frequency and number con-

Table 2.8: City-Centre Urban Background station clusters identified.

Cluster Results	**CCUB-SD -Cluster1**	**CCUB-SD -Cluster2**	**CCUB-SD -Cluster3**
20^{th} perc σ_g	1.2	1.42	1.45
50^{th} perc σ_g	1.2	1.57	1.81
80^{th} perc σ_g	1.2	1.74	2.1
20^{th} perc d_g	5.5	93.7	25.4
50^{th} perc d_g	6.5	116.9	39.7
80^{th} perc d_g	6.6	139	51.57
20^{th} perc N	$> 1 \times 10^5$	1.6×10^3	2.3×10^3
50^{th} perc N	$> 1 \times 10^5$	3.4×10^3	5.3×10^3
80^{th} perc N	$> 1 \times 10^5$	5.9×10^3	10.7×10^3
Cluster Source	Traffic episode	Condensational growth, Regional background	Vehicle emissions, fresh and aged
Cluster Frequency	0.7 %	74 %	100 %

centration in the early morning and late evening and it could be attributed to vehicle emissions. Its 50^{th} percentile d_g corresponds to Aitken mode. This cluster is mainly attributed to fresh and aged vehicle emissions as its diurnal variation is similar to HOA-1 and HOA-2 sources [45]. It should be noted that this cluster is always present at the City-Centre Urban Background station. There is also a very infrequent nuclei mode cluster (CCUB-SD-Cluster1) which has an estimated d_g of less than 6.5 nm. The particle number concentration of this cluster has high uncertainty, since the measured size distribution range begins from 10 nm and measurement uncertainty is higher in the size range from 10 to 20 nm. In Figure 2.5 we observe that this cluster occurs at 06:00 UTC and from 12:00 to 18:00 UTC. It could be attributed to local pollution events due to combustion.

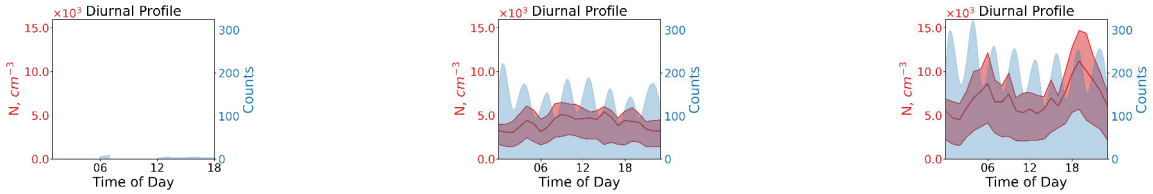

(a) CCUB-SD-Cluster1 (b) CCUB-SD-Cluster2 (c) CCUB-SD-Cluster3

Figure 2.5: City-Centre Urban Background station diurnal frequency of occurrence (blue area, counts per hour) and median number concentration N_{median} (red line) for all identified clusters. The area around N_{median} corresponds to 25^{th} and 75^{th} percentiles of the quantity.

2.2.3.2 Urban Background stations (ICE-HT, DEM and EPT) identified clusters

In order to run the clustering algorithms, we combined the data available from Urban Background stations in one dataset. Even though we miss circa 8 days from beginning and 8 days from end of the time period at ICE-HT and EPT in comparison to DEM station, the actual difference is small. If we remove the extra days from DEM station dataset, the difference in mean concentration, for all DEM station size bins presented in Table 2.3, is less than 10%. Please keep in mind that the measurement uncertainty is 10% for the size range 20-200 nm and significantly higher for the smaller and larger particle sizes. The HDBSCAN algorithm results (4 clusters) presented in Table 2.9 were the best fit for the dataset. In order to acquire these results, a minimum cluster size of 73 data points is used. The Dunn Index for these results is 5.9×10^{-3} while the corresponding value for the K-means algorithm (4 clusters) is equal to 0.9×10^{-3}. The highest Dunn Index for the K-means results is equal to 1.7×10^{-3} and corresponded to 2 clusters. Nevertheless, it is still less than the Dunn Index acquired by the HDBSCAN algorithm results for a minimum cluster size of 73 data points. The results for each Background station are presented in the Appendix (Tables A.4-A.6, Figures A.23-A.25). Figure 2.6 shows the frequency of occurrence at each hour of the day for each cluster. UB-SD-Cluster1 (Cluster1 for the Size Distribution clustering at the Urban Background sites) has a frequency of 7% and could be mainly attributed to traffic due to the fact that an increased frequency and particle number concentration is observed at 06:00 and 18:00 UTC. There is also a peak at noon, which could be attributed to new particle formation. UB-SD-Cluster2 is very stable in frequency and particle number concentration throughout the day, as we observe in

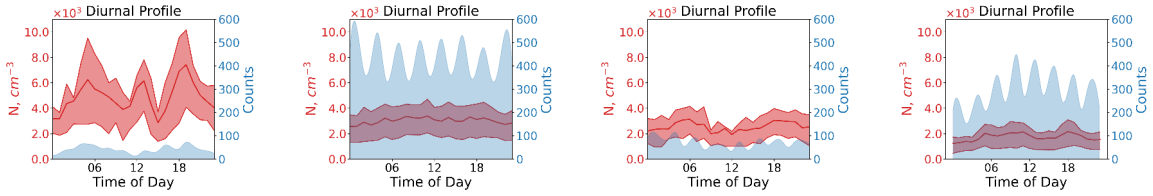

(a) UB-SD-Cluster1 (b) UB-SD-Cluster2 (c) UB-SD-Cluster3 (d) UB-SD-Cluster4

Figure 2.6: Urban Background stations diurnal frequency of occurrence (blue area, counts per hour) and median number concentration N_{median} (red line) for all identified clusters. The area around N_{median} corresponds to 25^{th} and 75^{th} percentiles of the quantity.

Figure 2.6. This mode is the sum of the regional background concentration and the condensational growth of particles produced locally. This is supported by the fact that its 50^{th} percentile d_g corresponds to Accumulation mode. UB-SD-Cluster3 has increased frequency and particle number concentration in the morning and the evening, which probably relates this cluster also to traffic exhaust (due to vehicle circulation peaks when people go to and return from work) occurring at the city highways and center, and subsequently transported to the urban background stations. Its profile corresponds to sources HOA-1 and HOA-2, which are attributed to traffic, cooking and other local sources. UB-SD-Cluster4 has increased frequency and number concentration in the middle of the day, therefore it probably relates to freshly emitted traffic particles, or particles generated elsewhere and subsequently transported to the background site, growing in size as they adsorb photochemically produced pollutant gases. Its 50^{th} percentile d_g corresponds to Aitken mode.

2.2.3.3 Regional Background station (FIN) identified clusters

The HDBSCAN algorithm results presented in Table 2.10 (3 clusters) were the best fit for the dataset. In order to acquire these results, a minimum cluster size of 28 data points is used. The Dunn Index for these results is 12.5×10^{-3} while the corresponding value for the K-means algorithm for 3 clusters is 1.7×10^{-3}. The highest Dunn Index for the K-means results is 5.4×10^{-3} and corresponded to 2 clusters. Nevertheless, it is still less than the Dunn Index acquired by the HDBSCAN algorithm results for a minimum cluster size of 28 data points. Figure 2.7 shows the frequency of occurrence at each hour of the day for each cluster. RB-SD-Cluster1 (Cluster1 for the Size Distribution clustering

Table 2.9: Urban Background stations clusters identified.

Cluster Results	**UB-SD -Cluster1**	**UB-SD -Cluster2**	**UB-SD -Cluster3**	**UB-SD -Cluster4**
20^{th} perc σ_g	3	1.55	2.06	1.34
50^{th} perc σ_g	3	1.68	2.1	1.52
80^{th} perc σ_g	3	1.84	2.16	1.73
20^{th} perc d_g	8.3	98.9	27.7	18.5
50^{th} perc d_g	15.1	122.4	48.4	42.5
80^{th} perc d_g	25.6	154.1	61.6	53
20^{th} perc N	2.2×10^3	1.4×10^3	1.1×10^3	0.7×10^3
50^{th} perc N	4.1×10^3	2.7×10^3	2.3×10^3	1.4×10^3
80^{th} perc N	7.9×10^3	4.5×10^3	3.9×10^3	2.7×10^3
Cluster Source	Nucleation, Vehicle emissions	Condensational growth, Regional background	Vehicle emissions, aged	Vehicle emissions, fresh and aged
Cluster Frequency	7 %	79 %	13 %	53 %

Table 2.10: Regional Background station clusters identified.

Cluster Results	**RB-SD -Cluster1**	**RB-SD -Cluster2**	**RB-SD -Cluster3**
20^{th} perc σ_g	2.1	1.31	1.42
50^{th} perc σ_g	2.1	1.45	1.56
80^{th} perc σ_g	2.1	1.6	1.76
20^{th} perc d_g	7.3	28.5	111.8
50^{th} perc d_g	11.1	50.6	147.6
80^{th} perc d_g	20.4	78.7	194.6
20^{th} perc N	0.2×10^3	0.5×10^3	0.7×10^3
50^{th} perc N	0.3×10^3	10^3	1.8×10^3
80^{th} perc N	0.5×10^3	1.8×10^3	3×10^3
Cluster Source	Local activities, nucleation	Tourism activities, aged	Condensational growth, Regional background
Cluster Frequency	1.7 %	65 %	83 %

at the Regional Background site) is very infrequent and it occurs in the early morning or late evening, therefore it can only be partly related to photochemistry, as we have only identified 5 cases of nucleation events. It is mainly related to pollution transported within the island of Crete, as indicated in earlier studies. RB-SD-Cluster2 relates to the aged pollution produced from Cretan cities and activities related to tourism, including cooking. RB-SD-Cluster3 is the regional background concentration. [31] report for FIN that the variability in OA composition could be explained by two factors of oxygenated organic aerosol (OOA) with differing extents of oxidation but similar volatility. This is in-line with our classification, where 2 clusters corresponding to aged aerosol dominate the frequency of occurrence at the site.

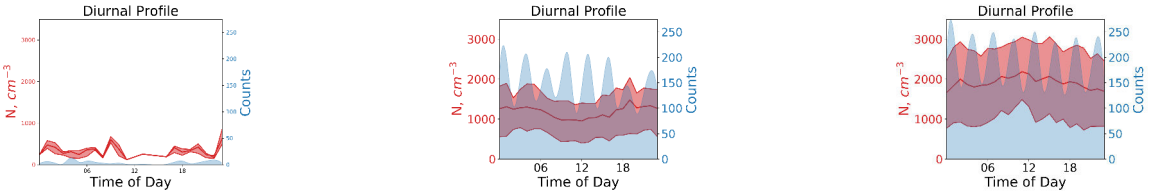

(a) RB-SD-Cluster1 (b) RB-SD-Cluster2 (c) RB-SD-Cluster3

Figure 2.7: Regional Background station diurnal frequency of occurrence (blue area, counts per hour) and median number concentration N_{median} (red line) for all identified clusters. The area around N_{median} corresponds to 25^{th} and 75^{th} percentiles of the quantity.

2.2.4 New Particle Formation (NPF) Events

Combining the two methods mentioned in the New Particle Formation (NPF) Events Analysis section, 5 nucleation events were identified at FIN over 61 days (cf. Figure A.12 displays the contour plots and Figure A.13 displays the origin of air masses for nucleation days, Appendix), 5 nucleation events at DEM over 54 days (cf. Figures A.8 and A.9, Appendix), 4 nucleation events at EPT over 43 days (cf. Figures A.10 and A.11, Appendix), while at Patras-C and ICE-HT there were no nucleation events.

1 nucleation event day at EPT (18^{th} of June) coincided with 1 nucleation event day at FIN. Figures A.11, A.13 display that the origins of air masses reaching the two stations for the day mentioned (18^{th} of June) were very similar. 1 nucleation event day at DEM coincided with 1 nucleation event day at EPT (14^{th} of June). The origins of the air masses during this event day reaching the two sites are also very similar (cf. Figures A.9, A.11, Appendix). We conclude that approximately 1 in 5 of the nucleation events that we have identified occurred simultaneously at a broader geographic area, where conditions favorable for nucleation prevail, probably due to the origin of the air masses reaching the measurement stations.

The results evaluating the strength of the nucleation events at the Regional Background station and the two Urban Background stations that nucleation events were identified, are presented in Table 2.11.

One may observe in Table 2.11 that at EPT, 56% of particles in the size range N_{10-20} during nucleation days originate from NPF, while the corresponding percentages at DEM and FIN are 30

Table 2.11: Absolute and relative contributions of NPF at DEM, EPT, FIN in the size range N_{10-20} during the measurement period (cm^{-3}). N_{NPF} is the daily average number concentration of newly formed aerosol, N_{Bg} is the daily average number concentration of Background aerosol, and $N_{NPF-PERC}$ is the relative contribution of NPF during nucleation days. $N_{NPF-CONTR}$ is the relative contribution of NPF events during the entire measurement period.

Station	N_{NPF}	N_{Bg}	$N_{NPF-PERC}$	$N_{NPF-CONTR}$
DEM	0.35×10^3	0.7×10^3	30%	4%
EPT	0.5×10^3	0.4×10^3	56%	12%
FIN	0.03×10^3	0.1×10^3	20%	1%

and 20%, respectively. Nevertheless, keeping the whole measurement period in mind, the impact of NPF is insignificant at FIN (1%) and DEM (4%), but much more pronounced at EPT (12%). This size range was chosen as it proved to be useful for the detection of photochemical particle formation bursts. [52] reported a relative contribution of 23.8% of NPF with regard to the annual average of N_{5-20} at Leipzig-TROPOS in 2012. [55] report that the maximum in new particle formation occurrence in Finokalia was during the winter months. [38] report a minimum in atmospheric ion concentrations during June-September. [101] report that during the summer campaign at Finokalia (10-31 July 2000), new particle formation events were not observed. However, they also report that during the winter campaign (7-14 January 2001), new particle formation events were observed in almost half of the days (three nucleation events during the 7 days of the measurements). The fact that nucleation events are infrequent during summer months at the Regional Background station is also reported by [76]. We intend to investigate the frequency of occurrence of NFP in the Eastern Mediterranean in the winter months in another manuscript.

2.2.5 Regional background concentration variation based on air masses origin

The prevailing synoptic pattern over the Aegean Sea during summer is characterized by strong northern winds (Etesians) transporting dry and cool air masses downwind of Southern Russia, Ukraine, Central/Eastern Europe, the Balkan countries and Turkey. Detailed aerosol chemical

predictions by a comprehensive model system showed that more than 70% of the predicted aerosol mass over the Aegean Sea during these synoptic conditions is associated with the transport of aerosols and their precursors from outside the modeling domain (domain included Greece and Asia Minor Coast), as reported by [5]. [93] indicate that during July and August using the 40-yr ECMWF Re-Analysis (ERA-40) dataset, the average wind direction in the Eastern Mediterranean is from the North - North East and North West (Figure A.27, Appendix). In other words, the contribution of air mass transport from the south to the Eastern Mediterranean is insignificant during the Etesians.

In order to estimate the effect of aerosol transport from distant areas to the regional background concentration, the origin of the air-masses for RB-SD-Cluster3 of the Regional Background station (FIN), which represents the long range transported aerosol, was investigated. Clusters from other stations were not used, as they are Urban Background stations and their particle size distributions are affected by local pollution. The HDBSCAN algorithm provided the best fit for a minimum cluster size of 44 data points, with a minimum sample size of 1, producing 5 clusters for the origin of air-masses at FIN, regarding the regional background concentration. The clusters produced are depicted in Figure 2.8, where we have also included the Potential Source Contribution Function analysis (PSCF) at the 75^{th} percentile. The Dunn Index for these results is 1.87×10^{-1} while the corresponding value for the K-means algorithm for 5 clusters is 0.79×10^{-1}. The highest Dunn Index for the K-means results was 1.04×10^{-1} and corresponded to 6 clusters. Nevertheless, it is still less than the Dunn Index acquired by the HDBSCAN algorithm results for a minimum cluster size of 44 data points. The PSCF results indicate that there are many potential source areas, extending from the Caspian Sea to North-East and North-Central Europe. There are also hot-spots over Bulgaria and Turkey.

One may observe that the origin of RB-AMO-Cluster1 (the first cluster identified based on Air Mass Origin clustering) is from the Mediterranean Sea and it represents slow moving air masses, as we can see that its centroid has traveled the distance from North Italy to Crete in 7 days. Also, the air masses residence time, depicted by the color scale, lays over the Mediterranean Sea. We have to keep in mind that the residence time depicted corresponds to a height of 0 to 100 meters agl. We would expect this cluster to represent the background concentration of the Mediterranean basin.

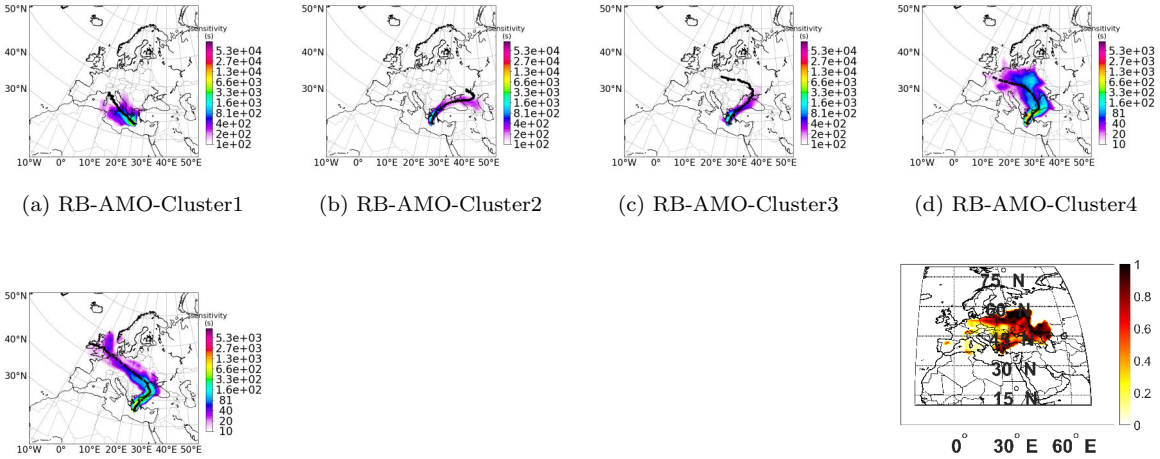

(a) RB-AMO-Cluster1 (b) RB-AMO-Cluster2 (c) RB-AMO-Cluster3 (d) RB-AMO-Cluster4

(e) RB-AMO-Cluster5 (f) PSCF at the 75^{th} percentile

Figure 2.8: Maps showing the air mass origin for the clusters identified through Air Mass Origin clustering and potential source areas from PSCF analysis. RB-AMO-Cluster1 corresponds to the first cluster identified based on Air Mass Origin clustering, referring to the cluster RB-SD-Cluster3 mentioned in Table 2.12. Subfigures a-e: Regional background concentration air mass origin clustering, based on centroids. The color corresponds to residence time in each cell, while the black dots correspond to the centroid of mass for all 3-hour releases of 4×10^4 finite air masses in the cluster, for each 3-hour backward step in time. Subfigure f: Potential Source Contribution Function analysis (PSCF) at the 75^{th} percentile of the total number concentration N of each mode obtained through modal analysis for the cluster RB-SD-Cluster3.

We should consider that the low precipitation in the Mediterranean basin favors the long residence time of PM (particulate matter) in the atmosphere with the consequent impact on air quality [77]. Table 2.12 shows that this cluster has the largest median d_g and the lowest number concentration compared to all clusters. That indicates probably aged aerosol particles, as particles have had time to grow to large accumulation mode sizes due to condensation, strong photochemistry and long time over Southern European areas. The particle number concentration of this cluster should be considered the regional background concentration of the Mediterranean basin during this period. RB-AMO-Cluster2 originates from the Caspian Sea region, passes over the Black Sea and finally over the Aegean Sea. The median particle number concentration of this cluster is three times higher than that of RB-AMO-Cluster1 and similar to those of the other clusters. We should also notice that at the 80^{th} percentile of d_g RB-AMO-Cluster2 has a value similar to RB-AMO-Cluster1, indicating aged aerosol. The origin of RB-AMO-Cluster3 is from Central Europe, but its main residence time in the height from 0 to 100 m agl is over the Black Sea and Ukraine, Bosporus Strait and the Aegean Sea. RB-AMO-Cluster4 originates from Western Europe, but it has much higher residence time in Central Europe than RB-AMO-Cluster3. Nevertheless, it demonstrates very similar particle number concentration values to RB-AMO-Cluster3, for all 3 percentiles presented. This could be an indication that a potentially significant source area of aerosol particles for these two clusters is the Bosporus Strait area. RB-AMO-Cluster5 originates from Great Britain, passes over Belgium and the Netherlands, Central Europe, the Black Sea and the Aegean Sea. Its median particle number concentration is similar, but somehow lower than the particle number concentrations of RB-AMO-Cluster2, RB-AMO-Cluster3 and RB-AMO-Cluster4. As shown in Figure 2.8, it is the cluster that has the highest centroid speed, perhaps leading to a less efficient collection of precursor gases and aerosol particles. Overall, the air masses during the campaign originate from the North-East, North-West and the Mediterranean Sea. Particle number concentration originating from the Mediterranean Sea are much lower, consisting of a median value of 0.7×10^3 particles per cm^3. Clusters with origin from North-East and North-West have particle number concentrations with median values ranging from 1.7×10^3 to 2.5×10^3 particles per cm^3. Therefore, we may conclude that the Etesian flow increases the regional background particle concentration in the Mediterranean basin by a factor of

2.5, to 4.

As demonstrated in Table 2.12 the identified clusters represent roughly 80% of the centroids, as intermediate centroids have been considered outliers. We have to keep in mind that the HDBSCAN algorithm distinguishes high and low density areas in order to separate clusters. Low density areas are considered outliers and are not included in the clusters. Figure A.26 (Appendix) shows the emission sources for SO_2. We observe that there are significant emission sources near the Bosporus area, which is also depicted as the closest to FIN potential source area indicated by the PSCF analysis. In an attempt to estimate the impact of this area, we included the residence time in this region for each cluster in Table 2.12. Considering all clusters, we observe that there is good agreement between residence time in this area and particle concentration. If we only consider RB-AMO-Clusters2-5 (the ones that have a significant residence time), we cannot distinguish between the amount of aerosol particles and precursor gases acquired by air masses in the Bosporus region and the regions they resided on earlier. If we apply a regression on the residence times in Bosporus area of RB-AMO-Clusters2-5 and the 80^{th} percentile of the total number concentration for each mode determined by modal analysis (N), we acquire an R^2 of 0.66. Based on these facts, we conclude that the Bosporus area is a significant source area for the regional background concentration in the Eastern Mediterranean during the Etesian flow, but there are also other source areas in the North-Central and North-Eastern Europe, that influence the regional background particle concentration in the Eastern Mediterranean. Similar results were obtained by PSCF analyses at the 80^{th} to the 95^{th} percentiles of N (included as Appendix, Figure A.29).

In order to have an estimate of the impact on the NSD of Southern winds, which, as mentioned earlier, are infrequent during the Etesians, we have identified by visual inspection 26 3-hour FLEX-PART sensitivity plumes that originate to some extend from the south (Figure A.28). All of these plumes are already included in RB-AMO-Cluster1, and thus the percentiles of their size distributions are similar (see Table A.7, Appendix).

Table 2.12: Characteristics of Regional background concentration identified clusters based on air mass origin. After the frequency of occurrence of each cluster during the campaign, we have included cluster residence time in the Bosporus area (latitude 40°-42° , longitude 25°-30°) normalized to frequency.

Cluster Results	**RB-AMO -Cluster1**	**RB-AMO -Cluster2**	**RB-AMO -Cluster3**	**RB-AMO -Cluster4**	**RB-AMO -Cluster5**
20^{th} percentile σ_g	1.37	1.43	1.46	1.48	1.49
50^{th} percentile σ_g	1.47	1.63	1.59	1.62	1.57
80^{th} percentile σ_g	1.68	1.88	1.75	1.72	1.73
20^{th} percentile d_g	129.1	107.2	115.2	97.7	117.5
50^{th} percentile d_g	179.5	136.6	145.6	126.7	145.9
80^{th} percentile d_g	216	205.2	170.2	173.7	168
20^{th} percentile N	0.4×10^3	0.9×10^3	1.5×10^3	1.1×10^3	1.1×10^3
50^{th} percentile N	0.7×10^3	2.3×10^3	2.5×10^3	2.2×10^3	1.7×10^3
80^{th} percentile N	1.9×10^3	3.3×10^3	3.1×10^3	3.4×10^3	2.4×10^3
Frequency %	25.1	16.9	17.3	10.4	10.9
Residence time	106	478	528	568	436

Chapter 3

Development of a new method to retrieve the real part of the Equivalent Refractive Index of atmospheric aerosol

In the context of the international experimental campaign Hygroscopic Aerosols to Cloud Droplets (HygrA-CD, 15 May to 22 June 2014), dry aerosol size distributions were measured at Demokritos station (DEM) using a Scanning Mobility Particle Sizer (SMPS) in the size range from 10 to 550 nm (electrical mobility diameter), and an Optical Particle Counter (OPC model Grimm 107 operating at the laser wavelength of 660 nm) to acquire the particle size distribution in the size range of 250 nm to 2.5 μm optical diameter. This work describes a method that was developed to align size distributions in the overlapping range of the SMPS and the OPC, thus allowing for the retrieval of an aerosol equivalent refractive index (ERI). The objective is to show that size distribution data acquired at in situ measurement stations can provide an insight to the physical and chemical properties of aerosol particles, leading to better understanding of aerosol impact on human health and earth radiative

balance. The resulting ERI could be used in radiative transfer models to assess aerosol forcing direct effect, as well as an index of aerosol chemical composition. To validate the method, a series of calibration experiments were performed using compounds with known refractive index (RI). This led to a corrected version of the ERI values, (ERI_{COR}). The ERI_{COR} values were subsequently compared to model estimates of RI values, based on measured $PM_{2.5}$ chemical composition, and to aerosol RI retrieved values by inverted lidar measurements on selected days.

3.1 Experimental Procedure

The international experimental campaign Hygroscopic Aerosols to Cloud Droplets (HygrA-CD), organized in the Athens Metropolitan Area (AMA), Greece, from 15 May to 22 June 2014, provided an extended record of data on aerosols and their role in cloud formation [71]. The major sampling site of the campaign was the Demokritos station (DEM), member of the GAW and ACTRIS Networks (37.995° N 23.816° E, at 270 m a.s.l), which is situated on the foot of Mount Hymettus in Agia Paraskevi. The DEM monitoring site belongs to the National Centre of Scientific Research "Demokritos", which is situated about 7 km to the north from downtown Athens, in a pine forest. It is representative of the atmospheric aerosol at suburban areas of the Athens Metropolitan area. The station is frequently influenced by katabatic winds [20], during which, air masses from mount Hymettus (peak height 1,024 meters) are brought over the station. Also, the lowering of nocturnal boundary layer height (NBLH) is occasionally resulting in an increase in particle number concentration, even in the absence of aerosol particle sources.

The instruments that were in operation during the campaign included:

1. an SMPS to acquire the particle size distribution of atmospheric aerosol in the size range from 10 to 550 nm (electrical mobility diameter). The instrument provides a full size distribution in the above mentioned range every 5 minutes. The SMPS has been calibrated against a reference SMPS system at the WCCAP (World Calibration Centre for Aerosol Physics) in 2013 and participated in an intercomparison workshop in 2016 at the WCCAP, exhibiting a counting accuracy within 10% for the size range 30-550 nm against a reference system under controlled laboratory conditions [106]. The instrument is calibrated at DEM station with PSL

spheres that have an electrical mobility diameter of 200 nm.

2. an OPC (Grimm 107@660 nm laser light wavelength) to acquire the particle size distribution in the size range of 250 nm to 2.5 μm optical diameter. The OPC in a similar intercomparison at the WCCAP exhibited a counting accuracy within 10% for the size range 250 nm to 1 μm. This instrument acquires a full size distribution every 1 minute. The instrument uses laser light of 660 nm, opening angles detected are 29.5 °-150.5 ° and 81 °-99 ° [14]. After its manufacture, the instrument follows an electronical adjustment of 1 μm channel with mono-disperse PSL 1 μm spheres (Duke Scientific, NIST traceable, m = 1.59, according to ISO 21501-1) [80, 26]. Afterwards the unit is calibrated to a reference Grimm OPC, using dolomite aerosols (i.e. different refractive index and a full size distribution). The particle number concentration in each size bin of the unit is adjusted to the one measured by the reference instrument. The adjustment is performed by changing the detection limits thresholds for each size bin [51, 80, 26]. The reference Grimm OPC is checked and certified with monodisperse Latex aerosol [26]. According to [29], the OPC counting accuracy is within 10% of the ideal 100% for sizes from 0.3 to 1 μm (electrical mobility diameter). The sizing accuracy decreases from around 0.8 μm up to approximately 2 μm.

3. an AE33 dual spot aethalometer in order to acquire the equivalent black carbon concentration (EBC) at seven wavelengths (370, 470, 520, 590, 660, 880, 950 nm). This instrument completes an EBC measurement for all wavelengths every 1 minute and operated after a $PM_{2.5}$ inlet [41].

4. an Ecotech 3-wavelength nephelometer to acquire the aerosol scattering and backscattering coefficient at 450, 525 and 625 nm. The instrument operated after a PM_{10} inlet and completes a measurement for all wavelengths every 1 minute [69].

5. a Sunset Lab Elemental Carbon - Organic Carbon (EC/OC) measurement instrument. The instrument acquires one measurement every 3 hours. It operates after a $PM_{2.5}$ cyclone and it has participated in an intercomparison exercise [70, 2]. During that exercise, the reproducibility relative standard deviation for all participants, was within 30%, without any correction applied.

6. a Droplet Measurement Technologies (DMT) streamwise thermal-gradient CCN counter. Through-

out the campaign, the instrument was operated at a total flow rate of 0.5 LPM, with a sheath-to-aerosol flow ratio of 10:1, and a top-bottom column difference, ΔT between 4 and 15 K. Concentrations were measured at each supersaturation for 10 min, yielding a CCN spectrum consisting of 5 different supersaturations every 50 min [11].

7. a multi-wavelength Raman lidar system (EOLE) deployed at the National Technical University of Athens (NTUA) (37.97° N, 23.79° E, 212 m a.s.l.), approximately 4 km from DEM station and 4.5 km from the city center which was used to provide the vertical profile of the optical properties of aerosols (backscatter and extinction coefficients) at 355-532-1064 nm [44]. Using these data as input, we can derive the vertical profile of the aerosol microphysical properties (i.e. refractive index, effective radius, volume concentration, etc.) based on inversion techniques [54, 96].

Inlet aerosol flows are dried to relative humidity (RH) below 40%, while particle losses due to diffusion in the pipe lines are calculated and corrected for SMPS. Other losses are not corrected for the OPC and the SMPS, as their inlet line is vertical and therefore losses in the size range 0.2 to 1 μm (aerodynamic diameter) are not significant.

The analysis of $PM_{2.5}$ filters was performed by:

1. An accredited according to EN14902 high-resolution energy dispersive X-Ray fluorescence spectrometer Epsilon 5 by PANanalytical (XRF). Epsilon 5 is constructed with optimized Cartesian-geometrical design for lower background and with extended K line excitation 100 kV X-ray capability. The spectrometer provides selection of 8 secondary targets (Al, CaF_2, Fe, Ge, Zr, Mo, Al_2O_3, LaB_6), that can polarize the X ray beam. All measurements were performed under vacuum [19].

2. Ion Chromatography (IC). The concentrations of Cl^-, NO_3^-, SO_4^{2-}, Na^+, K^+, NH_4^+, Ca^{2+}, Mg^{2+} were determined by a Metrohm 732 IC Separation Center connected to a 732 IC conductivity detector and a 753 Suppressor Module for anions determination as described in [57].

3.2 ERI optimal solution algorithm

The aerosol particle's scattering process is described by four amplitude functions, S_1, S_2, S_3, S_4, all functions of θ (angle of incident light to scattered light in the direction of light propagation). Spherical particles have $S_3 = S_4 = 0$. So two complex amplitude functions occur for any direction; these functions are $S_1(\theta)$ and $S_2(\theta)$; they depend only on the scattering angle θ. We have to compute the numbers [33]:

$$i_1 = |S_1(\theta)|^2 \, and \, i_2 = |S_2(\theta)|^2 \tag{3.1}$$

$$Q_{sca} = \frac{1}{x^2} \int_0^{\pi} \{i_1(\theta) + i_2(\theta)\} \sin(\theta) \, \mathrm{d}\theta \tag{3.2}$$

where x is the size parameter ($x = k_w r$, k_w is the wave number and r is the radius). Q_{sca} is the scattering efficiency. Then we obtain the scattering effective cross section S_{sca} by multiplying Q_{sca} to the particle cross section area. The angular integration is performed over the solid angle corresponding to Grimm 107 (described earlier). The resulting scattering effective cross section S_{sca}, ($\mu m/m^2$), is calculated for each OPC size bin using the function Mie_*abcd* of [58].

The following assumptions apply for OPC measurements:

1. Absorption is negligible and particles are spherical.
2. The aerosol is internally mixed.
3. The size distribution measured by the OPC represents particles of sizes equivalent to those corresponding to PSL spheres with a real part of refractive index equal to 1.585 at 660 nm wavelength.

The fitting procedure consists of several steps. In the first step, the algorithm assumes that RI can range from 1.3 to 2.2 in steps of 0.1 (i.e. 1.3, 1.4, etc.). For these refractive indices, the Grimm size distribution is recalculated for size bins corresponding to SMPS. The Root Mean Square Error (RMSE) of the difference between the SMSP and OPC number size distributions (NSD) is calculated:

$$\mathrm{RMSE} = \frac{100}{\sqrt{\mathrm{n}}} \left(\sum_{i=1}^{n} \left[N_{Di}^{SMPS} - N_{Di}^{OPC} \right]^2 \right)^{0.5} \tag{3.3}$$

where n is the number of size bins in the overlapping range of SMPS and OPC size distributions. N_{Di}^{SMPS} is the number concentration measured by SMPS at size bin i corresponding to particle diameter D and N_{Di}^{OPC} is the number concentration measured by OPC at diameter D. The overlapping range varies with respect to the RI assumed. For assumed RIs below 1.3, the overlapping range has very few size bins. Subsequently, an algorithm is employed in order to find the ERI that minimizes RMSE [66].

3.2.1 OPC diameter recalculation for assumed RIs

Based on the assumptions mentioned earlier for the OPC,

S_{sca} is calculated for OPC size bins. S_{sca} is not monotonically increasing with particle size, therefore it is fitted to the function

$$S_{sca} = \ a \ D^b \tag{3.4}$$

where D is particle diameter, and a,b derived fitted constants. This provides a good approximation in the particle size range from 100 - 1200 nm (Figures A.34-A.39, Appendix). This approximation is from now on considered as the instrument primary measurement for each OPC size bin.

In order to invert the OPC size bins particle size for any other RI, we calculate S_{sca} for a range of diameters extending from 100 to 1200 nm. Then, we calculate the constants a,b in the S_{sca} relation to diameter D for the new RI, according to equation 4. Subsequently, we find the particle size diameters corresponding to the OPC primary measured S_{sca}.

3.3 Method Evaluation - Calibration Procedure

In order to evaluate the method for the ERI retrieval, a series of calibration experiments were made. For this purpose, we generated test aerosol of known chemical composition.

Bulk materials were chosen from common chemical species found in the atmospheric aerosol or used in instrument calibration, with RI values according to the literature: Ammonium Sulfate (RI = 1.53@580 nm wavelength) [88], Di-Ethyl-Hexyl-Sebacate (RI = 1.45@650 nm) [90] and Polystyrene

Latex Spheres (PSL) with sizes of 262 and 490 nm (RI = 1.585@660 nm) [87]. Calculations of the response function were performed and ERI was calculated for each chemical compound.

Based on the PSL experiment it was concluded that S_{sca} has to be corrected for a sizing error in OPC NSD, within the ERI retrieval algorithm according to equation 5.

$$S_{sca-cor} = \frac{S_{sca}}{1.5} \tag{3.5}$$

The next step is to find a correction factor for aerosols with RI different from PSL spheres, incorporating all experiments. The final ERI correction equation for the dependence on aerosol RI follows:

$$RI = \ 1.7 \exp((-(ERI_{COR} - 2)/1.5)^2) \tag{3.6}$$

The calibration procedure, setup, and results in detail are presented as Appendix. Regression analysis of the literature RI and ERI derived from the calibration procedure, yielded an overall standard error (uncertainty) of ± 0.1. The discrepancies between literature and calculated RI can be attributed to the OPC measurement principal and subsequent signal treatment by the instrument, which leads to a distortion of the particle size distribution for substances with RIs other than 1.6.

The DEM station is a background station and the overlapping range of SMPS and OPC is in accumulation mode, therefore ERI_{COR} is expected to frequently correspond to aged, internally mixed aerosol. Nevertheless, occasionally, particles might have variable RIs, even if they are measured in the same optical size range (externally mixed). The measurement error is expected to be higher in this situation.

3.4 Major findings

After fitting the SMPS and the OPC size distributions obtained at DEM station during HygrA-CD campaign, we acquire the optimal solution ERI, as depicted in Figure 3.1. The correction of equation 6 has not yet been applied.

We observe that the original SMPS - OPC size distributions are quite different in these 4 cases, leading to large differences in ERI retrieved.

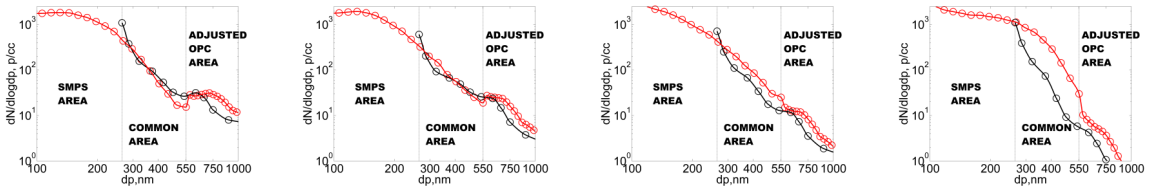

(a) SMPS - OPC FIT, ERI = 1.8

(b) SMPS - OPC FIT, ERI = 1.7

(c) SMPS - OPC FIT, ERI = 1.6

(d) SMPS - OPC FIT, ERI = 1.5

Figure 3.1: SMPS - OPC fit examples for various ERI values. Red circles and line denote the measured SMPS size distribution (SD) combined with the fitted Grim 107 size distribution, while the black circles and line represents the Grim 107 measured SD. The Grim 107 SD is moved to the right at ERI = 1.6, as it should, in order to compensate for the sizing error in relation to the SMPS observed at the PSL calibration experiment.

In Figure A.40 (see Appendix), the same size distributions are depicted but in a smaller diameter range and therefore differences in number concentration between the size distributions are more profound. From both Firures (1 and A.40), the adjustment of the size distributions is very good.

We have to keep in mind that the ERI is not the actual RI of the aerosol measured by SMPS and OPC, but rather a number describing the optimal solution of a fitting procedure between the size distributions of the two instruments. Aerosol RI could be variable even within each size bin measured by the OPC. We expect it to be closely related to an average overall RI of the size distribution, but the relation might depend on factors like aerosol mixing state and the presence of more than one modes in the overlapping range. The transfer functions of the two instruments and subsequent data treatment, also lead to discrepancies in the size distributions measured. This optimal solution in Figure 3.1 includes the correction for the sizing error of the OPC.

In order to correct for the relation of ERI to RI, as observed in the calibration experiments, we apply equation 6 and acquire ERI_{COR}. An overview of ERI_{COR} during HygrA-CD campaign is presented in Figure 3.2. The histogram of the measured values (276 3hr intervals) indicates that most of the values are in the range between 1.62 and 1.68.

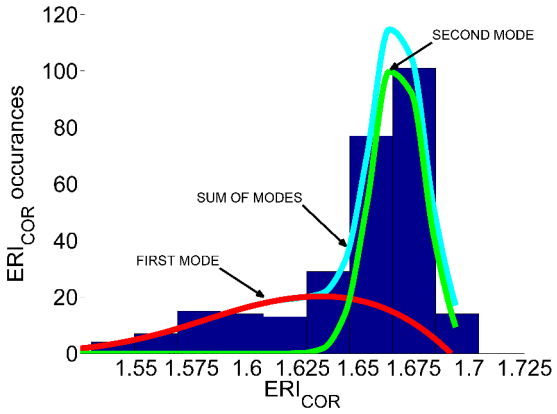

Figure 3.2: ERI_{COR} histogram evolution of the 3hr mean values during the whole period of HygrA-CD campaign. Blue boxes denote the number of ERI_{COR} occurrences in each size bin, while the cyan line denotes the best fit of the histogram using Gaussian distributions.

3.4.1 ERI_{COR} comparison to aerosol mass constituents

According to [1], soil dust constituted 12% of $PM_{2.5}$ mass (6% annual average Sahara dust and 6% local soil dust) during 2013 at the DEM station. In order to investigate if the presence of dust can be identified in the range of values of the ERI_{COR} dataset during the Hygra campaign, we calculated the Single Scattering Albedo Exponent a_{SSA} at 450-625 nm wavelength. We accomplished that using absorption and scattering coeffient data obtained from the AE33 and the Ecotech Nephelometer measurements respectively.

In Figure 3.3 we observe that a Sahara dust episode is indicated on the 27th to 30th of May 2014 by SKIRON model [40]. When coarse particles are present (during Sahara dust events), a_{SSA} becomes clearly negative with values usually falling between -0.1 and -0.5, according to [16]. We observe in Figure 3.3 that when a_{SSA} is below -0.1, ERI_{COR} increases. This could be attributed to dust constituents with high RI.

In order to evaluate the ERI_{COR} variability against aerosol components and various aerosol types, 24hr averages of ERI_{COR} and EC/OC were obtained at the time intervals corresponding to XRF measurements. In Figure 3.4, the OC values were adjusted for carbon and hydrogen weights by multiplying with a mass correction factor of 1.4 [27].

In Figure 3.4, when the Sulfur to Organic Carbon ratio increases, ERI_{COR} increases, as sulfuric

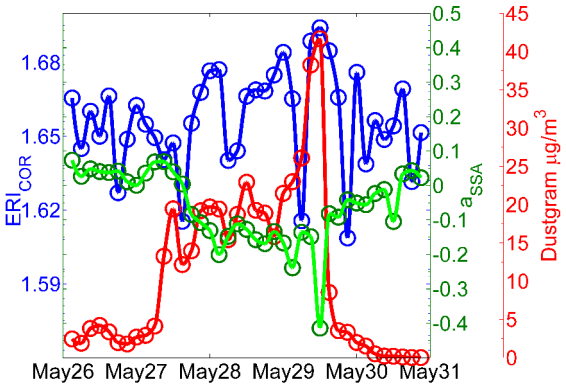

Figure 3.3: ERI_{COR} (blue) in comparison to Single Scattering Albedo exponent (a_{SSA}, green) derived from DEM station instrument measurements. The SKIRON Sahara dust model output ($\mu g/m^3$) at 400 m above ground level (agl) is also depicted (red). Circles are actual data points, while lines are interpolation.Data are taken from 26 to 31 May 2014.

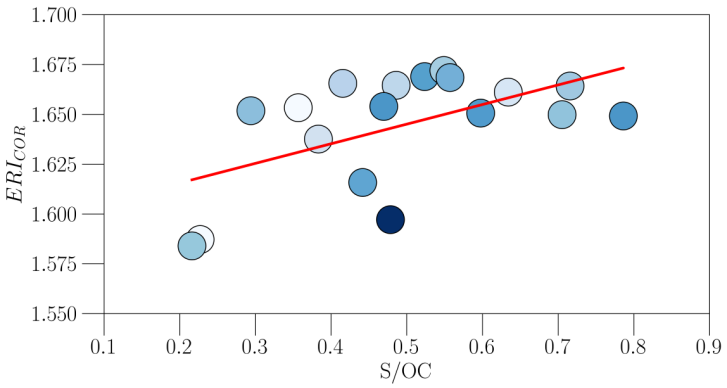

Figure 3.4: ERI_{COR} 24hr averages in comparison to Sulfur per Organic Carbon mass ratio of aerosols up to 2.5 μm (aerodynamic diameter) during HygrA-CD campaign.The red line depicts the linear fit for the data points. The color corresponds to EC concentration measured (darker color corresponds to higher concentration). Linear fit R^2 equals to 0.32.

compounds have almost the same RI compared to organic compounds, but most organic compounds emission sources are associated with Elemental Carbon, the major absorbing species. The linear fit R^2 is low, which indicates that other components (EC, dust content), also play an importand role in determining ERI_{COR} values.

In order to compare ERI_{COR} to aerosol composition, mineral dust (or soil dust) was estimated based on XRF measurements and average crust composition [65], as

$$\text{Mineral Dust} = 1.35\ Na + 1.66\ Mg + 1.89Al + 2.14\ Si + 1.21\ K + 1.40\ Ca + 1.67\ Ti + 1.43\ Fe \quad (3.7)$$

Some corrections were however applied to this formula to take into account sea-salt contributions to Na and Mg, and possible anthropogenic contributions to the other elements. The sea salt fractions of Na and Mg were calculated using the measured Cl concentration and the Na/Cl and Mg/Cl ratios 0.56 and 0.07, respectively. Due to possible Cl losses in aerosol samples, this approach may overestimate the non-sea salt component of Na (nss_{Na}) and Mg (nss_{Mg}).

3.4.2 RI_{IC} acquired by Ion Chromatography, EC/OC and dust measurements

A filter sampler was deployed at the National Technical University of Athens (NTUA) (37.97° N, 23.79° E, 212 m a.s.l.), approximately 3.3 km from DEM station. Ion Chromatography was used in order to separate anions and kations of the aerosol collected. The model ISORROPIA (II) [21] was applied to the results and the water content of the aerosol species was calculated. The RH and temperature used were the average values recorded at DEM station SMPS and OPC inlet line, over the corresponding time intervals. Based on the assumption that during daytime, the air masses over the AMA are well mixed, we also used the EC/OC measured at DEM station. Dust derived at the DEM station was also used, but we have to keep in mind that it is derived from filter samples with 24hr duration. Two samples were excluded, as at the time of measurement there was strong mixing in the vertical, bringing aerosol from higher layers (probably dust), leading to very high ERI_{COR}

Table 3.1: Physical constants of species used in refractive index and density calculations from [27] and [42].

Species	Density (g cm^{-3})	Refractive index
$(NH_4)_2\ SO_4$	1.76	1.53
$NaNO_3$	2.26	1.59
Organic Carbon	1.40	1.55
Elemental Carbon	2.00	1.96 − 0.66 i
Mineral dust	1.99	$1.59 - 7 * 10^{-3}$ i

values, not corresponding to 24hr averages of dust concentration (Figures A.41, A.42, Appendix).

The density and refractive index data for the mass constituents calculated are presented in Table 3.1.

According to [42], the imaginary part strongly decreases with increasing particle size, reflecting the fact that the highly absorbing components (hematite and soot) are predominantly found in the small particle range. Therefore, at the size range that ERI_{COR} is calculated (approximately 260-550 nm electrical mobility diameter), we expect significant absorption. This is attributed not only to the dust absorption, but also to the fact that during Sahara dust events in HygrA-CD campaign, the Planetary Boundary Layer Height (PBLH) reduces significantly according to [6], leading to higher concentrations of pollutants, including EC. Despite all that, the ERI_{COR} values increase during dust events (see Figure 3.3), as it appears that the effect of constituents with high real part of RI like dolomite (RI = 1.62), calcite (RI = 1.6), chloritoid (RI = 1.73), hematite (3.05 - 0.3 i) and ilmenite (2.4 - 0.3 i) is significant [42].

The aerosol density was computed from the chemical analysis data following [28] using Equation 8:

$$\rho^{-1} = \sum_i \frac{X_i}{\rho_i} \tag{3.8}$$

where X_i is the mass fraction for species i and ρ_i is the individual species density (gcm^{-3}). Refractive index can be computed by different mixing rules, 2 of which are partial molar refraction [83] and volume-weighted method [28].

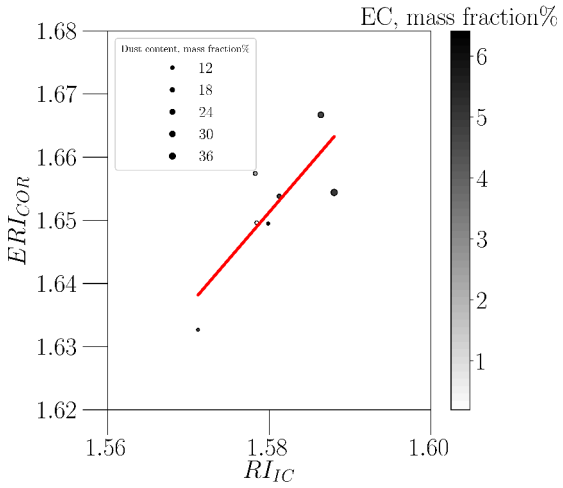

Figure 3.5: ERI_{COR} averages in comparison to RI_{IC} derived from IC, EC/OC and XRF measurements during HygrA-CD campaign. The red line depicts the linear fit for the data points. The size of the markers corresponds to dust mass fraction, while the color corresponds to EC mass fraction.

The volume-weighted method was used (Equation 9) to calculate mean refractive index ($m = m_r - k_i$).

$$m = \rho \sum_i \frac{X_i m_{r,i}}{\rho_i} - \rho \sum_i \frac{X_i k_i}{\rho_i} i \tag{3.9}$$

where m_r is the real part of a complex refractive index for species i and k_i is the imaginary part. The only absorbing species included were EC and Dust. The imaginary part of the refractive index was not calculated, as it could not be compared to ERI_{COR}.

In Figure 3.5, ERI_{COR} and RI_{IC} seem to have a standard offset during these hours (around 0.05-0.1). ERI_{COR} and RI_{IC} are well correlated ($R^2 = 0.88$ for a linear fit). We also observe that when the dust mass fraction is high, ERI_{COR} is high. The uncertainty of RI_{IC} depends on the uncertainty of the XRF, EC/OC and IC measurements. Reported uncertainties range between less than 10% (IC) and up to 20% (XRF), [56, 70, 57]. Therefore, an overall uncertainty of ± 0.15 could be considered suitable for RI_{IC}, given that most of the particulate mass comes form IC measurements. ERI_{COR} averages in comparison to RI_{IC} are also presented in table A.9 (Appendix).

3.4.3 Lidar inversion algorithm description to acquire aerosol RI_{LI} and comparison to ERI_{COR}

The 6-wavelength Raman lidar system (EOLE) was operated at National Technical University of Athens (NTUA) (37.97° N, 23.79° E, 212 m a.s.l.), during selected daytime/nighttime slots (37 days and nights out of 39), to provide the vertical profiles of the aerosol backscatter coefficient (b_{aer}) (at 355, 532 and 1064 nm) and aerosol extinction coefficient (a_{aer}) (at 355 and 532 nm), the lidar ratio (S = a_{aer}/b_{aer}) (at 355 and 532 nm), and the aerosol Ångström exponent AE-related to backscatter and extinction coefficients. During nighttime the vertical profiles of b_{aer}, a_{aer}, S, and AE-related to extinction and backscatter coefficients are retrieved with 10-20%, 10-15%, 10% and 25% uncertainty, respectively [44].

During daytime, using as input a constant S value (constrained by the mean Aerosol Optical Depth (AOD) value obtained from a nearby sunphotometer), we retrieve only the b_{aer} and the AE-related to backscatter coefficient values with an average uncertainty (due to both statistical and systematic errors) of 20-30% and 25%, respectively [44]. Moreover, EOLE provided the water vapor mixing ratio profiles from 0.5 to 6-7 km height, during nighttime, with a statistical error less than 8% at heights up to 2 km and 10-15% from 2.5 to 6 km [53].

Although full overlap of EOLE occurs at 600-700 m above ground level, an experimental method has been applied [102] to derive the overlap correction vertical profile down to about 400 m. The real part of RI (RI_{LI}) has been retrieved from multi-wavelength Raman lidar data, without the use of any a priori assumption. The inversion algorithm is based on the minimum discrepancy criterion and is implemented with the use of regularization techniques [96].

Aerosol backscatter coefficient at 355, 532, and 1064 nm and extinction coefficient at 355 and 532 nm have been used in order to obtain the refractive index with an uncertainty of 0.1. The particle extinction coefficient stabilises the solution and decreases the discrepancy of the retrieval. In addition, base functions are used to stabilise the inverted quantity (e.g. the particle refractive index). From the mathematically correct solution space, only the physically meaningful subspace is accepted [62]. In this study, only solutions with a discrepancy lower than 1% have been considered and the aerosol radius range has been restricted from 0.03 to 10 μm.

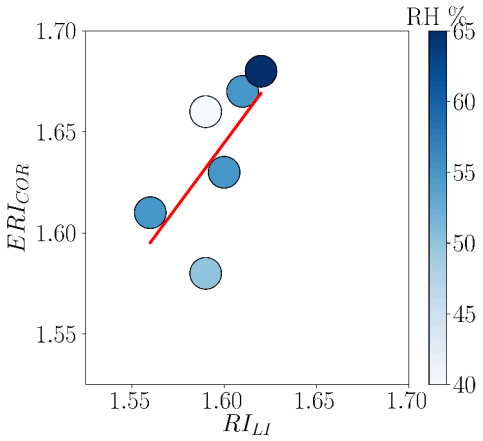

Figure 3.6: ERI_{COR} to RI_{LI} values. The red line depicts the linear fit for the data points. The color corresponds to RH measured between 1 to 1.2 km a.g.l. (darker blue means higher RH value).

In Figure 3.6 the ERI_{COR} versus the RI_{LI} for six coinciding OPC-SMPS and lidar measurements is shown. We observe that ERI_{COR} and RI_{LI} are reasonably correlated ($R^2 = 0.6$ for a linear fit). The RH during the lidar measurements in Figure 3.6 ranged from 40 to 65%, increasing the discrepancy between ERI_{COR} and RI_{LI}. We observe that the RH has little effect on the correlation of ERI_{COR} and RI_{LI} for the measurements presented in Figure 3.6. We may thus conclude that the main mechanism that influences the ERI_{COR} and RI_{LI} correlation is the state of mixing in the vertical. Hygroscopicity data were not availiabe for all measurements shown in Figure 3.6 and could not be included. ERI_{COR} averages in comparison to RI_{LI} are also presented in table A.10 (Appendix).

Chapter 4

Comparison of in situ and remote sensing aerosol measurements in the Athens Metropolitan Area

In the summer of 2014 in situ and remote sensing instruments were deployed in Athens, in order to study the concentration, physical properties, and chemical composition of aerosols and their contribution to cloud formation. We also aimed to find the atmospheric conditions that allow the direct comparison of collocating in situ and remote sensing stations measurements and demonstrate the mixing of regional and local aerosol in the vertical. On selected days that displayed significant turbulence up to approximately 1,000 m above ground level (agl), we acquired the aerosol extinction or scattering coefficient by in situ instruments using three methods. In the first method the aerosol extinction coefficient was acquired by adding a Nephelometer scattering coefficient in ambient conditions and an Aethalometer absorption coefficient. The correlation between the in situ and remote sensing instruments was good (coefficient of determination R^2 equal to 0.74). In the second method we acquired the aerosol refractive index by fitting dry Nephelometer and Aethalometer measurements with Mie code calculations of the scattering and absorption coefficients for the size distribution up to 1,000 nm obtained by in situ instruments. The correlation in this case was rea-

sonably good (R^2 equal to 0.62). Our next step was to compare the extinction coefficient acquired by remote sensing instruments to the scattering coefficient calculated by Mie code using the size distribution up to 1,000 nm and ERI_{COR}, which is the real part of the equivalent refractive index acquired by the comparison of the size distributions obtained by a Scanning Mobility Particle Sizer (SMPS) and an Optical Particle Counter (OPC). The agreement between the in situ and remote sensing instruments in this case was not good (R^2 equal to 0.45). The last comparison for the selected days was between the aerosol extinction Ångström exponent acquired by in situ and remote sensing instruments. The correlation was not good (R^2 equal to 0.4), probably due to differences in the number size distributions present in the air volumes measured by in situ and remote sensing instruments. Nevertheless, if turbulent conditions prevail in the atmosphere, extending from ground level up to the height at which the lidar measurements take place, good agreement between the extinction coefficients of in situ and remote sensing instruments can be achieved, as indicated by the first two methods mentioned earlier. Furthermore, we also present a day that a Saharan dust event occurred in Athens. At first, the Saharan dust layer was evident in lidar measurements at a height of 2,000 m agl. Due to the high turbulence in the atmosphere, in the afternoon the Saharan dust layer gradually descended to ground level and it was detected by in situ instruments. The origin of air masses from North Africa reaching Athens was also depicted by FLEXPART air mass transport model 3-hourly plots. Thus, we obtained an insight on how regional aerosol is added to local aerosol, especially during pollution events due to long range transport.

4.1 Materials and Methods

The international experimental campaign Hygroscopic Aerosols to Cloud Droplets (HygrA-CD), organized in the Athens Metropolitan Area (AMA), Greece, from 15 May to 22 June 2014, provided an extended record of data on aerosols and their role in cloud formation [71]. The major sampling site of the campaign was the Demokritos station (DEM, purple marker, Figure 4.1), member of the GAW and ACTRIS Networks (37.995° N 23.816° E, at 270 m above sea level (asl)). The DEM monitoring site belongs to the National Centre of Scientific Research "Demokritos", which is situated on the foot of Mount Hymettus, about 8 km to the north from downtown Athens, in a pine

Figure 4.1: Experimental sites over Attica (Greece) during the HygrA-CD campaign. The altitudes of the stations are given in parenthesis (in meters above sea level: asl).

forest. It is representative of the atmospheric aerosol at suburban areas of the Athens Metropolitan Area. The station is frequently influenced by katabatic winds [20], during which, air masses from Mount Hymettus (peak height 1,024 meters) are brought over the station. Also, the lowering of nocturnal boundary layer height (NBLH) is occasionally resulting in an increase in particle number concentration, even in the absence of aerosol particle sources.

The instruments that were in operation at DEM station during the campaign included:

1. a Scanning Mobility Particle Sizer (SMPS) to acquire the particle size distribution of atmospheric aerosol in the size range from 10 to 550 nm (electrical mobility diameter) comprised of a TSI Model 3080L electrostatic classifier (TSI Inc., Shoreview, MN, USA) and a condensation particle counter (CPC; TSI Model 3772, TSI Inc., Shoreview, MN, USA). The instrument provides a full size distribution in the above mentioned range every 5 minutes. The SMPS has been calibrated against a reference SMPS system at the WCCAP (World Calibration Centre for Aerosol Physics) in 2013 and participated in an intercomparison workshop in 2016 at the WCCAP, exhibiting a counting accuracy within 10% for the size range 30-550 nm against a reference system under controlled laboratory conditions [106]. The instrument is calibrated at DEM station with PSL spheres that have an electrical mobility diameter of 200 nm.

2. an Optical Particle Counter (OPC) (Grimm 107@660 nm laser light wavelength) to acquire the particle size distribution in the size range of 250 nm to 2.5 μm optical diameter. The OPC in a similar intercomparison at the WCCAP exhibited a counting accuracy within 10% for the size range 250 nm to 1 μm. This instrument acquires a full size distribution every 1 minute. The

instrument uses laser light of 660 nm, opening angles detected are 29.5°-150.5° and 81°-99° [14]. After its manufacture, the instrument follows an electronic adjustment of 1 μm channel with 1 μm monodisperse polystyrene latex spheres (PSL) (Duke Scientific, NIST traceable, m = 1.59, according to ISO 21501-1) [80, 26]. Then, the unit is calibrated to a reference Grimm OPC, using dolomite aerosols (i.e. different refractive index and a full size distribution). The particle number concentration in each size bin of the unit is adjusted to the one measured by the reference instrument. The adjustment is performed by changing the detection limits thresholds for each size bin [51, 80, 26]. The reference Grimm OPC is checked and certified with monodisperse Latex aerosol [26]. The OPC number size distribution acquired by the instrument was adjusted based on a calibration measurement with PSL spheres of 262 and 490 nm ([99], see Appendix, Figures A30 - A32).

3. an AE33 dual spot Aethalometer in order to acquire the equivalent black carbon concentration (eBC) at seven wavelengths (370, 470, 520, 590, 660, 880, 950 nm). This instrument completes an eBC measurement for all wavelengths every 1 minute and operated after a $PM_{2.5}$ inlet. The aerosol absorption coefficient was acquired using a multiple scattering correction factor due to filter fibers (C_0) equal to 3.5 in order to correct for multiple scattering by the filter fibers and the scattering of the aerosols embedded in the filter [41]. The instrument participated in an intercomparison workshop in 2017 at the WCCAP, exhibiting an equivalent Black Carbon (eBC) counting accuracy within 4% against a reference system (MAAP) under controlled laboratory conditions.

4. an Ecotech 3-wavelength Nephelometer to acquire the aerosol scattering and backscattering coefficient at 450, 525 and 635 nm. The instrument operated after a PM_{10} inlet and completes a measurement for all wavelengths every 1 minute [69]. The instrument participated in an intercomparison workshop in 2016 at the WCCAP, exhibiting counting accuracy at 450 and 635 nm wavelength within 6% against a reference system (Aurora4000) under controlled laboratory conditions.

5. a Hygroscopic Tandem Differential Mobility Analyzer (HTDMA) in order to acquire the hygroscopicity of aerosol particles. The instrument consists of two Differential Mobility Analyzers

(DMAs) for sizing particles in the fine aerosol range, a humidification system, and an Ultrafine Condensation Particle Counter [86]. Aerosol particles were initially dried and passed through a bipolar charger before entering the first DMA (DMA-1). The monodisperse aerosol flow downstream DMA-1 was then exposed to elevated RH conditions inside the humidifier. The second DMA (DMA-2), which was also operated with a sheath flow of elevated RH, and the UCPC were used for measuring the size distribution of the particles downstream the humidifier [9].

6. A pulsed Doppler scanning lidar system (StreamLine Wind Pro model, HALO Photonics) at 1.5 μm was deployed at the DEM site by the Finnish Meteorological Institute (FMI). The system was operated in the vertical azimuth display (VAD) mode and the 3-beam Doppler beam swinging (DBS) mode. It mainly provided the vertical profiles of the radial wind and 2-3D wind fields, as well as the atmospheric turbulent properties (e.g. turbulent dissipation rate, ϵ) [67]. The wind velocity is provided with accuracy better than 0.1 and 0.5 ms^{-1} for VAD and DBS mode, respectively. The range resolution of the measurements is 30 m, and the temporal resolution is 14 seconds and 15 min for DBS and VAD modes, respectively; the maximum range achieved is 2-3 km (or even 10 km height, under the presence of clouds) depending on the atmospheric aerosol load [71].

7. An accredited according to EN14902 high-resolution energy dispersive X-Ray fluorescence spectrometer Epsilon 5 by PANanalytical (XRF). Epsilon 5 is constructed with optimized Cartesian-geometrical design for lower background and with extended K line excitation 100 kV X-ray capability. The spectrometer provides selection of 8 secondary targets (Al, CaF_2, Fe, Ge, Zr, Mo, Al_2O_3, LaB_6), that can polarize the X ray beam. All measurements were performed under vacuum [19].

The second campaign site was located at the National Technical University of Athens (NTUA, blue marker, Figure 4.1, 37.97° N, 23.79° E, 212 m asl), about 5 km to the north from downtown Athens. The instruments that were in operation at NTUA station during the campaign included:

1. The 6-wavelength Raman lidar system (EOLE) which operated during selected daytime/nighttime slots (37 days and nights out of 39), to provide the vertical profiles of the aerosol backscatter

coefficient (b_{aer}) (at 355, 532 and 1064 nm) and aerosol extinction coefficient (a_{aer}) (at 355 and 532 nm), the lidar ratio (S = a_{aer}/b_{aer}) (at 355 and 532 nm), and the aerosol Ångström exponent (AE)-related to backscatter and extinction coefficients. During nighttime the vertical profiles of b_{aer}, a_{aer}, S, and AE-related to extinction and backscatter coefficients are retrieved with 10 - 20%, 10 - 15%, 10% and 25% uncertainty, respectively [44]. During daytime, using as input a constant S value (constrained by the mean Aerosol Optical Depth (AOD) value obtained from a nearby sun-photometer), we retrieve only the b_{aer} and the AE-related to backscatter coefficient values with an average uncertainty (due to both statistical and systematic errors) of 20 - 30% and 25%, respectively [44]. Moreover, EOLE provided the water vapor mixing ratio profiles from 0.5 to 6-7 km height, during nighttime, with a statistical error less than 8% at heights up to 2 km and 10 - 15% from 2.5 to 6 km [53]. The measurements of extinction and backscatter coefficient above the height of 1200 m above sea level (asl) were considered meaningfull and the average from 1200 m asl to 1300 m asl was used for the comparison to the in situ instruments.

2. A microwave radiometer (RPG-HATPRO model, RPG Radiometer Physics), operated at NTUA, was used to detect the microwave radiation emitted by the atmosphere at several channels (22.2 - 31.4 GHz and 51.3 - 59 GHz) to provide temperature and Absolute Humidity (AH) and RH vertical profiles [47]. The root-mean-square (rms) accuracy of temperature was 0.6 K near the surface, increasing to 1.5 - 2.0 K in the middle troposphere [17, 49]. The rms of absolute humidity was 0.4 gm^{-3}. The integrated water vapour (IWV) and the liquid water path (LWP) retrievals had accuracies of 0.3 - 1.0 kgm^{-1} and 20 - 30 gm^{-2} , respectively [50].

For in situ instruments, inlet aerosol flows are dried to RH below 40%, while particle losses due to diffusion in the pipe lines are calculated and corrected for SMPS. Other losses are not corrected for the OPC and the SMPS, as their inlet line is vertical and therefore losses in the size range 0.2 to 1 μm (aerodynamic diameter) are not significant.

Radiosondes were also launched from the HNMS or the NKUA (Figure 4.1). The radiosonde (RS92-SGP model, Vaisala Oyj) equipped with a GPS receiver, temperature, humidity, and pressure sensors, was used to measure the vertical profiles (with a height uncertainty of 20 m) of temperature

(uncertainty 0.3 - 0.4 °C), RH (uncertainty 4%), pressure (uncertainty 0.5 - 1 hPa for pressures ≥ 100 hPa) and wind speed and direction (uncertainties of 0.15 ms^{-1} and 2°, respectively) according to [64] and [95, 94]. .

4.1.1 Choice of dry aerosol particle number size distribution extent

The aerosol dry size distribution used is obtained during the procedure in order to acquire the Equivalent Refractive Index (ERI_{COR}) optimal solution by fitting the SMPS and OPC size distributions in the overlapping range [99]. Since the OPC number size distribution was corrected based on calibration measurements with PSL spheres of 262 and 490 nm (see Appendix, Figures A30 - A32), we used the combined size distribution up to the size of 1,000 nm (corresponds to dry electrical mobility diameter). After this size, we cannot be sure that ERI_{COR} corresponds to the aerosol particle's refractive index. Also, according to [29], the OPC counting accuracy is within 10% of the ideal 100% for sizes from 0.3 to 1 μm (electrical mobility diameter). The sizing accuracy decreases from around 0.8 μm up to approximately 2 μm. The obtained combined size distribution up to 1,000 nm from the SMPS and OPC (considered to correspond to electrical mobility diameter) is used from now on as the aerosol size distribution whose optical properties are compared to the EOLE lidar measurements. The counting accuracy of the SMPS in the size range 30 - 550 nm is 10%, therefore we expect the error in the size distribution produced by the combination and adjustment of SMPS and OPC measurements to be within an uncertainty of 10%. Furthermore, we expect the uncertainty of all comparisons presented in this work to be within 20%.

4.1.2 $RI_{AE33-NEPH}$ optimal solution algorithm

The Root Mean Square Error (RMSE) of the difference between the aerosol scattering and absorption coefficients measured by the Nephelometer ($Scat_{NEPH}$) and AE33 (Abs_{AE33}), and the scattering ($Scat_{NSD}$) and absorption (Abs_{NSD}) calculated using Mie theory for the combined size distribution of SMSP and OPC up to 1,000 nm (NSD) is produced according to equation 1:

$$\text{RMSE} = \left([Scat_{NEPH} - Scat_{NSD}]^2 + [Abs_{AE33} - Abs_{NSD}]^2 \right)^{0.5} \quad (4.1)$$

The $RI_{AE33-NEPH}$ optimal solution is obtained when we acquire the minimum RMSE in a fiting procedure where the aerosol refractive index is the independent variable. The resulting complex refractive index may be used to calculate the absorption and scattering coefficients at specific angles (i.e. backscattering), keeping in mind that we refer to spherical particles, as we use Mie code.

4.1.3 Truncation error correction and calculation of the scattering coefficient for ambient conditions

The Nephelometer measurements are corrected for truncation errors following [63], while the scattering Ångström exponent is used to adjust the scattering coefficient to 660 nm. In order to calculate the ambient scattering coefficient so as to compare to EOLE lidar extinction coefficient, the aerosol hygroscopic exponent γ was used [24]. The ambient RH is computed using the microwave radiometer measurements. The ambient aerosol scattering coefficient $\sigma_{scat,amb}$, at RH_{amb} is determined as

$$\sigma_{scat,amb} = \sigma_{scat,dry} \left(\frac{100 - RH_{dry}}{100 - RH_{amb}} \right)^{\gamma} \tag{4.2}$$

4.1.4 Refractive index in ambient conditions

The aerosol ERI_{COR} and $RI_{AE33-NEPH}$ were adjusted to ambient conditions, using the hygroscopicity κ acquired by the HTDMA measurements for a dry particle electrical mobility diameter equal to 250 nm. The aerosol density was computed following [28] using Equation 3:

$$\rho^{-1} = \sum_{i} \frac{X_i}{\rho_i} \tag{4.3}$$

where X_i is the mass fraction for species i and ρ_i is the individual species density (gcm^{-3}). Species 1 refers to the dry aerosol size distribution up to 1,000 nm with a refractive index equal to ERI_{COR} or $RI_{AE33-NEPH}$ and a density equal to 1.48 gcm^{-3} [25]. Species 2 refers to water. Refractive index can be computed by different mixing rules, 2 of which are partial molar refraction [83] and volume-weighted method [28].

The volume-weighted method was used (Equation 4) to calculate mean refractive index ($m = m_r - k_i$).

$$m = \rho \sum_i \frac{X_i m_{r,i}}{\rho_i} - \rho \sum_i \frac{X_i k_i}{\rho_i} i \tag{4.4}$$

where m_r is the real part of a complex refractive index for species i and k_i is the imaginary part.

4.1.5 Flexible Particle Dispersion Model (FLEXPART)

The Flexible Particle Dispersion Model (FLEXPART) was used to find the possible aerosol source areas of the measured atmospheric volume. To do this, FLEXPART simulates the backward trajectories of a large number of air parcels and estimates their residence time over each geographic grid cell (sensitivity) [85, 84]. These residence times indicate how sensitive the measurements at a station are to emissions occurring at each geographic grid cell. FLEXPART runs account for grid scale wind as well as for turbulent and mesoscale wind fluctuations. Drift correction, to prevent accumulation of the released computational particles, and density correction, to account for the decrease of air density with height, were both applied. Seven-day backward runs with the release of 4×10^4 air parcels every 3 hours beginning from DEM station were produced. Residence times in each grid cell, for a height from 0 to 100 m agl, were acquired.

4.1.6 Aerosol mineral dust concentration estimation based on XRF measurements

The estimation is based on XRF measurements and following [65]:

$$\text{Mineral Dust} = 1.35\ Na + 1.66\ Mg + 1.89 Al + 2.14\ Si + 1.21\ K + 1.40\ Ca + 1.67\ Ti + 1.43\ Fe \tag{4.5}$$

Some corrections were however applied to take into account sea-salt contributions to Na and Mg, and possible anthropogenic contributions to the other elements. The sea salt fractions of Na and Mg were calculated using the measured Cl concentration and the Na/Cl and Mg/Cl ratios 0.56 and 0.07, respectively. Due to possible Cl losses in aerosol samples, this approach may overestimate the non-sea salt component of Na (nss_{Na}) and Mg (nss_{Mg}).

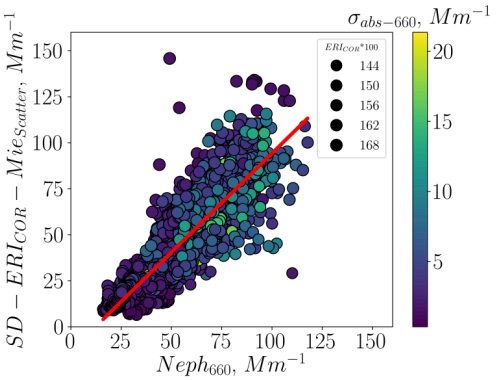

Figure 4.2: Comparison of the dry scattering coefficient $\sigma_{scat,dry}$ obtained by Mie code calculation using ERI_{COR}, for sizes up to 1,000 nm (electrical mobility diameter), and the dry scattering coefficient obtained by Ecotech Nephelometer adjusted to 660 nm wavelength, corresponding to OPC. The color of the marker corresponds to the absorption coefficient measured by AE33, normalized between 0 and 100. The minimum value of the AE33 absorption depicted is 0.3 Mm^{-1} and the maximum value is 16 Mm^{-1}. The area of each marker corresponds to ERI_{COR}, normalized between 0 and 100. The maximum value of ERI_{COR} depicted is 1.7 and the minimum is 1.43. The red line depicts the relation of $SD - ERI_{COR} - Mie_{Scatter}$ = 1.07 * $Neph_{660}$-13 Mm^{-1}, which is the best linear fit obtained, with a coefficient of determination (R^2) equal to 0.72.

4.2 Results and Discussion

4.2.1 Comparison of Nephelometer to ERI calculated total scattering coefficient

In Figure 4.2 we present the comparison of the scattering coefficient measured by Ecotech Nephelometer (adjusted to 660 nm wavelength, $Neph_{660}$) to the scattering coefficient ($SD - ERI_{COR} - Mie_{Scatter}$) obtained by the application of Mie code on the unified aerosol size distribution (SD) of the instruments SMPS and OPC acquired in the process of defining ERI_{COR} [99]. The refractive index used was ERI_{COR}. If we apply a linear fit, $SD - ERI_{COR} - Mie_{Scatter}$ equals 1.07 * $Neph_{660}$-13 Mm^{-1} with a coefficient of determination (R^2) equal to 0.72. $SD - ERI_{COR} - Mie_{Scatter}$ values are almost the same to those of the dry Nephelometer scattering coefficient, and there is a reasonably good agreement between the two quantities. This is an indication that the portion of the size

distribution up to 1,000 nm can be used in order to compare optical properties of aerosols from in situ and remote sensing instruments. Keeping in mind the uncertainties in the size distribution measurements of SMPS, OPC and the uncertainty of ERI_{COR}, we expect the uncertainty in the estimation of $SD-ERI_{COR}-Mie_{Scatter}$ to be within 20%. In Figure 4.2, $SD-ERI_{COR}-Mie_{Scatter}$ values below the red fitting line correspond to lower ERI_{COR} values and higher absorption coefficient values measured by AE33 ($AE33_{abs-660}$) as indicated by the color and area of the markers. Higher ERI_{COR} values and low $AE33_{abs-660}$ values correspond to very high $SD - ERI_{COR} - Mie_{Scatter}$ values, in relation to the red line.

4.2.2 Comparison of EOLE lidar to Nephelometer and Aethalometer total ambient extinction coefficient

In order to compare in situ and remote sensing instruments, we calculated the average EOLE extinction coefficients at 355 and 532 nm for a height from 1,200 m asl to 1,300 m asl for days selected based on dissipation rate ϵ. For these days ϵ exhibited values higher than 10^{-4} for a height extending from 15 to 1,000 m agl. The comparison days included the 21^{st} of May 20:00 to 21:00, 22^{nd} of May 20:30 to 21:30, 23^{rd} of May 20:30 to 21:30, 7^{th} of June 22:00 to 23:00 and 10^{th} of June 18:45 to 19:45. Then, we deduced the EOLE extinction Ångström exponent and calculated the EOLE extinction coefficient at the wavelength of 660 nm. The in situ ambient scattering coefficient was calculated using the Nephelometer measurements, equation 2 and a γ factor equal to 0.57, corresponding to polluted marine aerosol [24]. We consider this γ factor suitable for the selected days that display high turbulence in the atmosphere, as the AMA has in general a high impact from anthropogenic activities (vehicle emissions, cooking, shipping) and it is also frequently under the influence of the sea breeze [25]. We assumed that the absorption coefficient, measured by the AE33, did not change due to hygroscopic growth of particles. This assumption is plausible, as the scattering is the dominant part of the extinction (the minimum single scattering albedo for the selected days is 0.94). We excluded days that we identified dust in the SD during the HygrA-CD campaign, by calculating the single scattering albedo exponent a_{SSA} using Nephelometer and Aethalometer data and the origin of airmasses calculated by FLEXPART (included in Appendix, Figures A.62-A.66). During

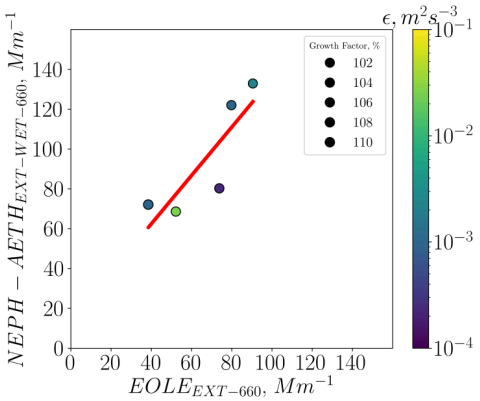

Figure 4.3: Comparison of the ambient extinction coefficient from Nephelometer and Aethalometer for ambient conditions, and the extinction coefficient obtained by EOLE for a height up to 1,300 m asl (DEM station is at 270 m asl). Both scattering coefficients were adjusted to the wavelength of 660 nm. The size of the marker corresponds to the growth factor measured by the HTDMA (range: 1.004-1.21) and the color of the markers corresponds to the average ϵ value for a height extending from 15 to 1,000 m agl (range: 8×10^{-4} - 2.5×10^{-1}). The red line depicts the relation of $NEPH - AETH_{EXT-WET-660} = 1.21 * EOLE_{EXT-660}$+13.8 Mm^{-1}, which is the best linear fit obtained, with a coefficient of determination (R^2) equal to 0.74.

Saharan dust events, a_{SSA} becomes clearly negative with values usually falling between -0.1 and -0.5, according to [16].

We observe in Figure 4.3 that there is good agreement between the extinction coefficient from in situ instruments to the EOLE lidar extinction coefficient for selected days that exhibit turbulence to heights above 1,000 m agl. The vertical distribution plots of the ϵ values for these selected days are presented as Appendix (Figures A46 - A50, depicting 21-23 of May, 7 and 10 of June). $NEPH - AETH_{EXT-WET-660}$ and $EOLE_{EXT-660}$ are well correlated (R^2 equal to 0.74 for the linear fit $NEPH - AETH_{EXT-WET-660} = 1.21 * EOLE_{EXT-660}$+13.8 Mm^{-1}). The RH during the lidar measurements in Figures A51 - A55 (Appendix) at a height of 1000 m agl ranged from 55% to 75%. We observe that the growth factor has little effect on the correlation of $NEPH - AETH_{EXT-WET-660}$ and $EOLE_{EXT-660}$ for the measurements presented in Figure 4.3. The data point with the highest ϵ value is at the center of the variance, indicating that the main

Table 4.1: $EOLE_{EXT-660}$ and $NEPH - AETH_{EXT-WET-660}$ values for the selected days.

Date, Time (UTC)	$EOLE_{EXT-660}$, Mm^{-1}	$NEPH - AETH_{EXT-WET-660}$, Mm^{-1}
21^{st} of May 2014, 20:00-21:00	52.2	68.6
22^{nd} of May 2014, 20:30-21:30	79.8	122
23^{rd} of May 2014, 20:30-21:30	73.8	80.2
7^{th} of June 2014, 22:00-23:00	38.5	72
10^{th} of June 2014, 18:45-19:45	90.5	132.9

mechanism that influences the $NEPH - AETH_{EXT-WET-660}$ and $EOLE_{EXT-660}$ correlation is the state of mixing in the vertical, while the growth factor impact appears to be insignificant. The backscatter EOLE lidar measurements at the wavelength of 1064 nm are presented as Appendix (Figures A56 - A60). These vertical distribution plots indicate that the aerosol concentration during the comparison hours is almost uniform from ground level up to approximately 1,000 m agl, probably due to high turbulence in the atmosphere. The extinction values for the $EOLE_{EXT-660}$ and $NEPH - AETH_{EXT-WET-660}$ are also presented in Table 4.1:

4.2.3 Comparison of EOLE lidar and $RI_{AE33-NEPH}$ calculated extinction coefficients

In Figure 4.4 there is good agreement between $NEPH-AETH_{RI-EXT-WET-660}$ and $EOLE_{EXT-660}$ (R^2 is equal to 0.62, $NEPH - AETH_{RI-EXT-WET-660} = 0.64 * EOLE_{EXT-660}+7.6\ Mm^{-1}$) for selected days that exhibit turbulence to heights up to 1,000 m agl. We have to keep in mind that during the deduction of $RI_{AE33-NEPH}$ the size distribution (SD) up to 1,000 nm dry diameter was

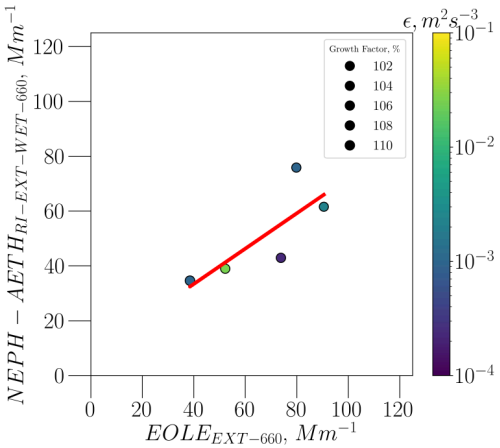

Figure 4.4: Comparison of the ambient extinction coefficient obtained by Mie code calculation using $RI_{AE33-NEPH}$ retrieved from Nephelometer and Aethalometer for ambient conditions, for sizes up to 1,000 nm, and the extinction coefficient obtained from EOLE for a height up to 1,300 m asl. Both extinction coefficients were adjusted to the wavelength of 660 nm. The size of the marker corresponds to the growth factor measured by the HTDMA (range: 1.004-1.21) and the color of the markers corresponds to the average ϵ value for a height extending from 15 to 1,000 m agl (range: 8×10^{-4} - 2.5×10^{-1}). The red line depicts the relation of $NEPH - AETH_{RI-EXT-WET-660}$ = 0.64 * $EOLE_{EXT-660}$+7.6 Mm^{-1} which is the best linear fit obtained, with a coefficient of determination (R^2) equal to 0.62.

Table 4.2: $EOLE_{EXT-660}$ and $NEPH - AETH_{RI-EXT-WET-660}$ values for the selected days.

Date, Time (UTC)	$EOLE_{EXT-660}$, Mm^{-1}	$NEPH - AETH_{RI-EXT-WET-660}$, Mm^{-1}
21^{st} of May 2014, 20:00-21:00	52.2	39
22^{nd} of May 2014, 20:30-21:30	79.8	75.8
23^{rd} of May 2014, 20:30-21:30	73.8	42.9
7^{th} of June 2014, 22:00-23:00	38.5	34.6
10^{th} of June 2014, 18:45-19:45	90.5	61.6

used, leading to possible errors related to larger sizes of particles that were not included. We observe that the growth factor has little effect on the correlation of $NEPH - AETH_{RI-EXT-WET-660}$ and $EOLE_{EXT-660}$ for the measurements presented in Figure 4.4. The data point with the highest ϵ value is at the center of the variance, indicating that the main mechanism that influences the $NEPH - AETH_{RI-EXT-WET-660}$ and $EOLE_{EXT-660}$ correlation is the state of mixing in the vertical, while the growth factor impact appears to be insignificant. The extinction values for the $EOLE_{EXT-660}$ and $NEPH - AETH_{RI-EXT-WET-660}$ are also presented in Table 4.2:

4.2.4 Comparison of EOLE lidar extinction coefficient to ERI_{COR} calculated ambient scattering coefficient

In Figure 5 we observe that there is reasonable agreement between the ERI_{COR} calculated ambient scattering coefficient to the EOLE lidar extinction coefficient for selected days that exhibit turbulence to heights above 1,000 m agl (R^2 is equal to 0.45). We have to keep in mind that the absorption coefficient cannot be calculated, as ERI_{COR} corresponds to the real part of the aerosol refractive

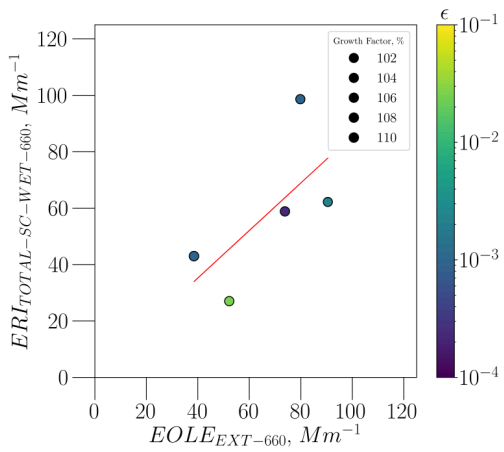

Figure 4.5: Comparison of the ambient scattering coefficient obtained by Mie code calculation using ERI_{COR} for ambient conditions, for sizes up to 1,000 nm, and the extinction coefficient obtained from EOLE. Both coefficients were adjusted to the wavelength of 660 nm. The size of the marker corresponds to the growth factor measured by the HTDMA (range: 1.004-1.21) and the color of the markers corresponds to the average ϵ value for a height extending from 15 to 1,000 m agl (range: 8×10^{-4} - 2.5×10^{-1}). The red line depicts the relation of $ERI_{TOTAL-SC-WET-660}$ = 0.84 * $EOLE_{EXT-660}$+1.5 Mm^{-1} which is the best linear fit obtained, with a coefficient of determination (R^2) equal to 0.45.

Table 4.3: $EOLE_{EXT-660}$ and $ERI_{TOTAL-SC-WET-660}$ values for the selected days.

Date, Time (UTC)	$EOLE_{EXT-660}$, Mm^{-1}	$ERI_{TOTAL-SC-WET-660}$, Mm^{-1}
21^{st} of May 2014, 20:00-21:00	52.2	27
22^{nd} of May 2014, 20:30-21:30	79.8	98.6
23^{rd} of May 2014, 20:30-21:30	73.8	58.8
7^{th} of June 2014, 22:00-23:00	38.5	43
10^{th} of June 2014, 18:45-19:45	90.5	62.2

index. There is also the problem with the use of the SD up to 1,000 nm mentioned in section 3.3. Neither growth factor or ϵ appear to have a significant impact on the correlation between $ERI_{TOTAL-SC-WET-660}$ and $EOLE_{EXT-660}$. Nevertheless, as indicated in Figure 6, ERI_{COR}, which is calculated based on the size distributions of SMPS and OPC, provides a useful insight into the optical properties of aerosols in the atmosphere not only at ground level but also at higher altitudes.

The extinction values for the $EOLE_{EXT-660}$ and the scattering values for $ERI_{TOTAL-SC-WET-660}$ are also presented in Table 4.3:

4.2.5 Comparison of EOLE lidar to Nephelometer and Aethalometer extinction Ångström exponent

In Figure 6 we compare the extinction Ångström exponent from EOLE lidar and in situ measurements. The comparison is not good, as the R^2 is equal to 0.4. We have to keep in mind that the EOLE extinction Ångström exponent is calculated based on measurements at 355, 532 nm, while the

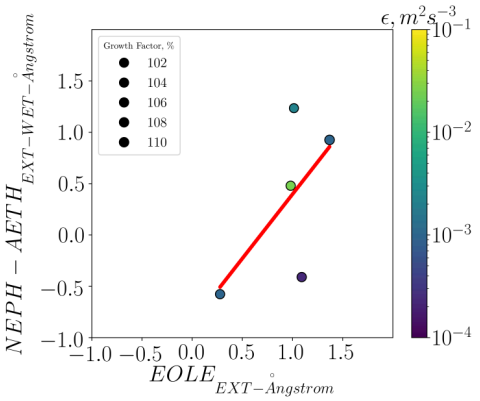

Figure 4.6: Comparison of the Ångström exponent obtained from EOLE for the height 1,200 m to 1,300 m asl to the one acquired by in situ Nephelometer-Aethalometer measurements. The size of the marker corresponds to the growth factor measured by the HTDMA (range: 1.004-1.21) and the color of the markers corresponds to the average ϵ value for a height extending from 15 to 1,000 m agl (range: 8×10^{-4} - 2.5×10^{-1}). The red line depicts the relation of $NEPH - AETH_{EXT-WET-\text{Ångström}} = 1.25 * EOLE_{EXT-\text{Ångström}}$-0.86, which is the best linear fit obtained, with a coefficient of determination (R^2) equal to 0.4.

in situ extinction Ångström exponent is calculated based on 470, 660 nm wavelength. These differences in the extinction Ångström exponent indicate that the size distribution at ground level and at a height between 1,200 and 1,300 m asl are different, even though we adjusted the in situ size distribution up to 1,000 nm considering its hygroscopic growth. The Ångström exponent discrepancies may be attributed to particles with aerodynamic diameter larger than 10 μm that could be present in the atmosphere but not sampled by the in situ instruments due to their PM_{10} inlet heads. We observe that the growth factor has little effect on the correlation of $NEPH - AETH_{EXT-WET-\text{Ångström}}$ and $EOLE_{EXT-\text{Ångström}}$ for the measurements presented in Figure 6. The data point with the highest ϵ value is at the center of the variance, indicating that the main mechanism that influences the $NEPH - AETH_{EXT-WET-660}$ and $EOLE_{EXT-660}$ correlation is the state of mixing in the vertical.

The values for the $EOLE_{EXT-\text{Ångström}}$ and $NEPH - AETH_{EXT-WET-\text{Ångström}}$ are also presented in Table 4.4:

Table 4.4: $EOLE_{EXT-\text{Ångström}}$ and $NEPH - AETH_{EXT-WET-\text{Ångström}}$ values for the selected days.

Date, Time (UTC)	$EOLE_{EXT}$ Ångström	$NEPH - AETH_{EXT-WET}$ Ångström
21^{st} of May 2014, 20:00-21:00	0.98	0.48
22^{nd} of May 2014, 20:30-21:30	0.28	-0.58
23^{rd} of May 2014, 20:30-21:30	1.09	-0.41
7^{th} of June 2014, 22:00-23:00	1.37	0.92
10^{th} of June 2014, 18:45-19:45	1.01	1.23

4.2.6 Mixing of local and regional aerosol on the 27^{th} of May 2014

The $PM_{2.5}$ concentration of mineral dust on a 24-h filter at DEM station on the 27^{th} of May was 3.5 $\mu g m^{-3}$. The estimation is based on XRF measurements and equation 4.5.

In Figure 4.7a (EOLE range-corrected signal (A.U.) at 1064 nm), a Saharan dust layer is present above 1,500 m asl (06:00-09:00 UTC) and a local pollution layer is present at lower altitudes. At 12:00 UTC (due to turbulence in the atmosphere as indicated in Figure 4.8a), the two layers are mixing. In the afternoon, a well mixed layer (local pollution and Saharan dust) is present up to 2,000 asl (Figure 4.7a). This is also indicated in Figure 4.7c, where the Ångström exponent for the averaged period 11:30-12:30 UTC and for the height between 1,800 and 2,500 m agl is below 1, while for the averaged period 19:30-20:30 UTC the Saharan dust layer has descended to heights below 1,000 m asl, as the Ångström exponent $AE_{b-355/532}$ is above 1 for all altitudes depicted. Figure 4.8a displays the ϵ values on the 27^{th} of May. From 09:00 UTC until almost the end of the day, there is turbulence in the atmosphere up to the height of 1,000 m agl. In Figure 4.8b, after 12:00, the aerosol

scattering coefficient values measured at ground level (wavelength of 470 and 660 nm) are getting very close to each other (Ångström exponent is decreasing, an indication of Saharan dust, [16]) and finally at 18:00, the Saharan dust layer is at ground level, as the scattering coefficient at 660 nm is higher than that at 470 nm. Figure 4.8c demonstrates that air masses reaching DEM station have a significant residence time in a height up to 100 m agl (very close to the ground) in North Africa. As indicated by the residence time color plot, the air masses from North Africa are partly lifted to altitudes higher than 100 m agl and subsequently they move downwards to DEM station, depositing Saharan dust. Figure A61 (Appendix) presents a radiosonde measurement at 12:00 UTC. It demonstrates a region of low RH, which is consistent with a Saharan dust layer, mainly between 1,000 and 2,000 m agl.

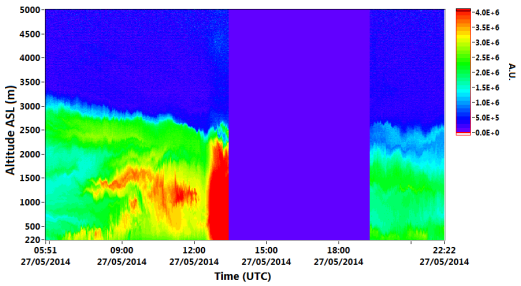

(a) Temporal evolution of the range-corrected lidar signal (RCS) at 1064 nm observed by EOLE, in arbitrary units (A.U.)

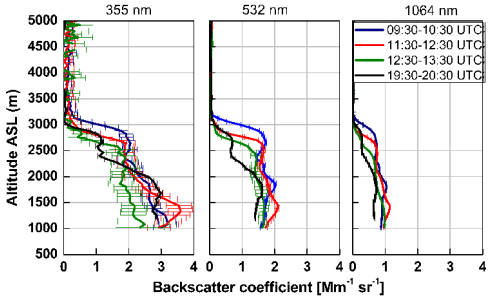

(b) EOLE backscatter lidar signals at 355, 532 and 1064 nm.

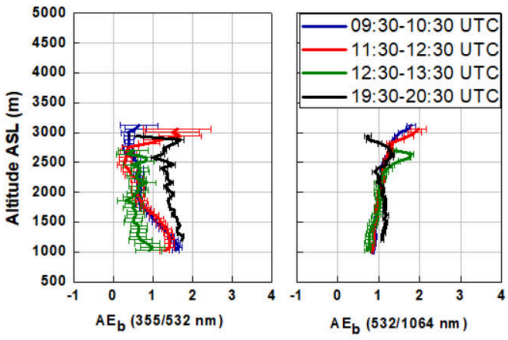

(c) EOLE Ångström exponent.

Figure 4.7: Subfigure a: Temporal evolution of the range-corrected lidar signal (RCS) at 1064 nm observed by EOLE, in arbitrary units (A.U.). Until 09:00 UTC a Saharan dust layer is present above 1,500 m asl and a local pollution layer at ground level. At 12:00, due to strong turbulence up to 1,000 m, the two layers are mixing. In the afternoon, a well mixed layer up to 2,000 asl has developed. This is also demonstrated in subfigure c, where the Ångström exponent at 11:30 to 12:30 indicates that a Saharan dust layer is present at 1,800 to 2,500 m asl (Ångström below 1), but at 19:30 to 20:30 the Saharan dust layer is missing, indicating that it has descended to lower altitudes. Subfigure b: EOLE backscatter lidar signals at 355, 532 and 1064 nm. Subfigure c: EOLE Ångström exponent.

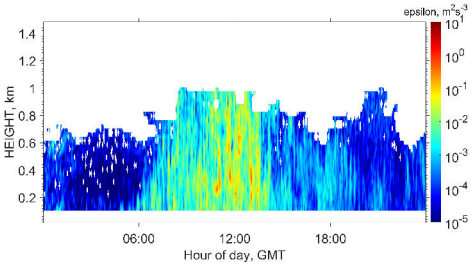

(a) ϵ vertical distribution.

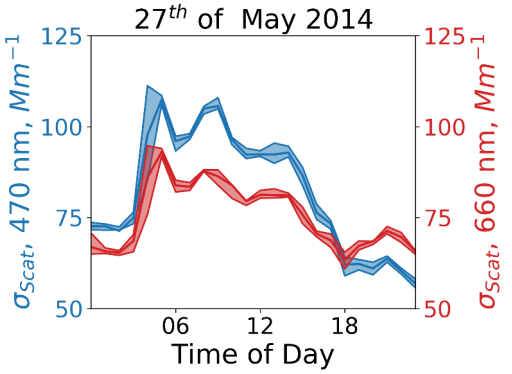

(b) Nephelometer scattering coefficient, 470-660 nm.

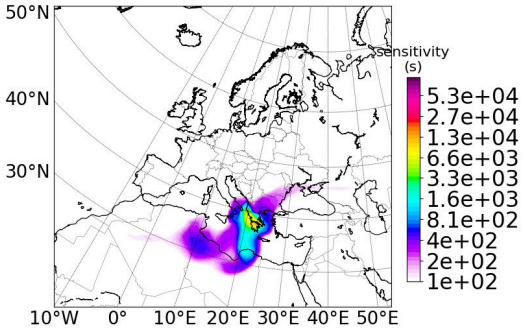

(c) Air mass origin from a height up to 100 m agl.

Figure 4.8: Subfigure (a) displays the ϵ values during the 27^{th} of May. From 09:00 UTC until almost the end of the day, there is turbulence in the atmosphere up to the height of 1,000 m agl. Subfigure b: After 12:00, the aerosol scattering coefficient values measured at ground level (470 and 660 nm) are getting very close (Ångström exponent is decreasing, an indication of Saharan dust) and finally at 18:00, the Saharan dust layer is at ground level dominating particle concentration, as the scattering coefficient at 660 nm is higher than that at 470 nm. Subfigure (c) indicates that air masses with significant residence time over North Africa from a height up to 100 m agl reach DEM station on the 27^{th} of May at 18:00-21:00.

Chapter 5

Conclusions and perspectives

In the context of this Ph.D thesis in Chapter "Particle number size distribution statistics at City-Centre Urban Background, Urban Background, and Remote stations in Greece during summer" the particle number concentration in the Eastern Mediterranean during the Etesian flow, in City-Centre Urban Background, Urban Background and Regional Background stations using high time resolution instrumentation was studied. The peak concentration at the City-Centre Urban Background station is approximately at 60 nm, while at the Urban and Regional Background stations is at approximately 100 nm. The highest particle number concentration values were observed at the City-Centre Urban Background station (Patras-C). Also, the median particle number concentration for the size fraction N_{20-50} is higher than the corresponding concentration for the size fraction N_{50-100}, indicating a domination of freshly emitted road traffic exhaust. This is not the case for the Regional Background and the Urban Background stations, where the median particle number concentration for the fraction N_{50-100} is higher than in the fraction N_{20-50}. As shown in Table 2.2, the Regional Background station median concentrations for the size ranges N_{10-20}, N_{20-50}, N_{50-100}, $N_{100-200}$, $N_{200-500}$, N_{tot}, are the 5%, 16%, 45%, 63%, 99% and 36% of the respective median concentrations of the City-Centre Urban Background station. The remainder percentages may be attributed to traffic, cooking, condensational growth of locally produced particles, and other local activities. Compared to the Urban Background stations, the Regional Background station median concentrations correspond to the 17%, 55%, 97%, 91%, 79% and 77% of the respective mean of the Urban Background

stations. The remainder percentages may be attributed to traffic (aged and fresh), cooking, other local activities, condensational growth of locally produced particles and NPF.

By combining these estimations and diurnal variation of the size fractions in Figure 2.4, we conclude that the fractions that are similar in number mean concentration and diurnal variation at all station types are $N_{100-200}$ and $N_{200-500}$. The median values of the fraction N_{50-100} at the Regional Background station and the Urban Background stations have similar values but their diurnal patterns are dissimilar. While at the Urban Background stations this fraction appears to be related to traffic, there is no such relation at the Regional Background station. Assuming that these fractions ($N_{100-200}$, $N_{200-500}$) measured at the Regional Background station constitute the regional background concentration, we conclude that the transported part of the median particle number concentrations for the City-Centre Urban Background station is 13%, for the Urban Background stations 29%, and for the Regional Background station 45%. Other fractions should mainly be attributed to NPF, freshly emitted traffic exhaust, aged traffic, cooking, and other local sources. This estimation is based on empirically divided particle size fractions.

Based on the diurnal variations and previous studies, main sources for the City-Centre Urban Background station that were identified are traffic (freshly emitted and aged, corresponding to size fractions N_{10-20}, N_{20-50}, N_{50-100}) and the regional background concentration estimated earlier. $N_{100-200}$ has a much higher concentration at the City-Centre Urban Background station than at the Urban Background and the Regional Background stations, but it is also stable throughout the day, which indicates that the difference stems from the accumulation of particles in smaller size fractions taking place at the City-Centre Urban Background station area. Sources for the Urban Background stations include fresh traffic and nucleation (N_{10-20}, N_{20-50}), aged traffic and cooking (N_{50-100}) and the regional background concentration estimated earlier. The Regional Background station dominant sources are local aged sources (cooking and other sources related to tourism) and regional background concentration.

When we compare the diurnal variation (Figure A.4, Appendix) of the three Urban Background stations, we observe that DEM station has a higher background number concentration in the size ranges N_{10-20}, N_{20-50}. We have to keep in mind that this station is relatively close to the center of

Athens, and therefore it is probably influenced by fresh traffic related particles in a higher extend than the two other stations. ICE-HT is influenced mainly by early morning traffic, probably transported from Patras city center.

It should be noted that the Urban Background sites number fractions are very similar to the K-Puszta station (representative of the Central-Eastern European regional conditions). This could be partly attributed to the Etesians, as they transport aerosol and precursor gases from Eastern and Central Europe. The long range transported aerosol (N_{100}) at the Regional Background station has higher values than the corresponding aerosol at Harwell station (a rural station representative of large scale air masses affecting Southern England).

New Particle Formation events were identified at DEM station, where the newly formed particles account for 4% of the total particle concentration in the size fraction N_{10-20} during the measurement period, EPT, where they account for the 12%, and FIN, where they account for 1%, respectively. NPF events contribution to summer Condensation Cloud Nuclei (CCN) and in other words climate in South-Eastern Europe appears to be insignificant in this and previous studies mentioned earlier. 1 NPF event occurred the same day at EPT-FIN and 1 at EPT-DEM stations, indicating that conditions favorable for nucleation at a large geographic area may exist, but events may or may not occur, depending on local sources and sinks at each station.

The size distribution modal analysis results were subsequently divided in clusters. The daily frequency of occurrence and particle number concentration for each cluster were identified. Based on diurnal variation of frequency of occurrence and number concentration, we identified that at the City-Centre Urban Background station the source that dominates is related to traffic (CCUB-SD-Cluster3). At the Urban Background we can identify in UB-SD-Cluster1 fresh traffic and NPF, in UB-SD-Cluster2 the regional background concentration and the condensational growth of locally produced particles, while in UB-SD-Cluster3 we identify the aged traffic with a broad σ_g. UB-SD-Cluster4 is a mixture of fresh and aged traffic exhaust, but it also displays a peak at noon, indicating similarities to the diurnal profile of moderately oxygenated organic aerosol (M-OOA) identified at ICE-HT and DEM stations in earlier studies. At the Regional Background station, number and frequency are dominated by the regional background concentration in accumulation

mode, but there is also a frequent cluster related to aerosol from sources within Crete, like activities related to tourism (cooking included). This is similar to the behavior of the size fractions N_{20-50} and N_{50-100} mentioned earlier for the Regional Background station. If we make the assumption that the accumulation cluster identified at the Regional Background station corresponds to the transported from other areas particle fraction, and use the median number concentration from each cluster, we conclude that 18% of the particle number distribution is transported at the City-Centre Urban Background site, 37% at the Urban Background sites, and 59% at the Regional Background site.

After we cluster the modal analysis results for ICE-HT, DEM, EPT, and make the same assumption regarding the transported from other areas number concentration fraction, 45% of the particle number distribution is transported at the ICE-HT, 22% at DEM, and 55% at EPT.

Based on the air mass origin clustering of the regional background concentration measured at FIN, we concluded that the regional particle number concentrations when air masses originate from the Mediterranean Sea is much lower than when they originate from the North-East and North-West direction. Etesian flow conditions were found to increase the regional background particle concentration in the Mediterranean basin by a factor of 2.5 to 4.

In order to have a better assessment of the NPF impact on Condensation Cloud Nuclei, further work should include measurements with SMPS systems that can measure particles with sizes below 10 nm.

In Chapter "Development of a new method to retrieve the real part of the Equivalent Refractive Index of atmospheric aerosol" a new method in order to acquire the real part of the aerosol Refractive Index was proposed. As indicated in Figure 3.3, the ERI_{COR} is influenced strongly by dust light scattering and absorption, in the size range that ERI_{COR} is defined (accumulation mode). During Sahara dust events, ERI_{COR} values approach values as high as 1.7.

As the sulfur per organic carbon ratio increases, ERI_{COR} increases, but the correlation is weak. Their relation could not be easily attributed to these two constituents alone, as high dust mass fraction values could influence ERI_{COR}, as we see in Figure 3.4.

ERI_{COR} overestimates RI in relation to RI_{IC}. Nevertheless, correlation between the estimated values from the two methods is very good. Higher dust mass fraction leads to higher ERI_{COR}.

ERI_{COR} relation to RI_{LI} is more complex. RI_{LI} values were obtained at a height between 1 to 1.2 km. There was good mixing in the vertical during chosen days, therefore a good correlation between ERI_{COR} and RI_{LI} is expected (Figures A.41-A.45, Appendix). There is also the RH difference problem between the station measurements and those made by the lidar, that increases the discrepancies. Nevertheless, the main difference should be attributed to the state of mixing in the vertical, as indicated in Figure 3.6.

Overall, the SMPS-OPC system is considered a valuable method so as to estimate real part of RI for ambient aerosol. This is supported by the chemical composition RI (RI_{IC}) and RI_{LI} when there is good mixing in the atmosphere. Considering that many stations have long series of SMPS and OPC data, deriving ERI_{COR} could provide valuable information on aerosol properties.

Further work on the subject should include acquiring detailed aerosol composition of PM1, in order to estimate RI in a size range corresponding to ERI_{COR}. The imaginary part of the ERI_{COR} should be estimated along with the real part, based on SMPS, OPC, EC/OC, and AE33 measurements. A model to estimate the imaginary part and the real part of RI could be derived, based on the measurements from the above mentioned instruments.

In Chapter "Comparison of in situ and remote sensing aerosol measurements in the Athens Metropolitan Area" the main aim, in addition to reporting the aerosol measurements conducted, is to find the atmospheric conditions that allow the direct comparison of in situ and remote sensing measurements. This is a very important point as it will allow collocating in situ and remote sensing aerosol measurement stations to combine their measurements, so as to investigate the vertical mixing of aerosols and acquire a profile of aerosol properties extending from ground level to several km above ground level (agl). Thus, we will obtain an insight on how regional aerosol is added to local aerosol, especially during pollution events due to long range transport (Saharan dust, Biomass Burning, etc.).

Within the systematic uncertainties associated with each instrument described, comparison between in situ and remote sensing instruments is possible for collocating in situ and remote sensing stations, even when the sampled volume is not the same (in situ measurements take place at ground level, while lidar measurement volume is at a height of several hundred meters agl). The main

condition for this comparison to be valid is the existence of high turbulence in the atmosphere up to a height of at least 800 m agl. There are of course discrepancies associated with the in situ instruments inlets (aerosol particles with aerodynamic diameter above 10 μm are not sampled), but there is also high uncertainty in the measurement of particles with optical diameter above 1 μm measured by OPCs. Errors in the measurement of RH in the atmosphere and hygroscopicity κ applied to all particle sizes (estimated based on a dry particle size of 250 nm electrical mobility diameter), could lead to erroneous hygroscopic growth factors and therefore distorted size distributions on which Mie code is applied in order to obtain in situ optical properties.

In Figure 4.2 we observe that there is good agreement between dry Nephelometer scattering coefficient and ERI_{COR} calculated scattering coefficient for the size distribution acquired by SMPS and OPC up to a size of 1,000 nm (electrical mobility diameter). This indicated that this size distribution fraction is a good choice so as to calculate, using Mie code, the optical properties of the aerosol volume sampled by in situ instruments.

In Figure 4.3 the Nephelometer and Aethalometer calculated total ambient extinction coefficient is compared to EOLE extinction coefficient. Good agreement is observed between the two quantities, indicating that Nephelometer and Aethalometer can provide aerosol optical properties representative of the MH volume.

In Figure 4.4 we present the comparison of EOLE lidar to $RI_{AE33-NEPH}$ calculated extinction coefficient. $RI_{AE33-NEPH}$ is the refractive index acquired by fitting the Mie code solution for the combined size distribution of SMPS and OPC up to 1,000 nm to the Nephelometer and Aethalometer scattering and absorption coefficients. The obtained refractive index is then adjusted to ambient conditions. The results indicate good agreement between in situ and remote sensing instruments.

In Figure 4.5 we compared the EOLE lidar extinction coefficient to ERI_{COR} calculated ambient scattering coefficient. The results were not in good agreement, but we have to keep in mind that ERI_{COR} corresponds to the real part of the refractive index and we can not calculate the absorption coefficient. Still, we have a useful result for days with high turbulence in the atmosphere, even for higher altitudes.

In Figure 4.6, the Nephelometer and Aethalometer calculated extinction Ångström exponent is

compared to the one calculated for EOLE lidar. The agreement is not good and this probably displays that the size distributions measured by in situ and remote sensing instruments have differences that lead to different Ångström exponents. This could be partly attributed to particles with aerodynamic diameter larger than 10 μm present in the atmosphere but not sampled by the in situ instruments due to their PM_{10} inlet heads. We should also keep in mind that the uncertainty in the EOLE extinction Ångström exponent measurement is 25%.

The mixing of local and regional aerosol is presented in Figures 4.7 and 4.8, demonstrating the results that can be obtained by the synergy of in situ and remote sensing instruments. A Saharan dust layer, observed by EOLE lidar at an altitude of 2,000 m agl, reaches the ground level due to high turbulence in the atmosphere and dominates the aerosol measured at DEM station as indicated by Figure 4.8b. Thus, we obtained an insight on how regional aerosol is added to local aerosol, especially during pollution events due to long range transport.

Further work on the subject should include the comparison of high altitude in situ station measurements to remote sensing instrument measurements placed at a lower altitude (all instruments measuring the same air volume). We will compare the extinction and backscattering coefficients acquired by remote sensing instruments to the extinction and scattering coefficients acquired by in situ instruments. We will also compare the shape factor acquired by in situ instruments to the polarization acquired by lidar measurements. Thus we will be able to study in more detail aerosol physico-chemical properties, aerosol-cloud interactions, cloud micro-physics, Condensation Cloud Nuclei formation and the impact of aerosols and clouds on climate change.

Bibliography

[1] F. Amato, A. Alastuey, A. Karanasiou, F. Lucarelli, S. Nava, G. Calzolai, M. Severi, S. Becagli, V. L. Gianelle, C. Colombi, C. Alves, D. Custódio, T. Nunes, M. Cerqueira, C. Pio, K. Eleftheriadis, E. Diapouli, C. Reche, M. C. Minguillón, M.-I. Manousakas, T. Maggos, S. Vratolis, R. M. Harrison, and X. Querol. AIRUSE-LIFE+: a harmonized PM speciation and source apportionment in five southern European cities. *Atmos. Chem. Phys.*, 16:3289–3309, 2016.

[2] V. Amiridis, C. S. Zerefos, S. Kazadzis, E. Gerasopoulos, M. Eleftheratos, M. Vrekoussis, A. Stohl, R. Mamouri, P. Kokkalis, A. Papayannis, K. Eleftheriadis, E. Diapouli, I. Keramitsoglou, C. Kontoes, V. Kotroni, K. Lagouvardos, E. Marinou, E. Giannakaki, E. Kostopoulou, C. Giannakopoulos, A. Richter, J. Burrows, and N. Mihalopoulos. Impact of the 2009 Attica Wild Fires on the Air Quality in Urban Athens. *Atmos. Environ.*, 46:536–544, 2012.

[3] A. Argyrouli. *Study of the planetary boundary layer & its influence on cloud properties.* PhD thesis, School of Applied Mathematics & Physical Sciences, National Technical University of Athens, Sept. 2016.

[4] A. Asmi, A. Wiedensohler, P. Laj, A. M. Fjaeraa, K. Sellegri, W. Birmili, E. Weingartner, U. Baltensperger, V. Zdimal, N. Zikova, J.-P. Putaud, A. Marinoni, P. Tunved, H.-C. Hansson, M. Fiebig, N. Kivekäs, H. Lihavainen, E. Asmi, V. Ulevicius, P. P. Aalto, E. Swietlicki, A. Kristensson, N. Mihalopoulos, N. Kalivitis, I. Kalapov, G. Kiss, G. de Leeuw, B. Henzing, R. M. Harrison, D. Beddows, C. O'Dowd, S. G. Jennings, H. Flentje, K. Weinhold, F. Meinhardt, L. Ries, and M. Kulmala. Number size distributions and seasonality of submicron particles in Europe 2008–2009. *Atmos. Chem. Phys.*, 11:5505–5538, 2011.

[5] E. Athanasopoulou, A. P. Protonotariou, E. Bossioli, A. Dandou, M. Tombrou, J. D. Allan, H. Coe, N. Mihalopoulos, J. A. Kalogiros, A. Bacak, J. Sciare, and G. Biskos. Aerosol chemistry above an extended archipelago of the eastern Mediterranean basin during strong northern winds. *Atmos. Chem. Phys.*, 15:8401–8421, 2015.

[6] R. F. Banks, J. Tiana-Alsina, J. M. Baldasano, F. Rocadenbosch, A. Papayannis, S. Solomos, and C. G. Tzanis. Sensitivity of boundary-layer variables to PBL schemes in the WRF model based on surface meteorological observations, lidar, and radiosondes during the HygrA-CD campaign. *Atmos. Res.*, 176-177(10):185–201, 2016.

[7] D. C. S. Beddows, M. Dall'Osto, and R. M. Harrison. Cluster Analysis of Rural, Urban, and Curbside Atmospheric Particle Size Data. *Environ. Sci. Technol.*, 43:4694–4700, 2009.

[8] D. C. S. Beddows, M. Dall'Osto, R. M. Harrison, M. Kulmala, A. Asmi, A. Wiedensohler, P. Laj, A. M. Fjaeraa, K. Sellegri, W. Birmili, N. Bukowiecki, E. Weingartner, U. Baltensperger, V. Zdimal, N. Zikova, J.-P. Putaud, A. Marinoni, P. Tunved, H.-C. Hansson, M. Fiebig, N. Kivekäs, E. Swietlicki, H. Lihavainen, E. Asmi, V. Ulevicius, P. P. Aalto, N. Mihalopoulos, N. Kalivitis, I. Kalapov, G. Kiss, G. de Leeuw, B. Henzing, C. O'Dowd, S. G. Jennings, H. Flentje, F. Meinhardt, L. Ries, H. A. C. Denier van der Gon, and A. J. H. Visschedijk. Variations in tropospheric submicron particle size distributions across the European continent 2008–2009 . *Atmos. Chem. Phys.*, 14(8):4327–4348, 2014.

[9] S. Bezantakos, K. Barmpounis, M. Giamarelou, E. Bossioli, M. Tombrou, N. Mihalopoulos, K. Eleftheriadis, J. Kalogiros, J. D. Allan, A. Bacak, C. J. Percival, H. Coe, and G. Biskos. Chemical composition and hygroscopic properties of aerosol particles over the Aegean Sea. *Atmos. Chem. Phys.*, 13:11595–11608, 2013.

[10] C. Bohren and D. R. Huffman. *Absorption and Scattering of Light by Small Particles*. Wiley Science Paperback Series, 1998.

[11] A. Bougiatioti, A. Argyrouli, S. Solomos, S. Vratolis, K. Eleftheriadis, A. Papayannis, and A. Nenes. CCN Activity, Variability and Influence on Droplet Formation during the HygrA-Cd Campaign in Athens. *Atmosphere*, 8(108), 2017.

[12] A. Bougiatioti, I. Stavroulas, E. Kostenidou, P. Zarmpas, C. Theodosi, G. Kouvarakis, F. Canonaco, A. S. H. Prévôt, A. Nenes, S. N. Pandis, and N. Mihalopoulos. Processing of biomass - burning aerosol in the eastern Mediterranean during summertime. *Atmospheric Chemistry and Physics*, 14:4793–4807, 2014.

[13] M. Brines, M. Dall'Osto, D. Beddows, R. Harrison, F. Gómez-Moreno, L. Núñez, B. Artíñano, F. Costabile, G. P. Gobbi, F. Salimi, L. Morawska, C. Sioutas, and X. Querol. Traffic and nucleation events as main sources of ultrafine particles in high-insolation developed world cities. *Atmos. Chem. Phys.*, 15:5929–5945, 2015.

[14] N. Bukowiecki, P. Zieger, E. Weingartner, Z. Juranyi, M. Gysel, B. Neininger, B. SCHNEIDER, C. Hueglin, A. Ulrich, A. Wichser, S. Henne, D. Brunner, R. Kaegi, M. Schwikowski, L. Tobler, F. G. Wienhold, I. Engel, B. Buchmann, T. Peter, and U. Baltensperger. Ground-based and airborne in-situ measurements of the Eyjafjallaj okull volcanic aerosol plume in Switzerland in spring 2010. *Atmos. Chem. Phys.*, 11:10011–10030, 2011.

[15] T. Caliński and J. Harabasz. A dendrite method for cluster analysis. *Communications in Statistics - Theory and Methods*, 3(1):1–27, 1974.

[16] M. Coen, E. Weingartner, D. Schaub, C. Hueglin, C. Corrigan, S. Henning, M. Schwikowski, and U. Baltensperger. Saharan dust events at the Jungfraujoch: detection by wavelength dependence of the single scattering albedo and first climatology analysis. *Atmos. Chem. Phys.*, 4:2465–2480, Dec. 2004.

[17] S. Crewell, H. Czekala, U. Lohnert, C. Simmer, T. Rose, and R. Zimmermann. Micro- wave radiometer for cloud cartography: a 22-channel ground-based microwave radi- ometer for atmospheric research. *Radio Sci.*, 36(4):621–638, 2001.

[18] M. Dal Maso, M. Kulmala, I. Riipinen, R. Wagner, T. Hussein, P. P. Aalto, and L. K. E. J. Formation and growth of fresh atmospheric aerosols: eight years of aerosol size distribution data from SMEAR II, Hyytiälä, Finland. *BOREAL ENVIRONMENT RESEARCH*, 10:323–336, 2005.

[19] C. Emmanouil, E. Drositi, V. Vasilatou, E. Diapouli, K. Krikonis, K. Eleftheriadis, and A. Kungolos. Study on particulate matter air pollution, source origin, and human health risk based of PM_{10} metal content in Volos City. *Toxicol. Environ. Chem.*, pages 1–19, 2017.

[20] H. A. Flocas, C. G. Helmis, S. N. Blikas, D. N. Asimakopoulos, J. G. Bartzis, and D. G. Deligiorgi. Mean Characteristics of the Katabatic Flow of a 1024 m High Knife Edge Mountain. *Theor. Appl. Climatol.*, 59:237–249, 1998.

[21] C. Fountoukis and A. Nenes. ISORROPIAII: A computationally efficient thermodynamic equilibrium model for K+-Ca2+-Mg2+-NH4 +-Na+-SO42–NO3 –Cl–H2O aerosols. *Atmos. Chem. Phys.*, 7(17):4639–4659, 2007.

[22] N. A. Fuchs and A. G. Sutugin. *Highly Dispersed Aerosols*. Ann Arbor Science, Ann Arbor, MI, 1970.

[23] S. Fuzzi, U. Baltensperger, K. Carslaw, S. Decesari, H. Denier van der Gon, M. C. Facchini, D. Fowler, I. Koren, B. Langford, U. Lohmann, E. Nemitz, S. Pandis, I. Riipinen, Y. Rudich, M. Schaap, J. G. Slowik, D. V. Spracklen, E. Vignati, M. Wild, M. Williams, and S. Gilardoni. Particulate matter, air quality and climate: lessons learned and future needs. *Atmos. Chem. Phys.*, 15:8217–8299, 2015.

[24] S. Gassó, D. A. Hegg, D. S. Covert, D. Collins, K. J. Noone, E. Öström, B. Schmid, P. B. Russell, J. M. Livingston, P. A. Durkee, and Å. M. Jonsson. Influence of humidity on the aerosol scattering coefficient and its effect on the upwelling radiance during ACE-2. *Tellus B: Chemical and Physical Meteorology*, 52(2):546–567, 2000.

[25] M. Gini, E. Diapouli, S. Vratolis, C. Helmis, and K. Eleftheriadis. Microphysical and selected chemical properties of ambient aerosol at a suburban environment with emphasis on the size resolved Fuchs surface area and air circulation patterns . *In preparation*, 2019.

[26] Grimm-Aerosoltechnik. *Portable Dust Monitor SERIES 1.100*, 2005.

[27] J. L. Hand and S. M. Kreidenweis. A New Method for Retrieving Particle Refractive Index and

Effective Density from Aerosol Size Distribution Data. *Aerosol Sci. Technol.*, 99:3247–3259, 2002.

[28] H. Hasan and T. G. Dzubay. Apportioning light extinction coefficients chemical species in atmospheric aerosol. *Atmos. Environ.*, 17(8):1573–1581, 1983.

[29] M. Heim, B. J. Mullins, H. Umhauer, and G. Kasper. Effects of Mixing on Extinction by Carbonaceous Particles. *J. Aerosol Sci*, 39:1019–1031, 2008.

[30] J. Heintzenberg, B. Wehner, and W. Birmili. 'How to find bananas in the atmospheric aerosol': new approach for analyzing atmospheric nucleation and growth events. *Tellus*, 59B:273–282, 2007.

[31] L. Hildebrandt, G. J. Engelhart, C. Mohr, E. Kostopoulou, V. A. Lanz, A. Bougiatioti, P. F. DeCarlo, A. S. H. Prevot, U. Baltensperger, N. Mihalopoulos, N. M. Donahue, and S. N. Pandis. Aged organic aerosol in the Eastern Mediterranean: the Finokalia Aerosol Measurement Experiment – 2008. *Atmos. Chem. Phys.*, 10:4167–4186, 2010.

[32] W. C. Hinds. *Aerosol technology: properties, behavior, and measurement of airborne particles.* Wiley-Interscience, 2nd ed edition, 1998.

[33] H. Hulst van de. *Light Scattering by Small Particles.* Dover Publications, Inc. New York, 1981.

[34] T. Hussein, M. Dal Maso, T. Petäjä, I. K. Koponen, P. Paatero, P. P. Aalto, K. Hämeri, and M. Kulmala. Evaluation of an automatic algorithm for fitting the particle number size distributions. *BOREAL ENVIRONMENT RESEARCH*, 10:337–355, 2005.

[35] U. Im and M. Kanakidou. Impacts of East Mediterranean megacity emissions on air quality. *Atmospheric Chemistry and Physics*, 12:6335–6355, 2012.

[36] Å. M. Jonsson, J. Westerlund, and M. Hallquist. Sizeresolved particle emission factors for individual ships. *GEOPHYS RES LETT*, 38:L13809, 2011.

[37] N. Kalivitis, V.-M. Kerminen, G. Kouvarakis, I. Stavroulas, A. Bougiatioti, A. Nenes, H. E. Manninen, T. Petäjä, M. Kulmala, and N. Mihalopoulos. Atmospheric new particle formation

as a source of CCN in the eastern Mediterranean marine boundary layer. *Atmos. Chem. Phys.*, 15(16):9203–9215, 2015.

[38] N. Kalivitis, I. Stavroulas, A. Bougiatioti, G. Kouvarakis, S. Gagné, H. E. Manninen, M. Kulmala, and N. Mihalopoulos. Night-time enhanced atmospheric ion concentrations in the marine boundary layer. *Atmos. Chem. Phys.*, 12:3627–3638, 2012.

[39] P. Kalkavouras, E. Bossioli, S. Bezantakos, A. Bougiatioti, N. Kalivitis, I. Stavroulas, G. Kouvarakis, A. P. Protonotariou, A. Dandou, G. Biskos, N. Mihalopoulos, A. Nenes, and M. Tombrou. New particle formation in the southern Aegean Sea during the Etesians: importance for CCN production and cloud droplet number . *Atmos. Chem. Phys.*, 17:175–192, 2017.

[40] G. Kallos, A. Papadopoulos, P. Katsafados, and S. Nickovic. Transatlantic Saharan dust transport: Model simulation and results. *J. Geophys. Res.*, 111(D09204), 2006.

[41] A.-C. Kalogridis, S. Vratolis, E. Liakakou, E. Gerasopoulos, N. Mihalopoulos, and K. Eleftheriadis. Assessment of wood burning versus fossil fuel contribution to wintertime black carbon and carbon monoxide concentrations in Athens, Greece. *Atmos. Chem. Phys.*, 18:10219–10236, 2018.

[42] K. Kandler, N. Benker, U. Bundke, E. Cuevas, M. Ebert, P. Knippertz, S. Rodrıguez, L. Schutz, and S. Weinbruch. Chemical composition and complex refractive index of Saharan Mineral Dust at Izanã, Tenerife (Spain) derived by electron microscopy. *Atmos. Environ.*, 41:8058–8074, 2007.

[43] M. Koçak, C. Theodosi, P. Zarmpas, U. Im, A. Bougiatioti, O. Yenigun, and N. Mihalopoulos. Particulate matter (PM10) in Is- tanbul: Origin, source areas and potential impact on surrounding regions. *Atmospheric Environment*, 45:6891–6900, 2011.

[44] P. Kokkalis, A. Papayannis, R. Mamouri, G. Tsaknakis, and V. Amiridis. The EOLE lidar system of the National Technical University of Athens. *Proc. 26th International Laser Radar Conference (26th ILRC), Porto Heli, Greece*, pages 629–632, 2012.

[45] E. Kostenidou, K. Florou, C. Kaltsonoudis, M. Tsiflikiotou, S. Vratolis, K. Eleftheriadis, and S. N. Pandis. Sources and chemical characterization of organic aerosol during the summer in the eastern Mediterranean. *Atmos. Chem. Phys.*, 15:11355–11371, 2015.

[46] M. Kulmala, H. Vehkamäki, T. Petäjä, M. Dal Maso, A. Lauri, V.-M. Kerminen, W. Birmili, and P. H. McMurry. Formation and growth rates of ultra*neatmosphericparticles* : *areviewofobservations*. *J. Aerosol Sci*, 35:143 – 176, 2004.

[47] L. D. Labzovskii, A. Papayannis, I. Binietoglou, R. F. Banks, J. M. Baldasano, F. Toanca, C. G. Tzanis, and J. Christodoulakis. Relative humidity vertical profiling using lidar-based synergistic methods in the framework of the Hygra-CD campaign. *Ann. Geophys.*, 36:213–229, 2018.

[48] J. Lelieveld, H. Berresheim, S. Borrmann, P. J. Crutzen, F. J. Dentener, H. Fischer, J. Feichter, P. J. Flatau, J. Heland, R. Holzinger, R. Korrmann, M. G. Lawrence, Z. Levin, K. M. Markowicz, N. Mihalopoulos, A. Minikin, V. Ramanathan, M. de Reus, G. J. Roelofs, H. A. Scheeren, J. Sciare, H. Schlager, M. Schultz, P. Siegmund, B. Steil, E. G. Stephanou, P. Stier, M. Traub, C. Warneke, J. Williams, and H. Ziereis. Global Air Pollution Crossroads over the Mediterranean. *Science*, 298(5594):794–799, Oct. 2002.

[49] J. C. Liljegren, S.-A. Boukabara, K. Cady-Pereira, and S. Clough. The effect of the half- width of the 22-GHz water vapour line on retrievals of temperature and water va- pour profiles with a 12-channel microwave radiometer. *IEEE Trans. Geosci. Remote Sens.*, 43(5):1102–1108, 2005.

[50] U. Loehnert and S. Crewell. Accuracy of cloud liquid water path from ground-based microwave radiometry. *Radio Sci.*, 38(3):8042, 2003.

[51] Y. Lymperopoulos. Personal communication. *Grimm Aerosoltechnik*, 2015.

[52] N. Ma and W. Birmili. Estimating the contribution of photochemical particle formation to ultrafine particle number averages in an urban atmosphere. *Science of the Total Environment*, 512-513:154–166, 2015.

[53] R. Mamouri, A. Papayannis, G. Tsaknakis, and V. Amiridis. Six-month ground-based water vapour Raman lidar measurements over Athens, Greece and system validation. *J. Optoel. Adv. Materials*, 9:3546–3549, 2007.

[54] M. M. Mamun and D. Müller. Retrieval of Intensive Aerosol Microphysical Parameters from Multiwavelength Raman/HSRL Lidar: Feasibility Study with Artificial Neural Networks. *Atmos. Meas. Tech. Discuss.*, 7, 2016.

[55] H. E. Manninen, T. Nieminen, E. Asmi, S. Gagné, S. Häkkinen, K. Lehtipalo, P. Aalto, M. Vana, A. Mirme, S. Mirme, U. Hõrrak, C. Plass-Dülmer, G. Stange, G. Kiss, A. Hoffer, N. Törő, M. Moerman, B. Henzing, G. de Leeuw, M. Brinkenberg, G. Kouvarakis, A. Bougiatioti, N. Mihalopoulos, C. O'Dowd, D. Ceburnis, A. Arneth, A. Svenningsson, E. Swietlicki, L. Tarozzi, S. Decesari, M. C. Facchini, W. Birmili, A. Sonntag, A. Wiedensohler, J. Boulon, K. Sellegri, P. Laj, M. Gysel, N. Bukowiecki, E. Weingartner, G. Wehrle, A. Laaksonen, A. Hamed, J. Joutsensaari, T. Petäjä, V.-M. Kerminen, and M. Kulmala. EUCAARI ion spectrometer measurements at 12 European sites – analysis of new particle formation events. *Atmos. Chem. Phys.*, 10:7907–7927, 2010.

[56] M. Manousakas, E. Diapouli, H. Papaefthymiou, V. Kantarelou, C. Zarkadas, A.-C. Kalogridis, K. A.-G., and K. Eleftheriadis. XRF characterization and source apportionment of PM10 samples collected in a coastal city. *X-Ray Spectrometry*, pages 1–11, 2017.

[57] E. Mantas, E. Remoundaki, I. Halari, P. Kassomenos, C. Theodosi, A. Hatzikioseyian, and N. Mihalopoulos. Mass closure and source apportionment of $PM_{2.5}$ by Positive Matrix Factorization analysis in urban Mediterranean environment. *Atmos. Environ.*, 94:154–163, 2014.

[58] C. Mätzler. MATLAB Functions for Mie Scattering and Absorption. *Institude of Applied Physics, University of Bern, Research Report*, 2002-08, june 2002.

[59] L. McInnes, H. Healy, and S. Astels. hdbscan: Hierarchical density based clustering. *The Journal of Open Source Software*, 2(11):33–42, Mar. 2017.

[60] N. Mihalopoulos, E. Stephanou, M. Kanakidou, S. Pilitsidis, and P. Bousquet. Tropospheric

aerosol ionic composition in the Eastern Mediterranean region. *Tellus B*, 49(3):314–326, July 1997.

[61] B. Mølgaard, W. Birmili, S. Clifford, A. Massling, K. Eleftheriadis, M. Norman, S. Vratolis, B. Wehner, J. Corander, K. Hämeri, and T. Hussein. Evaluation of a statistical forecast model for size-fractionated urban particle number concentrations using data from five European cities. *J AEROSOL SCI*, 66:96–110, 2013.

[62] D. Müller, U. Wandinger, and A. Ansmann. Microphysical particle parameters from extinction and backscatter lidar data by inversion with regularization: theory. *Appl. Opt.*, 38(12):2346–2357, 1999.

[63] T. Müller, M. Laborde, G. Kassell, and A. Wiedensohler. Design and performance of a three-wavelength LED-based total scatter and backscatter integrating nephelometer . *Atmos. Meas. Tech.*, 4:1291–1303, 2011.

[64] J. Nash, T. Oakley, H. Vömel, and L. Wei. WMO intercomparison of high quality radiosonde systems, Yangjiang, China, 12 July–3 August 2010. *World Meteorological Organization*, Instruments and Observing Methods, Report No. 107, 2011.

[65] S. Nava, S. Becagli, G. Calzolai, M. Chiari, F. Lucarelli, P. Prati, R. Traversi, R. Udisti, G. Valli, and R. Vecchi. Saharan dust impact in central Italy: An overview on three years elemental data records. *Atmos. Environ.*, 60:444–452, 2012.

[66] J. A. Nelder and R. Mead. A simplex method for function minimization. *COMPUT J*, 7:308–313, 1965.

[67] E. O'Connor, A. Illingworth, I. Brooks, C. Westbrook, R. Hogan, F. Davies, and B. Brooks. A Method for Estimating the Turbulent Kinetic Energy Dissipation Rate from a Vertically Pointing Doppler Lidar, and Independent Evaluation from Balloon-Borne In Situ Measurements. *JOURNAL OF ATMOSPHERIC AND OCEANIC TECHNOLOGY*, 27:1652–1664, 2010.

[68] R. Pachauri, L. Meyer, and C. W. Team. IPCC, 2014: Climate Change 2014: Synthesis Report. Contribution of Working Groups I, II and III to the Fifth Assessment Report of the

Intergovernmental Panel on Climate Change. Technical report, IPCC, Geneva, Switzerland, 2014.

[69] M. Pandolfi, L. Alados-Arboledas, A. Alastuey, M. Andrade, B. Artiñano, J. Backman, U. Baltensperger, P. Bonasoni, N. Bukowiecki, M. Collaud Coen, S. Conil, E. Coz, V. Crenn, V. Dudoitis, M. Ealo, K. Eleftheriadis, O. Favez, P. Fetfatzis, M. Fiebig, H. Flentje, P. Ginot, M. Gysel, B. Henzing, A. Hoffer, A. Holubova Smejkalova, I. Kalapov, N. Kalivitis, G. Kouvarakis, A. Kristensson, M. Kulmala, H. Lihavainen, C. Lunder, K. Luoma, H. Lyamani, A. Marinoni, N. Mihalopoulos, M. Moerman, J. Nicolas, C. O'Dowd, T. Petäjä, J.-E. Petit, J. M. Pichon, N. Prokopciuk, J.-P. Putaud, S. Rodríguez, J. Sciare, K. Sellegri, D. B. Stamenov, E. Swietlicki, G. Titos, T. Tuch, P. Tunved, V. Ulevicius, A. Vaishya, M. Vana, A. Virkkula, S. Vratolis, E. Weingartner, A. Wiedensohler, and P. Laj. A European aerosol phenomenology-6: Scattering properties of atmospheric aerosol particles from 28 ACTRIS sites. *Atmos. Chem. Phys.*, 18:7877–7911, 2018.

[70] P. Panteliadis, T. Hafkenscheid, B. Cary, E. Diapouli, A. Fischer, O. Favez, P. Quincey, M. Viana, R. Hitzenberger, R. Vecchi, D. Saraga, J. Sciare, J. L. Jaffrezo, A. John, J. Schwarz, M. Giannoni, J. Novak, A. Karanasiou, P. Fermo, and W. Maenhaut. ECOC comparison exercise with identical thermal protocols after temperature offsets correction – instrument diagnostics by in-depth evaluation of operational parameters. *Atmos. Meas. Tech.*, 8(2):779–792, 2015.

[71] A. Papayannis, A. Argyrouli, A. Bougiatioti, E. Remoundaki, S. Vratolis, A. Nenes, S. Solomos, M. Komppula, E. Giannakaki, J. A. Kalogiros, R. F. Banks, K. Eleftheriadis, E. Mantas, E. Diapouli, C. G. Tzanis, S. A. Kazadzis, I. Binietoglou, L. Labzovskiĭ, J. D. Vande Hey, and C. S. Zerefos. An overview from hygroscopic aerosols to cloud droplets: The HygrA-CD campaign in the Athens basin . *Sci. Total Environ.*, 574:216–233, 2017.

[72] G. Pearson, F. Davies, and C. Collier. An Analysis of the Performance of the UFAM Pulsed Doppler Lidar for Observing the Boundary Layer. *J. Atmos. Ocean. Tech.*, 26:240–250, 2009.

[73] F. Pedregosa, G. Varoquaux, A. Gramfort, V. Michel, B. Thirion, O. Grisel, M. Blondel,

P. Prettenhofer, R. Weiss, V. Dubourg, J. Vanderplas, A. Passos, D. Cournapeau, M. Brucher, M. Perrot, and E. Duchesnay. Scikit-learn: Machine Learning in Python. *Journal of Machine Learning Research*, 12:2825–2830, 2011.

[74] M. G. Perrone, S. Vratolis, E. Georgieva, S. Torok, K. Sega, B. Veleva, J. Osan, I. Beslic, Z. Kertesz, D. Pernigotti, K. Eleftheriadis, and C. A. Bellis. Sources and geographic origin of particulate matter in urban areas of the Danube macro-region: the cases of Zagreb (Croatia), Budapest (Hungary) and Sofia (Bulgaria). *Sci. Total Environ.*, 619-620:1515–1529, 2018.

[75] M. Pikridas, A. Bougiatioti, L. Hildebrandt, G. J. Engelhart, E. Kostopoulou, C. Mohr, A. S. H. Prévôt, G. Kouvarakis, P. Zarmpas, J. F. Burkhart, B.-H. Lee, M. Psichoudaki, N. Mihalopoulos, C. Pilinis, A. Stohl, U. Baltensperger, M. Kulmala, and S. N. Pandis. The Finokalia Aerosol Measurement Experiment – 2008 (FAME-08): an overview. *Atmos. Chem. Phys.*, 10:6793–6806, 2010.

[76] M. Pikridas, A. Tasoglou, K. Florou, and S. N. Pandis. Characterization of the origin of fine particulate matter in a medium size urban area in the Mediterranean. *Atmos. Environ.*, 80:264–274, 2013.

[77] X. Querol, J. Pey, M. Pandolfi, A. Alastuey, M. Cusack, N. Pérez, T. Moreno, M. Viana, N. Mihalopoulos, G. Kallos, and S. Kleanthous. African dust contributions to mean ambient PM 10 mass-levels across the Mediterranean Basin. *Atmos. Environ.*, 43:4266–4277, 2009.

[78] P. J. Rousseeuw. Silhouettes: a graphical aid to the interpretation and validation of cluster analysis . *Journal of Computational and Applied Mathematics*, 20:53–65, 1987.

[79] P. Sawamura, R. H. Moore, S. P. Burton, E. Chemyakin, D. Müller, A. Kolgotin, R. A. Ferrare, C. A. Hostetler, L. D. Ziemba, A. J. Beyersdorf, and B. E. Anderson. HSRL-2 aerosol optical measurements and microphysical retrievals vs. airborne in situ measurements during DISCOVER-AQ 2013: an intercomparison study. *Atmos. Chem. Phys.*, 17:7229–7243, 2017.

[80] F. Schneider. Personal communication, 2016.

[81] J. H. Seinfeld and S. N. Pandis. Atmospheric Chemistry and Physics: From Air Pollution to Climate Change. *Wiley Interscience*, 1998.

[82] D. Siakavaras, C. Samara, M. Petrakakis, and G. Biskos. Nucleation events at a coastal city during the warm period: Kerbside versus urban background measurements. *Atmospheric Environment*, 140:60–68, 2016.

[83] A. W. Stelson. Urban Aerosol Refractive Index Prediction by Partial Molar Refraction Approach. *Environ. Sci. Technol.*, 24:1676–1679, 1990.

[84] A. Stohl, C. Forster, A. Frank, P. Seibert, and G. Wotawa. Technical Note: The Lagrangian particle dispersion model FLEXPART version 6.2. *Atmos. Chem. Phys*, 5:2461–2474, 2005.

[85] A. Stohl and D. J. Thomson. A density correction for Lagrangian particle dispersion models. *Bound.-Layer Met.*, 90:155–167, 1999.

[86] M. R. Stolzenburg and P. H. McMurry. An Ultrafine Aerosol Condensation Nucleus Counter. *Aerosol Science and Technology*, 14:48–65, 1991.

[87] N. Sultanova, S. Kasarova, and I. Nikolov. Dispersion Properties of Optical Polymers. *Acta Phys. Pol. A*, 116, 2009.

[88] I. Tang. Chemical and size effects of hygroscopic aerosols on light scattering coefficients. *J. Geophys. Res.*, 101:19245 – 19250, 1996.

[89] M. Tombrou, E. Bossioli, J. Kalogiros, J. D. Allan, A. Bacak, G. Biskos, H. Coe, A. Dandou, G. Kouvarakis, N. Mihalopoulos, C. J. Percival, A. P. Protonotariou, and B. Szabó-Takács. Physical and chemical processes of air masses in the Aegean Sea during Etesians: Aegean-GAME airborne campaign. *Science of the Total Environment*, 506–507:201–216, 2015.

[90] TOPAS. Di-Ethyl_Hexyl_Sebacat. *Excerpt from the Producer's Material Safety Data Sheet (29 June 2008)*, 2008.

[91] E. Triantafyllou, M. Giamarelou, E. Bossioli, P. Zarmpas, C. Theodosi, C. Matsoukas, M. Tombrou, N. Mihalopoulos, and G. Biskos. Particulate Pollution Transport Episodes

from Eurasia to a Remote Region of Northeast Mediterranean. *Atmospheric Environment*, 128:45–52, 2016.

[92] S. Tucker, A. W. Brewer, R. M. Banta, C. J. Senff, P. Sandberg, L. D. C., A. M. Weickmann, and M. R. Hardesty. Doppler Lidar Estimation of Mixing Height Using Turbulence, Shear, and Aerosol Profiles. *JOURNAL OF ATMOSPHERIC AND OCEANIC TECHNOLOGY*, 26:673–688, 2009.

[93] E. Tyrlis and J. Lelieveld. Climatology and Dynamics of the Summer Etesian Winds over the Eastern Mediterranean. *J. Atmos. Sci.*, 70:3374–3396, 2013.

[94] Vaisala. Vaisala radiosonde RS92 performance in the WMO intercomparison of high quality radiosonde systems, Yangjiang, China 2010. *Vaisala White Paper May 2013, Ref. B211129EN-D*, 2013.

[95] Vaisala. Vaisala radiosonde RS92-SGP datasheet, ref. B210358EN-F, 2013.

[96] I. Veselovskii, A. Kolgotin, V. Griaznov, D. Muller, U. Wandinger, and D. N. Whiteman. Inversion with regularization for the retrieval of tropospheric aerosol parameters from multi-wavelength lidar sounding. *Appl. Opt.*, 41(18):3685–3699, 2002.

[97] C. von Bismarck-Osten and S. Weber. A uniform classification of aerosol signature size distributions based on regression-guided and observational cluster analysis. *Atmospheric Environment*, 89:346–357, 2014.

[98] D. Voutsa, C. Samara, T. Kouimtzis, and K. Ochsenkühn. Elemental composition of airborne particulate matter in the multi-impacted urban area of Thessaloniki, Greece. *Atmospheric Environment*, 36(28):4453–4462, Sept. 2002.

[99] S. Vratolis, P. Fetfatzis, A. Argyrouli, A. Papayannis, D. Muller, I. Veselovskii, A. Bougiatioti, A. Nenes, E. Remoundaki, E. Diapouli, M. Manousakas, M. Mylonaki, and K. Eleftheriadis. A new method to retrieve the real part of the equivalent refractive index of atmospheric aerosols. *Journal of Aerosol Science*, 117:54–62, 2018.

[100] S. Vratolis, M. Gini, S. Bezantakos, I. Stavroulas, N. Kalivitis, E. Kostenidou, E. Louvaris, D. Siakavaras, G. Biskos, N. Mihalopoulos, S. N. Pandis, C. Pilinis, A. Papayannis, and K. Eleftheriadis. Particle number size distribution statistics at City-Centre Urban Background, Urban Background, and Remote stations in Greece during summer. *Atmos. Environ.*, 213:711–726, 2019.

[101] V. Ždímal, S. Jiri, K. Eleftheriadis, Z. Wagner, C. Housiadas, N. Mihalopoulos, P. Mikuška, Z. Večeřa, I. Kopanakis, and M. Lazaridis. Dynamics of Atmospheric Aerosol Number Size Distributions in the Eastern Mediterranean During the "SUB-AERO" Project. *Water Air Soil Pollut*, 214:133–146, 2011.

[102] U. Wandinger and A. Ansmann. Experimental determination of the lidar overlap profile with Raman lidar. *Appl Opt*, 41(3):511–4, Jan. 2002.

[103] L. Wang, S. Stanič, K. Bergant, W. Eichinger, G. Močnik, L. Drinovec, J. Vaupotič, M. Miler, M. Gosar, and A. Gregorič. Retrieval of Vertical Mass Concentration Distributions—Vipava Valley Case Study. *Remote Sensing*, 11(106), 2019.

[104] T. Wegner, T. Hussein, K. Hämeri, T. Vesala, M. Kulmala, and S. Weber. Properties of aerosol signature size distributions in the urban environment as derived by cluster analysis. *Atmospheric Environment*, 61:350–360, 2012.

[105] C. Weitkamp. *Lidar Range-Resolved Optical Remote Sensing of the Atmosphere*, volume 102. Springer-Verlag New York, 2005.

[106] A. Wiedensohler, W. Birmili, A. Nowak, A. Sonntag, K. Weinhold, M. Merkel, B. W. T. Tuch, S. Pfeifer, M. Fiebig, A. M. Fjäraa, E. Asmi, K. Sellegri, R. Depuy, H. Venzac, P. Villani, P. Laj, P. Aalto, J. A. Ogren, E. Swietlicki, P. Williams, P. Roldin, P. Quincey, C. Hüglin, R. Fierz-Schmidhauser, M. Gysel, E. Weingartner, F. Riccobono, S. Santos, C. Grüning, K. Faloon, D. Beddows, R. Harrison, C. Monahan, S. G. Jennings, C. D. O'Dowd, A. Marinoni, H.-G. Horn, L. Keck, J. Jiang, J. Scheckman, P. H. McMurry, Z. Deng, C. S. Zhao, M. Moerman, B. Henzing, G. de Leeuw, G. Löschau, and S. Bastian. Mobility particle size spectrometers: harmonization of technical standards and data structure to facilitate high quality long-term

observations of atmospheric particle number size distributions. *Atmos. Meas. Tech.*, 5:657–685, 2012.

[107] P. Zieger, E. Kienast-Sjögren, M. Starace, J. von Bismarck, N. Bukowiecki, U. Baltensperger, F. G. Wienhold, T. Peter, T. Ruhtz, M. C. Coen, L. Vuilleumier, O. Maier, E. Emili, C. Popp, and E. Weingartner. Spatial variation of aerosol optical properties around the high-alpine site Jungfraujoch (3580 m a.s.l.). *Atmos. Chem. Phys.*, 12:7231–7249, 2012.

[108] P. Zieger, E. Weingartner, B. Henzing, M. Moerman, G. d. Leeuw, J. Mikkilä, M. Ehn, T. Petäjä, K. Clémer, M. van Roozendael, S. Yilmaz, U. Frieß, H. Irie, T. Wagner, R. Shaiganfar, S. Beirle, A. Apituley, K. Wilson, and U. Baltensperger. Comparison of ambient aerosol extinction coefficients obtained from in-situ, MAX-DOAS and LIDAR measurements at Cabauw. *Atmos. Chem. Phys.*, 11:2603–2624, 2011.

Appendix A

A.1 Appendix of the chapter "Particle number size distribution statistics at City-Centre Urban Background, Urban Background, and Remote stations in Greece during summer"

Overview of concentration levels and size distributions

DEM station in Athens and ICE-HT in Patras have the main peak at 100 nm. However, in the case of DEM station (Figure A.1), at the 84^{th} percentile, an increase in the number concentration of $N_{<15}$ mode particles (see Table 4) was observed, indicating that new particle formation may occur. As DEM station is situated in a pine tree area, biogenic aerosol is probably contributing significantly to the size distribution (oxidation of hydrocarbons emitted by vegetation, like terpenes). The size distribution at EPT station demonstrates an elongated shape, indicating multiple mixed sources. Apart from the well-aged accumulation mode, an Aitken mode (A_{30-60}) was observed as well. The station is a typical Urban Background station, strongly affected by road traffic exhaust.

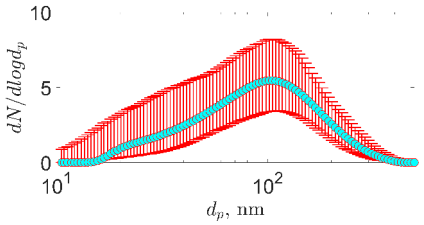

(a) ICE-HT

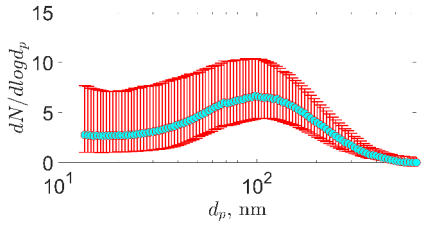

(b) DEM

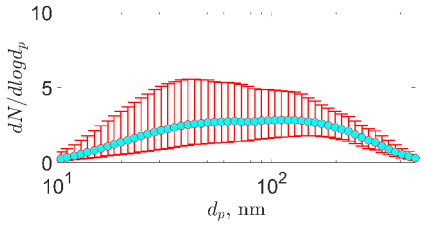

(c) EPT

Figure A.1: Overview of Particle Size Distribution statistics for each size bin: geometric mean (G_m), the 16^{th} and 84^{th} percentiles of the measured concentrations. The area below the lower end of the error bars corresponds to the 16^{th} percentile, while the area below the higher end of the error bars corresponds to the 84^{th} percentile.

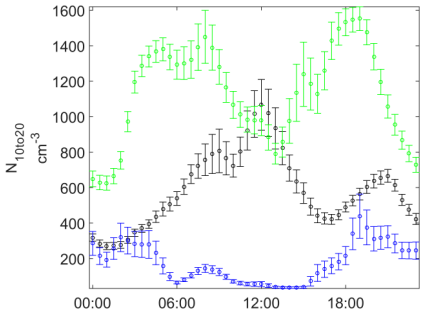

(a) N_{10-20}

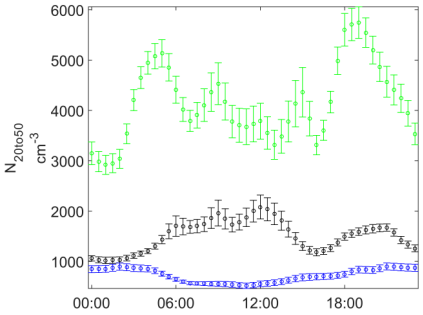

(b) N_{20-50}

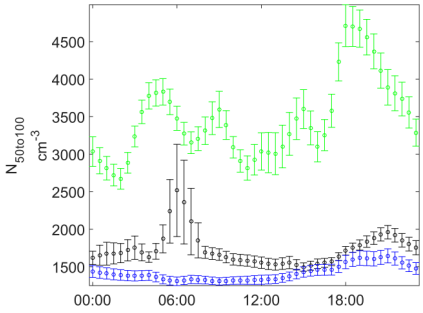

(c) N_{50-100}

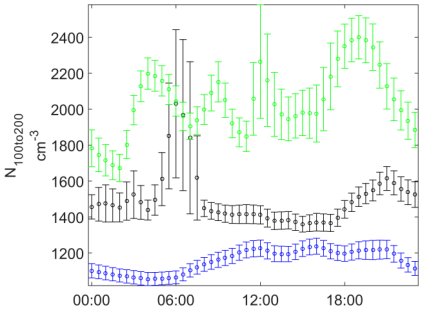

(d) $N_{100-200}$

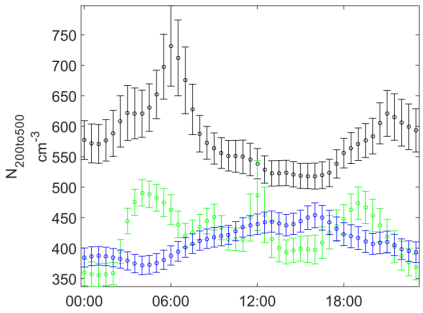

(e) $N_{200-500}$

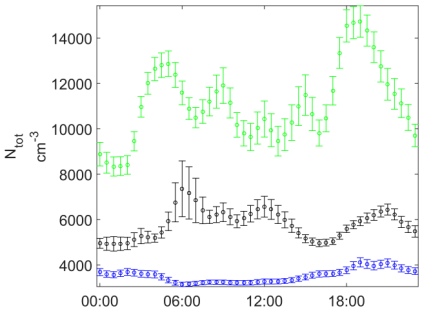

(f) N_{tot}

Figure A.2: Diurnal variation (UTC) for City-Centre Urban Background (green), Urban Background (black), and Regional Background (blue) stations. The error bars correspond to one tenth of the standard deviation.

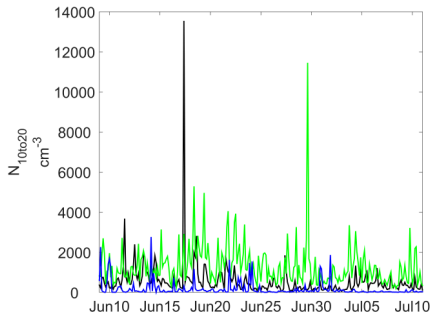

(a) N_{10-20}

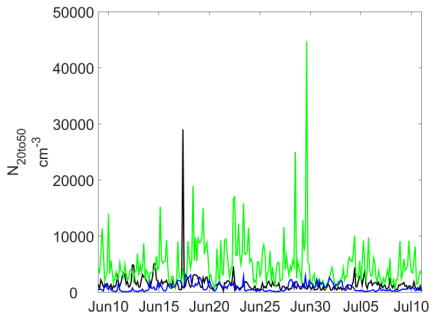

(b) N_{20-50}

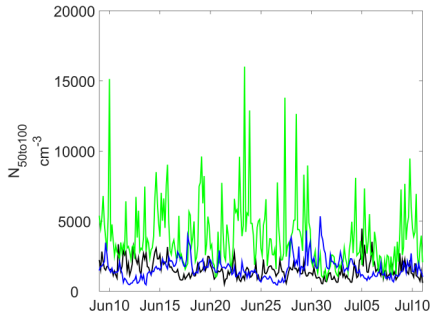

(c) N_{50-100}

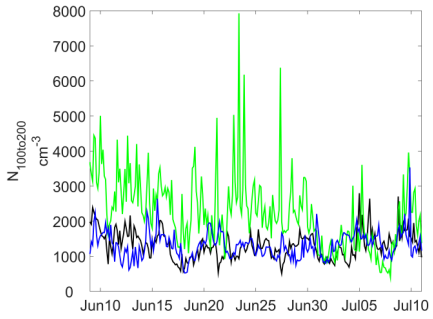

(d) $N_{100-200}$

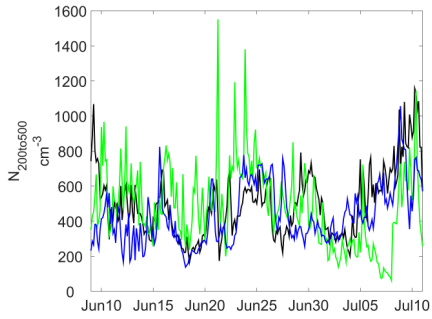

(e) $N_{200-500}$

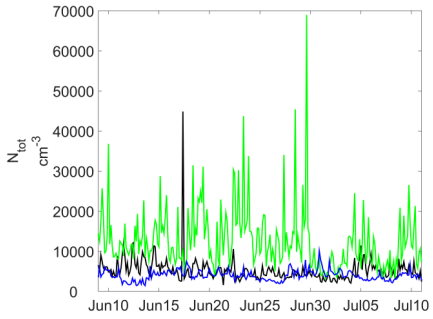

(f) N_{tot}

Figure A.3: Time-series (UTC) for City-Centre Urban Background (green), Urban Background (black), and Regional Background (blue) stations.

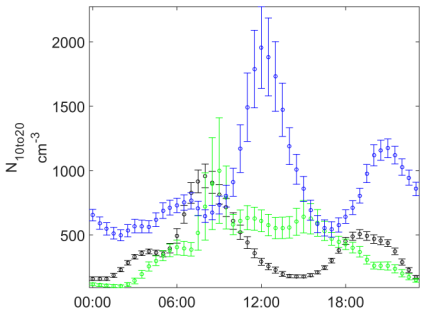

(a) N_{10-20}

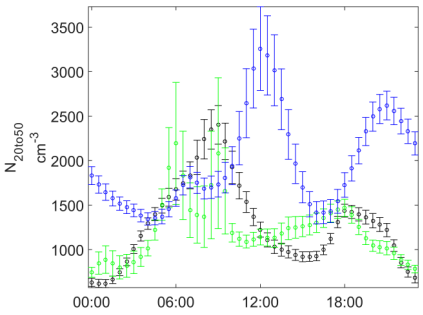

(b) N_{20-50}

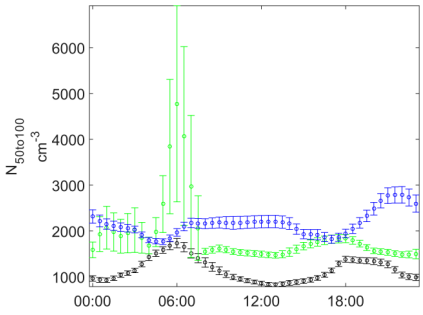

(c) N_{50-100}

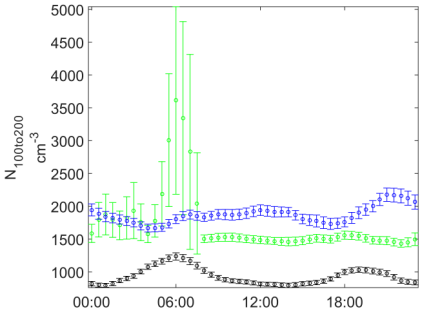

(d) $N_{100-200}$

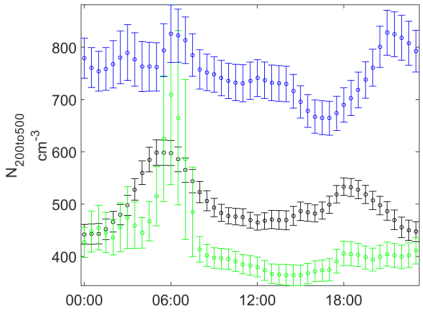

(e) $N_{200-500}$

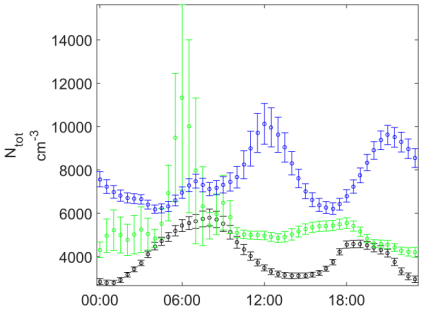

(f) N_{tot}

Figure A.4: Diurnal variation (UTC) for ICE-HT (green), EPT (black), and DEM (blue) stations. The error bars correspond to one tenth of the standard deviation.

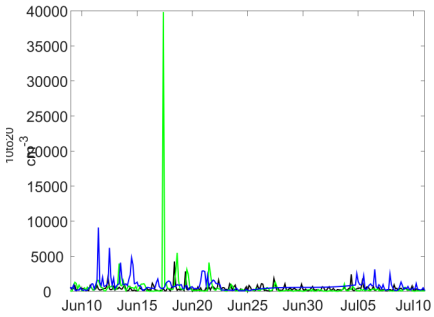

(a) N_{10-20}

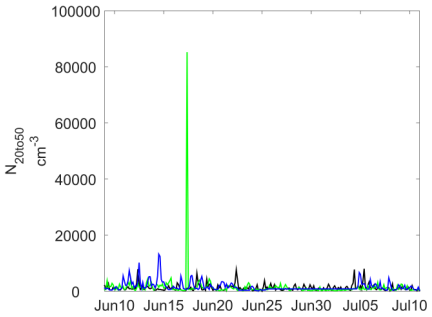

(b) N_{20-50}

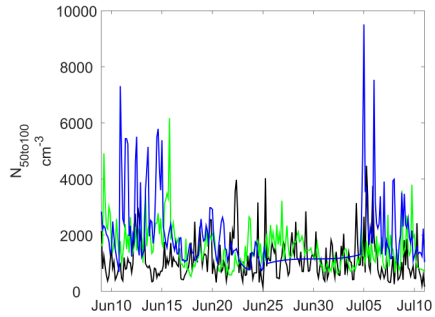

(c) N_{50-100}

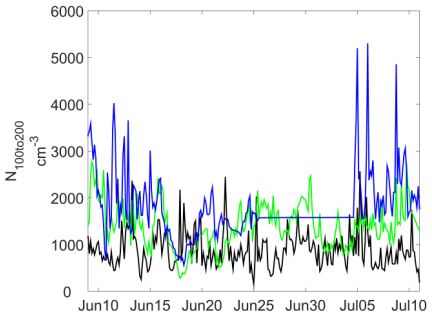

(d) $N_{100-200}$

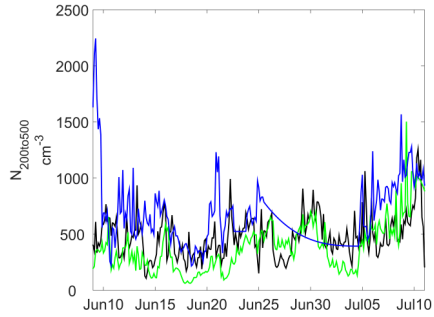

(e) $N_{200-500}$

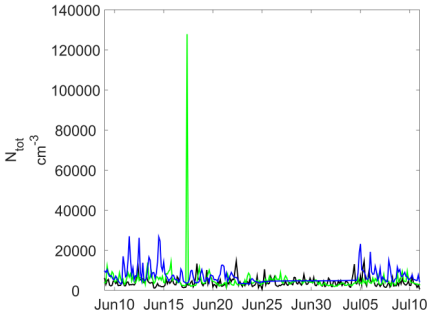

(f) N_{tot}

Figure A.5: Time-series (UTC) for ICE-HT (green), EPT (black), and DEM (blue) stations.

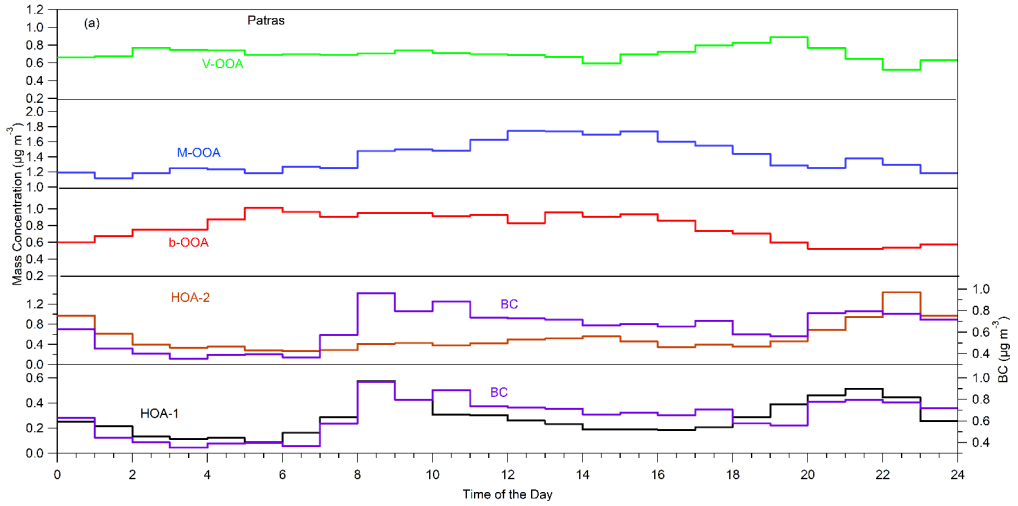

(a) ICE-HT

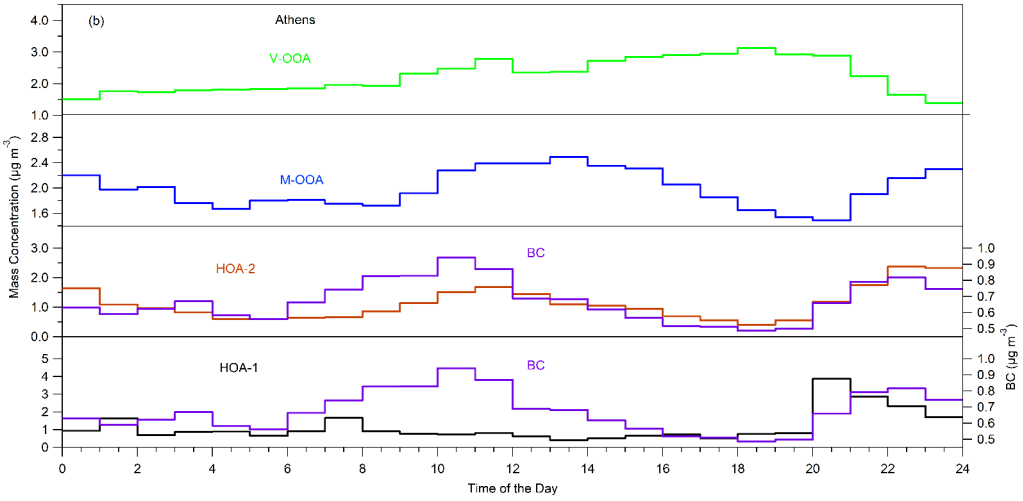

(b) DEM

Figure A.6: Diurnal cycles of the PMF factors (a) in ICE-HT and (b) in DEM. [45]

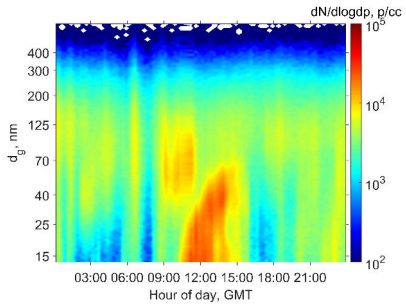

(a) DEM, 4^{th} of June

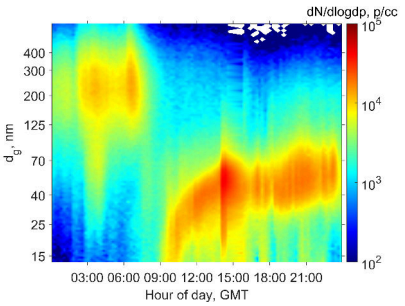

(b) DEM, 6^{th} of June

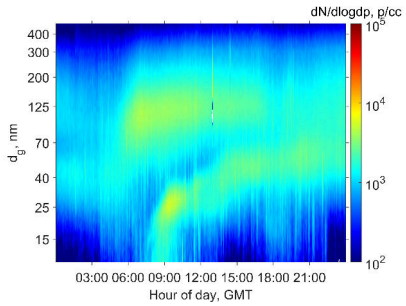

(c) EPT, 14^{th} of June

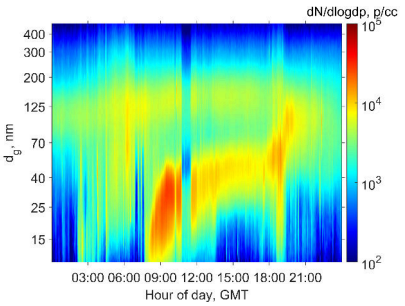

(d) 18^{th} of June

Figure A.7: Summer 2012, exemplary NPF events used in order to develop an algorithm for the detection of NPF at all stations, time is GMT.

New Particle Formation (NPF) Events

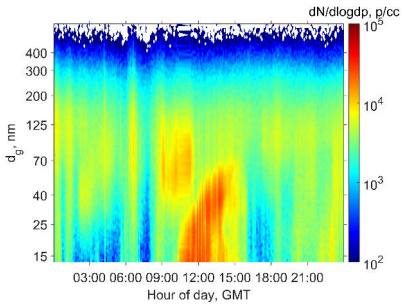

(a) 4^{th} of June

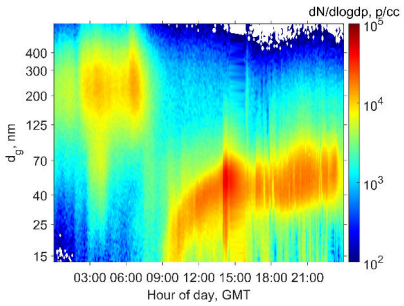

(b) 6^{th} of June

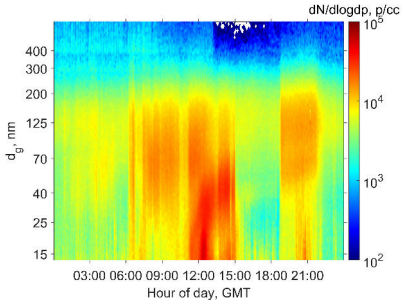

(c) 12^{th} of June

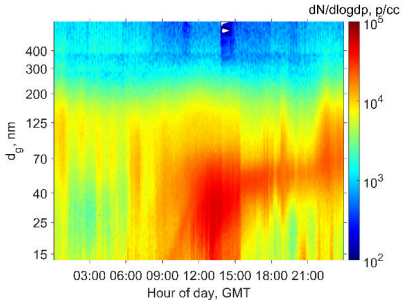

(d) 14^{th} of June

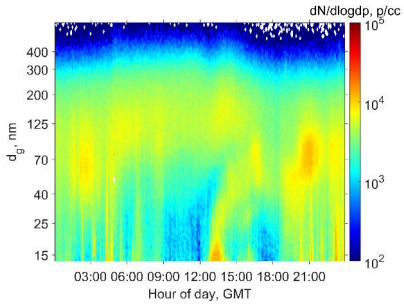

(e) 27^{th} of July

Figure A.8: Summer 2012, DEM, time is GMT. Contour plots of the particle number concentration (color bar), particle size (y-axis) and time (x-axis) at DEM. On the above Figures we observe nucleation events, where particles grow from 13 nm to approximately 70 nm.

Statistics and phenomenology of size distribution at different station types

Each mode identified by the size distribution modal analysis algorithm was classified according to its geometric mean diameter (d_g) in a structure consisting of two submodes corresponding to the Nucle-

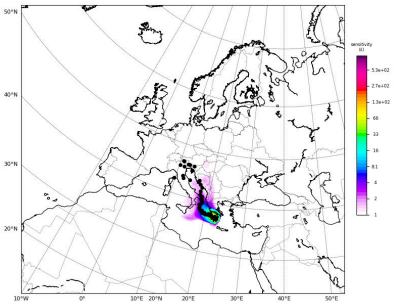

(a) 4^{th} of June

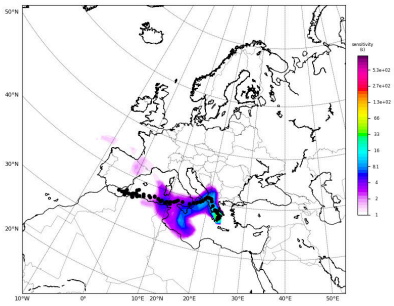

(b) 6^{th} of June

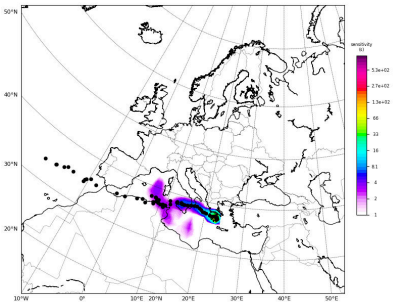

(c) 12^{th} of June

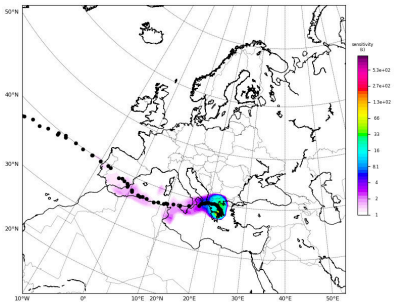

(d) 14^{th} of June

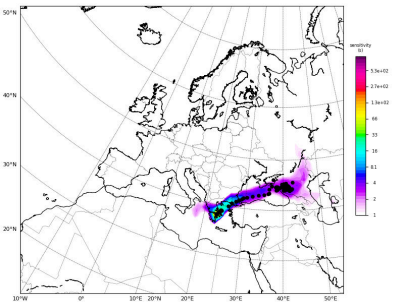

(e) 27^{th} of July

Figure A.9: Summer 2012, DEM, time is GMT. Origin of air masses for nucleation events identified. The centroid of residence time plume is also displayed (black dots).

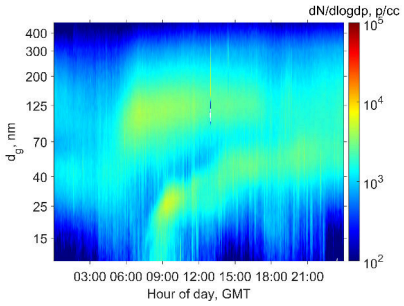

(a) 14^{th} of June

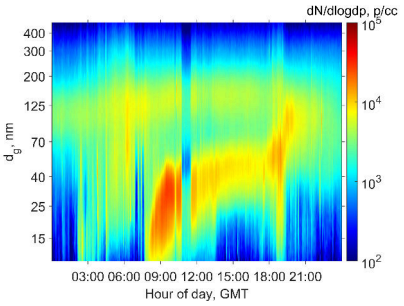

(b) 18^{th} of June

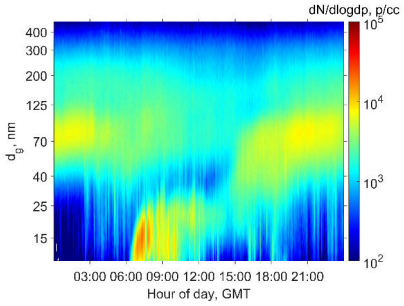

(c) 27^{th} of June

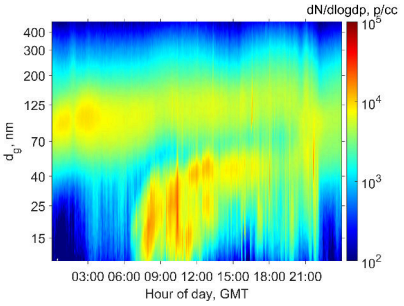

(d) 18^{th} of July

Figure A.10: Summer 2012, EPT, time is GMT. Contour plots of the particle number concentration (color bar), particle size (y-axis) and time (x-axis) at EPT. We observe nucleation events, where particles grow from a size of 10 nm to approximately 70 nm.

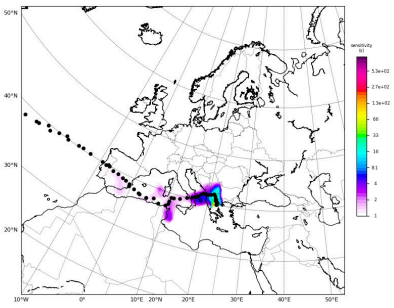

(a) 14^{th} of June

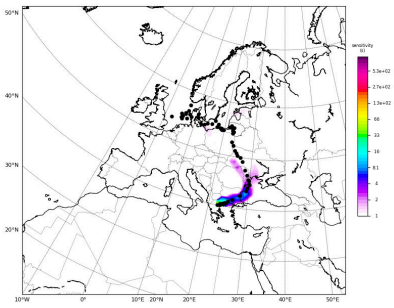

(b) 18^{th} of June

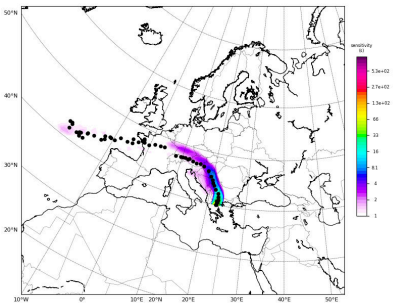

(c) 27^{th} of June

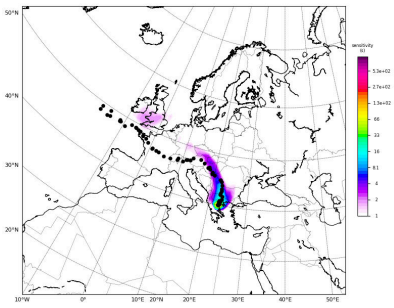

(d) 18^{th} of July

Figure A.11: Summer 2012, EPT, time is GMT. Origin of air masses for nucleation events identified. The centroid of residence time plume is also displayed (black dots).

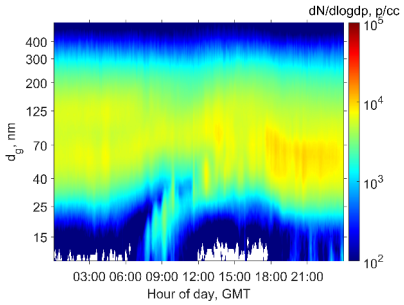

(a) 16^{th} of June

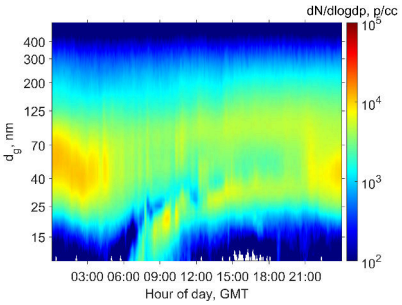

(b) 18^{th} of June

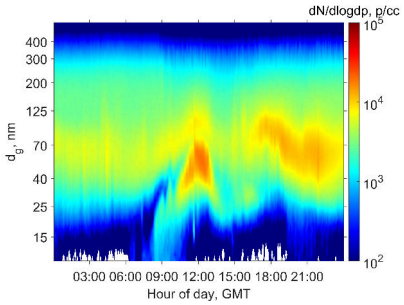

(c) 29^{th} of June

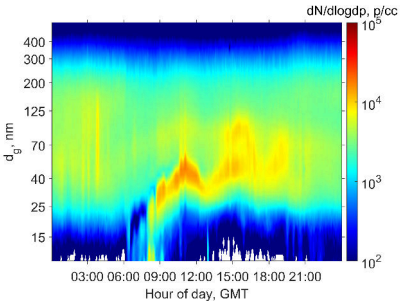

(d) 19^{th} of July

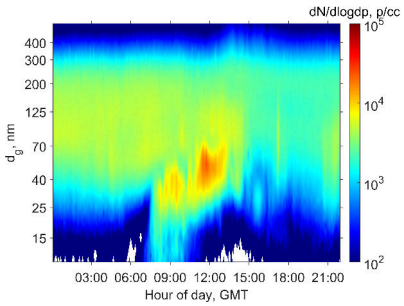

(e) 31^{st} of July

Figure A.12: Summer 2012, FIN, time is GMT. Contour plots of the particle number concentration (color bar), particle size (y-axis) and time (x-axis). We observe nucleation events, where particles grow from a size of 10 nm to approximately 70 nm.

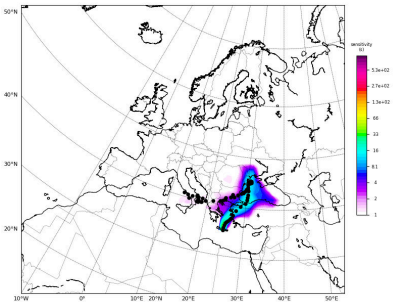

(a) 16^{th} of June

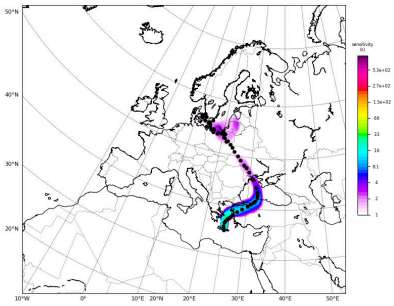

(b) 18^{th} of June

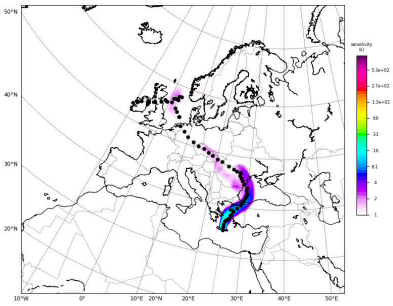

(c) 29^{th} of June

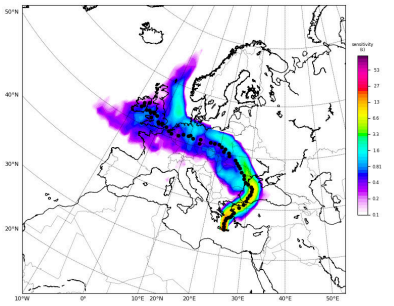

(d) 19^{th} of July

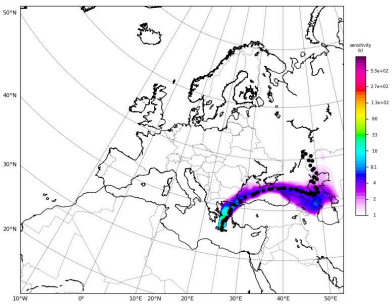

(e) 31^{st} of July

Figure A.13: Summer 2012, FIN, time is GMT. Origin of air masses for nucleation events identified. The centroid of residence time plume is also displayed (black dots).

ation mode ($N_{<15}$, N_{15-30}), two submodes corresponding to the Aitken mode (A_{30-60}, A_{60-90}) and two submodes corresponding to the Accumulation mode (C_{90-120}, $C_{>120}$). This finer classification was carried out in order to distinguish the aerosol sources more precisely. The nomenclature of this work is provided in Table 2.4.

The dataset acquired by modal analysis and subsequent classification in six submodes, was separated in 2-hour intervals, in order to obtain the diurnal variation of modes for the whole period of the campaign. The results are displayed in Figures A.14 to A.22.

City-Centre Urban Background station (Patras-C)

Figure A.14 and Figure A.15 (Appendix) display the number concentration and frequency spider plots for the City-Centre Urban Background station. N_{15-30} has a maximum concentration from 14:00 to 16:00 UTC, which corresponds to M-OOA source diurnal profile identified by [45].

A_{30-60} mode exhibits peaks corresponding to traffic rush hours for both frequency and number concentration (06:00 to 10:00 and 18:00 to 20:00 UTC). A_{60-90} mode is not as frequent as A_{30-60}, and its maximum lies in the time period from 20:00 to 22:00 UTC. This mode is probably the result of the A_{30-60} mode particle growth. $C_{>120}$ has a maximum of particle number in the interval 14:00 to 16:00, and it's number concentration throughout the day lays between 2×10^3-3×10^3 particles per cm^{-3}. Fresh ship emissions display a peak at 35 nm, according to [36], thus we expect this source to mainly contribute to Aitken mode as well.

Overall, the Aitken modes (A_{30-60} and A_{60-90}) dominate the particle number concentration and correspond to HOA-1 and HOA-2 sources mentioned earlier, while modes C_{90-120} and $C_{>120}$ are stable throughout the day. $N_{<15}$ mode is infrequent, as the particles emitted at street-level are lost by the time they reach the urban background stations due to polydisperse coagulation, diffusion and dry deposition. They also have grown out of the nucleation mode due to condensational growth. [13] report that a mode was identified at Barcelona, Madrid and Brisbane, where the traffic related 20-40 nm peak shifted towards the nucleation mode and that might indicate particle evaporation. Therefore, there are a few cases where traffic combustion exhaust particles could reduce in size towards nucleation mode particles.

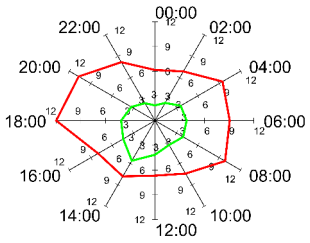

(a) N_{15-30} (green), A_{30-60} (red) modes

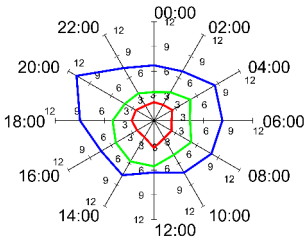

(b) A_{60-90} (blue), C_{90-120} (green), $C_{>120}$ (red) modes

Figure A.14: Summer 2012 diurnal variation spider plots for the City-Centre Urban Background station. Submodes (whose characteristics and sources are described in detail in Table 4) are classified in 2-hour intervals in order to acquire the diurnal variation for the average number concentration. The hour displayed on the axes corresponds to the start of the two hour interval (UTC), while smaller numbers (in size) correspond to the average number concentration depending on the hour of the day, for all modes in thousands of particles per cm^3.

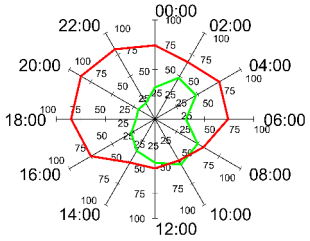

(a) N_{15-30} (green), A_{30-60} (red) modes

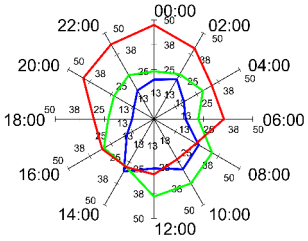

(b) A_{60-90} (blue), C_{90-120} (green), $C_{>120}$ (red) modes

Figure A.15: Summer 2012 spider plots for the City-Centre Urban Background station. Submodes are classified in 2-hour intervals in order to acquire the diurnal variation for the frequency of occurrence. The hour displayed on the axes corresponds to the start of the 2-hour interval (GMT), while smaller numbers (in size) 100, 75, 50 correspond to frequency of occurrence.

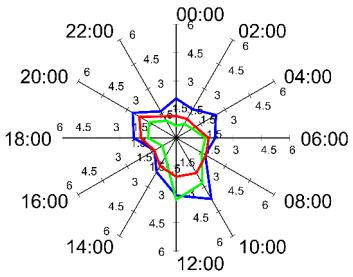

(a) $N_{<15}$ mode (blue), N_{15-30} (green), A_{30-60} (red) modes

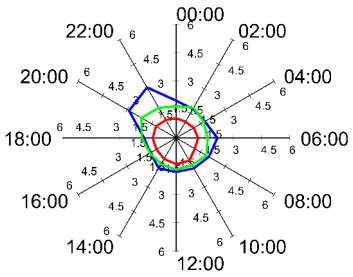

(b) A_{60-90} (blue), C_{90-120} (green), $C_{>120}$ (red) modes

Figure A.16: Summer 2012 diurnal variation spider plots for Urban Background stations. Submodes (whose characteristics and sources are described in detail in Table 4) are classified in 2-hour intervals in order to acquire the diurnal variation for the average number concentration. The hour displayed on the axes corresponds to the start of the 2-hour interval (UTC), while smaller numbers (in size) correspond to the average number concentration depending on the hour of the day, for all modes in thousands of particles per cm^3.

Urban Background stations (ICE-HT, DEM and EPT)

At the Urban Background stations, $C_{>120}$ and C_{90-120} modes are almost constant in frequency and particle number concentration throughout the day (Figures A.16, A.17-Appendix). A_{60-90} and A_{30-60} have three peaks in number concentration, two corresponding to the diurnal profile of sources HOA-1 and HOA-2, and one corresponding to M-OOA. N_{15-30} has a maximum frequency from 08:00 to 10:00 UTC and 20:00 to 22:00 UTC. Its highest concentration values are observed from 10:00 to 12:00 UTC. $N_{<15}$ has the most complex pattern, with 3 maxima in number and frequency: 04:00 to 06:00, 10:00 to 12:00, and 20:00 to 22:00 UTC. $N_{<15}$ peak at 04:00 to 06:00 UTC may be attributed to early morning traffic. $N_{<15}$ and N_{15-30} peaks at noon may be attributed to new particle formation and subsequent growth.

We conclude that the Urban Background stations size distributions, are influenced by both primary emissions and secondary aerosol.

In Tables A.1-A.3 (Appendix), we present the most frequent mode combinations for each Urban

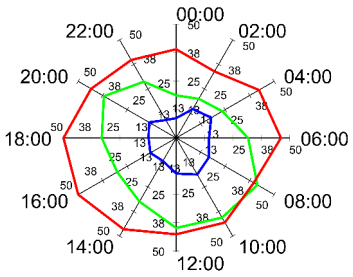

(a) $N_{<15}$ mode (blue), N_{15-30} (green), A_{30-60} (red) modes

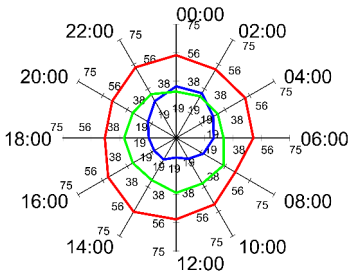

(b) A_{60-90} (blue), C_{90-120} (green), $C_{>120}$ (red) modes

Figure A.17: Summer 2012 spider plots for UB stations. Submodes are classified in 2-hour intervals in order to acquire the diurnal variation for the frequency of occurrence for $N_{<15}$ to $C_{>120}$ modes. The hour displayed on the axes corresponds to the start of the 2-hour interval (GMT), while the smaller numbers (in size) 50, 38, 25 correspond to frequency of occurrence.

Background station (ICE-HT, DEM, EPT).

(ICE-HT)

At ICE-HT (Figure A.18), $C_{>120}$ has a high frequency of occurrence at night, but very low number concentration. C_{90-120} has a high frequency of occurrence at daytime and high particle number concentration from 06:00 to 08:00 GMT. A_{60-90} has a high frequency of occurrence from 00:00 to 02:00 GMT, but its highest number concentration values are observed from 06:00 to 08:00 GMT. A_{30-60} has high frequency and high number concentrations from 06:00 to 08:00 GMT and 18:00 to 20:00 GMT. N_{15-30} has a maximum frequency from 12:00 to 14:00 GMT, and high concentration values from 10:00 to 12:00 GMT. $N_{<15}$ has a maximum in particle concentration from 06:00 to 08:00 GMT, and from 16:00 to 22:00 GMT. Its maximum frequency is observed from 16:00 to 18:00 GMT. Overall, the station's particle number concentration has a maximum in the morning hours (06:00-08:00 GMT), which can be attributed to morning traffic from Patras city, and a maximum in the evening (18:00-20:00 GMT), which can be attributed to the lowering of the boundary layer, while aerosol sources are still active. Also, aerosol removal processes effect (transport, coagulation) is more apparent at night time, where $C_{>120}$ mode dominates frequency. Table A.1 demonstrates the most frequent mode combination. One may observe that Aitken and Accumulation modes contribute almost equally to the most frequent mode combinations.

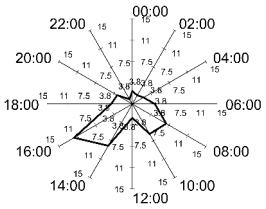

(a) $N_{<15}$ mode

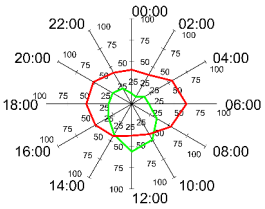

(b) N_{15-30} (green), A_{30-60} (red) modes

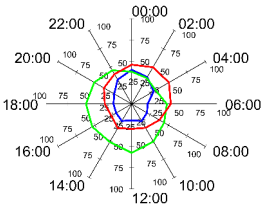

(c) A_{60-90} (blue), C_{90-120} (green), $C_{>120}$ (red) modes

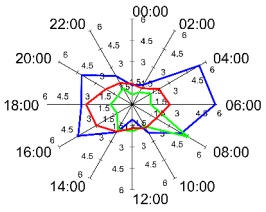

(d) $N_{<15}$ mode (blue), N_{15-30} (green), A_{30-60} (red) modes

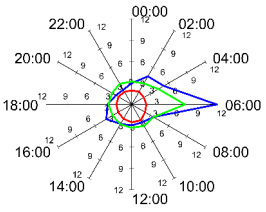

(e) A_{60-90} (blue), C_{90-120} (green), $C_{>120}$ (red) modes

Figure A.18: Summer 2012 spider plots for ICE-HT station. Sub-modes are classified in 2-hour intervals in order to acquire the diurnal variation for the frequency of occurrence. Sub-figures a, b, c: the frequency of occurrence for $N_{<15}$ to $C_{>120}$ modes. The hour displayed on the axes corresponds to the start of the 2-hour interval (GMT), while the smaller numbers (in size) 50, 38, 25 correspond to frequency of occurrence. Sub-figures d,e: the average number concentration depending on the hour of the day, for all modes in thousands of particles per cm^3.

Table A.1: ICE-HT most frequent mode combinations

Mode Combination	$\mathbf{A_{30-60}C_{>120}}$ **Median**	$\mathbf{A_{30-60}C_{90-120}}$ **Median**	$\mathbf{N_{15-30}C_{90-120}}$ **Median**	$\mathbf{A_{60-90}C_{>120}}$ **Median**	$\mathbf{C_{90-120}}$ **Median**	$\mathbf{A_{60-90}}$ **Median**
N_{15-30} σ_g	-	-	1.5	-	-	-
N_{15-30} d_g	-	-	24	-	-	-
N_{15-30} N	-	-	0.9×10^3	-	-	-
A_{30-60} σ_g	1.9	1.9	-	-	-	-
A_{30-60} d_g	46	39	-	-	-	-
A_{30-60} N	1.6×10^3	1.6×10^3	-	-	-	-
A_{60-90} σ_g	-	-	-	1.9	-	1.9
A_{60-90} d_g	-	-	-	71	-	77
A_{60-90} N	-	-	-	1.9×10^3	-	4×10^3
C_{90-120} σ_g	-	1.6	1.7	-	1.7	-
C_{90-120} d_g	-	111	105	-	102	-
C_{90-120} N	-	2.8×10^3	3.3×10^3	-	4×10^3	-
$C_{>120}$ σ_g	1.6	-	-	1.5	-	-
$C_{>120}$ d_g	134	-	-	142	-	-
$C_{>120}$ N	2.3×10^3	-	-	1.4×10^3	-	-
Frequency %	20	16	12	12	9	6

(DEM)

At DEM (Figure A.19), local topography favors the development of katabatic winds, under certain conditions of atmospheric stability. Katabatic winds may transport the well-aged particles to the DEM station, leading to an increase in the particle number concentration. Also, the formation of the shallow nocturnal boundary layer (NBL) has major effect on the number size distribution pattern, by trapping aerosol particles within a layer of a few meters. At DEM, $C_{>120}$ and C_{90-120} modes are almost constant in frequency and particle number concentration throughout the day. A_{60-90} and A_{30-60} have their highest number concentration values from 20:00 to 24:00 GMT. N_{15-30} has a maximum frequency from 06:00 to 14:00 GMT and 20:00 to 22:00 GMT. Its highest concentration values are observed from 12:00 to 14:00 and 20:00 to 22:00 GMT. $N_{<15}$ has the most complex pattern, with 3 maximums in number and frequency: 04:00 to 06:00, 10:00 to 14:00, and 20:00 to 22:00 GMT. Peaks at nighttime are probably due to katabatic winds. One may observe that all modes are influenced, as we see peaks in frequency and number at night for all modes. $N_{<15}$ peak at 04:00 to 06:00 GMT may be attributed to early morning traffic, brought to the station by sea-breeze and anabatic wind. $N_{<15}$ and N_{15-30} peaks at noon may be attributed to new particle formation and subsequent growth (Figure 5, subfigure 5b). Table A.2 demonstrates the most frequent mode combinations: 4 out of 6 of the most frequent combinations are Nucleation mode – Accumulation mode.

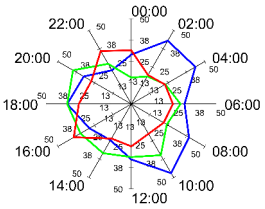

(a) $N_{<15}$ mode (blue), N_{15-30} (green), A_{30-60} (red) modes

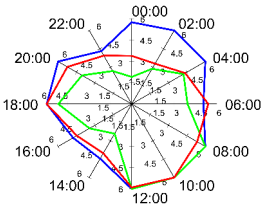

(b) $N_{<15}$ mode (blue), N_{15-30} (green), A_{30-60} (red) modes

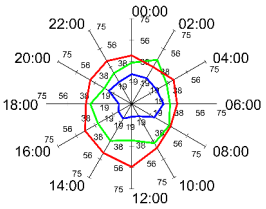

(c) A_{60-90} (blue), C_{90-120} (green), $C_{>120}$ (red) modes

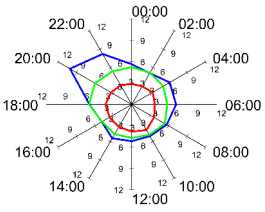

(d) A_{60-90} (blue), C_{90-120} (green), $C_{>120}$ (red) modes

Figure A.19: Summer 2012 spider plots for DEM station. Submodes are classified in 2-hour intervals in order to acquire the diurnal variation for the frequency of occurrence. On the left: the frequency of occurrence for $N_{<15}$ to $C_{>120}$ modes. The hour displayed on the axes corresponds to the start of the 2-hour interval (GMT), while the smaller numbers (in size) 50, 38, 25 correspond to frequency of occurrence. On the right: the average number concentration depending on the hour of the day, for all modes in thousands of particles per cm^3.

(EPT)

At EPT (Figure A.20), $C_{>120}$ is almost constant in frequency and particle number concentration throughout the day. C_{90-120}, A_{60-90} and A_{30-60} have their highest number concentration values from 06:00 to 10:00 and 18:00 to 20:00 GMT. There is some resemblance for these modes to the situation at ICE-HT. $N_{<15}$ mode indicates new particle formation at 06:00 to 12:00 GMT with low frequency of occurrence. It might also be influenced by early morning traffic. N_{15-30} has a maximum frequency and number concentration from 08:00 to 10:00 GMT and 20:00 to 22:00 GMT. These particles may be attributed to the growth of $N_{<15}$ mode particles and traffic in the morning, while in the evening, the lowering of the boundary layer might enhance particle concentration, similar to DEM station. Overall, the particle number concentration has a maximum in the morning (06:00 to 10:00) related to traffic and a peak in the evening, related to the boundary layer's lowering.

Table A.3 (Appendix) demonstrates the most frequent mode combinations, which are a combination of Aitken mode – Accumulation mode.

Table A.2: DEM most frequent mode combinations

Mode Combination	$\mathbf{N_{<15}C_{90-120}}$ **Median**	$\mathbf{A_{30-60}C_{>120}}$ **Median**	$\mathbf{N_{15-30}C_{>120}}$ **Median**	$\mathbf{N_{15-30}C_{90-120}}$ **Median**	$\mathbf{N_{<15}C_{>120}}$ **Median**	$\mathbf{N_{<15}A_{60-90}}$ **Median**
$N_{<15}$ σ_g	2.5	-	-	-	2.9	1.8
$N_{<15}$ d_g	10	-	-	-	10	12
$N_{<15}$ N	4.5×10^3	-	-	-	4.4×10^3	4.1×10^3
N_{15-30} σ_g	-	-	2.9	1.9	-	-
N_{15-30} d_g	-	-	23	19	-	-
N_{15-30} N	-	-	2.9×10^3	2.8×10^3	-	-
A_{30-60} σ_g	-	2.4	-	-	-	-
A_{30-60} d_g	-	42	-	-	-	-
A_{30-60} N	-	3.2×10^3	-	-	-	-
A_{60-90} σ_g	-	-	-	-	-	2.1
A_{60-90} d_g	-	-	-	-	-	80
A_{60-90} N	-	-	-	-	-	7.4×10^3
C_{90-120} σ_g	1.9	-	-	1.8	-	-
C_{90-120} d_g	106	-	-	107	-	-
C_{90-120} N	4.8×10^3	-	-	4.7×10^3	-	-
$C_{>120}$ σ_g	-	1.7	1.7	-	1.8	-
$C_{>120}$ d_g	-	141	132	-	128	-
$C_{>120}$ N	-	2.8×10^3	3.7×10^3	-	4.3×10^3	-
Frequency %	11	10	10	8	8	7

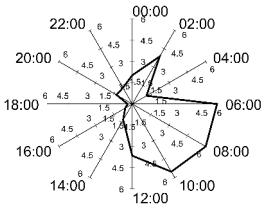

(a) $N_{<15}$ mode

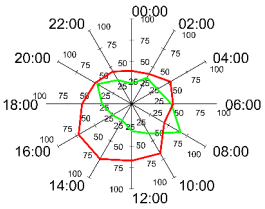

(b) N_{15-30} (green), A_{30-60} (red) modes

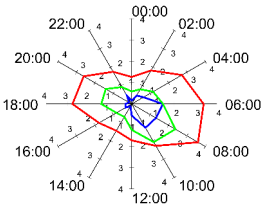

(c) $N_{<15}$ mode (blue), N_{15-30} (green), A_{30-60} (red) modes

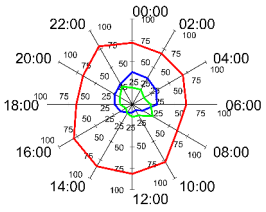

(d) A_{60-90} (blue), C_{90-120} (green), $C_{>120}$ (red) modes

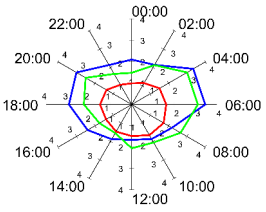

(e) A_{60-90} (blue), C_{90-120} (green), $C_{>120}$ (red) modes

Figure A.20: Summer 2012 spider plots for EPT station. Submodes are classified in 2-hour intervals in order to acquire the diurnal variation for the frequency of occurrence. Subfigures a, b, d: the frequency of occurrence for $N_{<15}$ to $C_{>120}$ modes. The hour displayed on the axes corresponds to the start of the 2-hour interval (GMT), while the smaller numbers (in size) 50, 38, 25 correspond to frequency of occurrence. Subfigures c,e: the average number concentration depending on the hour of the day, for all modes in thousands of particles per cm^3.

Table A.3: EPT most frequent mode combinations

Mode Combination	$\mathbf{A_{30-60}C_{>120}}$ **Median**	$\mathbf{N_{15-30}A_{30-60}C_{>120}}$ **Median**	$\mathbf{N_{15-30}A_{60-90}C_{>120}}$ **Median**	$\mathbf{N_{15-30}C_{>120}}$ **Median**	$\mathbf{A_{60-90}C_{>120}}$ **Median**	$\mathbf{A_{60-90}}$ **Median**
N_{15-30} σ_g	-	1.4	1.6	1.6	-	-
N_{15-30} d_g	-	21	23	26	-	-
N_{15-30} N	-	0.9×10^3	0.7×10^3	1.3×10^3	-	-
A_{30-60} σ_g	1.9	1.5	-	-	-	-
A_{30-60} d_g	41	48	-	-	-	-
A_{30-60} N	1.8×10^3	1.6×10^3	-	-	-	-
A_{60-90} σ_g	-	-	1.5	-	2.3	2.4
A_{60-90} d_g	-	-	69	-	68	77
A_{60-90} N	-	-	1.2×10^3	-	2×10^3	3.7×10^3
$C_{>120}$ σ_g	1.6	1.7	1.5	1.9	1.5	-
$C_{>120}$ d_g	175	158	197	140	208	-
$C_{>120}$ N	1.4×10^3	1.8×10^3	1×10^3	1.8×10^3	0.8×10^3	-
Frequency %	35	11	8	8	7	6

Regional Background station (FIN)

Nucleation events are infrequent during summer months at the Regional Background station [76]. We have identified 5 nucleation events during these days. The small Nucleation mode observed in Figure A.21 ($N_{<15}$) could be mainly attributed to particles formed elsewhere and transported to the station. The station is probably influenced by both katabatic and anabatic winds. At FIN (Figures A.21, A.22-Appendix), $C_{>120}$, C_{90-120}, A_{60-90}, and A_{30-60} are almost constant in frequency and particle number concentration throughout daytime. N_{15-30} and $N_{<15}$ are probably related to local pollution events and transported aerosol from cities within Crete produced by combustion, cooking, and activities related to tourism. Overall, the particle number concentration is dominated by Aitken and Accumulation modes, which are almost stable throughout day and night.

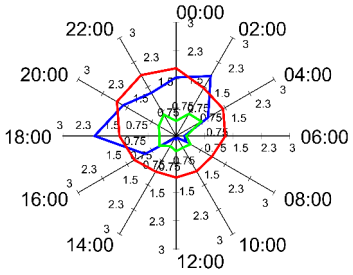

(a) $N_{<15}$ mode (blue), N_{15-30} (green), A_{30-60} (red) modes

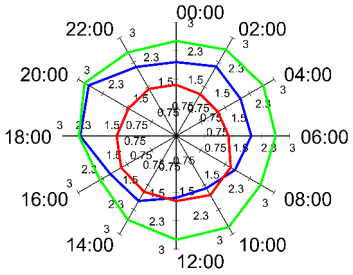

(b) A_{60-90} (blue), C_{90-120} (green), $C_{>120}$ (red) modes

Figure A.21: Summer 2012 diurnal variation spider plots for the Regional Background station. Submodes (whose characteristics and sources are described in detail in Table 4) are classified in 2-hour intervals in order to acquire the diurnal variation for the average number concentration. The hour displayed on the axes corresponds to the start of the 2-hour interval (UTC), while smaller numbers (in size) correspond to the average number concentration depending on the hour of the day, for all modes in thousands of particles per cm^3.

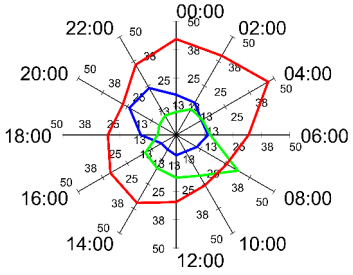

(a) $N_{<15}$ mode (blue), N_{15-30} (green), A_{30-60} (red) modes

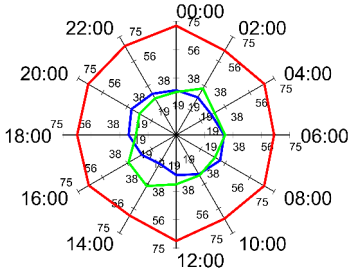

(b) A_{60-90} (blue), C_{90-120} (green), $C_{>120}$ (red) modes

Figure A.22: Summer 2012 spider plots for FIN. Submodes are classified in 2-hour intervals in order to acquire the diurnal variation for the frequency of occurrence. Numbers 1, 3, 5 correspond to hours of day (GMT), while the smaller numbers 50, 38, 25 correspond to frequency of occurrence.

Table A.4: ICE-HT station Clusters identified

Cluster Results	σ_g **Median**	d_g **Median**	**N Median**	**Cluster Source**	**Frequency %**
ICE-HT-SD-Cluster1	3	13.6	1.8×10^3	Vehicle emissions	5
ICE-HT-SD-Cluster2	1.61	115.5	2.6×10^3	Condensational growth-Regional Background	80
ICE-HT-SD-Cluster3	1.93	68.2	2×10^3	Vehicle emmissions, aged	17
ICE-HT-SD-Cluster4	1.3	18.7	0.9×10^3	Vehicle emissions, growth	9
ICE-HT-SD-Cluster5	1.48	27	1×10^3	Vehicle emmissions, fresh	9

Cluster analysis of size distribution at different station types

ICE-HT station identified clusters

The HDBSCAN algorithm results presented in Table A.4 were the best fit for the dataset. In order to acquire these results, a minimum cluster size of 69 data points was used.

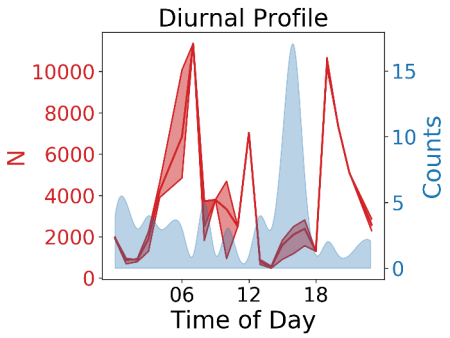

(a) ICE-HT-SD-Cluster1

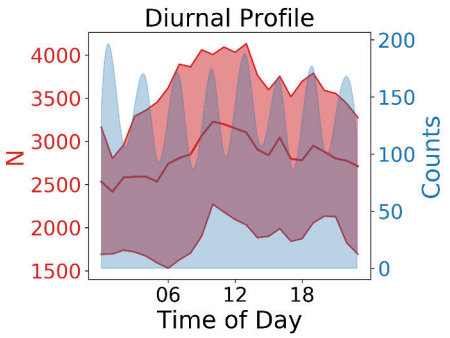

(b) ICE-HT-SD-Cluster2

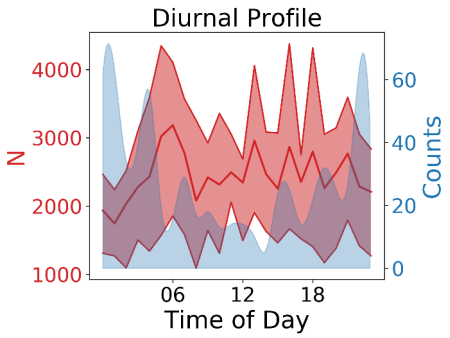

(c) ICE-HT-SD-Cluster3

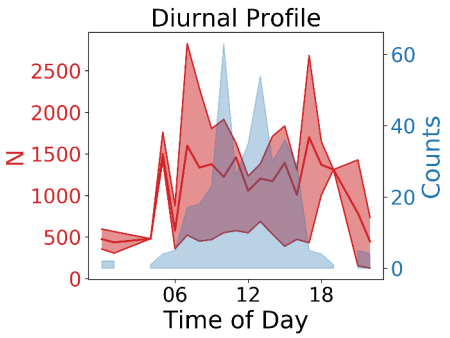

(d) ICE-HT-SD-Cluster4

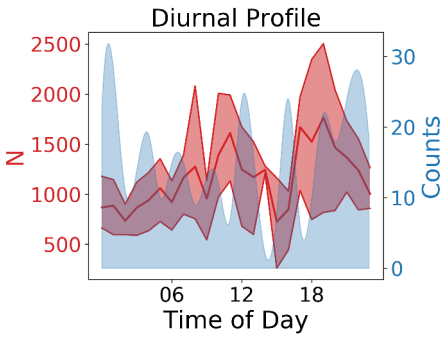

(e) ICE-HT-SD-Cluster5

Figure A.23: ICE-HT diurnal frequency of occurrence (blue area, counts per hour) and median number concentration N_{median} (red line) for all identified clusters. The area around N_{median} corresponds to 25^{th} and 75^{th} percentiles of the quantity.

In Figure A.23, the frequency of occurrence at each hour of the day is presented for each cluster. ICE-HT-SD-Cluster1 has a frequency of 5% and should mainly be attributed to local pollution

events. As one may observe in Figure A.23, it has low frequency but high number concentration in the morning and evening (local traffic), but high frequency at noon (growth of particles nucleated at another location). It has a very large σ_g, indicating a very broad size distribution. ICE-HT-SD-Cluster2 is very stable in frequency and particle number concentration throughout the day, as one may observe in Figure A.23. This mode is the sum of the regional background concentration and the coagulation of particles produced locally. ICE-HT-SD-Cluster3 has increased frequency at night, but increased particle number concentration in the morning and the evening, which probably relates it also to traffic exhaust occurring at the city highways and center, and subsequently transported to ICE-HT. ICE-HT-SD-Cluster4 has increased frequency and number concentration in the middle of the day, therefore it probably relates to M-OOA. It has a very small σ_g, indicating a very narrow size distribution. ICE-HT-SD-Cluster 5 has increased frequency and number concentration in the evening. This cluster is mainly attributed to fresh vehicle emissions.

Table A.5: DEM station Clusters identified

Cluster Results	σ_g **Median**	d_g **Median**	**N Median**	**Cluster Source**	**Frequency %**
DEM-SD-Cluster1	1.36	532.6	0.8×10^3	Condensational growth-long range transport	1.5
DEM-SD-Cluster2	3	20.2	4.2×10^3	Vehicle emmissions, fresh, nucleation	30
DEM-SD-Cluster3	1.58	227.5	3.1×10^3	Condensational growth-long range transport	1
DEM-SD-Cluster4	1.58	17.8	2.3×10^3	Nucleation, Vehicle emissions	44
DEM-SD-Cluster5	1.8	115.5	4.2×10^3	Condensational growth-regional background	83

DEM station identified clusters

The HDBSCAN algorithm results presented in Table A.5 were the best fit for the dataset. In order to acquire these results, a minimum cluster size of 44 data points was used.

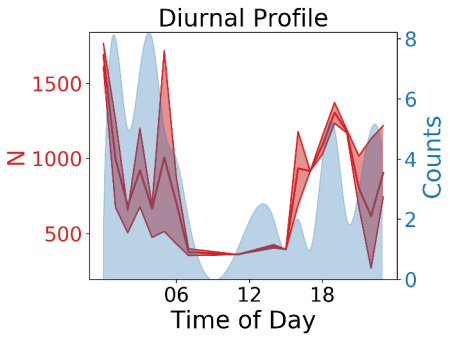

(a) DEM-SD-Cluster1

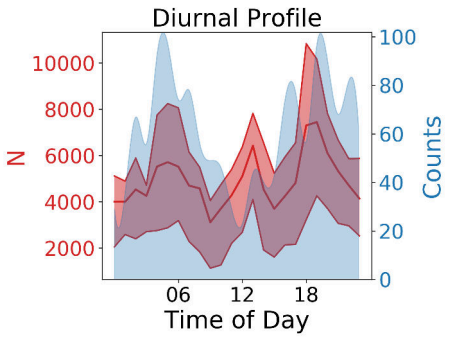

(b) DEM-SD-Cluster2

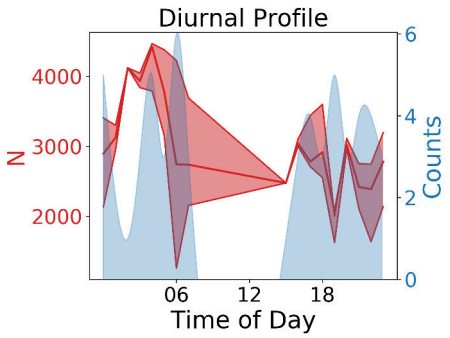

(c) DEM-SD-Cluster3

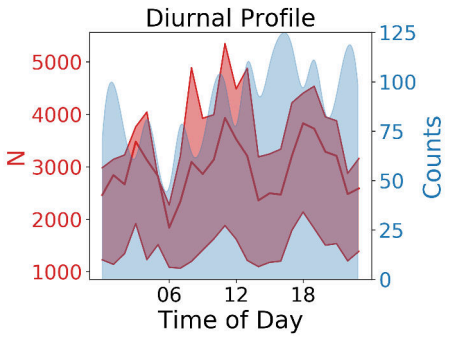

(d) DEM-SD-Cluster4

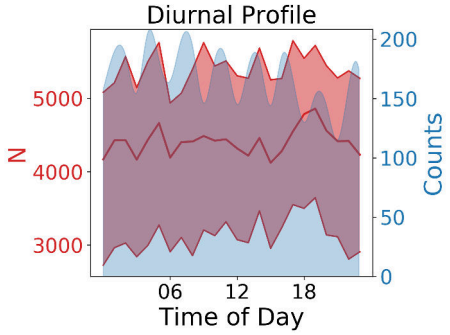

(e) DEM-SD-Cluster5

Figure A.24: DEM diurnal frequency of occurrence (blue area, counts per hour) and median number concentration N_{median} (red line) for all identified clusters. The area around N_{median} corresponds to 25^{th} and 75^{th} percentiles of the quantity.

In Figure A.24, the frequency of occurrence at each hour of the day is presented for each cluster.

DEM-SD-Cluster1 has a frequency of 1.5% and should mainly be attributed to local and transported dust. It occurs mostly at nighttime. DEM-SD-Cluster2 is very broad, including fresh and aged vehicle emissions. In Figure A.24, one may observe that its frequency and number concentration peaks coincide with the early morning and evening traffic. There is also a peak at noon, which could be partly attributed to NPF. DEM-SD-Cluster3 has increased frequency in the morning and the evening, which probably indicates that it is the product of coagulation of particles from smaller modes. Taking into account its d_g, one would expect that it is transported from another area, probably due to the Etesian flow. DEM-SD-Cluster4 has increased frequency and number concentration in the morning and in the evening, but also in the middle of the day, therefore it probably relates to freshly emitted traffic particles and particle nucleation. DEM-SD-Cluster5 is very stable in frequency and particle number concentration throughout the day, as one may observe in Figure A.24. This mode is the sum of the regional background concentration and the coagulation of particles produced locally.

Table A.6: EPT station clusters identified

Cluster Results	σ_g **Median**	d_g **Median**	**N Median**	**Cluster Source**	**Frequency %**
EPT-SD-Cluster1	3	61.3	1.7×10^3	Vehicle emissions, aged	1
EPT-SD-Cluster2	1.57	35.3	1.2×10^3	Vehicle emissions, growth of nucleated particles	96
EPT-SD-Cluster3	1.64	172	1.4×10^3	Condensational growth - regional background	76

EPT station identified clusters

The HDBSCAN algorithm results presented in Table A.6 were the best fit for the dataset. In order to acquire these results, a minimum cluster size of 16 data points was used.

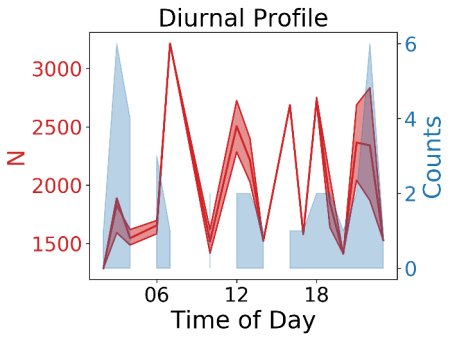

(a) EPT-SD-Cluster1

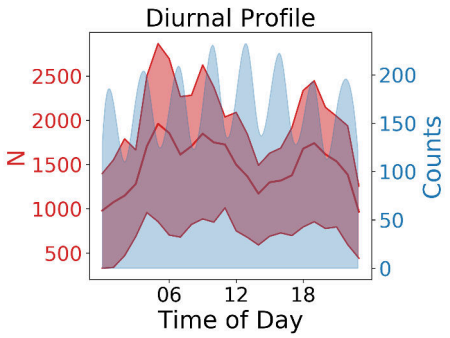

(b) EPT-SD-Cluster2

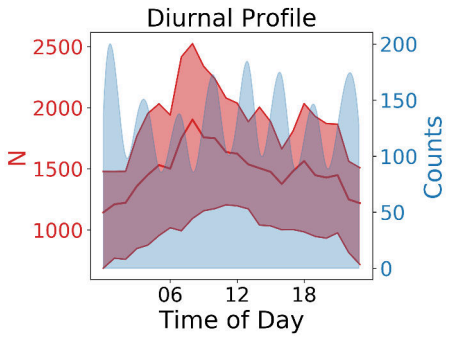

(c) EPT-SD-Cluster3

Figure A.25: EPT diurnal frequency of occurrence (blue area, counts per hour) and median number concentration N_{median} (red line) for all identified clusters. The area around N_{median} corresponds to 25^{th} and 75^{th} percentiles of the quantity.

In Figure A.25, the frequency of occurrence at each hour of the day is presented for each cluster.

EPT-SD-Cluster1 has a frequency of 1% and should mainly be attributed to aged transported vehicle emissions from the city center. It mostly occurs at nighttime. EPT-SD-Cluster2 is very stable in frequency, including fresh and aged vehicle emissions. In Figure A.25, one may observe that its frequency and number concentration peaks coincide with the early morning and evening traffic. Overall, it is a cluster with a very high frequency (96%) that represents the background concentration of the city. EPT-SD-Cluster3 is very stable in frequency and particle number concentration throughout the day. This mode is the sum of the regional background concentration and the coagulation of particles produced locally.

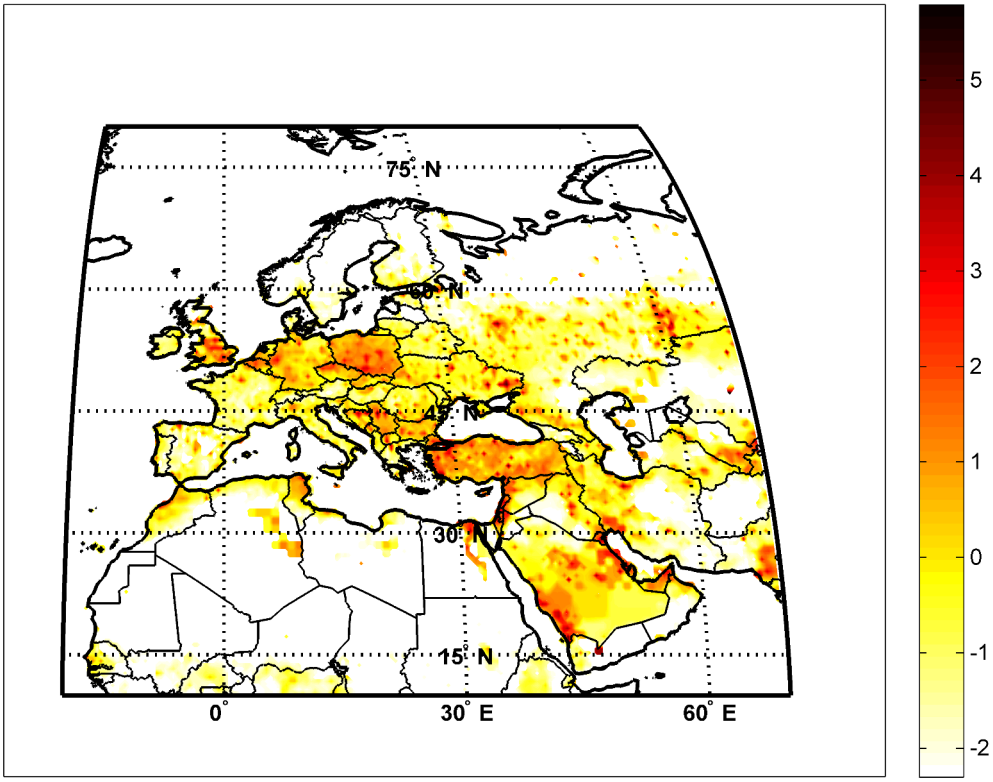

Figure A.26: Natural logarithm of SO_2 emissions (kt/year) map from ECLIPSE EMISSION DATASET (http://eclipse.nilu.no/) for 2015. Anthropogenic sources are included, excluding shipping and aviation.

Regional background concentration variation based on air masses origin.

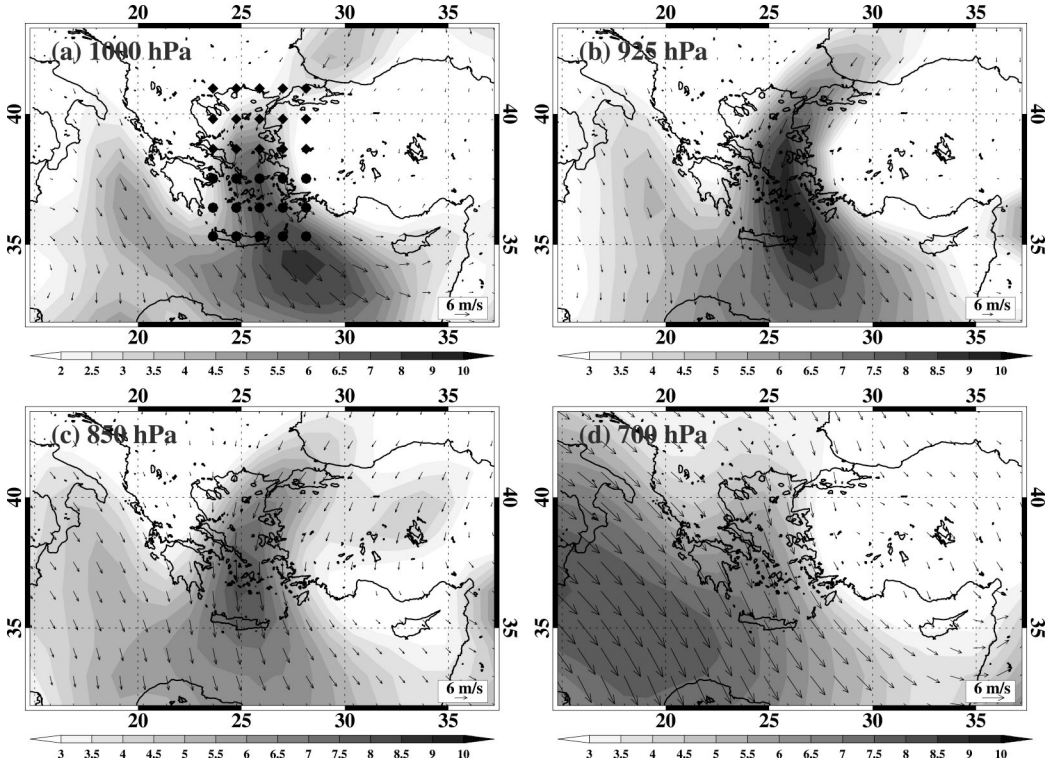

Figure A.27: Mean Jule - August wind at (a) 1000, (b) 925, (c) 850, and (d) 700 hPa. Wind speed (ms^{-1}, shaded) is also plotted. The grid points included in the calculation of mean wind speed and direction over the Aegean are marked with dots only in the upper left map [93].

Table A.7: Characteristics of Regional background concentration for air masses with partly southern origin.

Cluster	**South-West plumes**	**South-West plumes**	**South-West plumes**
Results	20^{th} **percentile**	50^{th} **percentile**	80^{th} **percentile**
σ_g	1.4	1.54	1.65
d_g	122.7	163.8	196.7
N	0.5×10^3	0.7×10^3	2.5×10^3

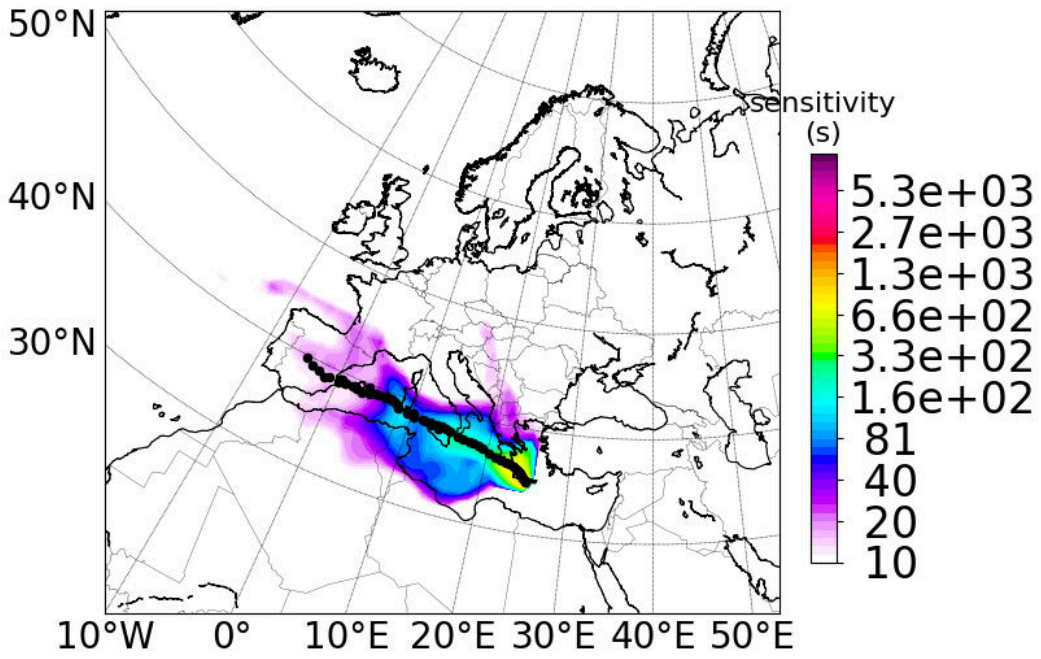

Figure A.28: Map showing the air mass origin for the 26 3-hour FLEXPART sensitivity plumes that the air masses are partly transported from the south.

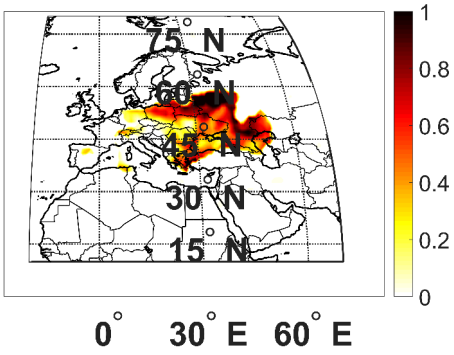

(a) PSCF at the 80^{th} percentile

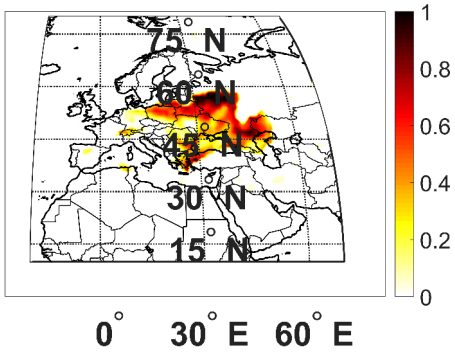

(b) PSCF at the 85^{th} percentile

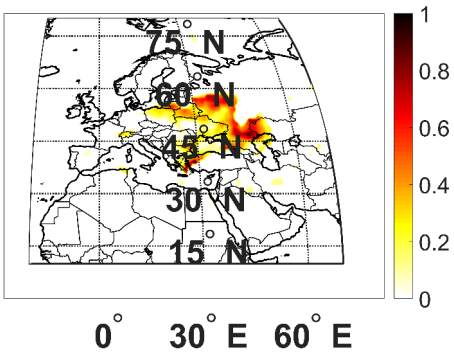

(c) PSCF at the 90^{th} percentile

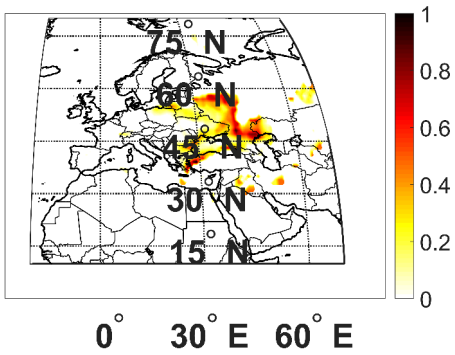

(d) PSCF at the 95^{th} percentile

Figure A.29: Potential Source Contribution Function analysis (PSCF).

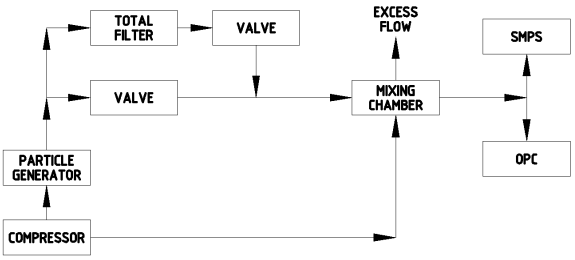

Figure A.30: Calibration of SMPS-OPC ERI setup.

A.2 Appendix of the chapter "A new method for the retrieval of the equivalent refractive index of atmospheric aerosols"

Method Evaluation - Calibration Procedure

Figure A.30 displays the layout during the experiments. The aerosol particle generator used was a TOPAS ATM 220, which provided a high number of aerosol particles in the overlapping range of the two instruments. The calibration was carried out at DEM-GAW station and the instruments were sampling from their station inlet line. The generated aerosol was brought to a mixing chamber, where it was mixed with dry, particle free air. Mixing ratios varied, depending on the final concentration needed for the calibration. The aerosol was then lead to the inlet line, into a vertical nafion dryer with a length of 60 cm and internal diameter approximately 1 cm, and was subsequently distributed to the two instruments. During the experiments, inlet flow had an RH equal to 15 ± 9%, while temperature was 22 ± 8 °C.

PSL spheres with nominal diameters of 262 and 490 nm were diluted in MilliQ water. A bimodal NSD for both instruments was expected, as both instruments are calibrated with this compound.

As denoted in Figure A.31, the OPC has a peak at 430 nm (corresponding to 490 nm PSL), while we cannot be sure about the peak for the 262 nm PSL. The lognormal fit based on the three first size bins of the OPC overestimates the PSL concentration dramatically. This is probably due to the fact that the boundaries of the first size bin of the OPC are not correctly attributed, while in these

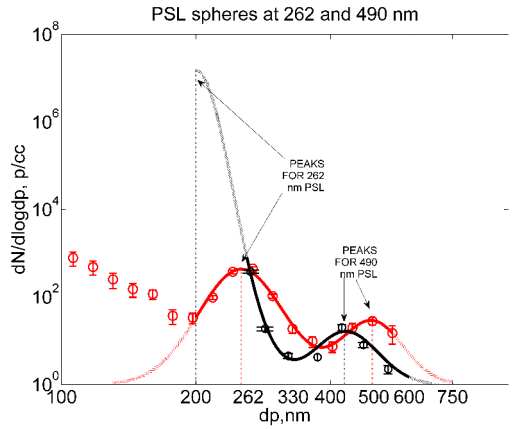

Figure A.31: Calibration of SMPS-OPC ERI with PSL spheres at 262 and 490 nm. Red circles correspond to SMPS average concentration during the PSL experiment. Error bars correspond to the standard deviation from the average of each bin, for all size distributions measured during the experiment. Red line corresponds to SMPS lognormal distributions identified for the PSL sizes. Intense red color corresponds to the part of the lognormal distribution based on measurements, while the fade red line corresponds to the extended part of the distribution. The black circles, error bars and line correspond to the OPC. We observe that while SMPS sizes PSL correctly at 490 nm, OPC has a peak concentration at 430 nm size bin.

size bins aerosol particles with smaller sizes than the nominal minimum are counted. Therefore, we have a very steep slope of the lognormal distribution fitted to the data, thus the error in the number concentration predicted is very large.

In order to correct for the sizing error, we consider the OPC measurement principal. It can be described as follows: Air containing particles is drawn through an illuminated volume, where light scattered by single particles is sensed and converted to an electrical signal, whose pulse height is analyzed. The pulse height is used to infer particle size. The measurement of many particles results in a size distribution. Particle concentration in every size bin is determined from total counts in that size range. An error in the electrical signal pulse height would result in erroneous sizing of the aerosol particle. We need to know the relation of this error in the working size range of the instrument.

The simplest assumption would be that the error is related to the amplification of the scattering signal, therefore the scattering signal expected should be divided by a constant factor. To investigate that, we plot S_{sca} calculated by Mie theory and given particle size, for the OPC geometry, assuming homogeneous aerosol particles with an RI equal to 1.585. According to the PSL experiment, 490 nm particles are detected as 430 nm. We need to adjust S_{sca} so that the signal that corresponds to a particle with a diameter of 430 nm, will now correspond to a 490 nm particle. According to Figure A.32 (Appendix), if we divide S_{sca} by a factor of 1.5, we have a signal curve that corrects the error observed at the PSL experiment.

The size correction for the OPC is incorporated into the optimal solution algorithm by assuming it is a constant factor in the common size range of the two instruments.

SMPS sizes the 490 nm PSL correctly and slightly underestimates the 262 nm PSL.

If the linear correction assumption is valid in the particle size range of interest, we would expect that the ERI we retrieve would be close to 1.585. The approximate solution for ERI during the PSL experiment was ranging from 1.57 to 1.6, which is close to the target value of 1.585. Therefore, we conclude that the OPC sizing error in the particle size range we are interested in, is corrected by applying a constant amplitude factor.

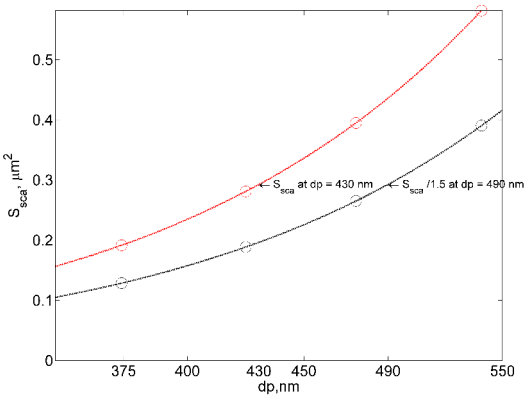

Figure A.32: S_{sca} values versus homogeneous aerosol particle diameter dp for the OPC geometry and RI = 1.585. Theoretical scattering intensity according to equation 2 multiplied by particle cross section (red line); idem, as previously, divided by 1.5 (blue line); We observe that the theoretically predicted S_{sca}, when we apply this factor, can approach the experimentally determined one, within the particle size range we are interested in.

S_{sca} has to be corrected in the ERI retrieval algorithm according to equation A.1.

$$S_{sca-cor} = \frac{S_{sca}}{1.5} \tag{A.1}$$

The next step is to find a correction factor for aerosols with different RI. The final ERI correction equation for the sizing error and their dependence on aerosol RI follows:

$$RI = \ 1.7 * \exp((-(ERI_{COR} - 2)/1.5)^2) \tag{A.2}$$

The next step is to evaluate if the above mentioned corrections can be applied to aerosols with different RI.

Figure A.33 displays the calibration of SMPS-OPC derived ERI with dried generated test aerosol, ERI to Literature RI (RI) for common pure compounds characteristic for atmospheric aerosol. There is good correlation between the ERI calculated and the RI of each substance. The median values for each calibration experiment are shown in red diamonds. DEHS calibration has 10 5-minute points while Ammonium Sulfate 15 and PSL more than 20. The black line displayed is the fit of all data points for the 3 calibration experiments.

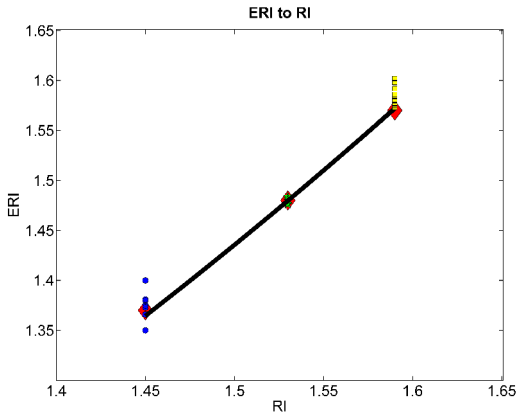

Figure A.33: Best fit (black line) ERI to RI values for the calibration of SMPS-OPC with generated aerosol. Blue spots denote the 5-minute data points for the DEHS Experiment; green spots denote the 5-minute data points for the Ammonium Sulfate Experiment; yellow rectangles denote the 5-minute data points for the PSL Experiment; red diamonds denote the median value for each experiment.

Table A.8: Literature RI (RI) versus ERI median values (MED ERI). Standard deviation (STDEV ERI), regression analysis R-squared and standard error (STD ERROR) are also presented.

PARAMETER	DEHS	AMMONIUM SULFATE	PSL SPHERES Diameter = 490 nm
RI	1.45	1.53	1.585
MED ERI	1.37	1.48	1.57
STDEV ERI	0.02	0.01	0.01
R-squared	0.98		
STD ERROR	0.1		

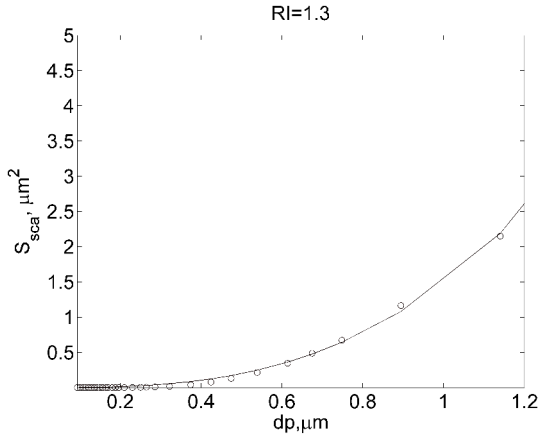

Figure A.34: Best fit of S_{sca} at OPC diameter range for RI = 1.3.

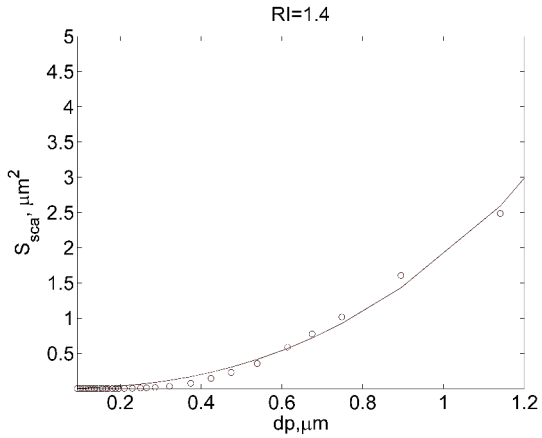

Figure A.35: Best fit of S_{sca} at OPC diameter range for RI = 1.4.

In Table A.8 we present the results of the calibration experiments. We observe that ERI underestimates RI for ammonium sulfate and DEHS, while it overestimates RI for PSL. Nevertheless, R-squared is close to 1 for all experiments, and the standard error is 0.1. Therefore we conclude that there is a good correlation between ERI and RI for these measurements.

Scattering effective cross section to diameters in the OPC size range and below

Figures A.34-A.39.

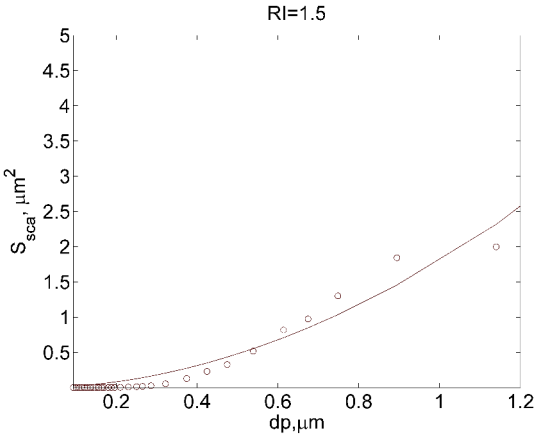

Figure A.36: Best fit of S_{sca} at OPC diameter range for RI = 1.5.

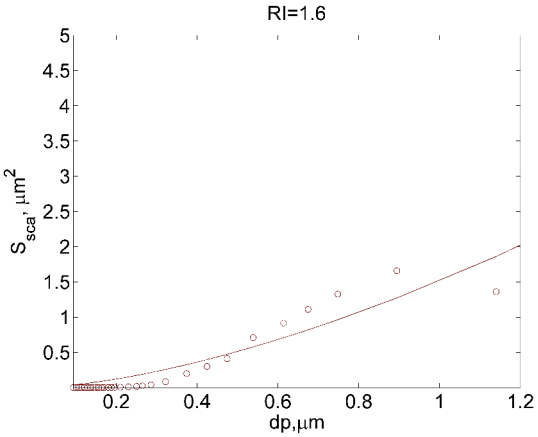

Figure A.37: Best fit of S_{sca} at OPC diameter range for RI = 1.6.

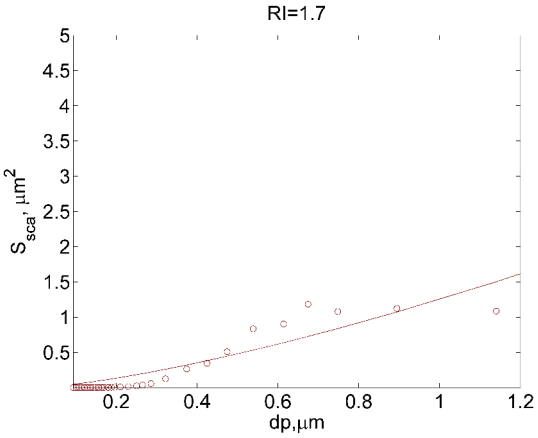

Figure A.38: Best fit of S_{sca} at OPC diameter range for RI = 1.7.

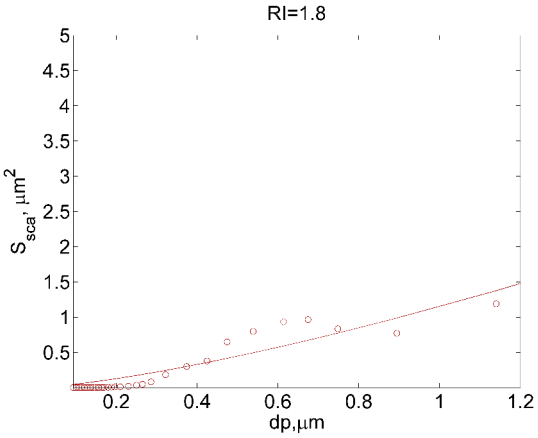

Figure A.39: Best fit of S_{sca} at OPC diameter range for RI = 1.8.

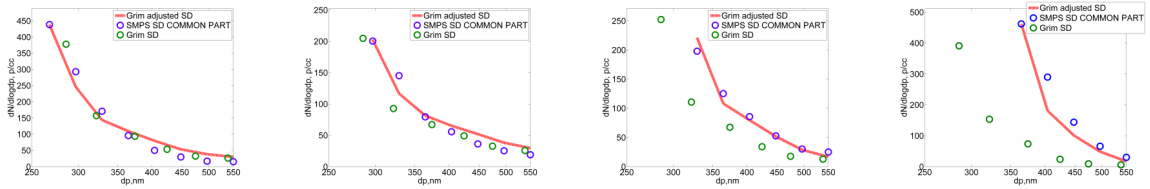

(a) SMPS - OPC FIT, ERI = 1.8

(b) SMPS - OPC FIT, ERI = 1.7

(c) SMPS - OPC FIT, ERI = 1.6

(d) SMPS - OPC FIT, ERI = 1.5

Figure A.40: SMPS - OPC fit examples for various ERI values. Green circles denote the measured OPC size distribution (NSD), blue circles denote the SMPS NSD, while the red line represents the OPC, adjusted NSD. We observe that the final adjusted Grim OPC size distribution (SD) is very close to the SMPS NSD. Also, the OPC NSD at 430 nm is moved to the right to 490 nm at ERI = 1.6, as it should, in order to compensate for the sizing error in relation to the SMPS observed at the PSL calibration experiment.

SMPS-OPC FIT in the overlapping range

Figure A.40.

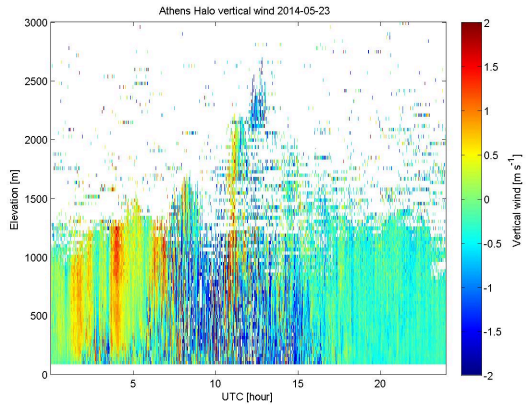

Figure A.41: We observe that from 8:30 to 13:30 (IC filter measurement hours) there is strong mixing in the vertical, leading dust to DEM station. RI_{LI} was also calculated for this day (19:00-20:00 UTC).

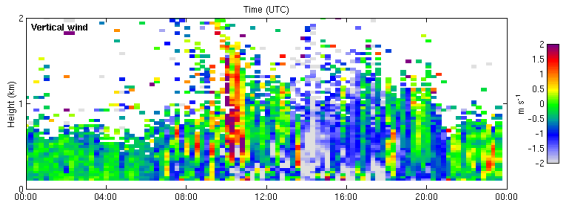

Figure A.42: We observe that from 8:30 to 13:30 (IC filter measurement hours) there is strong mixing in the vertical, leading dust to DEM station.

HALO lidar vertical wind for days that the hypothesis of uniform dust concentration during the day does not hold

In the calculation of RI_{IC}, the 24h average of dust concentration (calculated from XRF measurements) was used. The hypothesis was that dust concentration during the day was closely following the concentration of other aerosol constituents. This does not hold for days that exhibit strong mixing in the vertical during the filter measurements and less mixing the rest of the day, while a Sahara dust event is occurring. ERI_{COR} calculated for the hours corresponding to RI_{IC}, is significantly higher during these days, as expected. (Figures A.41-A.42).

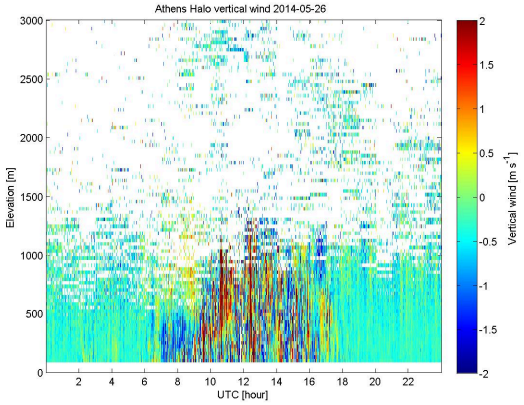

Figure A.43: We observe that from 19:00-20:00 there is strong mixing in the vertical.

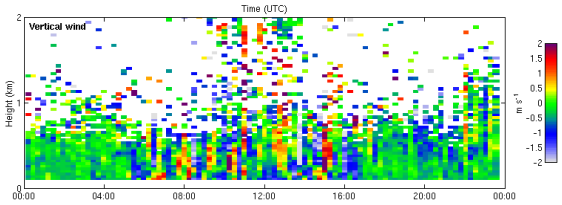

Figure A.44: We observe that from 22:00-23:00 there is strong mixing in the vertical.

HALO lidar vertical wind for days that RI_{LI} was calculated

Figures A.43-A.45.

On 17th of June 2014, 19:00-20:00, and 18th of June 2014, 19:00-20:00, the boundary layer heights are approximately 1.1 km and 1.0 km respectively, according to ECMWF ERA-INTERIM data.

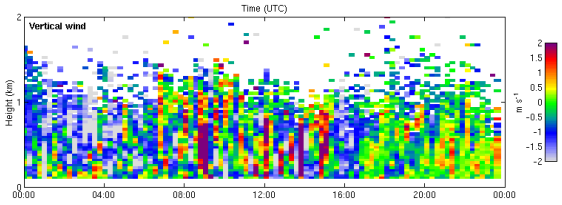

Figure A.45: We observe that from 18:45-19:45 there is strong mixing in the vertical.

Table A.9: RI_{IC} and ERI_{COR} obtained by IC, EC/OC, XRF and SMPS-OPC instruments.

Date, Time (UTC)	ERI_{COR}	RI_{IC}
21st of May 2014, 19:00-22:00	1.66±0.1	1.58±0.15
28th of May 2014, 08:30-13:30	1.65±0.1	1.59±0.15
28th of May 2014, 19:00-22:00	1.67±0.1	1.59±0.15
30th of May 2014, 08:30-13:30	1.65±0.1	1.58±0.15
30th of May 2014, 19:00-22:00	1.63±0.1	1.57±0.15
6th of June 2014, 19:00-22:00	1.65±0.1	1.58±0.15
7th of June 2014, 19:00-22:00	1.65±0.1	1.58±0.15

RI_{IC} and ERI_{COR} available values

The available values for RI_{IC} and ERI_{COR} are presented in Table A.9.

RI_{LI} and ERI_{COR} available values

The available values for RI_{LI} and ERI_{COR} are presented in Table A.3. In Figure 6, the value corresponding to the 22nd of June is not included, because RH was not available for that day.

A.3 Appendix of the chapter "Comparison of in situ and remote sensing aerosol measurements in the Athens Metropolitan Area"

ϵ vertical distribution plots for the days selected in order to compare in situ - remote sensing instruments

Table A.10: Comparison of lidar derived RI values (RI_{LI}) to ERI_{COR} values obtained by SMPS-OPC.

Date, Time (UTC)	ERI_{COR}	RI_{LI}
23th of May 2014, 19:00-20:00	1.61±0.1	1.56±0.1
26th of May 2014, 19:00-20:00	1.63±0.1	1.6±0.1
7th of June 2014, 22:00-23:00	1.67± 0.1	1.61±0.1
10th of June 2014, 18:45-19:45	1.68±0.1	1.62±0.1
17th of June 2014, 19:00-20:00	1.66±0.1	1.59±0.1
18th of June 2014, 19:00-20:00	1.58±0.1	1.59±0.1
22nd of June 2014, 19:00-20:00	1.6±0.1	1.56±0.1

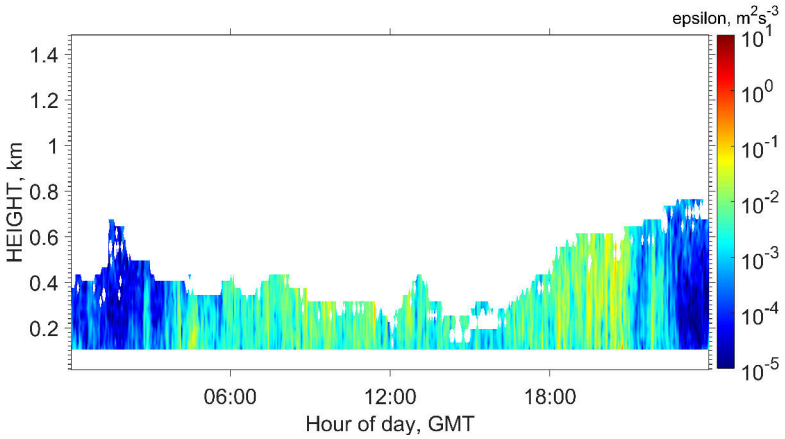

Figure A.46: ϵ vertical distribution plot for the 21^{st} of May, indicating turbulence in the troposphere. Notice that there is turbulence extending to a height approximating 800 m agl at 20:00 to 21:00, during in situ - remote sensing measurements comparison.

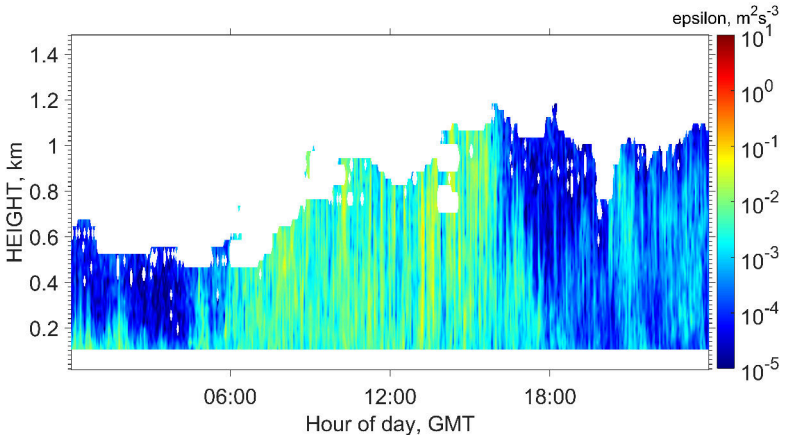

Figure A.47: ϵ vertical distribution plot for the 22^{nd} of May, indicating turbulence in the troposphere. Notice that there is turbulence extending to a height above 1,000 m agl at 20:30 to 21:30, during in situ - remote sensing measurements comparison.

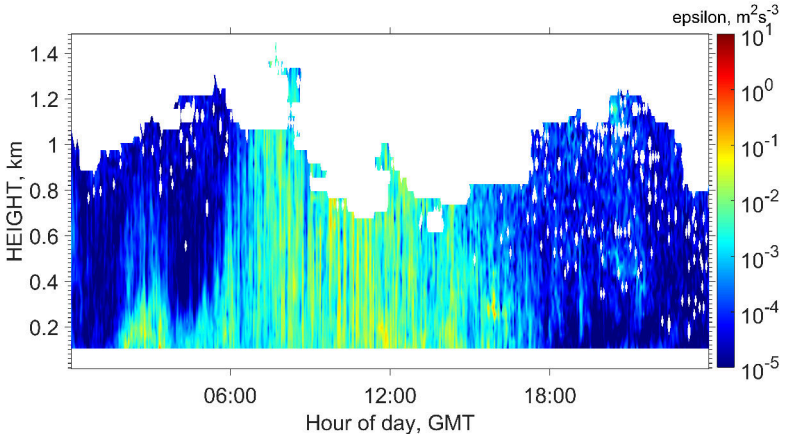

Figure A.48: ϵ vertical distribution plot for the 23^{rd} of May, indicating turbulence in the troposphere. Notice that there is turbulence extending to a height above 1,000 m agl at 20:30 to 21:30, during in situ - remote sensing measurements comparison.

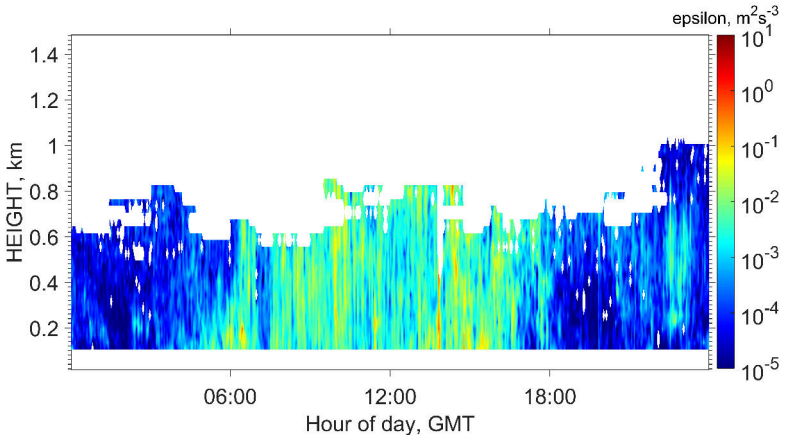

Figure A.49: ϵ vertical distribution plot for the 7^{th} of June, indicating turbulence in the troposphere. Notice that there is turbulence extending to a height above 1,000 m agl at 22:00 to 23:00, during in situ - remote sensing measurements comparison.

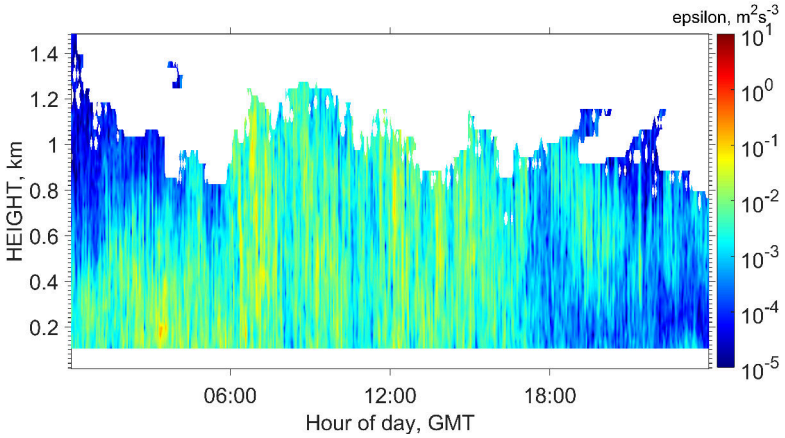

Figure A.50: ϵ vertical distribution plot for the 10^{th} of June, indicating turbulence in the troposphere. Notice that there is turbulence extending to a height above 1,000 m agl at 18:45 to 19:45, during in situ - remote sensing measurements comparison.

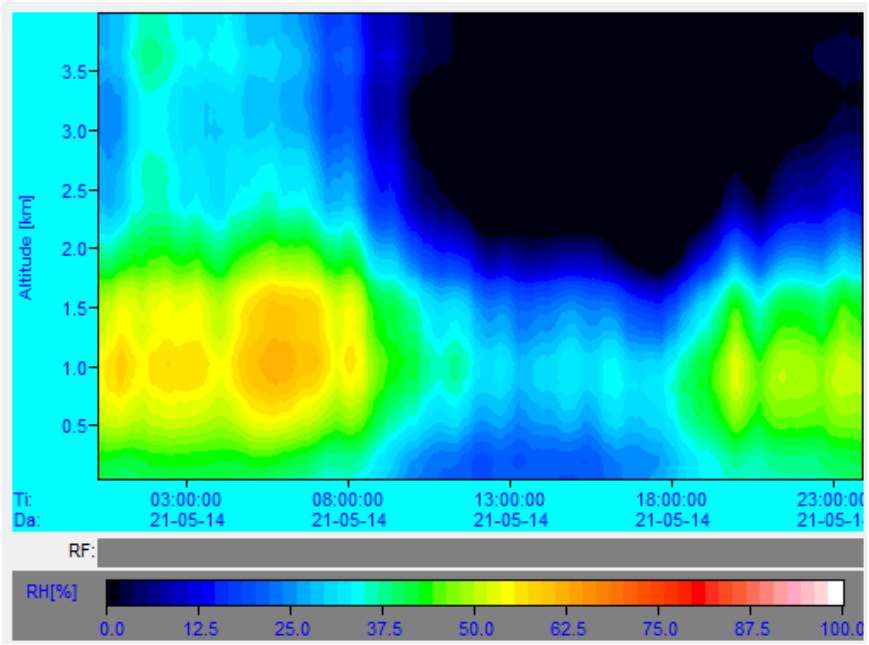

Figure A.51: RH vertical distribution plot for the 21^{st} of May. Notice that at 1,000 m agl, RH is approximately 55 at 20:00 to 21:00.

RH vertical distribution plots for the days selected in order to compare in situ - remote sensing instruments

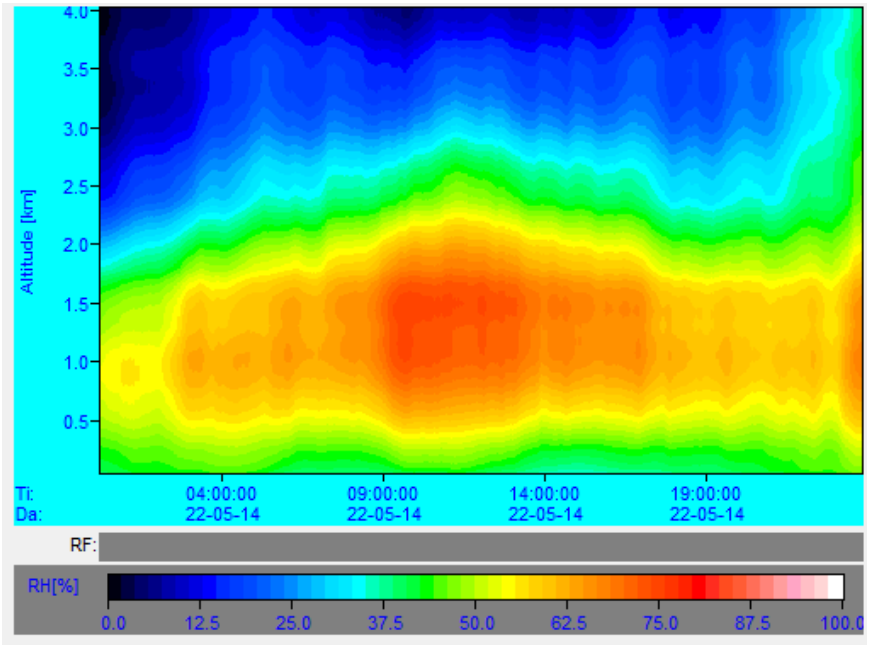

Figure A.52: RH vertical distribution plot for the 22^{nd} of May. Notice that at 1,000 m agl, RH is approximately 55 at 20:30 to 21:30.

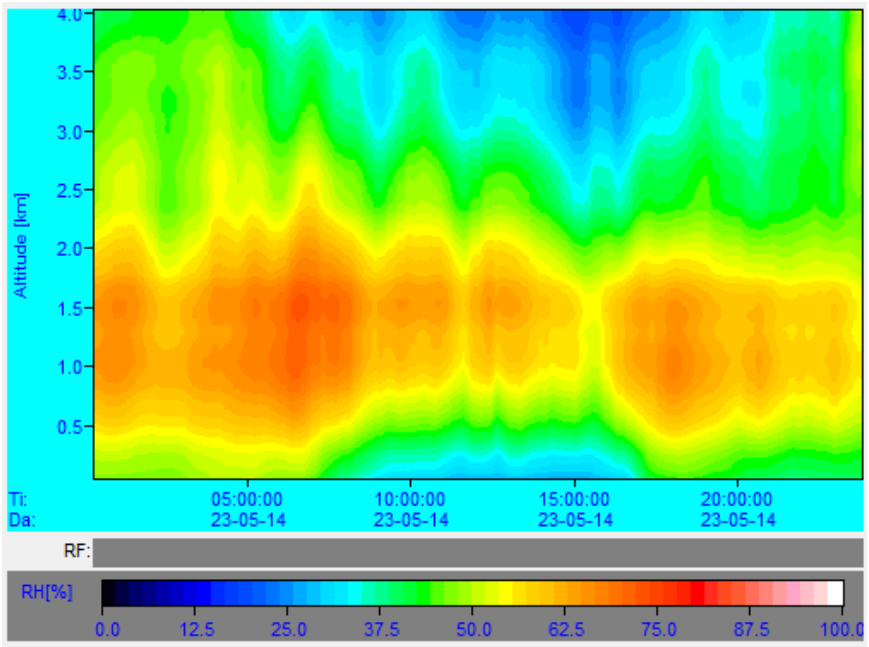

Figure A.53: RH vertical distribution plot for the 23^{rd} of May. Notice that at 1,000 m agl, RH is approximately 62.5 at 20:30 to 21:30.

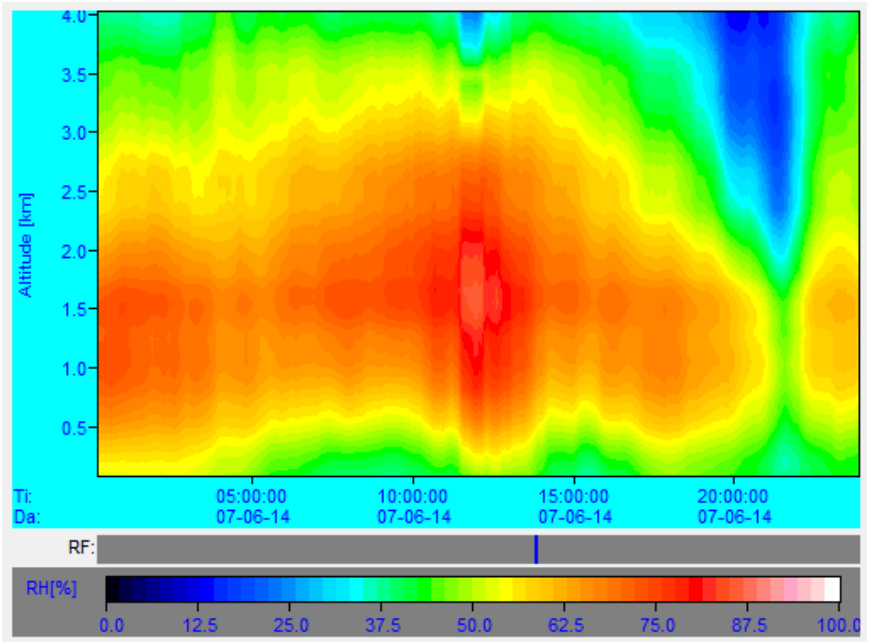

Figure A.54: RH vertical distribution plot for the 7^{th} of June. Notice that at 1,000 m agl, RH is approximately 55 at 22:00 to 23:00.

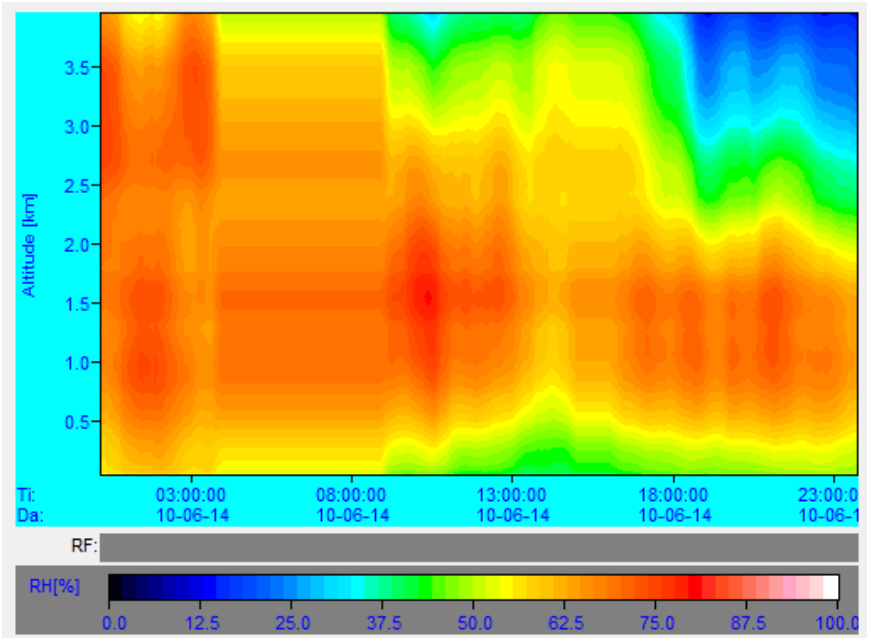

Figure A.55: RH vertical distribution plot for the 10^{th} of June. Notice that at 1,000 m agl, RH is approximately 75 at 18:45 to 19:45.

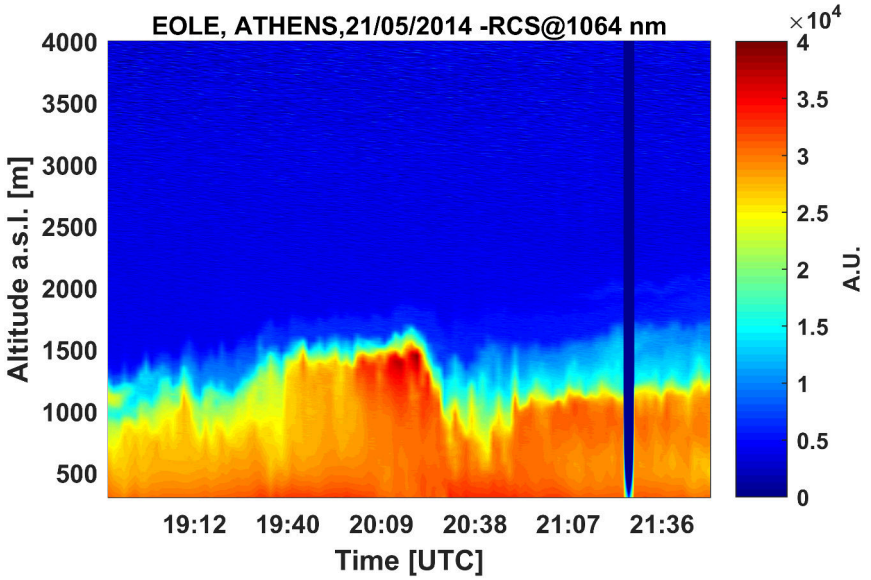

Figure A.56: Temporal evolution of the range-corrected lidar signal (RCS) at 1064 nm observed by EOLE, in arbitrary units (A.U.) for the 21^{st} of May. Notice that up to 1,000 m agl, there is a uniform aerosol concentration at 20:00 to 21:00.

Temporal evolution of the range-corrected lidar signal (RCS) at 1064 nm observed by EOLE, in arbitrary units (A.U.) for the days selected in order to compare in situ - remote sensing instruments

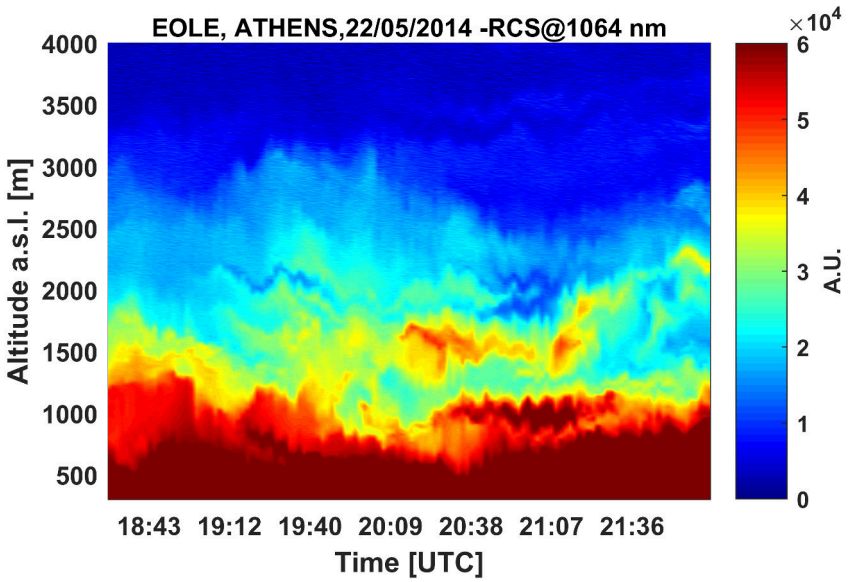

Figure A.57: Temporal evolution of the range-corrected lidar signal (RCS) at 1064 nm observed by EOLE, in arbitrary units (A.U.) for the 22^{nd} of May. Notice that up to 1,000 m agl, there is a uniform aerosol concentration at 20:30 to 21:30.

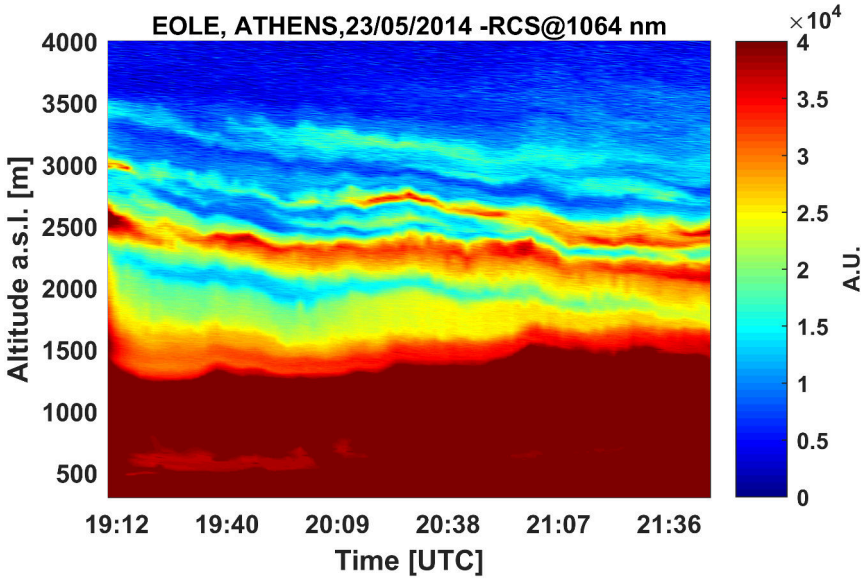

Figure A.58: Temporal evolution of the range-corrected lidar signal (RCS) at 1064 nm observed by EOLE, in arbitrary units (A.U.) for the 23^{rd} of May. Notice that up to 1,000 m agl, there is a uniform aerosol concentration at 20:30 to 21:30.

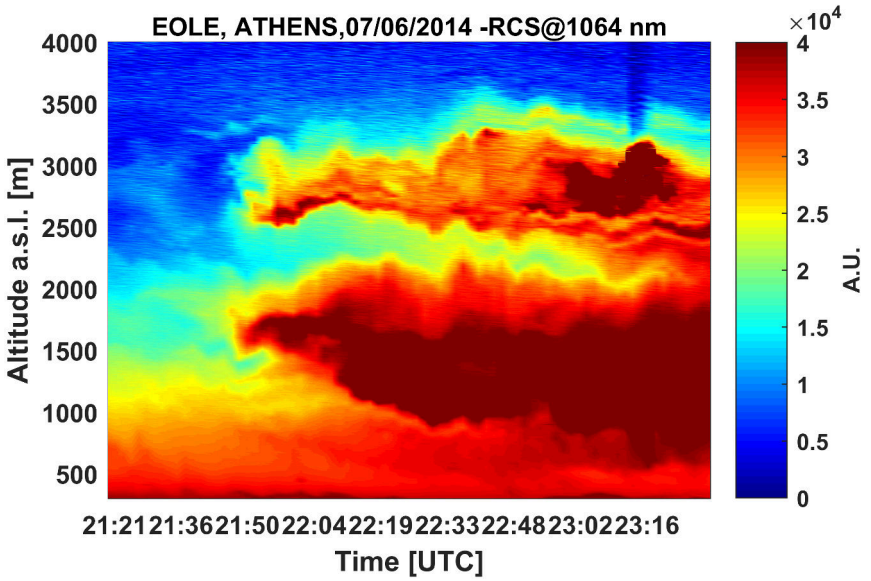

Figure A.59: Temporal evolution of the range-corrected lidar signal (RCS) at 1064 nm observed by EOLE, in arbitrary units (A.U.) for the 7^{th} of June. Notice that up to 1,000 m agl, there is an almost uniform aerosol concentration profile at 22:00 to 23:00.

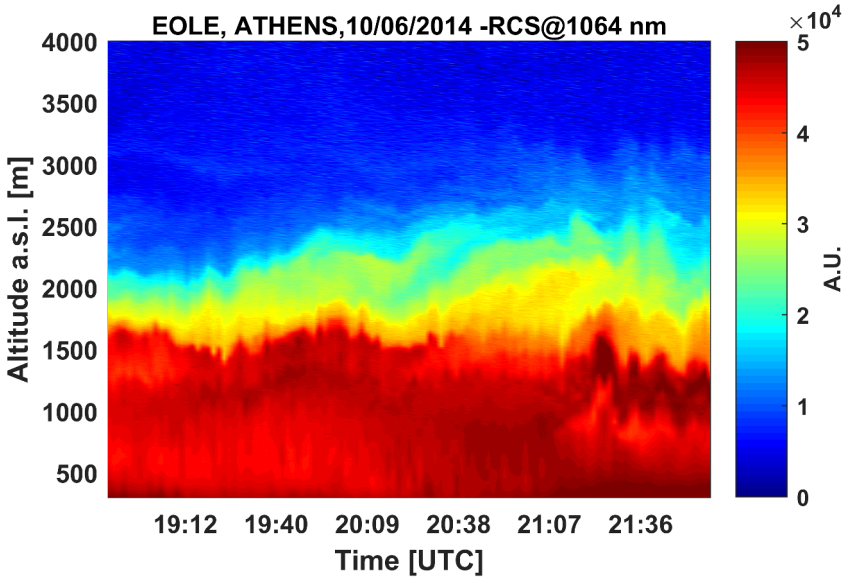

Figure A.60: Temporal evolution of the range-corrected lidar signal (RCS) at 1064 nm observed by EOLE, in arbitrary units (A.U.) for the 10^{th} of June. Notice that up to 1,000 m agl, there is an almost uniform aerosol concentration profile at 18:45 to 19:45.

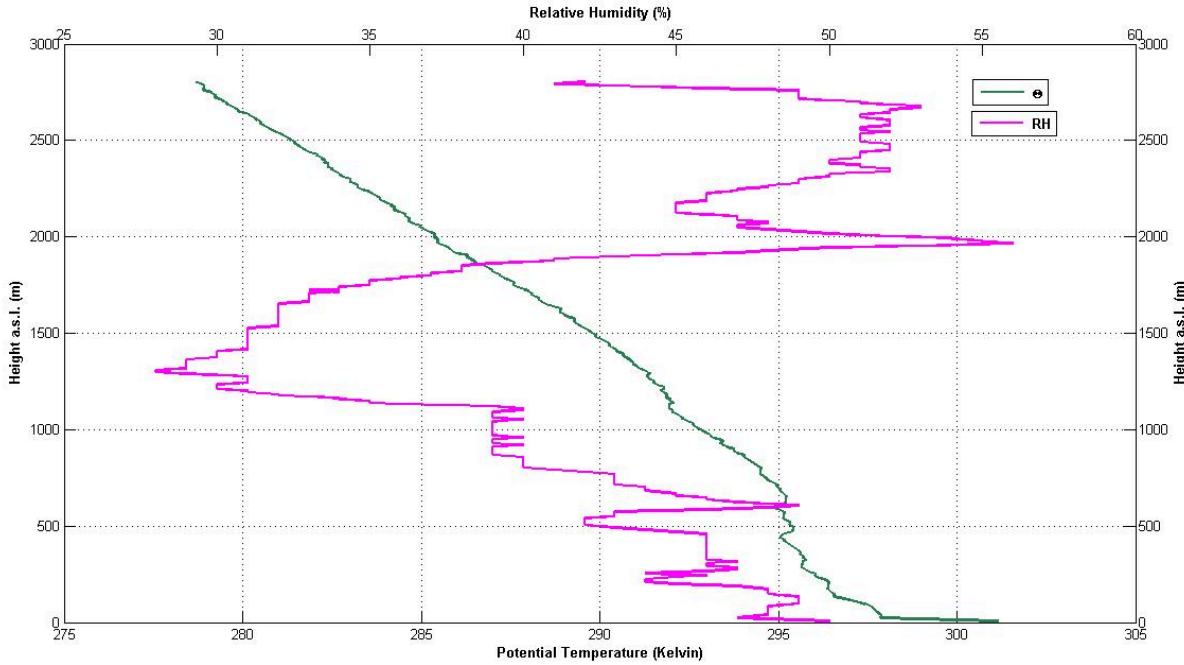

Figure A.61: Radiosounding at 12:00 UTC on the 27^{th} of May indicates a distinct aerosol layer mainly between 1,000 and 2,000 m (low Relative Humidity, an indication of a Sahara dust layer).

EOLE radiosonde profile on the 27^{th} of May.

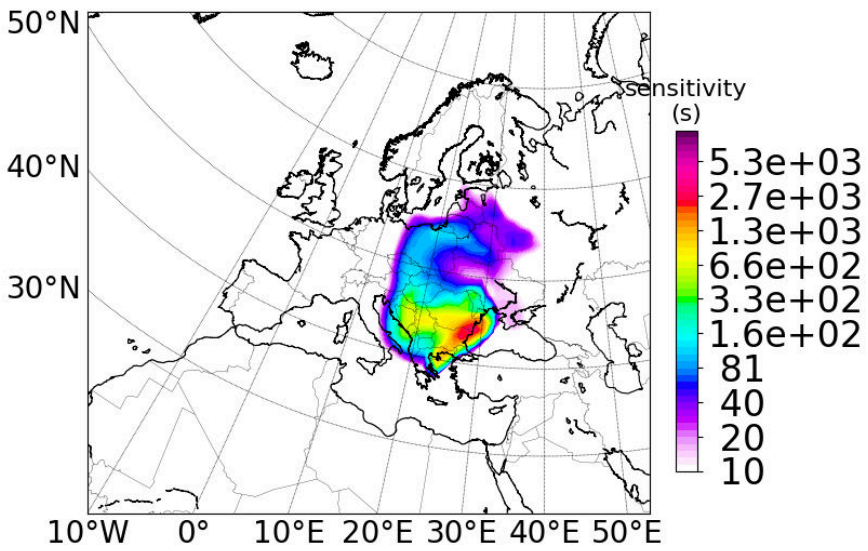

Figure A.62: Origin of airmasses for the 21^{st} of May, 18:00 - 21:00 UTC.

Origin of airmasses for comparison days

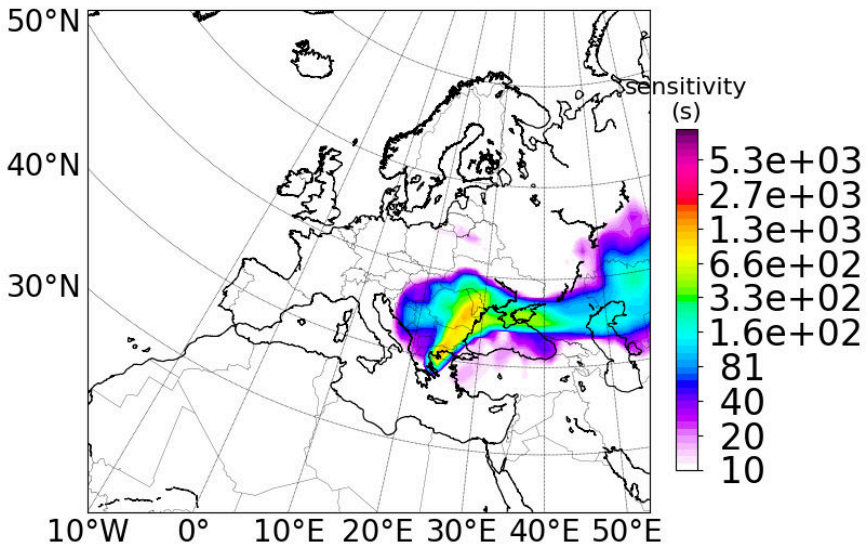

Figure A.63: Origin of airmasses for the 22^{nd} of May, 18:00 - 21:00 UTC.

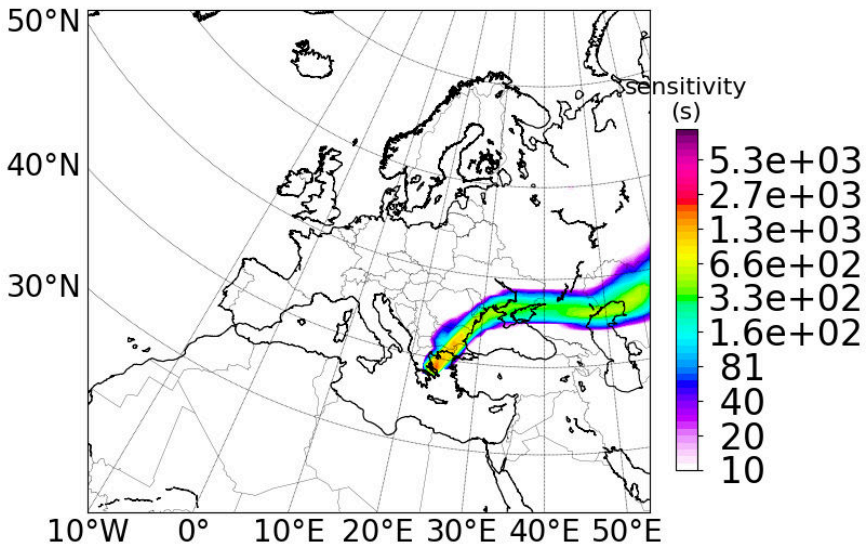

Figure A.64: Origin of airmasses for the 23^{rd} of May, 18:00 - 21:00 UTC.

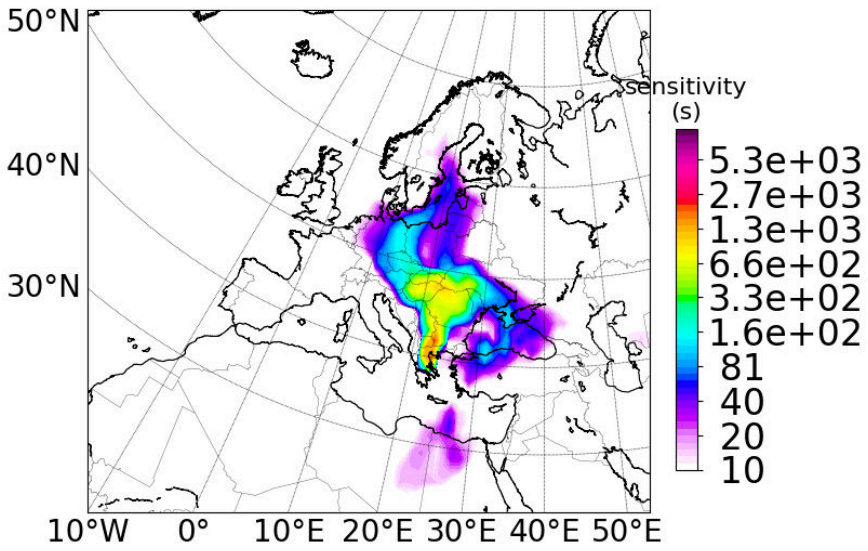

Figure A.65: Origin of airmasses for the 7^{th} of June, 21:00 - 24:00 UTC.

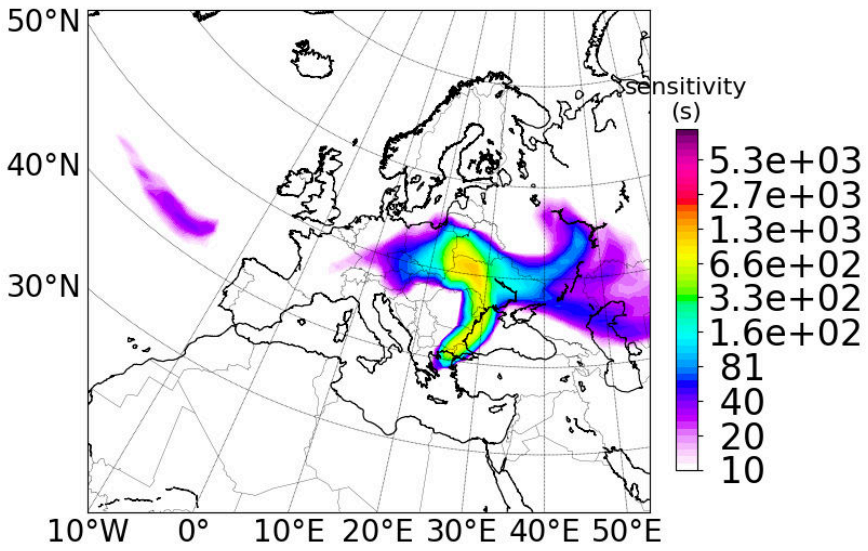

Figure A.66: Origin of airmasses for the 10^{th} of June, 18:00 - 21:00 UTC.

A.4 Publication list

1. Papayannis, A. D., Argyrouli, A., Bougiatioti, A., Remoundaki, E., Vratolis, S., Nenes, A., Solomos, S., Komppula, M., Giannakaki, E., Kalogiros, J. A., Banks, R. F., Eleftheriadis, K., Mantas, E., Diapouli, E., Tzanis, C. G., Kazadzis, S. A., Binietoglou, I., Labzovski, L. N., Vande Hey, J. D., Zerefos, C. S. An overview from hygroscopic aerosols to cloud droplets: The HygrA-CD campaign in the Athens basin. Sci. Total Environ. 574, 216-233, 2017.

2. Bougiatioti, A., Argyrouli, A., Solomos, S., Vratolis, S., Eleftheriadis, K., Papayannis, A., Nenes, A. CCN Activity, variability and influence on Droplet formation during the HygrA-Cd Campaign in Athens. Atmosphere 8 (108), 2017.

3. Diapouli, E., Manousakas, M., Vratolis, S., Vasilatou, V., Maggos, T., Saraga, D., Grigoratos, T., Argyropoulos, G., Voutsa, D., Samara, C., Eleftheriadis, K. Evolution of air pollution source contributions over one decade, derived by PM10 and PM2.5 source apportionment in two metropolitan urban areas in Greece. Atmos. Environ. 164, 416-430, 2017.

4. Diapouli, E., Manousakas, M. I., Vratolis, S., Vasilatou, V., Pateraki, S.,Bairachtari, K. A., Querol, X., Amato, F., Alastuey, A., Karanasiou, A. A., Lucarelli, F., Nava, S., Calzolai, G., Gianelle, V. L., Colombi, C., Alves, C., Custodio, D., Pio, C., Spyrou, C., Kallos, G. B., Eleftheriadis, K. AIRUSE-LIFE + : Estimation of natural source contributions to urban ambient air PM10 and PM2:5 concentrations in southern Europe - implications to compliance with limit values. Atmos. Chem. Phys., 17, 3673-3685, 2017.

5. Lazaridis, M., Eleftheriadis, K., Zdimal, V., Schwarz, J.,Wagner, Z., Ondracek, J., Drossinos, Y., Glytsos, T., Vratolis, S., Torseth, K., Moravec, P., Hussein, T., Smolik, J. Number concentrations and modal structure of indoor/outdoor fine particles in four European cities. Aerosol Air Qual. Res. 17 (1), 131-146, 2017.

6. Pandolfi, M., Alados-Arboledas, L., Alastuey, A., Andrade, M., Artinano, B., Backman, J., Baltensperger, U., Bonasoni, P., Bukowiecki, N., Collaud Coen, M., Conil, S., Coz, E., Crenn, V., Dudoitis, V., Ealo, M., Eleftheriadis, K., Favez, O., Fetfatzis, P., Fiebig, M., Flentje,

H., Ginot, P., Gysel, M., Henzing, B., Hoffer, A., Holubova Smejkalova, A., Kalapov, I., Kalivitis, N., Kouvarakis, G., Kristensson, A., Kulmala, M., Lihavainen, H., Lunder, C., Luoma, K., Lyamani, H., Marinoni, A., Mihalopoulos, N., Moerman, M., Nicolas, J., O'Dowd, C., Petaja, T., Petit, J.-E., Pichon, J. M., Prokopciuk, N., Putaud, J.-P., Rodriguez, S., Sciare, J., Sellegri, K., Stamenov, D. B., Swietlicki, E., Titos, G., Tuch, T., Tunved, P., Ulevicius, V., Vaishya, A., Vana, M., Virkkula, A., Vratolis, S., Weingartner, E., Wiedensohler, A., Laj, P. A European aerosol phenomenology- 6: Scattering properties of atmospheric aerosol particles from 28 ACTRIS sites. Atmos. Chem. Phys. 18, 7877-7911, 2018.

7. Perrone, M. G., Vratolis, S., Georgieva, E., Torok, S., Sega, K., Veleva, B., Osan, J., Beslic, I., Kertesz, Z., Pernigotti, D., Eleftheriadis, K., Bellis, C. A. Sources and geographic origin of particulate matter in urban areas of the Danube macro-region: the cases of Zagreb (Croatia), Budapest (Hungary) and Sofia (Bulgaria). Sci. Total Environ. 619-620, 1515-1529, 2018.

8. Schmeisser, L., Backman, J., Ogren, J. A., Andrews, E., Asmi, E., Starkweather, S., Uttal, T., Fiebig, M., Sharma, S., Eleftheriadis, K., Vratolis, S., Bergin, M., Tunved, P., Jefferson, A. Seasonality of aerosol optical properties in the Arctic. Atmos. Chem. Phys. 18, 11599-11622, 2018.

9. Soupiona, O., Papayannis, A., Kokkalis, P., Mylonaki, M., Tsaknakis, G., Argyrouli, A., Vratolis, S. Long-term systematic profiling of dust aerosol optical properties using the EOLE NTUA lidar system over Athens, Greece (2000-2016). Atmos. Environ. 183, 165-174, 2018.

10. Kalogridis, A.-C., Vratolis, S., Liakakou, E., Gerasopoulos, E., Mihalopoulos, N., Eleftheriadis, K. Assessment of wood burning versus fossil fuel contribution to wintertime black carbon and carbon monoxide concentrations in Athens, Greece. Atmos. Chem. Phys. 18, 10219-10236, 2018.

11. Zanatta, M., Laj, P., Gysel, M., Baltensperger, U., Vratolis, S., Eleftheriadis, K., Kondo, Y., Dubuisson, P., Winiarek, V., Kazadzis, S., Tunved, P., Jacobi, H. Effects of mixing state on optical and radiative properties of black carbon in the European Arctic. Atmos. Chem. Phys. 18, 14037-14057, 2018.

12. Vratolis, S., Fetfatzis, P., Argyrouli, A., Papayannis, A., Muller, D., Veselovskii, I., Bougiatioti, A., Nenes, A., Remoundaki, E., Diapouli, E., Manousakas, M., Mylonaki, M., Eleftheriadis, K. A new method to retrieve the real part of the equivalent refractive index of atmospheric aerosols. Journal of Aerosol Science 117, 54-62, 2018.

13. Vratolis, S., Gini, M., Bezantakos, S., Stavroulas, I., Kalivitis, N., Kostenidou, E., Louvaris, E., Siakavaras, D., Biskos, G.,Mihalopoulos, N., Pandis, S. N., Pilinis, C., Papayannis, A., Eleftheriadis, K. Particle number size distribution statistics at City-Centre Urban Background, Urban Background, and Remote stations in Greece during summer. Atmos. Environ. 213, 711-726, 2019.

14. Vratolis, S., Fetfatzis, P., Argyrouli, A., Mylonaki, M., Soupiona, O., Kalogridis, A.-C., Manousakas, M., Bezantakos, S., Binietoglou, I., Labzovski, L., Tzanis, C. G., Mocnik, G., O'Connor, E. J., Muller, D., Papayannis, A., Eleftheriadis, K. Comparison of in situ and remote sensing aerosol measurements in the Athens Metropolitan Area. Atmos. Environ. Under review, 2019.